

**Investigation of In-Situ Electrode Formation
With Respect to Potential Applications in
Intermediate Temperature Solid Oxide Fuel Cells**

Dissertation

zur Erlangung des akademischen Grades

Doktor der Ingenieurwissenschaften

(Dr.-Ing.)

der Technischen Fakultät

der Christian-Albrechts-Universität zu Kiel

Qingping Fang

Kiel, February 2007

1. Gutachter: Prof. Dr. Werner Weppner

2. Gutachter: Prof. Dr. Franz Faupel

Datum der mündlichen Prüfung: 23.04.2007

Contents

List of Symbols.....	I
Abbreviations.....	III
Chapter 1. Introduction.....	1
1.1 Fuel cell technology and state of the arts.....	1
1.2 Problems encountered in developing fuel cells.....	3
1.3 Present approach to solve the problems.....	4
1.4 SEA concept and the aim of this work.....	6
1.5 References.....	7
Chapter 2. Theoretical aspects.....	9
2.1 Fuel cell basics.....	9
2.1.1 Working principle of fuel cells.....	9
2.1.2 Types of fuel cells.....	13
2.2 Introduction to ionics.....	15
2.2.1 General aspects.....	15
2.2.2 Elementary defect chemistry.....	16
2.2.3 Conduction and transport mechanism.....	19
2.2.4 Defect equilibrium and defect diagram.....	23
2.2.5 Generation of OCV.....	28
2.2.6 SEA concept.....	33
2.3 Background to experimental methods.....	34
2.3.1 X-ray powder diffraction.....	34
2.3.2 Thermal analyses.....	35
2.3.3 Impedance spectroscopy.....	35
2.3.4 Gas mixture.....	42
2.3.5 EMF measurements.....	46
2.4 References.....	48

Chapter 3. Material aspects.....	50
3.1 General introduction.....	50
3.2 Fluorite type oxide electrolytes.....	51
3.3 Perovskite type oxide electrolytes I.....	53
3.4 Perovskite type oxide electrolytes II.....	55
3.5 References.....	56
 Chapter 4. Experimental aspects.....	 59
4.1 Sample preparation.....	59
4.1.1 Solid-State Reaction.....	59
4.1.2 Glycine-nitrate combustion.....	61
4.2 XRD.....	63
4.3 Electrical conductivity.....	63
4.4 “Brouwer Spectrometer”.....	64
4.5 EMF measurement.....	65
4.5.1 Kiukkola-Wagner cell.....	65
4.5.2 Gas concentration cell.....	65
4.6 References.....	66
 Chapter 5. Results and discussion I.....	 67
— Materials based on CeO ₂	
5.1 Phase characterization.....	67
5.1.1 CeO ₂ doped with Sm and Pr.....	67
5.1.2 CeO ₂ doped with Sm and other metal ions.....	70
5.2 Electrical conductivity.....	72
5.2.1 CeO ₂ doped with Sm and Pr.....	72
5.2.2 CeO ₂ doped with Sm and other metal ions.....	81
5.3 EMF and dilatometric measurement.....	83
5.4 References.....	84
 Chapter 6. Results and discussion II.....	 86
— Materials based on BaCeO ₃	
6.1 Phase characterization.....	86

6.1.1	$\text{BaCe}_{0.76}\text{Y}_{0.2}\text{Pr}_{0.04}\text{O}_{3-\delta}$	86
6.1.2	$\text{BaCe}_{0.76}\text{Y}_{0.2}\text{Pr}_{0.04}\text{O}_{3-\delta} (\text{TiO}_2)$	87
6.1.3	$\text{BaCe}_{0.8}\text{Y}_{0.2}\text{PrO}_{3-\delta} + \text{Ce}_{0.8}\text{Sm}_{0.2}\text{O}_{1.9}$	88
6.2	Electrical conductivity.....	89
6.2.1	$\text{BaCe}_{0.76}\text{Y}_{0.2}\text{Pr}_{0.04}\text{O}_{3-\delta}$	89
6.2.2	$\text{BaCe}_{0.76}\text{Y}_{0.2}\text{Pr}_{0.04}\text{O}_{3-\delta} (\text{TiO}_2)$	90
6.2.3	$\text{BaCe}_{0.8}\text{Y}_{0.2}\text{PrO}_{3-\delta} + \text{Ce}_{0.8}\text{Sm}_{0.2}\text{O}_{1.9}$	92
6.3	EMF measurement.....	93
6.3.1	$\text{BaCe}_{0.76}\text{Y}_{0.2}\text{Pr}_{0.04}\text{O}_{3-\delta}$	93
6.3.2	$\text{BaCe}_{0.76}\text{Y}_{0.2}\text{Pr}_{0.04}\text{O}_{3-\delta} (\text{TiO}_2)$	94
6.4	References.....	95
Chapter 7. Results and discussion III.....		96
—— Materials based on LaGaO_3		
7.1	Phase characterization.....	96
7.1.1	$\text{La}_{0.8}\text{Sr}_{0.2}\text{Ga}_{0.6}\text{Fe}_{0.4-x}\text{Ti}_x\text{O}_{3-\delta} (x=0\sim 0.2)$	96
7.1.2	$\text{La}_{0.56}\text{Sr}_{0.44}\text{Ga}_{0.64}\text{Mg}_{0.16}\text{Me}_{0.2}\text{O}_{2.8} (\text{Me}=\text{Ti} \text{ and } \text{Sn})$	98
7.1.3	$\text{La}_{0.9}\text{Sr}_{0.1}\text{Ga}_{1-x-y}\text{Mg}_y\text{Mn}_x\text{O}_{3-\delta} (x, y=0\sim 0.2)$	99
7.2	Electrical conductivity.....	100
7.2.1	$\text{La}_{0.8}\text{Sr}_{0.2}\text{Ga}_{0.6}\text{Fe}_{0.4-x}\text{Ti}_x\text{O}_{3-\delta} (x=0\sim 0.2)$	100
7.2.2	$\text{La}_{0.56}\text{Sr}_{0.44}\text{Ga}_{0.64}\text{Mg}_{0.16}\text{Me}_{0.2}\text{O}_{2.8} (\text{Me}=\text{Ti} \text{ and } \text{Sn})$	105
7.2.3	$\text{La}_{0.9}\text{Sr}_{0.1}\text{Ga}_{1-x-y}\text{Mg}_y\text{Mn}_x\text{O}_{3-\delta} (x, y=0\sim 0.2)$	111
7.3	References.....	138
Chapter 8. Summary.....		139
Chapter 9. Outlook.....		142
Acknowledgements.....		143
Curriculum Vitae.....		144

List of Symbols

a_i	Activity of species i
C	Capacitance
C_{dl}	Double layer capacitance
C_{geom}	Geometrical capacitance
C_{int}	Interface capacitance
C_{gb}	Grain boundary capacitance
c	Concentration of charge carriers
D_i	Diffusivity of the species i
D_i^T	Tracer diffusion coefficient of species i
\tilde{D}_i	Chemical diffusion coefficient of species i
E	Electromotive force
e	Electron
F	Faraday's constant
f	Frequency
f_i	Correlation factor
h	Electron hole
I	Electrical current
i^*	Neutral species i
j	Partial flux density; imaginary unit
j_i	Partial flux density of species i
j^*	Neutral species j
k	Boltzmann's constant; equilibrium constant
L_D	Debye Length
\log	Common logarithm with base 10
\ln	Natural logarithm with base e (~ 2.718281828459)
P	Partial pressure
q	Elementary charge
R	Gas constant; electrical resistance

R_{ct}	Charge-transfer resistance
R_{gb}	Grain boundary resistance
r	Ionic radii
T	Absolute temperature
t	Time; tolerance factor
t_i	Transference number of species i
U	Voltage
Z	Impedance
Z_W	Warburg impedance
z_i	Number of species i
α	Thermal expansion coefficient
ΔE_a	Formation energy
ΔG	Gibbs free energy change
ΔH	Enthalpy change
ΔS	Entropy change
δ	Oxygen deficiency
ε	Dielectric constant
ε_0	Permittivity in vacuum
θ	Phase shift between voltage and current
η_i	Electrochemical potential of species i
μ_i	Chemical potential of species i
σ	Electrical conductivity
Φ	Electrostatic potential
ω	Angular frequency

Abbreviations

AC	Alternating current
AFC	Alkaline fuel cell
APU	Auxiliary Power Unit
AR	Alkaline Resistant
BCY	Yttria doped barium cerate
BNC	Bayonet Neill-Concelman
CHP	Combined Heat and Power systems
CN	Coordination number
DC	Direct current
DIL	Dilatometry
DMFC	Direct methanol fuel cell
DOE	Department of Energy
DTA	Differential Thermal Analysis
EDB	Electrolyte domain boundary
EIS	Electrochemical impedance spectroscopy
EMF	Electromotive force
HDW	Howaldtswerke-Deutsche Werft GmbH
IS	Impedance spectroscopy
FCVs	Fuel cell vehicles
JCPDS	Joint Committee for Powder Diffraction Studies
LSGM	Strontium and magnesium doped lanthanum gallate
MCFC	Molten carbonate fuel cell
MIEC	Mixed ionic and electronic conductor
NASA	National Aeronautics and Space Administration

OCV	Open circuit voltage
PAFC	Phosphoric acid fuel cell
PEM	Polymer electrolyte membrane fuel cell
PEN	Positive electrode/Electrolyte/Negative electrode
R&D	Research and development
SDC	Samarium doped ceria
SEA	Single element arrangement
SECA	Solid State Energy Conversion Alliance
SEM	Scanning electron microscope
SOFC	Solid oxide fuel cell
TGA	Thermogravimetric analysis
TEC	Thermal expansion coefficient
XRD	X-ray diffraction
YSZ	Yttria stabilized zirconia

Chapter 1

Introduction

1.1. Fuel cell technology and state of the arts

It has been more than 160 years since 1839, when Sir William Robert Grove (1811-1896), a British judge and scientist, produced his 'gas battery', which would later be known as the world's first fuel cell. The term 'fuel cell' was first used by the chemists Ludwig Mond (1839-1909) and Charles Langer in 1889 as they attempted to build the practical device using air and industrial coal gas.

The interest on Grove's invention began to diminish soon after people had realized that there were many scientific obstacles to overcome before the commercial application of fuel cells. Also partly because of the 'success' of the internal combustion engine and the widespread exploitation of fossil fuels by the end of the 19th century, the development of fuel cell towards the real applications was slow.

The first truly workable fuel cell, a 5kW system that was capable of powering welding machinery, was demonstrated by Francis Thomas Bacon (1904-1992) in 1959, which was the first alkaline fuel cell (AFC). In the next year, Harry Karl Ihrig demonstrated a 20 horsepower tractor driven by Fuel cells. Research in the fuel cell field became exciting again from the early 1960s, partly driven by funding from NASA who was looking for low weight, clean and highly efficient electricity sources for their space program. But it's only limited in the space applications, due to the very high cost. The real serious effort trying to commercialize the fuel cell applications all over the world started from the 1970s, when governments tried to reduce their dependence on petroleum imports and find the solutions to the growing environment and energy crises.

Today fuel cells are attracting more and more attentions from the world because of their high efficiency, zero emissions and silence. Compared to the normal internal combustion engine, whose efficiency is limited to about 30%, current fuel cells, when operated alone have efficiencies of about 40%~55%, and when they are used with Combined Heat and Power systems (CHP) they can reach efficiencies of 80% [1]. Since the output of an ideal fuel cell is pure water, the emissions are extremely low. Another advantage of fuel cells is the silence of operation, which is important for many applications. All these futures make fuel cells an excellent choice of the future of power generation

Due to the capability of producing any power in the range of 1W~10MW, fuel cells can be used almost anywhere if power is required. However issues remain, such as standardization, pricing, safety and electrical and mechanical interface. These issues must be addressed before

mass production. A few applications could include:

- i) **Personal Electronic Devices (<1kW)**
Fuel cell has the potential to get into every electronic device we come in contact with. It offers the possibility with energy life measured in days or weeks, rather than hours. Many companies are working on developing fuel cells that could replace conventional batteries, and have demonstrated the prototype fuel cell modules for laptop, cell phones, PDA, MP3 player, and so on. Nowadays fuel cell systems can be packaged in containers of the same size and weight as conventional batteries and is recharged by refilling a fuel cartridge.
- ii) **Transportation (1kW~200kW)**
Fuel cells are being widely investigated to fit the requirement of either propulsive power or Auxiliary Power Unit (APU) in all transportation fields, from bicycle to spacecraft. Nearly all the big vehicle manufacturers are involved in this area. Several prototype vehicles have been demonstrated. Fuel cell cars and buses are available in the market, although the prices are still much high (1M\$/car, 2M\$/bus). HDW produced the world's first PEM fuel cell powered submarine, using the Siemens PEM units, which are ordered by a growing number of countries worldwide. A number of technical problems still remain, many relating to on-board fuel reformers and the fueling infrastructure, as well as high cost barriers. In addition, gasoline/electric hybrid vehicles have emerged recently. So the widespread commercialization of automotive fuel cells is not expected in the coming few years. With respect to the aircraft application, both Boeing and Airbus are concentrating on creating a heavy-duty APU for airplanes, and both are looking to the mid 2010s for the first on-board prototype [2].
- iii) **Stationary Power Production and Backup (1MW~10MW)**
Larger-scale fuel cells make it possible that the power generation could become so decentralized that each housing or apartment complex could be self-sustained with its own power. Hospitals and airports could have backup power supplies in case of a power failure. The major hurdle to overcome is still the cost. Fuel cells developed for the space program in the 1960s and 1970s were extremely expensive (\$600,000/kW). But as R&D has progressed in the last 40 years, the cost of fuel cells has dropped largely; and the current cost is about \$1,500/kW. According to the goal of the Solid State Energy Conversion Alliance (SECA), which was formed by the Department of Energy (DOE), the cost must be lowered down to \$400/kW by the end of this decade [3].

1.2. Problems encountered in developing fuel cells

Despite of the simple principle, high efficiency, zero pollutes and noise emission, and also the worldwide R&D, there is still quite a long way to go before the commercialization of the 'old' fuel cell technology. The high cost, as already pointed out before, is of course the biggest issue and challenge. It's also a good representative of different types of problems, which fuel cell people are facing with. Why fuel cells are so expensive? The followings are some aspects of the problems.

- i) Electrodes are the places, where the reactions take place. It must be mixed conducting, electrochemically active to the reaction in question, and stable with electrolyte under reducing or oxidizing atmospheres. Unfortunately, Pt is still the most important catalysts for low temperature fuel cells, like PEM, AFC and PAFC, which make it difficult to low down the prices. Besides the high cost of electrodes, the polymer membrane used in PEM and DMFC are also quite expensive.
- ii) Today, nearly half of the R&D is focused on PEM fuel cells, which are used primarily for transportation application. A significant barrier to this application is hydrogen storage. Most fuel cell vehicles (FCVs) powered by pure hydrogen must store the hydrogen in pressurized tanks. Due to the low energy density of hydrogen, it is difficult to store enough hydrogen onboard to allow vehicles to travel the same distance as gasoline-powered vehicles before refueling. Higher-density liquid fuels such as methanol, ethanol, and gasoline can be used for fuel, but the vehicles must have an onboard fuel processor to reform the methanol to hydrogen. This increases costs and maintenance requirements. By the way, generation of hydrogen itself is not as easy and cheap as it looks like.
- iii) For high temperature fuel cells, like SOFC, the high temperatures provide high efficiency and the ability to cope with different hydrocarbon fuels without reformer. But it also means a higher requirement for the cell components, concerning electrical property, thermal expansion, chemical stability, mechanical compatibility, etc. For example, the interconnect materials are critical to the real applications, because the single fuel cell can only provide about 1V. The interconnect materials must be a good electronic conductor, which is chemically and mechanically stable in both oxidizing and reducing environment at working temperatures. Sr-doped LaCrO_3 is the state of the art interconnect material for SOFC operating at temperatures $\sim 1000^\circ\text{C}$ because of its relatively high electronic conductivity and its stability under the operating conditions. The main drawback of this material is that it's difficult to sinter at temperature less than 1750°C , which is too high to the other parts of the cell. As the consequence, the manufacture cost is increased.

1.3. Present approach to solve the problems

Efforts have been underway for many decades to overcome the problems of fuel cell technology, and push it to transfer from a technology of tomorrow to that of today. Different approaches have been considered. On the one hand, from the engineering point of view, the production procedure and structure configuration should be further optimized to minimize the manufacture cost. On the other hand, new materials, including electrolytes, electrodes, catalysts and interconnect materials are being investigated to search for the alternative to the old parts, which are more costly and less effective. Although PEM and DMFC are still dominating today's research activity and application field, SOFC is attracting growing interests and attentions from governments and researchers, due to their remarkable advantages. From now on, we will concentrate merely on the field of SOFC in this work.

The most widely used SOFC consists of yttria stabilized zirconia (YSZ) electrolyte, Ni-YSZ cermet anode and Sr doped lanthanum manganite-YSZ cermet cathode [3,4,5]. YSZ was chosen for this purpose because of the relatively high ionic conductivity and good chemical stability. Since fuel cell must be able to sustain a certain amount of current, the conductivity of the electrolyte should be high enough to meet this requirement. A conductivity of 10^{-1} S/cm was needed for electrolyte-supported cells of about $200\ \mu\text{m}$ thickness [6]. That is the reason why YSZ-based fuel cells have to work under very high temperature.

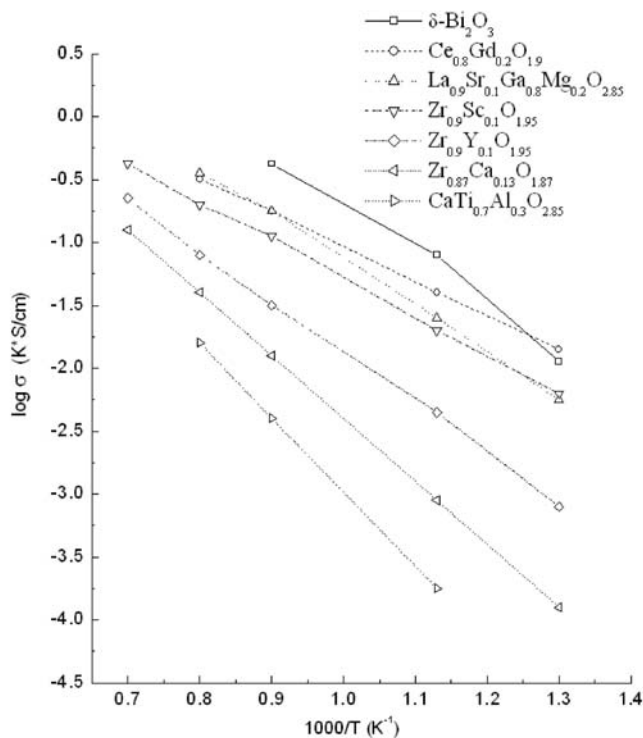


Figure 1.1. Electrical conductivities of selected oxides.

By decreasing the thickness of the electrolyte to 10~20 μm , YSZ can be used at temperature between 700 and 800°C [6]. But such thin films need to be mechanically supported, and there are limitations to this approach in terms of chemical interdiffusions and difficulty to make pinhole free films. Another approach to decrease the temperature is to find alternative materials, which have higher conductivities than YSZ. The most intensively studied candidates are doped ceria (CeO_2) [7-13] and doped lanthanum gallate (LaGaO_3) [14-18].

Figure 1.1 shows the conductivities of several oxides [9,19]. The conductivity of doped ceria is approximately an order of magnitude greater than that of YSZ, making it possible to be the electrolyte of SOFC working at the temperature between 500°C and 650°C. The reduction of cerium under reducing conditions, which introduces the n-type electronic conductivity, makes people hesitate to use it as electrolyte. Different ways [7,8] have been tried to minimize or block the electronic short circuit. A simple solution lies again in the operating temperature. At temperature below ~700°C (and at 10^{-18} atm O_2 partial pressure), the ionic transference of ceria is greater than 0.9, a value that results in good fuel cell efficiency [20]. With further decreasing temperature, the conductivity and the catalytic activity decline, causing higher polarization.

The history of perovskite LSGM is quite short. It was reported nearly simultaneously in 1994 by Goodenough [16] and Ishihara [14]. The AC conductivity was reported to be 0.10 S/cm at 800°C for the composition of $\text{La}_{0.9}\text{Sr}_{0.1}\text{Ga}_{0.8}\text{Mg}_{0.2}\text{O}_{2.85}$. Single SOFC based on the LSGM were demonstrated to have high power density even with a thick film (>500 μm) [21]. Since then, LSGM have become a significant potential electrolyte material for its high conductivity (comparable to that of ceria), which is entirely ionic over an extremely wide O_2 partial pressure range at temperature as high as 1000°C. The application of LSGM in fuel cells was hindered by the material's reactivity with Ni and/or CO_2 in the anode. However, these reactions can be eliminated by incorporating a buffer layer between the anode and the electrolyte [22].

Electrodes play an important role as the electrolyte in fuel cells. As already mentioned before, traditional electrodes must be mixed conducting, porous and highly catalytic active so that reactions can take place at the so-called triple phase boundary. Since electrodes are mostly where the rate-limiting steps are, different materials and approaches are being investigated to accelerate the electrode reaction. One of the most promising ways is to use mixed conductor as electrodes [23,24]. The electrode reaction is then no longer confined at the triple phase boundary. In fact, the reaction expands to all bulk volume of the electrode. Thus the porosity is no more a crucial factor. One of the problems using mixed conducting electrodes in practical applications is the relatively large thermal expansion coefficient (TEC). However, this problem can be solved to some extent by using composite mixed conductors. Then the thermal expansion match between electrolyte and electrode can be adjusted by the ratio of different phases.

If electronic conductivity can be introduced into the surface part of the electrolyte, then this part becomes mixed conducting, which will improve the kinetics of the interfacial redox processes of the mobile charge carrier. Once the surface electronic conductivity is high enough, the extra electrodes can be omitted, and the severe problems at the interface due to thermal expansion and charge transfer will be eliminated. Shouler et al. have doped the surface of a YSZ pellet with cerium turning it into an n-type semiconductor [25]. Worrell et al. dissolved titania

[26-28] and terbia [29,30] into YSZ for n and p type conductivity, separately. Based on these results, they tested their single-component solid oxide fuel cell [31] by doping of titania and terbia.

1.4. SEA concept and the aim of this work

Besides the application of mixed ionic and electronic conductors (MIECs) as electrodes for fuel cells, their application as electrolyte materials have also been investigated by some researchers. Riess discussed the possibility and conditions of MIECs being the electrolyte [32]. Weppner developed a new concept of single element arrangement (SEA) of galvanic cells, which consist of only one material [33-35]. This material becomes electron conducting at the anode and hole conducting at the cathode due to the stoichiometry change, but remains predominantly ionically conducting at intermediate activities of the electroactive component. Different from the previous single-component fuel cell, which needs extra surface modification by doping to provide faster electronic kinetics, the single material in SEA is homogeneously composed of the same material without a gradient in the composition except the minor non-stoichiometry generated by the different activities of the mobile component at both sides. Compared to the normal PEN structured fuel cell, SEA has the following remarkable advantages.

- i) As the electrodes are the part of the MIEC, no separate electrodes are required which simplify the cell construction. Most importantly, the problems due to the thermal mismatch and chemical reactivity between the electrolyte and the electrodes should be eliminated.
- ii) The charge transfer across the solid-solid interface between the electrolyte and the electrodes are always impeded in view of different crystal structures, air gaps and bad contact. Since there are no phase boundaries in SEA, the electrode polarization should be greatly minimized.
- iii) Since SEA consists of only one material, the manufacture cost should be lowered.

An example of SEA is the doping of conventional cubic stabilized or tetragonal zirconia by both titania and praseodymium oxide. Both oxides are mixed homogeneously with zirconia throughout the bulk of the material. Titania provides n-type conduction under reducing conditions while praseodymium oxide increase the p-type conduction in oxidizing atmospheres [36]. Thangadurai et al. found interesting properties also in Fe substituted SrSnO_3 [37].

In this work we will continue the investigation of SEA concept, mainly focusing the discussion on the influence of doping on the electrical conductivities of different group of materials, which could be possibly used as SEA solid oxide fuel cell at intermediate temperatures.

1.5. References

- [1]. EG&G Services, *Fuel Cell Handbook*. Parsons, Inc., Morgantown, West Virginia, 2000.
- [2]. Kerry-Ann Adamson, *Fuel Cell Today*. August, 2006.
- [3]. Chris Rayment, Scott Sherwin, *Introduction to Fuel Cell Technology*. Notre Dame, 2003.
- [4]. Y. Shibuya, H. Nagamoto, *Proceedings of the 5th International Symposium on Solid Oxide Fuel Cells (SOFC-V)*, 1997, 461.
- [5]. M. Juhl, S. Primdahl, C. Manon and M. Mogensen, *J. Power Sources* 1996, 61, 173.
- [6]. Michael Krumpelt, James Ralph, Terry Cruse, Joong-Myeon Bae, *5th European SOFC Forum*, Lucerne, Switzerland, July, 2002.
- [7]. K. Eguchi, T. Setoguchi, T. Inoue, H. Arai, *Solid State Ionics* 52,1992, 165.
- [8]. D.L. Maricle, T.E. Swarr, S. Karavolis, *Solid State Ionics* 52,1992, 173.
- [9]. Hideaki Inaba, Hiroaki Tagawa, *Solid State Ionics* 83,1996, 1.
- [10]. Keqin Huang, Man Feng, John B. Goodenough, *J. Am. Ceram. Soc.* 81 [2], 1998, 357.
- [11]. J. Liu, W. Weppner, *Ionics* 5, 1999.
- [12]. Mogens Mogensen, Nigel M. Sammes, Geoff A. Tompsett, *Solid State Ionics* 129, 2000, 63.
- [13]. B.C.H. Steele, *Solid State Ionics* 129, 2000, 95.
- [14]. Tatsumi Ishihara, Hideaki Matsuda, Yusaku Takita, *J. Am. Ceram. Soc.* 116, 1994, 3801.
- [15]. Tatsumi Ishihara, Hideaki Matsuda, Yusaku Takita, *Solid State Ionics* 79, 1995, 147.
- [16]. M. Feng, John B. Goodenough, *Eur. J. Solid State Inorg. Chem.* t.31, 1994, 663.
- [17]. Peng-nian Huang, Anthony Petric, *J. Electrochem. Soc.* 143, 1996, 1644.
- [18]. Keqin Huang, Robin S. Tichy, John B. Goodenough, *J. Am. Ceram. Soc.* 81 [10], 1998, 2565.
- [19]. V. Thangadurai, W. Weppner, *Ionics* 12, 2006.
- [20]. C. Milliken, S. Guruswamy, A. Khandkar, *J. Electrochem. Soc.* 146, 1999, 872.
- [21]. Keqin Huang, Robin S. Tichy, John B. Goodenough, *J. Am. Ceram. Soc.* 81 [10], 1998, 2581.

- [22]. Keqin Huang, Jen-Hau Wan, John B. Goodenough, *J. Electrochem. Soc.* 148, 2001, A788.
- [23]. Y. Teraoke, T. Nobunaga, N. Yamazoe, *Chem. Lett.* 503, 1988.
- [24]. L.-W.Tai, M.M. Nasrallah, H.U. Anderson, D.M. Sparlin and S.R. Sehlin, *Solid State Ionics*, 76, 1995, 259.
- [25]. E.J.L. Schouler, M. Kleitz, *J. Electrochem. Soc.* 134, 1987, 1045.
- [26]. S.S. Liou, Wayne L Worrell, *Appl. Phys. A* 49, 1989, 25.
- [27]. Wayne L Worrell, Werner Weppner, Helmut Schubert, *US Patent No.4, 931, 214*, 1990.
- [28]. Wayne L Worrell, *Solid State Ionics* 52, 1992, 147.
- [29]. H. Arashi, S. Shin, H. Miura, A. Nakashima, M. Ishigame, O. Shimomura, *Solid State Ionics* 35,1989, 323.
- [30]. P. Han, Wayne L Worrell, *The Electrochemical Society Proceeding Series*, Pennington, NJ, 1994.
- [31]. Wayne L Worrell, P. Han, Y. Uchimoto, P.K. Davies, in *Solid Oxide Fuel Cells IV*, PV 95-1 The Electrochem.Soc.Inc. Pennington, NJ, 50, 1995.
- [32]. Ilan Riess, *Solid State Ionics* 52, 1-3, 1992, 127.
- [33]. Werner Weppner, in: *Ceramics: Toward the 21st Century* (N. Soga and A. Kato, Eds.), *The Ceramic Soc. of Japan*, Tokyo, 1991, 19.
- [34]. Werner Weppner, *Ionics* 4, 1998, 422.
- [35]. Wing-Fong Chu, Venkataraman Thangadurai, Werner Weppner, *Ionics* 12, 2006, 1.
- [36]. Werner Weppner, *Ionics* 7, 2001, 404.
- [37]. Venkataraman Thangadurai, P. Schmid Beurmann, Werner Weppner, *Materials Science and Engineering B100*, 2003, 18.

Chapter 2

Theoretical aspects

2.1. Fuel cell basics

2.1.1. Working principle of fuel cells

Different from batteries, which are energy ‘storage’ devices, fuel cells ‘convert’ chemical energy directly to electrical energy. As long as a fuel, like H_2 , is supplied, fuel cell will generate electricity continually without charging.

The normal PEN structured fuel cells consist of positive electrode (cathode), electrolyte and negative electrode (anode). Although what we will mainly discuss in this work is SEA concept, which contains only one element, for general basic understanding we will still start from the conventional concept. Figure 2.1 shows schematically the working principle of a fuel cell, employing an oxide ion electrolyte.

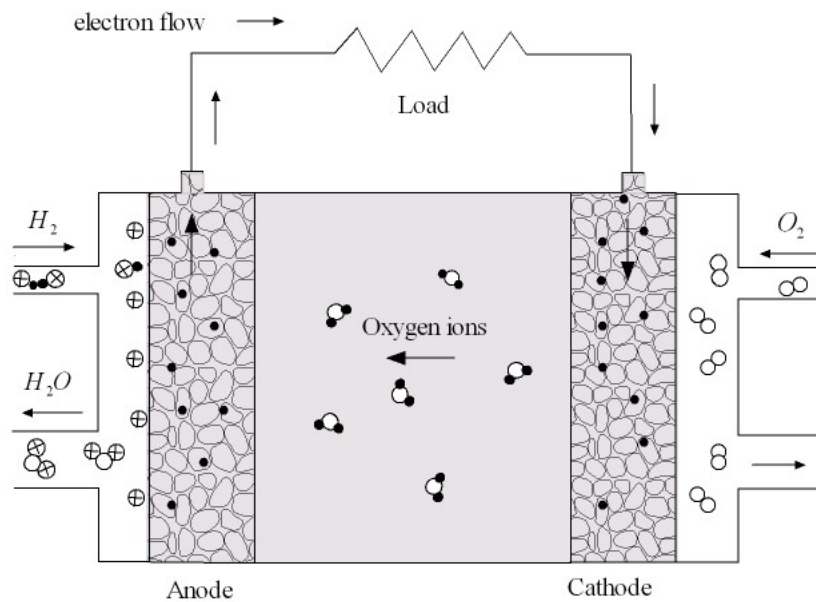
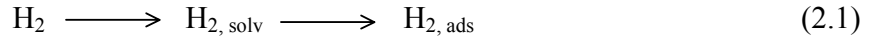


Figure 2.1. A schematic diagram of a conventional fuel cell, employing an oxide ion electrolyte.

At anode side, where H_2 is supplied, the oxidation of H_2 is completed in the following steps:

- i) Transport of molecular hydrogen from the gas phase to the electrode and adsorption on the surface:



- ii) Dissociation of the hydrogen molecule:



- iii) Ionisation:



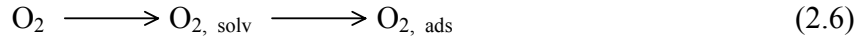
- iv) Desorption of products.

The total anode reaction is as follows:



At the cathode side, the following reaction mechanisms occur for oxygen reduction.

- i) Transport of molecular oxygen from the gas phase to the electrode and adsorption on the surface:



- ii) Dissociation of the oxygen molecule:



- iii) Ionisation:



- iv) Desorption of products and transport into the electrolyte.

The total cathode reaction is the following:



Electrons generated at the anode during oxidation pass through the external circuit on their way to cathode, where they complete the reduction reaction. During this process, electricity is generated, with the byproduct of only water and heat. The total fuel cell reaction is shown below:



During the reaction, the fuel and oxidant do not mix anywhere, and there is no actual combustion taken place. The fuel cell is therefore not limited by the Carnot efficiency [1].

The electromotive force (EMF) of the cell is determined by the Nernst equation:

$$\Delta G = -zFE \quad (2.11)$$

where ΔG is the Gibbs free energy change of the reaction (2.10), z is the number of electrons transferred, F is Faraday's constant and E is the EMF.

Under standard state, E has the value of 1.23V, which decreases with increasing temperature. The relation between E and temperature is shown in figure 2.2.

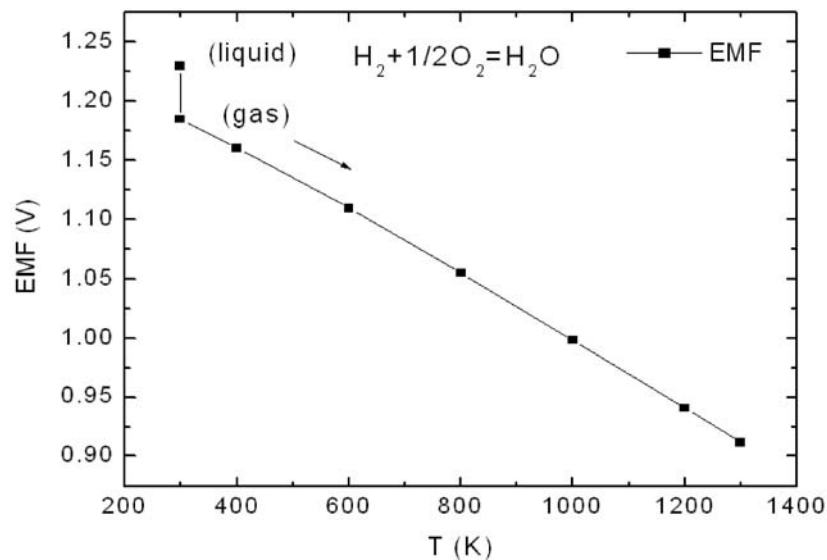


Figure 2.2. Calculated EMF of a H_2/O_2 cell vs. temperature.

In the ideal case, the cell voltage is independent on the current drawn. But practically, the cell potential will be decreased with increasing current because of the unavoidable irreversible losses. The potential difference measured between the open circuit voltage (OCV) and the terminal voltage under the conditions of current flowing has been termed as overpotential (or polarization). There are several sources of overpotential.

- i) **Activation overpotential** is present when the rate of an electrochemical reaction at an electrode surface is controlled by sluggish electrode kinetics. It's always dominant at low current density range, where the electronic barriers must be overcome prior to current and ion flow. Activation overpotential increases as current increases.

- ii) **Ohmic overpotential** is simply the voltage drop across the resistive component of the cell. There is no relation between the Ohmic losses and the chemical process at the electrodes. It varies directly with current.
- iii) **Concentration overpotential** stands for voltage changes caused by diffusion processes. Under high current densities, as a reactant is consumed at the electrode, there is a loss of potential due to the inability to maintain the initial concentration of the bulk fluid. The concentration polarization may arise due to different processes: slow diffusion in the gas phase in the electrode, solution/dissolution of reactants and products into and out of the electrolyte, or diffusion of reactants and products through the electrolyte to and from the electrochemical reaction site.
- iv) **Reaction overpotential** is the voltage difference appearing when the product of the chemical reaction changes the operating conditions. One example is the generation of water in Phosphoric Acid Fuel Cell (PAFC) dilutes the electrolyte, which then causes an electrolyte concentration change at the electrode interface.

A polarization curve of a $H_2 - O_2$ cell is shown in figure 2.3.

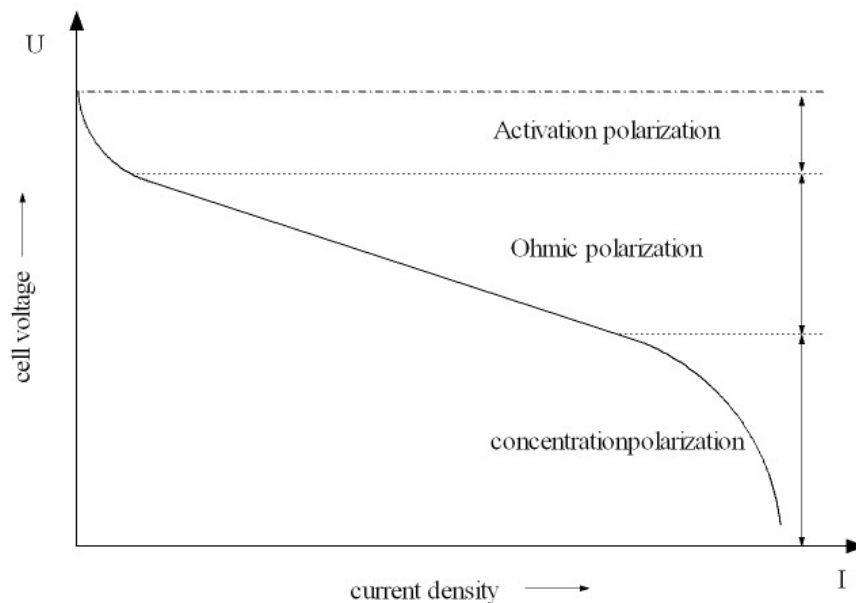


Figure 2.3. A schematic diagram of the polarization curve for fuel cells.

2.1.2. Types of fuel cells

Generally speaking, fuel cells are classified in term of the electrolyte, which determines the chemical reactions that take place in the cell, the kind of catalysts, the operating temperature, the type of fuels, and some other factors. These factors, in turn, affect the applications for which these cells are most suitable. There are several types of fuel cells under development, and each has its own advantages and limitations [2-4]. Table 2.1 compare the different type of fuel cells.

- i) **Polymer electrolyte membrane (PEM) fuel cell**—also called proton exchange membrane fuel cells—use a solid polymer, mostly Nafion[®], as the electrolyte and porous carbon electrodes containing a platinum catalyst. PEM operate at around 90°C. Low temperature results in fast start-up and less wear of the cell component. However, it needs high platinum loadings (0.4mg/cm²) to catalyse the electrode reaction, leading to high cost. Due to poisoning effect of CO on platinum, only pure humidified H₂ can be used as fuel in PEM. Because of the low operating temperature, it also requires cooling and management of the exhaust water in order to function properly. Another type of fuel cell that also use polymer as electrolyte is **Direct Methanol Fuel Cell (DMFC)**. It differs from PEM in the way that the liquid methanol (CH₃OH) instead of hydrogen is oxidized in the presence of water at the anode side. So DMFC doesn't have the problem of hydrogen storage. These cells have been tested in a temperature range of about 50°C-120°C. This low operating temperature and no requirement for a fuel reformer make the DMFC an excellent candidate for very small to mid-sized applications. But again, the requirement of large amount of platinum cause high cost of DMFC.
- ii) **Alkaline fuel cell (AFC)** was one of the first fuel cell technologies developed and the first type widely used in the U.S. space program to produce electrical energy and water onboard spacecraft. Alkaline fuel cells use potassium hydroxide as the electrolyte and operate at around 70°C. However, they are very susceptible to carbon contamination. Even a small amount of CO₂ in the air can affect the cell's operation, making it necessary to purify both the hydrogen and oxygen used in the cell.
- iii) **Phosphoric acid fuel cell (PAFC)** uses liquid phosphoric acid as the electrolyte and operates at about 200°C. It is one of the most mature cell types. Compared to the first two types of fuel cells, PAFC has higher tolerance ability to the CO content up to about 1.5%. Although PAFC can work at 85% efficiency when used for the co-generation of electricity and heat, it generates electricity alone at about 40% efficiency, which is only slightly higher than combustion-based power plants. PAFCs are also less powerful than other fuel cells, given the same weight and volume.

- iv) **Molten carbonate fuel cell (MCFC)** uses an electrolyte composed of a molten carbonate salt mixture suspended in a porous, chemically inert ceramic lithium aluminium oxide (LiAlO_2) matrix, and operates at approximately 650°C . It requires carbon dioxide and oxygen to be delivered to the cathode. Due to the high temperatures at which they operate, non-precious metals can be used as catalysts and there is no need for the external reformer to convert more energy-dense fuels to hydrogen. To date, MCFCs have been operated on hydrogen, carbon monoxide, natural gas, propane and simulated coal gasification products. The primary disadvantage of MCFC is durability due to the high temperature and the corrosive electrolyte.
- v) **Solid oxide fuel cell (SOFC)** uses a hard, non-porous ceramic compound as the electrolyte, and operates at very high temperatures. Similar to MCFC, there is no need for precious-metal catalyst and the lethal CO to the low temperature fuel cells can even be used as a fuel in SOFC. As the electrolyte is a solid, problems due to the liquid leakage and corrosion are also eliminated. The obstacles to the development and commercialisation of SOFC are still the cost and poor durability because of the high temperature. Therefore, solid oxide fuel cells working at intermediate temperature are more promising in this field.

Table 2.1 Comparisons of different type of fuel cells.

	PEM	DMFC	AFC	PAFC	MCFC	SOFC
Electrolyte	Polymer membrane	Polymer membrane	Solution of KOH	Phosphoric acid	Molten carbonate salt mixture	Solid metal oxides
Operating temperature	$60\sim 100^\circ\text{C}$	$50\sim 120^\circ\text{C}$	$25\sim 250^\circ\text{C}$	$150\sim 200^\circ\text{C}$	$600\sim 1000^\circ\text{C}$	$600\sim 1000^\circ\text{C}$
Fuel	Pure H_2	Methanol solution in water	Pure H_2	H_2	H_2 , CO , CH_4 , natural gas	H_2 , CO , CH_4 , natural gas
Oxidant	O_2 /air	O_2 /air	Pure O_2	O_2 /air	O_2 / CO_2 /air	O_2 /air
Reforming	External	/	External	External	Ex/internal	Ex/internal
Efficiency (without cogeneration)	35~60%	35~40%	50~70%	35~50%	45~60%	45~60%
Power range	~250kW	~5kW	~100kW	~1MW	~5MW	~10MW
Power density (Wcm^{-2})	0.35~0.7	0.25	0.1~0.3	0.14	0.1~0.12	0.15~0.7

2.2. Introduction to ionics

2.2.1. General aspects

Although it's well known that fuel cell is a type of clean energy converter that provides higher efficiency than the combustion engine, it's still just a promising solution to the energy and environment crises. Fuel cells have not yet come to the stage to replace the conventional techniques. In view of the difficulties in developing the fuel cell technology, which has been briefly mentioned in chapter 1, it's necessary to understand more about the operating principle and the parameters that control the material's performance before we can better improve the properties of the materials.

Ionics is the science and technology of the motion of ions alone or together with electrons within the bulk of materials and across interfaces [5-10]. It's a key technology for developing most of the energy related applications and devices, including fuel cells, water electrolysis cells, batteries, supercaps, thermoelectronic converters, photogalvanic solar cells, chemical sensors and electrochromic systems.

The materials with predominant and high ionic conductivity are the starting point of ionics. However, individual materials have no meaning for practical applications. All applications require the combination of materials with appropriate ionic and electronic properties. This is similar to electronics, which require combinations of semiconductors or metallic materials with differences in the chemical potential of electrons. While only electrons equilibrate across the semiconductor junctions, both electrons and ions equilibrate across the ionic junctions. Since all materials are sufficiently good electrical conductors, there should be no electrical field built up in the bulk of each material; all voltage drops occur across the interfaces. In another word, the interfaces (or 'ionic junctions') between the materials play the most important role in ionic devices. The interfaces have to be chemically and mechanically stable for the lifetime of the device, which is not easy to achieve due to the commonly large number of components present in both phases and the existence of mobile species with sometimes large variations in the activity of the electroactive component. Fast charge transfer across the interfaces is also required for high power density in many cases [11]. In the first approach, Debye's formula can be used to estimate the space charge region

$$L_D = \sqrt{\frac{\varepsilon\varepsilon_0 kT}{q^2 c}} \quad (2.12)$$

where $\varepsilon, \varepsilon_0, k, T, q$ and c are the dielectric constant of the material, the permittivity in vacuum, Boltzmann's constant, absolute temperature, elementary charge and concentration of charge carriers, i.e. ions for electrolyte and electrons for electrodes, respectively. Compared to semiconductor junctions, which normally have a width in the μm range, the width of the ionic junction is several orders of magnitude lower, i.e. 100~1000 pm due to the relatively higher

concentration of charge carriers. The narrow region of electrostatic potential drop at the interface is unique in comparison with semiconducting materials. Electronic junctions do not allow the building up of voltages which are measurable at the outside and do not produce a current in an outer electrical circuit, while solid electrolytes are blocking the electronic charge carriers which therefore have to move through the outer electrical circuit in order to compensate the local charge displacement of the ionic charge carriers in the electrolyte.

Ionics is the technology in which the properties of electrolytes have the central attention. Defects chemistry is inherently connected with ionics. From next section, an elementary introduction of defects, conducting mechanism of electrolyte and generation of voltage in ionic devices will be considered step by step.

2.2.2. Elementary defect chemistry

The perfect crystal is only an abstract concept in crystallographic descriptions. In reality, the lattice of a crystal always contains imperfections or defect at temperatures above 0K arising from the entropy contribution to the Gibbs free energy as a consequence of the disorder introduced by the presence of the defects [10].

If x is the mole fraction of a certain type of defect, the entropy increasing due to the formation of these defects is:

$$\Delta S = -R[x \ln x + (1-x) \ln(1-x)] \quad (2.13)$$

which is the mixing entropy of an ideal mixture of defects and occupied lattice positions. If the formation energy of the defect is ΔE J/mol, then the increase of the enthalpy is:

$$\Delta H = x \cdot \Delta E \quad (2.14)$$

The change in Gibbs free energy is:

$$\Delta G = \Delta H - T\Delta S = x \cdot \Delta E + RT[x \ln(x) + (1-x) \ln(1-x)] \quad (2.15)$$

Since G must be minimum at equilibrium, the partial differentiation:

$$\frac{\partial \Delta G}{\partial x} = \Delta E + RT[\ln(x) - \ln(1-x)] = 0 \quad (2.16)$$

then:

$$\frac{x}{1-x} = \exp\left(-\frac{\Delta E}{RT}\right) \quad (2.17)$$

If $x \ll 1$, then:

$$x = \exp\left(-\frac{\Delta E}{RT}\right) \quad (2.18)$$

The existence of imperfections in the material doesn't mean that it's really 'defect'. On the contrary, defects play an important role in solid state electrochemistry. Ion conduction or diffusion can only take place because of the presence of defects. Chemical reactions in the solid state are also fundamentally dependent upon imperfections. So a comprehensive understanding of all possible defects is necessary in the study and development of the technology of ionics.

Defects are generally classified according to their dimensions, i.e. point defect, such as vacancies, interstitial ions and substitution impurities; one-dimensional defects including dislocations; two-dimensional defects including grain boundaries, stacking faults and surfaces; three-dimensional defects including inclusions or precipitates in the crystal matrix. However, only point defects contribute to the electrical conductivity, and are thermodynamically stable, which means they are determined by a number of independent variables such as pressure, temperature, and chemical composition, while all the other defects also depend on the way of preparation. Defects can also be classified as intrinsic and extrinsic. If the concentration of the major defects are independent of the component activities and are only determined by pressure and temperature, then they are intrinsic disorders or thermal disorders.

In general, defects in ionic crystals possess an effective charge relative to the ideally ordered lattice. In the absence of electric fields and of gradients in the chemical potential, charge neutrality must be maintained throughout an ionic lattice. Thus a charged defect must be compensated by one (or more) other defect(s) having the same charge, but opposite sign. As a result of this condition, the total number of positively and negatively charged defects in the lattice must be equal. We can think of these defects as being grouped into neutral pairs, while they don't have to be close together in many cases.

Defects can be introduced into the lattice in three ways: (a) by thermal excitation, (b) by deviation from stoichiometry, and (c) by doping [12].

Two common types of disorder in ionic solids are Schottky and Frenkel defects. Schottky defects involve equivalent number of cation and anion vacancies. Frenkel defects consist of same amount of interstitial ions and corresponding ion vacancies. These two types of disorder are shown in Figure 2.4.

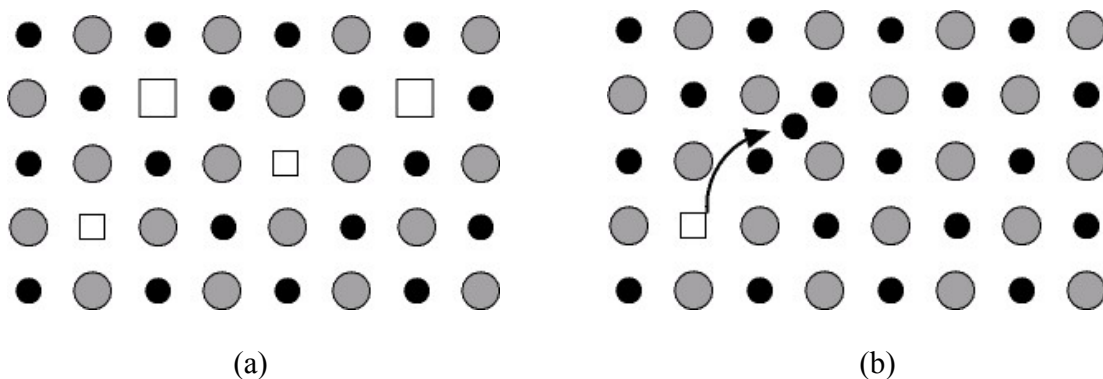


Figure 2.4. (a) Schottky defects, and (b) Frenkel defects.

Nonstoichiometry occurs when there is an excess of one type of defect relative to that at the stoichiometric composition. Since the ratio of cation to anion lattice sites is the same whether a compound is stoichiometric or nonstoichiometric, complementary electronic defects must be present to preserve electroneutrality. One example is given in figure 2.5 by NiO [13], which should be written strictly as $\text{Ni}_{1-\delta}\text{O}$, where δ is a measure of the concentration of nickel ion vacancies. Since the vacancies are negatively charged, an equivalent amount of electron holes should be present in the form of Ni^{3+} . By virtue of the chemical equilibrium between the oxygen and defects one can experimentally control the valence state of a component (i.e. $\text{Ni}^{3+}/\text{Ni}^{2+}$). Therefore one can control the electrical conductivity of a compound by fixing the component activities (i.e. the oxygen partial pressure). The extent of nonstoichiometry and defects as a function of activities of the electroactive component will be discussed later.

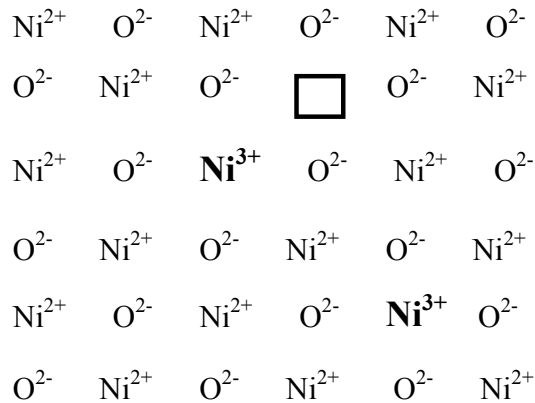


Figure 2.5. Disorder in NiO: cation vacancies and an equivalent number of trivalent nickel ions.

C. Wagner [14] was the first to point out the possibility of the controlled introduction of defects by means of dissolving a third heterovalent component in binary ionic crystals. The excess charge introduced by this third component will be compensated either by the controlled valence as discussed above, or by vacancies or interstitial ions. This theory can be easily extended to crystals and compounds with more than two or three components.

Electronic defects may arise as a consequence of the transition of electrons from valence band to conduction band, leaving an electron hole behind. When electrons or electron holes are localized on ions in the lattice, the semiconductivity arises from electrons or electron holes moving between the same ions with different valences, which is called the hopping mechanism.

2.2.3. Conduction and transport mechanism

Ionic conduction can take place in a solid via three types of mechanisms: Frenkel (ionic interstitial), Schottky (vacancy) and interstitialcy. A schematic interpretation of these three mechanisms is shown in figure 2.6.

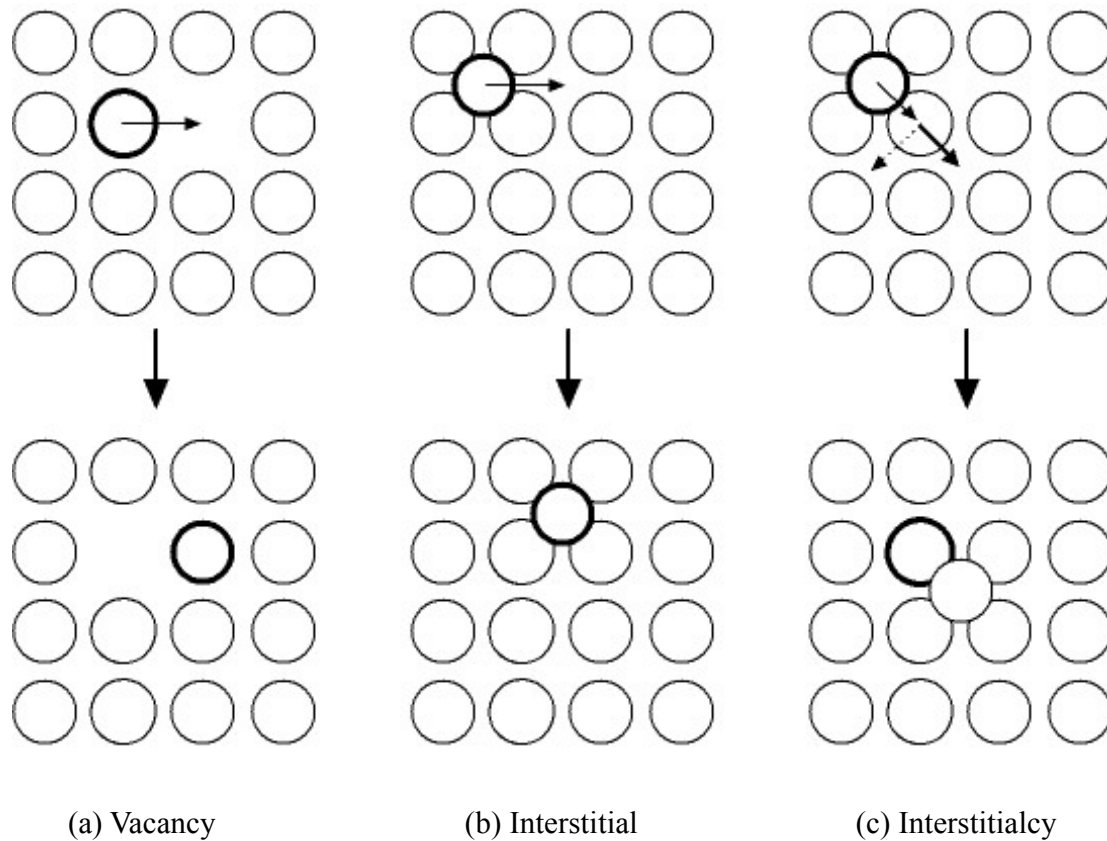


Figure 2.6. Mechanisms for transport of ions.

A detectable flow of ions only occurs when a series of ionic transport take place, which produces a net change in charge over the material. This can be modelled as a process of discrete jumps over the energy barriers.

Electrical conductivity is one of the most important properties of a material. The total conductivity can be written as a sum of the conductivity of the mobile species, including ionic and electronic charge carriers [15]:

$$\sigma = \sum_i \sigma_i = \sum_i c_i z_i q u_i = \sum_i \frac{c_i z_i^2 q^2 D_i}{kT} \quad (2.19)$$

where q is the elemental charge, k is Boltzmann's constant, c_i, z_i, u_i, D_i are the concentration, number of charge, electrical mobility and diffusivity of the species i , respectively. D_i can be determined from the tracer diffusion coefficient D_i^T through a correlation factor f_i :

$$D_i^T = f_i D_i \quad (2.20)$$

Since the mobility of an electronic carrier is often 100~1000 times larger than that of ions [16], this means the ionic conduction will only predominate if the concentration of ionic defect is 100~1000 times higher than that of electronic carriers.

For a thermally activated diffusion process, the ionic conductivity of a solid electrolyte with one mobile ion follows the Arrhenius dependence on the temperature:

$$\sigma = \frac{\sigma_0}{T} \exp\left(-\frac{\Delta E_a}{RT}\right) \quad (2.21)$$

Which can be written as the following:

$$\ln(\sigma T) = \ln \sigma_0 - \frac{\Delta E_a}{RT} \quad (2.22)$$

If we plot $\ln(\sigma T)$ against $1/T$, we produce a straight-line relationship. σ_0 is the value at $1/T=0$. The slope of this line is the activation energy, ΔE_a . The actual temperature dependence of conductivity can be shown as three regions [17,18]. In region I, which appear at high temperatures, the electrical conduction is determined by the intrinsic defects. In region II, electrical conduction is controlled by extrinsic defects. In region III, at low temperature, the number of charge carrying defects is determined by the thermodynamic equilibrium between the free defects and associated pairs.

When there are more than one type of mobile species in the material, the contribution of individual species to the total conduction is given by the transference number, which is the fraction of the conductivity of each species to the total conductivity:

$$t_i = \frac{\sigma_i}{\sum_j \sigma_j} \quad (2.23)$$

In an ionic device, the transference numbers are not only the properties of the electrolyte or mixed conductor but also influenced by what happens at the ionic junctions [19]. Only when there is no impedance to the transfer of either ions or electrons across the ionic interfaces, are they properties of the electrolyte or mixed conductor alone. The transference number is also not a constant throughout a given material, but instead, is dependent on the chemical potentials of the component within it. Different techniques to determine the transference number can be found elsewhere [20,21].

The electrical current that passes through a galvanic cell is directly related to the transport of mobile ionic and electronic species. The partial flux density j_i (particles/cm²·s) of any species i is

proportional to the overall transport force acting on it. This force can be expressed as the gradient of the electrochemical potential η_i :

$$j_i = -\frac{\sigma_i}{z_i^2 q^2} \frac{\partial \eta_i}{\partial x} \quad (2.24)$$

where η_i can be divided into an electrostatic potential component ϕ and a chemical potential component μ_i :

$$\eta_i = \mu_i + z_i q \phi = \mu_i^0 + kT \ln a_i + z_i q \phi \quad (2.25)$$

where μ_i^0, a_i stand for chemical potential in the standard state ($a_i = 1$) and the activity, respectively.

With the help of equation (2.19) and (2.25), equation (2.24) can be written as:

$$j_i = -D_i \left(\frac{z_i q c_i}{kT} \frac{\partial \phi}{\partial x} + \frac{\partial \ln a_i}{\partial \ln c_i} \frac{\partial c_i}{\partial x} \right) \quad (2.26)$$

For all species, if there is no externally applied electric potential difference, charge flux balance must be maintained:

$$\sum_i z_i j_i = 0 \quad (2.27)$$

Inserting equation (2.26) into (2.27) yields the relation between the flux density for species i and all other ionic and electronic species:

$$j_i = -D_i \left[(1-t_i) \frac{\partial \ln a_i}{\partial \ln c_i} - \sum_{j \neq i} t_j \frac{z_i}{z_j} \frac{\partial \ln a_j}{\partial \ln c_i} \right] \frac{\partial c_i}{\partial x} \quad (2.28)$$

which can be further transformed into the form only containing activity and concentration terms of neutral chemical species:

$$j_i = -D_i \left[(1-t_i) \frac{\partial \ln a_{i^*}}{\partial \ln c_{i^*}} - \sum_{j \neq i, e, h} t_j \frac{z_i}{z_j} \frac{\partial \ln a_{j^*}}{\partial \ln c_{i^*}} \right] \frac{\partial c_i}{\partial x} \quad (2.29)$$

where e, h, i^*, j^* stand for electron, electron hole and neutral species i, j respectively. This equation gives the flux density for any chemical component and holds both for the ionic species within the solid or for the effective flux density of such species in their neutral form [22]. The quantities in the square brackets can be defined as an enhancement factor (or Wagner factor) W :

$$j_i = -D_i W \frac{\partial c_i}{\partial x} = -\tilde{D}_i \frac{\partial c_i}{\partial x} \quad (2.30)$$

where \tilde{D}_i is the chemical diffusion coefficient for species i with reference to the crystal lattice. In the systems where two types of species dominate the transport phenomena, the chemical diffusion coefficients of the two species are equal, and we can use \tilde{D} for both. For the case in which only one ionic and one electronic species are considered, if the sample is predominantly an electronic conductor ($t_e \rightarrow 1$),

$$W = \frac{\partial \ln a_{i^*}}{\partial \ln c_{i^*}} \quad (2.31)$$

and

$$\tilde{D} = D_i \frac{\partial \ln a_{i^*}}{\partial \ln c_{i^*}} \quad (2.32)$$

If the sample is predominant an ionic conductor ($t_i \rightarrow 1$)

$$W = \frac{c_e D_e}{z_i^2 c_i D_i} \frac{\partial \ln a_{i^*}}{\partial \ln c_{i^*}} \quad (2.33)$$

and

$$\tilde{D} = \frac{c_e D_e}{z_i^2 c_i} \frac{\partial \ln a_{i^*}}{\partial \ln c_{i^*}} \quad (2.34)$$

In both cases the chemical diffusion coefficients are dependent on the diffusivity of the minority charge carriers. It should be noted that the charge flux density could be far more than what would be expected from the concentration gradient alone due to the presence of the Wagner factor. In some cases, W as large as 10^5 was observed experimentally [23]. In such a case, the transport originates from a concentration gradient, but the major driving force for the ions is the local electrical field, which results from the fast electronic charge carriers pulling the ions behind.

2.2.4. Defect equilibrium and defect diagram

In section 2.2.2 we gave a general introduction about the formation of defects, which is dependent on temperature, stoichiometry and doping level. In this section we will discuss primarily how the concentration of ionic and electronic defects are interrelated and their dependence on the above variables.

The charges of defects and of regular lattice particles are only important with respect to the neutral, ideal lattice. In the discussion the charges of all the point defects are defined relative to the neutral lattice. Using the notation of Kröger and Vink [24], point defects in a simple binary compound MX can be expressed as shown in Table. 2.2, given both M and X are divalent ions.

Table. 2.2. Kröger-Vink notation for point defects in crystals
(M and X are divalent ions.)

Type of defect	Symbol
Free electron	e'
Free electron hole	h^\bullet
Vacant M site	V_M''
Vacant X site	V_X'''
Interstitial M ion	M_i'''
Interstitial X site	X_i''
L^+ on M site	L_M'
N^{3+} on M site	N_M^\bullet
Ion on lattice site	M_M^\times, X_X^\times

i). Pure oxide compound

Starting from a simple binary metal oxide compound, which has Frenkel disorder in the oxygen sublattice, the Frenkel defect equilibrium can be written as:

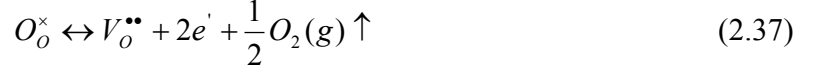


The thermal equilibrium between electrons in the conduction band and electron holes in the valence band is represented in similar way as:



As the partial pressure of the metal component is negligible compared to that of oxygen

under most conditions, nonstoichiometry is a result of the equilibrium of the oxide with the oxygen in the surrounding gas atmosphere:



By using the mass action law, these three equilibriums can be represented as the following:

$$[O_i^{\bullet}][V_o^{\bullet\bullet}] = K_F = K_F^0 \exp\left(-\frac{\Delta E_F}{kT}\right) \quad (2.38)$$

$$np = K_e = K_e^0 \exp\left(-\frac{\Delta E_g}{kT}\right) \quad (2.39)$$

$$[V_o^{\bullet\bullet}]n^2 P_{O_2}^{1/2} = K_R = K_R^0 \exp\left(-\frac{\Delta E_R}{kT}\right) \quad (2.40)$$

where $[]$, n and p are concentration of ionic species, electrons and electron holes, respectively. P_{O_2} is the partial pressure of oxygen in the gas. $\Delta E_F, \Delta E_g, \Delta E_R$ are the formation energy of Frenkel defect, energy band gap and the activation energy for the equilibrium with the gas phase, respectively, while K_F, K_e and K_R are the temperature dependent equilibrium constants.

With the help of electroneutrality condition, which can be written as:

$$n + 2[O_i^{\bullet}] = p + 2[V_o^{\bullet\bullet}] \quad (2.41)$$

The four defect concentrations as a function of temperature and oxygen partial pressure should be in principle solved from Eqs (2.38-41). In practice, to simplify the calculation process, it's easier to solve the equations for the limiting forms of Eq. (2.41), each of which is appropriate for a range of temperature and oxygen partial pressure [25]. At low P_{O_2} , Eq. (2.37) is predominate, so Eq.(2.41) can be simplified to $n = 2[V_o^{\bullet\bullet}]$; at high P_{O_2} , it becomes $p = 2[O_i^{\bullet}]$; and at intermediate P_{O_2} , intrinsic defects predominate, giving $[O_i^{\bullet}] = [V_o^{\bullet\bullet}]$ ($K_F \gg K_e$ in case of predominant ionic conductor). Under these conditions, the concentration of the defects can be easily calculated, which are shown in Table 2.3.

Table 2.3. Defect concentrations for pure Frenkel-like oxide

P_{O_2} range	Limiting condition	n	p	$[V_O^{\bullet\bullet}]$	$[O_i^{\bullet}]$
low	$n = 2[V_O^{\bullet\bullet}]$	$(2K_R)^{1/3} P_{O_2}^{-1/6}$	$K_e(2K_R)^{-1/3} P_{O_2}^{1/6}$	$\frac{n}{2}$	$K_F \left(\frac{4}{K_R}\right)^{1/3} P_{O_2}^{1/6}$
intermediate	$[O_i^{\bullet}] = [V_O^{\bullet\bullet}]$	$K_R^{1/2} K_F^{-1/4} P_{O_2}^{-1/4}$	$K_e K_R^{-1/2} K_F^{1/4} P_{O_2}^{1/4}$	$K_F^{1/2}$	$K_F^{1/2}$
high	$p = 2[O_i^{\bullet}]$	$\left(\frac{K_R K_e}{2K_F}\right)^{1/3} P_{O_2}^{-1/6}$	$\frac{K_e}{n}$	$\left(\frac{4K_R K_F^2}{K_e^2}\right)^{1/3} P_{O_2}^{-1/6}$	$\frac{p}{2}$

The concentration of the defects can be plotted on a logarithmic scale versus the logarithm of the oxygen partial pressure as shown in figure 2.8, which is called the defect equilibrium diagram, or Brouwer diagram.

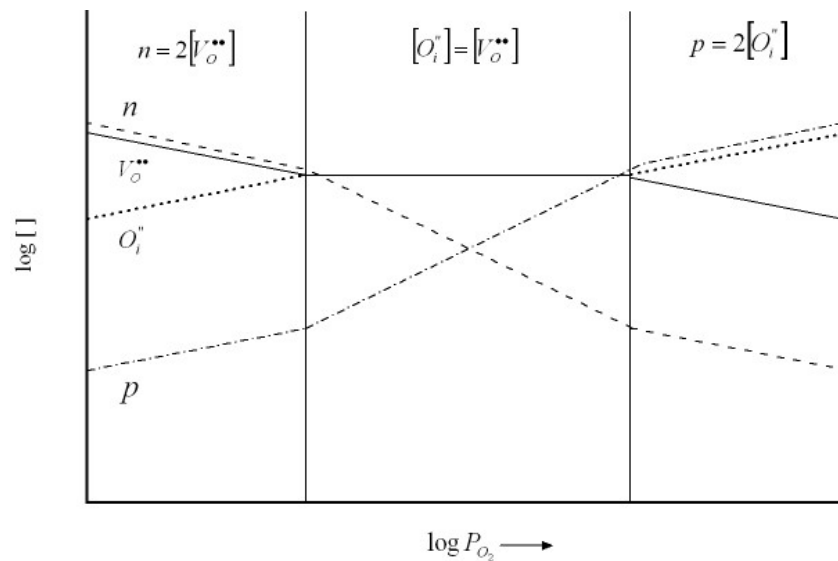


Figure 2.8. Defect concentration vs. oxygen partial pressure for pure oxide with Frenkel disorder.

The corresponding conductivity curves are obtained by multiplying the carrier concentration by their charge and mobility, respectively. Due to the high electron/ion mobility ratio, the electronic curves have the shifts upward relative to the ionic ones, as is shown in figure 2.9.

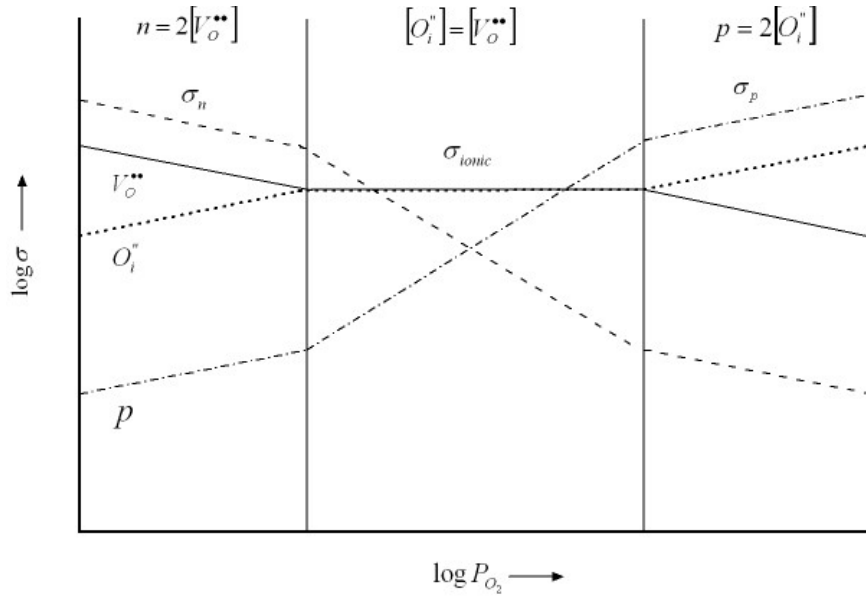
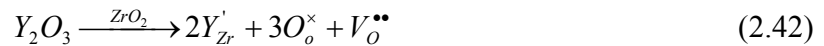


Figure 2.9. Conductivity vs. oxygen partial pressure for pure oxide with Frenkel disorder.

ii). Doped oxide

The electrical property can be largely improved by doping. For example, the ionic conductivity of fluorite phase of zirconia (ZrO_2) can be increased by dissolving aliovalent ions, like Y, into the lattice, generating oxygen vacancies. The defect reaction can be written as:



Taking into consideration of Eqs. (2.35), (2.36) and (2.37), the electroneutrality condition is modified into:

$$n + 2[O_i^\bullet] + [N'_M] = p + 2[V_O^{\bullet\bullet}] \quad (2.43)$$

It should be noted here that in Eq. (2.43), $[N'_M]$ is used instead of $[Y'_{Zr}]$ for a more general expression. The defect concentrations can be deduced from Eqs. (2.38), (2.39), (2.40) and (2.43) following the same way as described before. The defect concentrations and the corresponding Brouwer diagrams are shown in Table.2.4, figure 2.10 and 2.11, respectively. The defects in doped oxide have same relation as those in pure oxide at very low and high P_{O_2} limit. The difference from the previous situation is that there are now two intermediate regions, both being impurity-controlled.

Table 2.4. Defect concentrations for doped Frenkel-like oxide at intermediate P_{O_2} range.

P_{O_2} range	Limiting condition	n	p	$[V_O^{\bullet\bullet}]$	$[O_i^{\bullet}]$
intermediate	$[N'_M] = 2[V_O^{\bullet\bullet}]$	$\left(\frac{2K_R}{[N'_M]}\right)^{1/2} P_{O_2}^{-1/4}$	$\frac{K_e}{n}$	$\frac{[N'_M]}{2}$	$\frac{2K_F}{[N'_M]}$
higher	$[N'_M] = p$	$\frac{K_e}{[N'_M]}$	$[N'_M]$	$\frac{K_R [N'_M]^2}{K_e^2} P_{O_2}^{-1/2}$	$\frac{K_F K_e^2}{K_R [N'_M]^2} P_{O_2}^{1/2}$

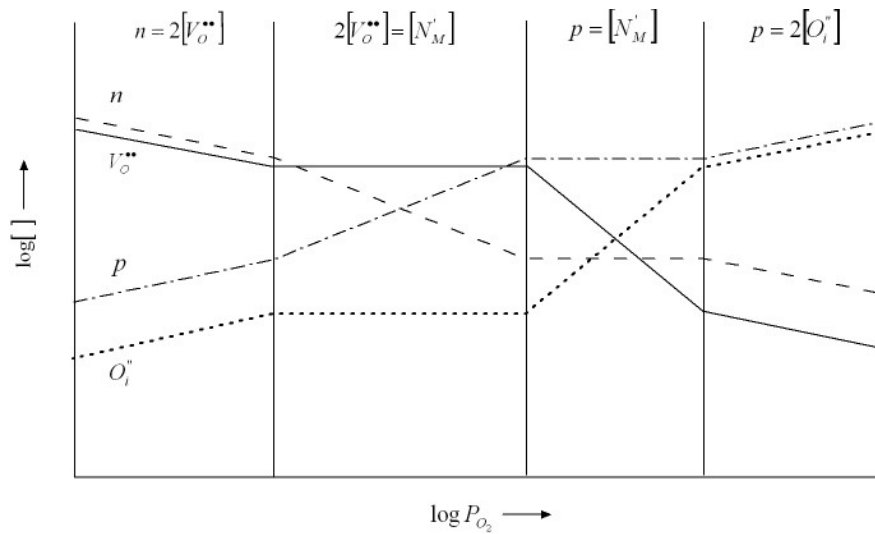


Figure 2.10. Defect concentration for acceptor-doped oxide with Frenkel disorder.

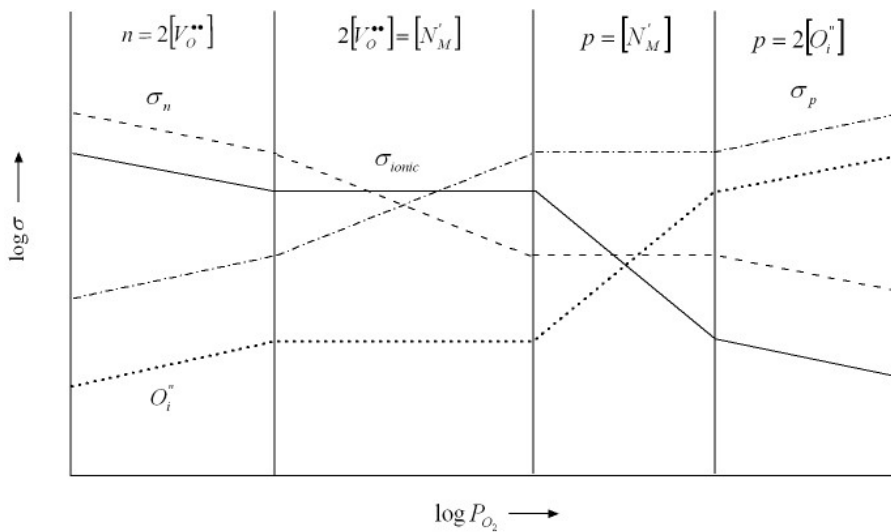


Figure 2.11. Conductivity of acceptor-doped oxide with Frenkel disorder.

2.2.5. Generation of OCV

The electrolytes and electrodes of a galvanic cell are predominant ionic and electronic conductors, respectively. The concentrations of the mobile charge carriers, i.e. ions in the electrolytes and electrons or holes (also ions for mixed conductors) in the electrodes, are high. Thus the chemical potential of the mobile charge carriers keep nearly constant inside the materials according to Eq. (2.25), in which the activity a_i can be replaced by the product of the activity coefficient γ_i and concentration c_i . As a result, there will be no electrical fields within the electrolyte and electrodes. Any possible electrical field will be destroyed by a small motion of large number of mobile charge carriers. On the other hand, both type of charge carriers have to be taken into consideration in the electrolyte and electrodes, even the concentrations of the minority charge carriers are normally very low. This will lead to large differences in chemical potentials of the minority charge carriers due to the large change of the chemical potential of the neutral electroactive component between the two electrodes according to the ionization equilibrium:

$$\mu_M = \eta_{M^{z+}} + z\eta_{e^-} \quad (2.44)$$

which can be transformed into:

$$\mu_M = \mu_{M^{z+}} + zq\phi + z(\mu_{e^-} - q\phi) = \mu_{M^{z+}} + z\mu_{e^-} \quad (2.45)$$

Inside the electrolyte, the chemical potential of the mobile ions $\mu_{M^{z+}}$ and electrostatic potential ϕ remain constant; the chemical potential of electronic species μ_{e^-} will change simultaneously with the neutral species μ_M .

Since there are no electrical fields available inside both the electrolyte and electrodes, generation of the open circuit voltage of the galvanic cell can only occur at the interfaces (or ionic junctions). Under the assumption of isothermal and isobaric conditions, the electrochemical potential will equilibrate across the interfaces for all mobile species. It should be noted here that, according to Duhem-Margules' equation, changes of activities of all other species in the material have an influence on those of the electroactive ones. Based on the assumption that all those species except the electroactive ones are sufficiently immobile and not able to achieve equilibrium across the interface within the given period of time, only the mobile ions and predominant electronic species are being considered in our discussion.

The equilibrium process of the electroactive species across the ionic interface is similar to what happens at the semiconductor junction. An electrical field at the interface is formed to compensate the driving forces for both ionic and electronic species in view of their concentration gradient between the two phases. For both species, the diffusion flux j_D is compensated by the drift flux j_E ,

$$0 = j_{D,i} + j_{E,i} = -D_i \frac{\partial c_i}{\partial x} - \frac{\sigma_i}{z_i q} \frac{\partial \phi}{\partial x} = -D_i \frac{\partial c_i}{\partial x} - \frac{c_i z_i q D_i}{kT} \frac{\partial \phi}{\partial x} \quad (2.46)$$

which means that the magnitude of the electrical field is only dependent on the concentration gradient of the mobile charge carriers, but not on the diffusivity or other factors. To achieve this equilibrium, there may be a large number of mobile species moving between the two phases, depending on their compositions. So the equilibrium of the second fastest species is the rate determining process. These are electrons in case of electrolytes and ions in case of electrodes.

The local variations of the electrostatic and chemical potential of the charged and neutral electroactive species at the interface before and after the contact of an oxide ion electrolyte and an electrode is shown in figure 2.12.

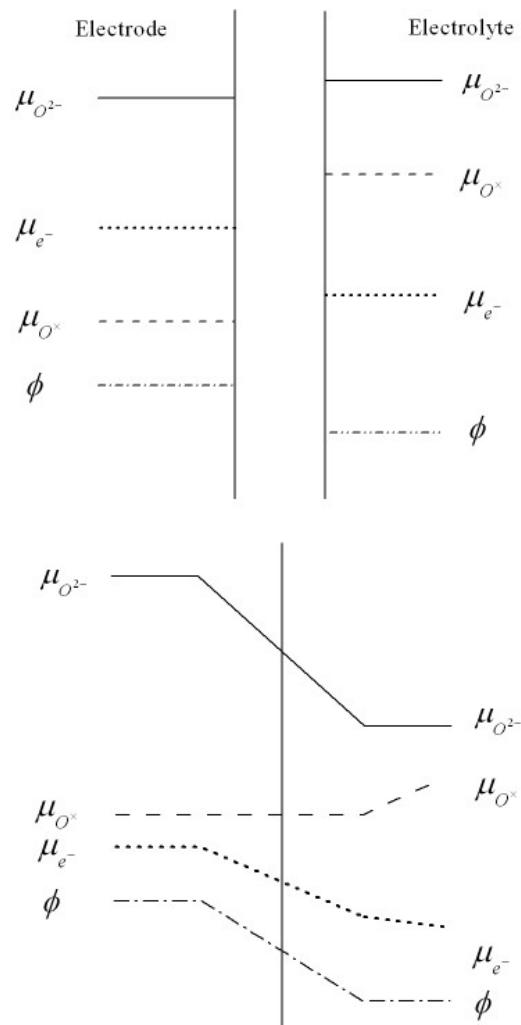


Figure 2.12. Local variations of $\mu_{O^{2-}}$, μ_{O^\times} , μ_{e^-} and ϕ before and after contact.

Two electrical fields are generated at the two interfaces in a galvanic cell. When there is a chemical potential difference of electrons between the two interfaces, which cannot be balanced by the motion of electrons through the electrolyte because of the blocking nature, an OCV is established. The local variations of the electrostatic and chemical potential of the charged and neutral electroactive species in the case of an oxide ion electrolyte is shown in figure 2.13 [6]. Both figure 2.12 and 2.13 are drawn based on the following requirement:

- i) Electrochemical potentials of the species are in equilibrium across the interface;
- ii) Electrostatic potential only changes across the interface under open circuit condition;
- iii) Chemical potentials of the majority charge carriers keep constant in their phases, while changes only occur at the interface;
- iv) The ionization equilibrium (2.44) holds everywhere in the galvanic cell.

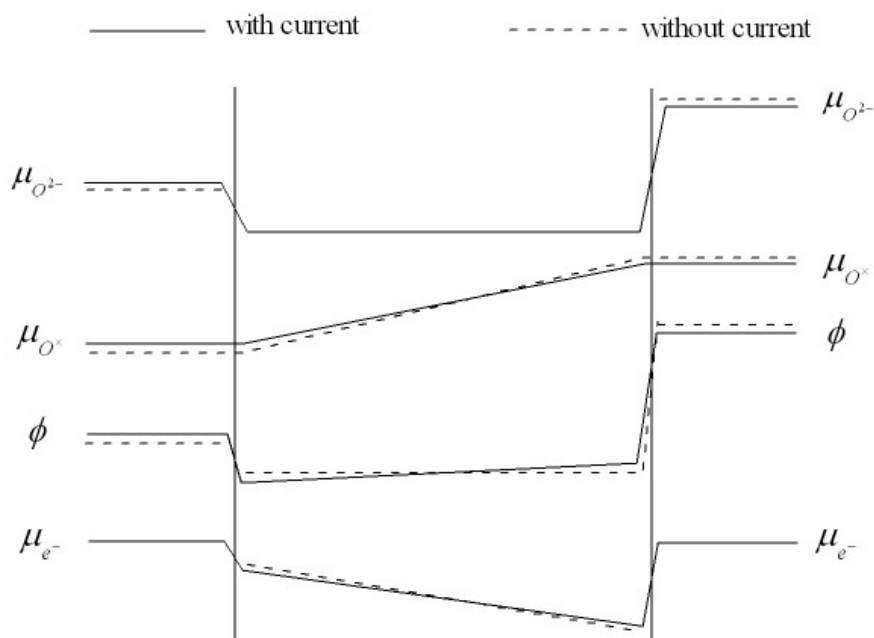


Figure 2.13. Local variations of chemical and electrostatic potential of the species in the case of an oxide ion conductor under open circuit condition and upon a current flux.

In the case of an electrical current across the galvanic cell, the chemical potentials of the majority charge carriers remain nearly unchanged, while those of the minority charge carriers are changed. Under this condition, the diffusion fluxes cannot be fully compensated by the drift fluxes. There is a net flux of the charge carriers, which is everywhere the same in the cell. In the case of an oxide ion conductor, the electrostatic potential drop at the cathode/electrolyte interface will be decreased to drive the oxide ions from the cathode to the electrolyte and the electron holes from the electrolyte to the cathode, while at the anode/electrolyte interface, the electrostatic

potential will be increased to allow the oxide ions and electrons to diffuse from the electrolyte to the anode. In order to drive the ions across the electrolyte, another electrostatic potential drop is required inside the electrolyte, which is always referred as the IR-drop. The local variations of the electrostatic and chemical potential of the charged and neutral electroactive species in the case of an oxide ion electrolyte when a current is passed is also shown in figure 2.13.

Figure 2.14 schematically shows the general arrangement of galvanic cells with the interfaces marked as I, II, III and IV.

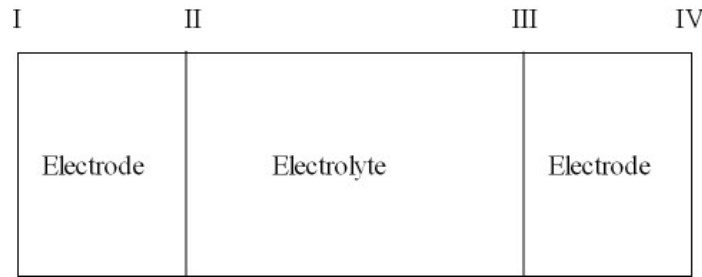


Figure 2.14. Schematic drawing of a galvanic cell with the interfaces marked as I, II, III and IV.

If two identical metal materials are used as electrical leads to connect the electrodes of the galvanic cell with a potential measuring device, the chemical potentials of the electrons in the two leads are same because of the large concentration of electrons:

$$\mu_e^I = \mu_e^{IV} \quad (2.47)$$

Using Eqs. (2.25) and (2.47), the difference in the electrostatic potential between the two metallic leads can be written in term of the difference in the electrochemical potential of the electrons:

$$E = \Delta\phi = \phi^{IV} - \phi^I = \frac{1}{q}(\eta_e^I - \eta_e^{IV}) \quad (2.48)$$

The electrode materials used in the galvanic cell should also have large number of electronic charge species. Therefore there should be no electrochemical potential gradients in the electrodes. Thus the cell voltage can also be expressed as the difference in the electrochemical potential of electrons between the interface II and III:

$$E = \Delta\phi = \phi^{IV} - \phi^I = \frac{1}{q}(\eta_e^I - \eta_e^{IV}) = \frac{1}{q}(\eta_e^{II} - \eta_e^{III}) \quad (2.49)$$

Utilizing the ionization equilibrium (2.44), the electrochemical potential of electrons can be

replaced by the differences in the electrochemical potential of the mobile ions and the chemical potential of the neutral species:

$$E = \frac{1}{q}(\eta_e^{II} - \eta_e^{III}) = \frac{1}{zq}(\mu_i^{II} - \mu_i^{III} + \eta_{i^{z+}}^{III} - \eta_{i^{z+}}^{II}) \quad (2.50)$$

The difference in the electrochemical potential of the ions can be neglected in view of the large concentration of ions in the electrolyte. So the cell voltage is simplified into:

$$E = \frac{1}{zq}(\mu_i^{II} - \mu_i^{III}) \quad (2.51)$$

which can be expressed in term of the activities of the neutral electroactive species:

$$E = \frac{kT}{zq} \ln \frac{a_i^{II}}{a_i^{III}} = \frac{RT}{zF} \ln \frac{a_i^{II}}{a_i^{III}} \quad (2.52)$$

Eq. (2.52) (Nernst's equation) holds for the electrolyte with the transference number $t_{ion} = 1$.

Although electrolytes are predominant ionic conductor, the minority electronic charge carriers play also important roles in such materials. They are responsible for many kinetic and other properties. Transports of the ionic fluxes are always accompanied with the electronic fluxes due to the local charge and charge flux neutrality conditions. If we assume that only one type of mobile ionic and electronic charge carriers are predominant, under open circuit condition, Eqs. (2.24) and (2.27) provide the relation between the electrochemical potentials of the two species:

$$\frac{\partial \eta_e}{\partial x} = \frac{\sigma_{i^{z+}}}{z\sigma_e} \frac{\partial \eta_{i^{z+}}}{\partial x} \quad (2.53)$$

Differentiating Eq. (2.50), and then substituting Eq. (2.53) into the new equation, we can get:

$$\frac{\partial \eta_{i^{z+}}^{II}}{\partial x} - \frac{\partial \eta_{i^{z+}}^{III}}{\partial x} = t_e \left(\frac{\partial \mu_i^{II}}{\partial x} - \frac{\partial \mu_i^{III}}{\partial x} \right) \quad (2.54)$$

It should be noted that the superscript II and III here don't mean the electrolyte/electrode interfaces any more. They are the boundaries of an infinite small region in the electrolyte. Substituting Eq. (2.54) into the differential form of Eq. (2.50), we can have the generalized Nernst's equation:

$$E = \frac{1}{zq} \int_{\text{electrolyte}} t_{ion} d\mu_i \quad (2.55)$$

which means that only the dependence of the transference number on the chemical potential of the mobile component plays the role in the formation of the voltage. When $t_{ion} = 1$, Eq. (2.55) is just the same as Eq. (2.52).

2.2.6. SEA concept

Figure 2.9 shows the dependences of the electrical conductivities in a pure oxide on the oxygen partial pressure. In principle, all the oxides are mixed ionic and electronic conductors. As long as the oxygen partial pressure is sufficiently high or low, the electronic conductivities become predominant and follow the $\pm 1/4$ slope dependence in Brouwer diagram. In a fuel cell, the partial pressure of oxygen changes from about 10^{-30} bar at the anode side to air or oxygen at the cathode side. Conventional fuel cells require that the electrolytes should be always predominantly ionic conducting in this range of the oxygen activity, while in SEA concept the electronic conductivity at the two ends should be higher than ionic conductivity. A schematic drawing of the conductivities in a normal fuel cell and SEA concept are shown in figure 2.15.

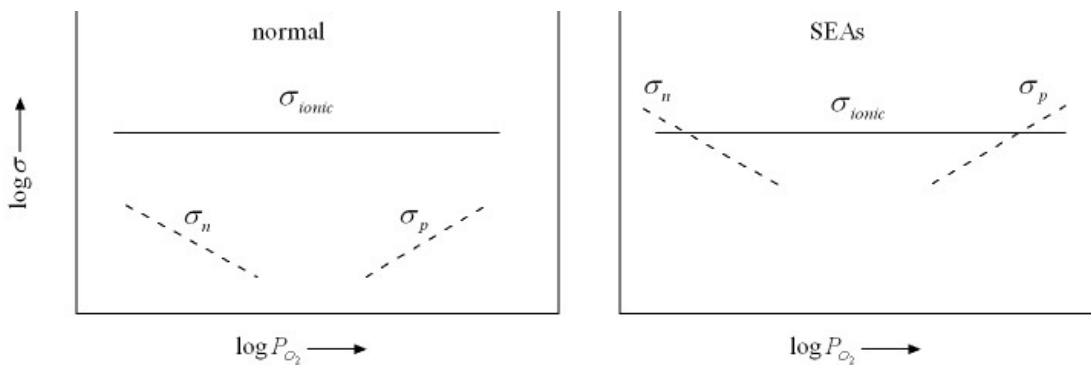


Figure 2.15. Schematic drawing of the conductivities in a normal fuel cell and SEA.

The strategy to fulfill the requirement of SEA is to increase the concentrations of the electronic charge carriers under the working conditions by doping. Once the concentrations of the charge carriers are increased, the ionic junctions are no longer as sharp as described before, but may extend over a wide regime, which may be comparable in thickness to those of the electronic pn-junctions. In case that the electronic conductivity becomes dominant and high enough at both interfaces, the surface charge region of the electrolyte can actually work as the electrode; and the separate electrode can be omitted [6,26]. Since the chemical potential of oxygen drops continuously through the cell, there will be always a region of predominant ionic conducting that blocks the electronic short circuit. The cell voltage will be reduced according to Eq. (2.55), which can be reflected from the narrowing of the electrolyte domain in Brouwer diagram by shifting the electronic lines upwards. However, this voltage drop could be much smaller than other overpotential losses in normal three component cells. Also, this energy loss due to the mixed conduction at the surfaces might be recovered as heat in real applications.

Different types of materials were chosen to be modified for SEA concept. Detailed discussions, regarding the structure and electrical properties, will be presented in chapter 3 and 5, respectively.

2.3. Background to experimental methods

2.3.1. X-Ray Powder Diffraction

X-rays are electromagnetic radiation with photon energies in the range of 100 eV-100 keV. For diffraction applications, only short wavelength x-rays in the range of a few angstroms to 0.1 angstrom (1 keV - 120 keV) are used. Because the wavelength of x-rays is comparable to the size of atoms, they are ideally suited for probing the structural arrangement in a wide range of materials. The energetic x-rays can penetrate deep into the materials and provide information about the bulk structure.

In laboratory x-ray instruments, x-rays are normally generated in x-ray tubes by a focused electron beam bombarding a solid target. Common targets used include Cu and Mo, which emit 8 keV and 14 keV x-rays with corresponding wavelengths of 1.54 Å and 0.8 Å, respectively.

Diffracted waves from different atoms can interfere with each other. If the atoms are arranged periodically as in crystals, the diffracted waves will consist of sharp interference peaks, which contain the information of the atomic arrangement. The peaks in an x-ray diffraction pattern are directly related to the atomic distances through the Bragg's law, which is shown in figure 2.16, where d is the distance between the lattice plane, λ is the wavelength of the x-ray and n is an integer representing the order of the diffraction peak.

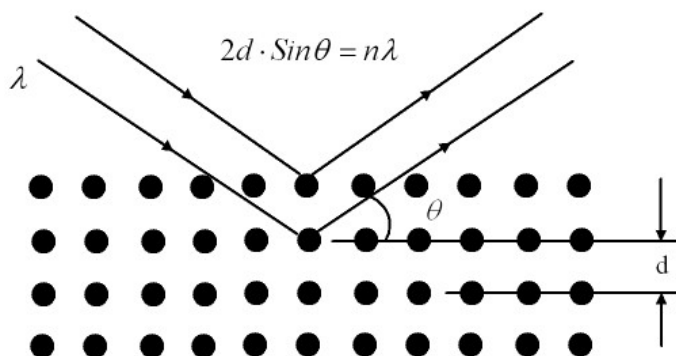


Figure 2.16. Bragg's law

Powder XRD (X-ray Diffraction) is perhaps the most widely used x-ray diffraction technique for characterizing materials. The term 'powder' really means that the crystalline domains are randomly oriented in the sample. The positions and the intensities of the peaks are used for identifying the structure, lattice constant and grain size of the material. Detailed discussions about XRD can be found in a lot of books and journal articles on this subject [27].

The database of diffraction patterns used is from the Joint Committee for Powder Diffraction Studies (JCPDS).

2.3.2. Thermal analyses

Thermal analyses include a group of methods by which physical and chemical properties of a substance and/or a mixture are determined as a function of temperature or time. Only three of the TA methods are listed below:

Differential Thermal Analysis (DTA) measures the difference in temperature between a sample and a thermally inert reference as the temperature is raised. The plot of this differential provides information on exothermic and endothermic reactions taking place in the sample. Temperatures for phase transitions, melting points, crystallization can all be determined using the computer controlled graphics package.

Thermogravimetric Analysis (TGA) measures changes in weight of a sample with increasing temperature. Moisture content and presence of volatile species can be determined with this technique. Computer controlled graphics can calculate weight percent losses. TGA gives no direct chemical information.

Dilatometry (DIL) is a technique by which the dimensional changes of the sample are monitored as a function of temperature or time.

2.3.3. Impedance spectroscopy

Electrochemical impedance spectroscopy (EIS) or impedance spectroscopy (IS) is one of the most powerful tools to analyze the characteristics of an electrochemical system. Compared to the DC techniques, which are mostly complicated and difficult to overcome the problems due to the nonlinear polarizations at the interfaces, impedance spectroscopy is easier to perform, with the capability to separate the contributions from different processes. Electrochemical Impedance is normally measured using a small excitation signal. This is done so that the cell's response is pseudo-linear, and the current response to a sinusoidal potential will be a sinusoid at the same frequency but shifted in phase. By applying a small AC voltage at varying frequencies, the phase shift and amplitude of the resulting current are recorded, from which the contributions from the bulk materials, grain boundaries in case of polycrystal, electrode processes and ionic junctions to the electrical properties could be distinguished from each other. The frequencies most employed in this technique can range from several mHz to more than 10 MHz, which are determined by the components of interest in the system. This is because in solid state systems all phenomenon have a characteristic capacitance and relaxation time [28]. Such capacitances are shown in Table 2.5.

Table. 2.5 Capacitance values with possible characteristics for a given capacitance.

Capacitance (F)	Characteristic responsible
10^{-12}	Bulk
10^{-11}	Second phase in minor quantities
$10^{-12} \sim 10^{-8}$	Grain boundary
$10^{-10} \sim 10^{-9}$	Bulk ferroelectric
$10^{-9} \sim 10^{-7}$	Surface layer
$10^{-7} \sim 10^{-5}$	Sample-electrode interface
10^{-4}	Electrochemical reactions

i). Basics

If a small voltage is applied in a sinusoidal manner with time as follows:

$$V(t) = V_0 \cos(\omega t) \quad (2.56)$$

where V_0 is the amplitude of the signal, ω is the angular frequency (radians/s), which is related to the frequency f (hertz) by:

$$\omega = 2\pi f \quad (2.57)$$

then the current response is also sinusoidal, but out of phase with the potential by an angle θ :

$$I(t) = I_0 \cos(\omega t + \theta) \quad (2.58)$$

where I_0 is the current amplitude.

The impedance is defined as the ratio between the voltage and current in the complex plane:

$$\dot{Z} = \frac{\dot{V}}{\dot{I}} \quad (2.59)$$

where $\dot{}$ represents the complex number.

Generally, it's convenient to describe these quantities in terms of real and imaginary coordinate. Then the ac voltage V can be expressed as a complex number:

$$V = V' + V''j \quad (2.60)$$

where $j = \sqrt{-1}$, V' and V'' are the real and imaginary part, respectively.

Using the Euler's relationship:

$$\exp(j\theta) = \cos \theta + j \sin \theta \quad (2.61)$$

Eq. (2.60) can be written as:

$$V = V_0 \cos \omega + jV_0 \sin \omega = V_0 \exp(j\omega) \quad (2.62)$$

In the same way, the current can be expressed as:

$$I = I_0 \exp(j\omega - \theta) \quad (2.63)$$

According to Eq. (2.59):

$$Z = Z' + Z'' j = |Z| \exp(j\theta) \quad (2.64)$$

with $|Z| = \sqrt{(Z')^2 + (Z'')^2} = \left| \frac{V_0}{I_0} \right|$, $\theta = \tan^{-1} \frac{Z''}{Z'}$, which can be plotted in a complex plane as shown in figure 2.17. This type plot is also known as Nyquist plot or Cole-Cole plot. Another type is called Bode plot, which is a plot of $\log|Z|$ vs. $\log \omega$.

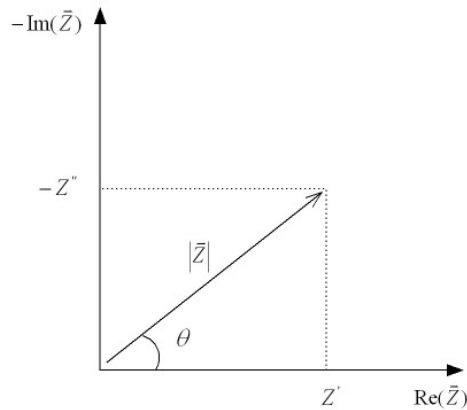


Figure 2.17. Complex plane representation of an impedance vector.

ii). Circuit elements

Given the basic theory, we can now look at impedance expressions for some simple electrical circuits as shown in Table 2.6. The impedance of a resistor Z_R is simply the resistance R , which is represented by a single point on the real axis in the Nyquist plot, while a capacitance $Z_C = 1/j\omega C$ is shown as a straight line on the imaginary axis. If there is a resistance in series

with a capacitance the impedance Z_{R-C} is given by:

$$Z_{R-C} = Z_R + Z_C = R + \frac{1}{j\omega C} \quad (2.65)$$

If they are combined in parallel, the impedance Z_{RC} is then given by:

$$\frac{1}{Z_{RC}} = \frac{1}{Z_R} + \frac{1}{Z_C} = \frac{1}{R} + j\omega C \quad (2.66)$$


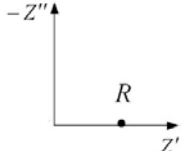
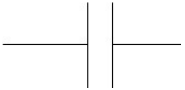
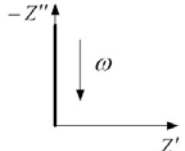

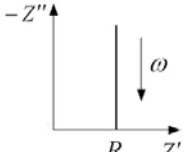
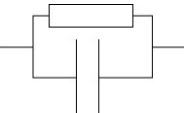
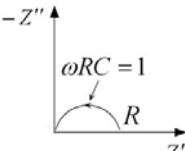
which gives:

$$Z_{RC} = \frac{R}{1 + R^2\omega^2 C^2} - \frac{R^2\omega C}{1 + R^2\omega^2 C^2} j \quad (2.67)$$

Z_{RC} has the shape of a semicircle on the complex impedance plane. At very low frequencies, all the current flows through the resistor, while at very high frequencies, the current is short circuited by the capacitor. On the top of the semicircle, the real and imaginary parts are equal, which define the relaxation time τ of the 'RC' element:

$$\tau = RC = \frac{1}{\omega} \quad (2.68)$$

Table 2.6. Basic circuit elements and their Nyquist plots.

Circuit elements	Impedance equation	Nyquist plot
	R	
	$Z_C = \frac{1}{j\omega C}$	
	$Z_{R-C} = R + \frac{1}{j\omega C}$	
	$Z_{RC} = \frac{R}{1 + R^2\omega^2 C^2} - \frac{R^2\omega C}{1 + R^2\omega^2 C^2} j$	

iii). Simple Circuit

The electrochemical cell can be described by a equivalent circuit, which is a combination of capacitors and resistors. A simple example is given in figure 2.18, where two ionic blocking electrodes are used on top of a solid electrolyte. The Ohmic resistance of the electrolyte can be represented as a pure resistor, R_i in figure 2.19. The capacitive properties of the two electrolyte/electrode interfaces are combined into one capacitor, C_{int} , with the subscript 'int' being the abbreviation of interface. C_{int} is sometimes also call the double layer capacitor C_{dl} .

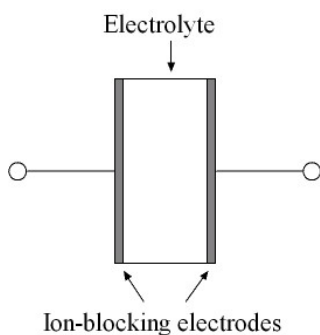


Figure 2.18. Solid electrolyte with two ion-blocking electrodes.

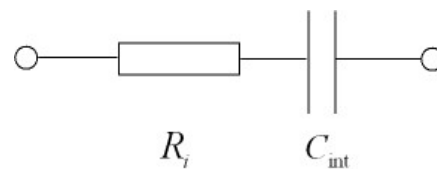


Figure 2.19. Equivalent circuit for the cell shown in figure 2.18 at low frequency.

At higher frequencies an additional geometrical capacitance, C_{geom} , due to the presence of a dielectric material between the two parallel metallic electrodes is involved as shown in figure 2.20. This is often called the “Debye circuit”. The corresponding Nyquist plot is shown in figure.2.21.

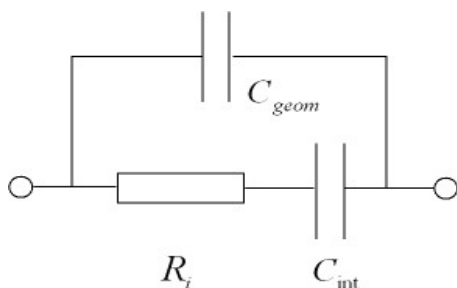


Figure 2.20. Debye circuit.

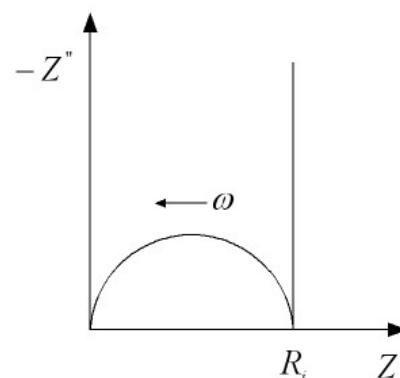


Figure 2.21. Nyquist plot of Debye circuit.

In figure 2.21, the impedance may not go all the way down to the real axis at intermediate frequencies if the values of C_{geom} and C_{int} are not sufficiently different from each other. The low frequency tail is not vertical in most cases, but is inclined at an angle from the vertical, as illustrated in figure 2.22.

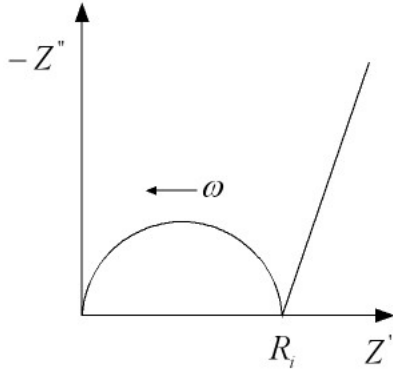


Figure 2.22. Nyquist plot showing tilted tail at low frequencies.

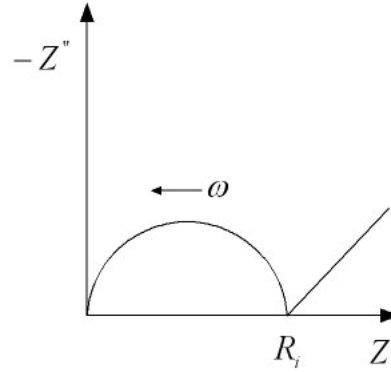


Figure 2.23. Nyquist plot showing Warburg impedance.

Such kind of deviation from the ideal Debye circuit behaviour is related to the processes occurring at the electrolyte/electrode interfaces [29]. These processes can be represented in the equivalent circuit by the following element:

$$Z = A\omega^{-\alpha} - jB\omega^{-\alpha} \quad (2.69)$$

If the electrodes are not completely blocking for the transport of ion, then the electroactive species can diffuse to or from the electrodes as a neutral reaction product according to Fick's second law. In this case, the low frequency tail will fall onto a straight line with a slope of 45 degrees, as shown in figure 2.23. Eq. (2.69) can then be written as:

$$Z_W = A\omega^{-1/2} - jB\omega^{-1/2} \quad (2.70)$$

where Z_W is the so called Warburg impedance, A and B include the information of the diffusion coefficient, the charge-transfer resistance, R_{ct} , and the interfacial capacitance, C_{int} .

If ionic transport through the solid is hindered by the presence of internal interfaces, e.g. grain boundaries, the additional ionic impedance, R_{gb} , must act in series with the bulk ionic resistance. The blocking effect from the grain boundaries can be represented by a parallel local capacitance, C_{gb} .

The equivalent circuit, considering the Warburg impedance and the grain boundary effect is shown in figure 2.24. The corresponding Nyquist plot consists of three semicircles with a straight line at the low frequency end following 45 degrees slope, as shown in figure 2.25. In the real electrochemical systems, the Nyquist plots may differ from figure 2.25, in view of the different

material properties and working conditions. Detailed discussion about impedance spectroscopy and their applications can be found elsewhere [19,30].

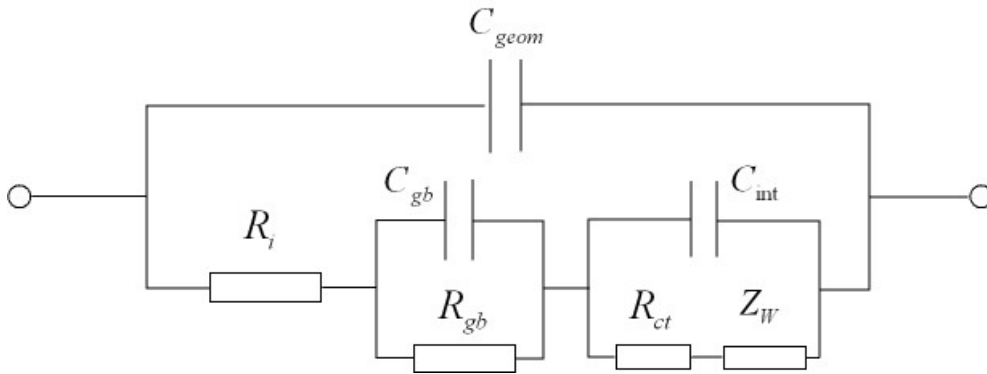


Figure 2.24. Equivalent circuit with the Warburg impedance and grain boundary impedance.

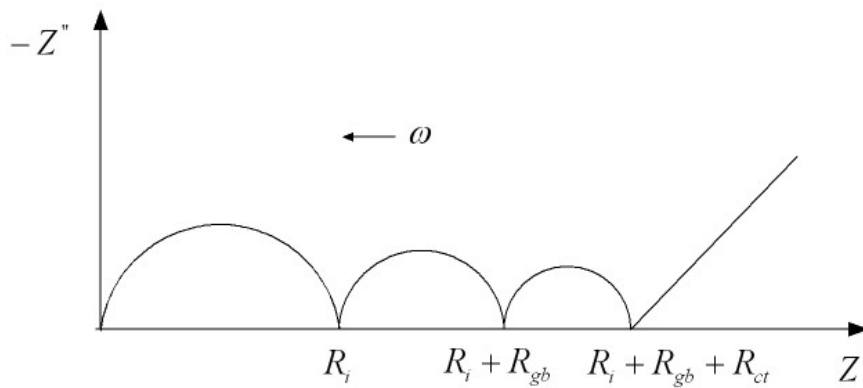


Figure 2.25. Nyquist plot of the equivalent circuit shown in figure 2.24.

2.3.4. Gas mixtures

Oxygen partial pressure can be controlled by means of different gas mixtures. For example, P_{O_2} range from 10^{-5} bar to 1 bar can be obtained by simply mixing O_2 , air or 1000 ppm O_2 with inert gas, like Ar . The value of P_{O_2} is determined by the ratio between the two gases. However, the control of oxygen partial pressure at very low values is much complicated than that of the other side. Normally this can be achieved by establishing the gas equilibriums between CO_2 and H_2 , or CO_2 and CO .

i) CO_2/H_2 mixture

Initially, when only CO_2 and H_2 are present in the gas system, equilibrium is established as below:



At high temperature, H_2O is present in gas state. Once CO and H_2O are introduced, there are two more equilibrium established simultaneously:



with the equilibrium constant k_1 and k_2 , respectively:

$$k_1 = \frac{P_{H_2O}}{P_{H_2} P_{O_2}^{1/2}} \quad (2.74)$$

$$k_2 = \frac{P_{CO_2}}{P_{CO} P_{O_2}^{1/2}} \quad (2.75)$$

In a closed system, the total amount of each element should be kept constant no matter in what form they are exist. Thus the following three conditions should be fulfilled for the amount of C , H and O , respectively:

$$[CO_2]^0 = [CO_2] + [CO] \quad (2.76)$$

$$2[H_2]^0 = 2[H_2] + 2[H_2O] \quad (2.77)$$

$$2[CO_2]^0 = 2[CO_2] + [CO] + [H_2O] + 2[O_2] \quad (2.78)$$

where the superscript denotes the initial concentration. The numbers (or concentrations) of the gas phases are proportional to their partial pressures. Thus Eqs (2.76)-(2.78) can be rewritten as:

$$p_{CO_2}^0 = p_{CO_2} + p_{CO} \quad (2.79)$$

$$p_{H_2}^0 = p_{H_2} + p_{H_2O} \quad (2.80)$$

$$2p_{CO_2}^0 = 2p_{CO_2} + p_{CO} + p_{H_2O} + 2p_{O_2} \quad (2.81)$$

From (2.79) and (2.81) we can have:

$$p_{CO} = p_{H_2O} + 2p_{O_2} \quad (2.82)$$

$$p_{CO_2} = p_{CO_2}^0 - p_{H_2O} - 2p_{O_2} \quad (2.83)$$

With the help of Eqs. (2.80), (2.82) and (2.83), the equilibrium constant k_1 and k_2 will have the following forms:

$$k_1 = \frac{p_{H_2O}}{(p_{H_2}^0 - p_{H_2O})p_{O_2}^{1/2}} \quad (2.84)$$

$$k_2 = \frac{p_{CO_2}^0 - p_{H_2O} - 2p_{O_2}}{(p_{H_2O} + 2p_{O_2})p_{O_2}^{1/2}} \quad (2.85)$$

From (2.84),

$$p_{H_2O} = \frac{k_1 p_{H_2}^0 p_{O_2}^{1/2}}{1 + k_1 p_{O_2}^{1/2}} \quad (2.86)$$

Substituting (2.86) into (2.85) for p_{H_2O} :

$$2k_1 k_2 p_{O_2}^2 + 2(k_1 + k_2) p_{O_2}^{3/2} + (k_1 k_2 p_{H_2}^0 + 2) p_{O_2} + k_1 (p_{H_2}^0 - p_{CO_2}^0) p_{O_2}^{1/2} - p_{CO_2}^0 = 0 \quad (2.87)$$

Since p_{O_2} is mostly in the range of $10^{-25} \sim 10^{-15}$ bar, so the first two items in Eq. (2.87) can be ignored, which leads to the form:

$$(k_1 k_2 p_{H_2}^0 + 2) (p_{O_2}^{1/2})^2 + k_1 (p_{H_2}^0 - p_{CO_2}^0) p_{O_2}^{1/2} - p_{CO_2}^0 = 0 \quad (2.88)$$

It's convenient to introduce the parameter, x , defined as:

$$x = \frac{p_{CO_2}^0}{p_{H_2}^0} \quad (2.89)$$

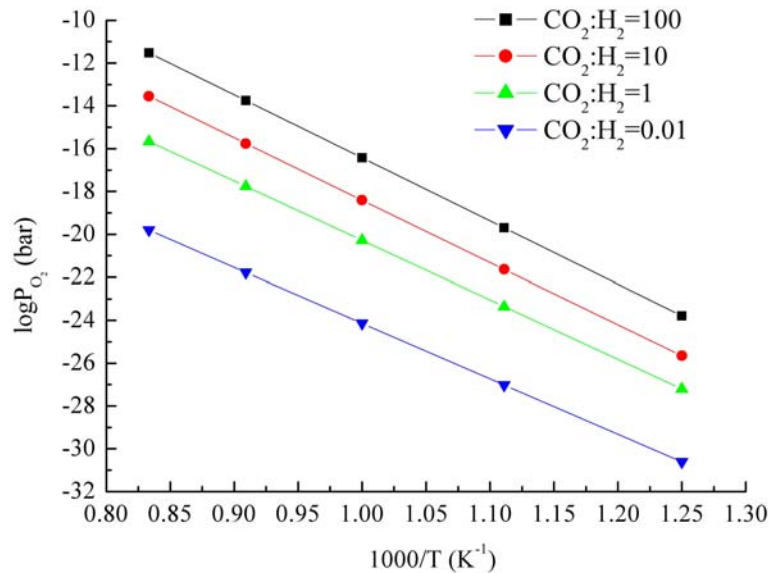
Under the condition of $p_{H_2}^0 \gg \frac{2}{k_1 k_2}$, the oxygen partial pressure can be calculated by:

$$P_{O_2}^{1/2} = \frac{x-1}{2k_2} + \sqrt{\frac{(1-x)^2}{4k_2^2} + \frac{x}{k_1k_2}} \quad (2.90)$$

k_1 is the equilibrium formation constant of gaseous H_2O , which can be directly taken from [31], while k_2 is the difference of the equilibrium formation constants of CO_2 and CO . Table 2.7 lists the k_1 , k_2 and P_{O_2} at different temperatures and x values. The results are also plotted in figure 2.26.

Table 2.7

T (K)	$\log k_1$	$\log k_2$	$\log P_{O_2}$ (bar)			
			$x_1=100$	$x_2=10$	$x_3=1$	$x_4=0.01$
800	13.293	13.909	-23.8	-25.6	-27.2	-30.6
900	11.503	11.856	-19.7	-21.6	-23.3	-27.0
1000	10.066	10.214	-16.4	-18.4	-20.3	-24.1
1100	8.888	8.874	-13.7	-15.7	-17.8	-21.8
1200	7.904	7.758	-11.5	-13.5	-15.7	-19.8

Figure 2.26. $\log P_{O_2}$ v.s. $1000/T$ of mixture of H_2 and CO_2 .

ii) CO_2/CO mixture

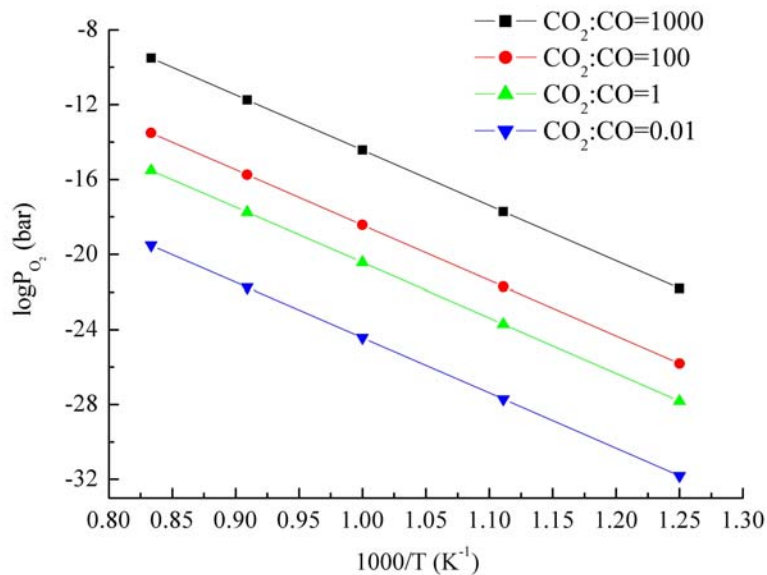
The oxygen partial pressure in CO_2/CO mixture is easily obtained by simply considering the equilibrium (2.73). From (2.75), the oxygen partial pressure is as follows:

$$p_{O_2} = \left(\frac{p_{CO_2}}{p_{CO} \cdot k_2} \right)^2 = \left(\frac{x}{k_2} \right)^2 \quad (2.91)$$

x is the ratio between p_{CO_2} and p_{CO} . Table 2.8 and figure 2.27 list some results from CO_2/CO mixture.

Table 2.8

T (K)	$\log k_2$	$\log P_{O_2}$ (bar)			
		$x_1=1000$	$x_2=10$	$x_3=1$	$x_4=0.01$
800	13.909	-21.8	-25.8	-27.8	-31.8
900	11.856	-17.7	-21.7	-23.7	-27.7
1000	10.214	-14.4	-18.4	-20.4	-24.4
1100	8.874	-11.7	-15.7	-17.7	-21.7
1200	7.758	-9.5	-13.5	-15.5	-19.5

Figure 2.27. $\log P_{O_2}$ v.s. $1000/T$ of mixture of CO_2 and CO .

2.3.5. EMF measurement

i) Kiukkola-Wagner cell

Kiukkola-Wagner type cells were initially used to determine the standard molar free energy of formation of several compounds such as CoO, NiO, Cu₂O, Ag₂S [32,33]. An oxide cell can be generally written as the following:



where A , B and AO , BO are metals and metal oxides, respectively. Assuming the ionic transference number of the electrolyte is 1, the EMF of such cell is:

$$E = -\frac{\Delta_r G}{zF} \quad (2.93)$$

z and F have the normal meanings, while $\Delta_r G = \Delta_F G_{AO} - \Delta_F G_{BO}$ stands for the Gibbs reaction energy of the following reaction:



If one of the Gibbs formation energies of the two oxides $\Delta_F G_{AO}$ and $\Delta_F G_{BO}$ is known, then the other one can be determined by Eq. (2.93).

The cell (2.92) is also a measure of the activity difference of oxygen, which is given by the mixtures of the metal and metal oxide. The Gibbs formation energy can be written as:

$$\Delta_F G_{AO} = -RT \ln K_{AO} = -RT \ln \frac{1}{p_{O_2}^{1/2}} = RT \ln p_{O_2}^{1/2} \quad (2.95)$$

$$\Delta_F G_{BO} = -RT \ln K_{BO} = -RT \ln \frac{1}{p_{O_2}^{n/2}} = RT \ln p_{O_2}^{n/2} \quad (2.96)$$

where K_{AO} , K_{BO} are the equilibrium constants of the formation reactions:



Thus Eq. (2.93) can be rewritten as:

$$E = \frac{RT}{2zF} \ln \frac{p_{O_2}^{1/2}}{p_{O_2}^{n/2}} \quad (2.99)$$

Eq. (2.99) is actually same as (2.52).

In this work, Kiukkola-Wagner type cells are used to estimate what type of conduction is predominant in the material. Figure 2.28 shows the oxygen partial pressures given by different metal and metal oxide mixtures.

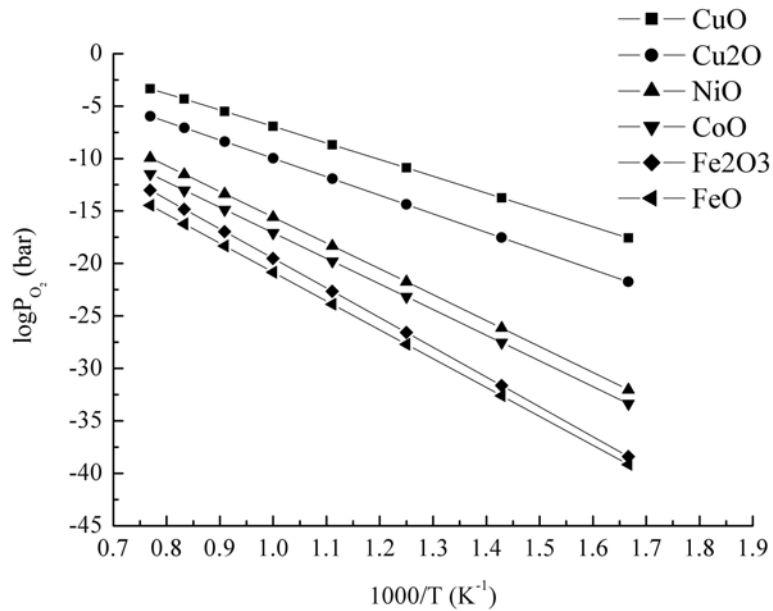


Figure 2.28. Oxygen partial pressures given by different metal and metal oxide mixtures.

ii) Gas concentration cell

Different from Kiukkola-Wagner type cells, the activities of the neutral electroactive species at the two electrodes are given by the gas phases directly. The EMF is calculated by Eq. (2.52).

2.4. References

- [1]. Karl Kordesch, Günter Simader, *Fuel cells and Their Applications*, VCH, Weinheim, Germany, 1996.
- [2]. Chris Rayment, Scott Sherwin, *Introduction to Fuel Cell Technology*. Notre Dame, 2003.
- [3]. L. Carrette, K.A. Friedrich, U. Stimming, *Fuel cells*, No.1, 2001, 5.
- [4]. Vijay Ramani, *The Electrochemical Society Interface*, Spring 2006, 41.
- [5]. Wing-Fong Chu, Venkataraman Thangadurai, Werner Weppner, *Ionics* 12, 2006, 1.
- [6]. Werner Weppner, *Ionics* 7, 2001, 404.
- [7]. Werner Weppner, *Ionics* 1, 1995, 1.
- [8]. Werner Weppner, in: *Solid State Ionics: Materials and Devices* (B.V.R. Chowdari and Wenji Wang, Eds.), World Scientific Publ. Co., Singapore, 2000, 3.
- [9]. Werner Weppner, in: *Materials for Lithium-Ion Batteries* (C. Julien and Z. Stoyanov, Eds.), Kluwer Acad. Publ., Dordrecht, NL, 2000, 401.
- [10]. P.J Gellings, H.J.M. Bouwmeester, *The CRC Handbook of Solid State Electrochemistry*, CRC press, Inc. 1997.
- [11]. Werner Weppner, in: *Materials for Lithium-Ion Batteries* (C. Julien and Z. Stoyanov, Eds.), Kluwer Acad. Publ., Dordrecht, NL, 2000, 413.
- [12]. Ilan Riess, *Solid State Ionics* 52, 1-3, 1992, 127.
- [13]. Hermann Schmalzried, *Solid State Reactions 2 ed.* Verlag Chemie, Weinheim, 1981.
- [14]. E. Koch, C. Wagner, *Z. Phys. Chem.(B)* 38, 1937, 295.
- [15]. Peter W. Atkins, *Physical Chemistry 7 ed.*, Oxford Univ. Press, 2001.
- [16]. H.L. Tuller, In: O. Toft Sørensen, Editor, *Nonstoichiometric Oxides*, Acad. Press, New York 1981, 271.
- [17]. J.A. Kliner, C.D. Walters, *Solid State Ionics* 6, 1982, 253.
- [18]. H. Inaba, H. Tagawa, *Solid State Ionics* 83, 1996, 1.
- [19]. Robert A. Huggins, *Ionics* 8, 2002, 300.

- [20]. Werner Weppner, Robert A. Huggins, In: *Annual Review of Materials Science*, Vol. 8, 1978, 269.
- [21]. M. Liu and H. Hu, *J. Electrochem. Soc.* 143, 1996, L109.
- [22]. Werner Weppner, Robert A. Huggins, *J. Electrochem. Soc.* 124, 1977, 1569.
- [23]. Weppner, Huggins, *J. Solid State Chem.* 22, 1977, 297.
- [24]. F.A. Kröger, H.J. Vink, *Solid State Phys.* 3, 1956, 307.
- [25]. G. Brouwer, *Philips Res. Rep.* 9, 1954, 366.
- [26]. Werner Weppner, *Ionics* 4, 1998, 422.
- [27]. E. Fuchs; H. Oppolzer; H. Rehme, *Particle Beam Microanalysis: Fundamentals, Methods and Applications*, VCH, Weinheim, 1990.
- [28]. John T.S. Irvine, Derek C. Sinclair, Anthony R. West, *Advanced Materials* 2, 1990, No.3, 132.
- [29]. I.D. Raistrick, C. Ho, R.A. Huggins, *J. Electrochem. Soc.* 123, 1976, 1469.
- [30]. J. R. Macdonald, *Impedance Spectroscopy*, Wiley, New York 1987.
- [31]. Ihsan Barin, *Thermochemical data of pure substances* Vol. 1, VCH, Weinheim, 1995.
- [32]. C. Wagner, *Proceedings of the International Commission on Electrochemical Thermodynamics and Kinetics Seventh Meeting*, Lindau, 1955 (Butterworth, London, 1957).
- [33]. Kalevi Kiukkola, Carl Wagner, *J. Electrochem. Soc.* 104, 1957, 379.

Chapter 3

Material aspects

3.1. General introduction

General requirements for electrolytes in fuel cells include:

- i) High ionic conductivity with negligible electronic conductivity;
- ii) High chemical stability in the working environment.

Both oxide ion and proton conductors can be used as electrolyte for fuel cells. Because of the high activation energy for oxide ion conduction, generally high temperatures ($>800^{\circ}\text{C}$) are required to reach the reasonable conductivity. At high temperatures, solid oxide materials are favorable for fuel cell applications due to the presence of high oxygen partial pressure under working conditions. Among those materials, yttria-stabilized-zirconia (YSZ) was found to be the best material for its high conductivity and chemical stability [1-5]. To date, YSZ is still the most widely used electrolyte for SOFC in the real applications. Higher oxide ion conductivities have been found in materials based on CeO_2 , LaGaO_3 ; however, their applications are limited to some extent by the low chemical stability [6-15]. Protons were shown to exist in some oxides as minority charge carriers in the 1960s [16,17]. Predominant protonic conductions were found in materials based on SrCeO_3 [18], SrZrO_3 [19], BaCeO_3 [20] and some other materials under hydrogen-containing atmospheres. Severe problems related to these materials are also mostly due to the stability, especially the high reactivity with CO_2 . More comprehensive reviews about the electrolyte materials can be found elsewhere [21,22].

Compared to normal fuel cells, SEA concept has several advantages that have been mentioned in chapter 1. It demands the new requirement for the materials as well. The following requirement should be fulfilled for SEA:

- i) Predominant electron hole conduction in oxidizing atmosphere;
- ii) Predominant electron conduction in reducing atmosphere;
- iii) Predominant ionic conduction at intermediate oxygen partial pressure range;
- iv) High catalytic effect on the surface under both oxidizing and reducing conditions.

In this chapter, we will give a brief introduction to the common electrolytes, and discuss the possibilities of using them for SEA concept by modifying their electrical properties.

3.2. Fluorite-type oxide electrolytes

The fluorite type material YSZ is the most widely used electrolyte in SOFC. To lower the operating temperature, extensive work has been done to look for new fluorite materials with high conductivity values than that of YSZ. A schematic view of the fluorite structure is show in figure 3.1.

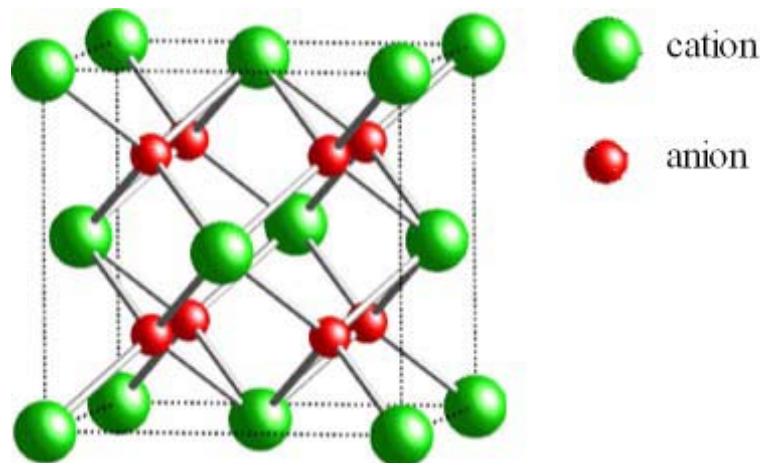


Figure 3.1. A schematic view of the fluorite type structure.

From the structural point of view, the oxide ion must cross a bottleneck limited by three cations located on one of the triangular faces of its coordination tetrahedron to reach to a new site. The simplest way to make this crossing easier is to occupy the cation sites with polarizable cations. As the polarizability of an ion increases with the size, big cations are preferred. On the other hand, the ratio between the cation and anion radii must be close to 0.7 to maintain the fluorite structure. Since the oxide ion radius is 1.38\AA when the coordination number is four, the optimum cation size should be close to 1\AA . Thus only elements located at the beginning of the lanthanide series can ideally fit the size requirement [23].

Pure ceria is basically a poor ionic conductor and its ionic conductivity is very low. The ionic conductivity can be significantly enhanced by cation doping as a result of the increase in oxygen vacancy concentration. The ionic conductivities of a series of ceria-based oxides are higher than YSZ, and Sm doped ceria was found to have the highest conductivity [24-26]. Figure 3.2 shows the conductivities of several ceria-based oxides according to Yahiro et al. [27]. The higher conductivities of Sm and Gd doped ceria are mainly due to the close radii to that of cerium, which leads to the smaller values of the association enthalpy [28].

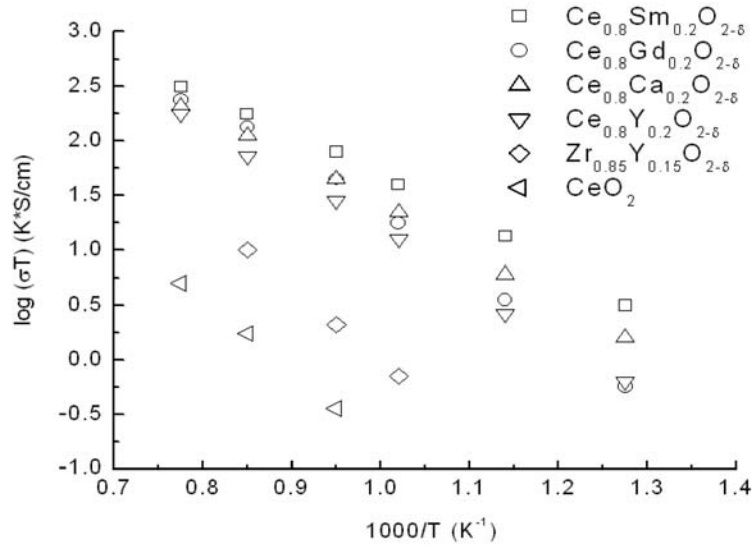
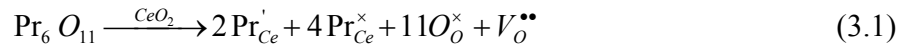


Figure. 3.2. Arrhenius plots of the ionic conductivity of ceria based oxides doped with rare-earth oxides according to Yahiro et al. [27].

The electrical conductivities of doped ceria are constant in the high and intermediate oxygen partial pressure region, but they increase at low oxygen partial pressure range with decreasing P_{O_2} . The n-type conduction appears because of the number of conductive electrons increase with the reduction of ceria. It also increases with increasing temperature. Different approaches have been conducted to minimize the electronic conduction. For examples, a thin YSZ layer is deposited between ceria and anode [29,30]; extra dopant is introduced into the lattice to trap the mobile electrons [31]. However, instead of try to block this electronic conduction, we can take advantage of it in SEA concept. A more critical problem related to the reduction could be the cracking due to the large difference on ionic radii between Ce^{4+} (0.97Å) and Ce^{3+} (1.143Å), which always cause failure during EMF and fuel cell measurement. In SEA concept, we need both n and p type conductions under the working conditions. To do so, dopant with mixed valence, like Pr, was also introduced into the lattice:



Under oxidizing conditions, the electron hole conduction is supposed to take place via the hopping mechanism:



3.3. Perovskite-type oxide electrolytes I

The name perovskite is generally used for metal oxides with the formula ABO_3 , where A is the larger twelve-coordinated cation and B is the smaller six-coordinated cation. A unit cell of the perovskite structure and the BO_6 polyhedron stacking are shown in figure 3.4.

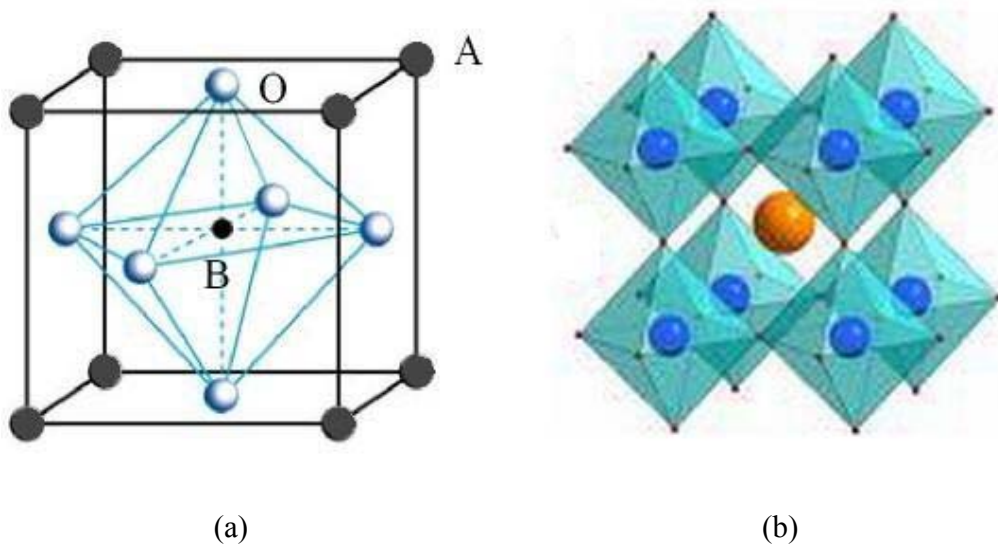


Figure 3.4. (a) Perovskite type structure, (b) Stacking of the BO_6 polyhedron.

The ions on A site should be large in order to achieve the large free volume, while the ions on B site should be chosen to adjust the so called tolerance factor (or Goldschmidt factor) to be close to 1 [32]. The tolerance factor, introduced by Goldschmidt [33], describes the relationship between symmetry and ionic radii in the perovskite:

$$t = \frac{r_A + r_O}{\sqrt{2}(r_B + r_O)} \quad (3.3)$$

When the factor is close to 1, the structure of the perovskite should be cubic.

Similar to fluorite type materials, substitution of A or/and B cations by aliovalent dopants will introduce vacancies in the anion network that may lead to significant oxygen mobility. The first successful composition with high oxide ion conductivity was obtained by Feng and Goodenough in 1994 with the composition of $La_{0.9}Sr_{0.1}Ga_{0.8}Mg_{0.2}O_{2.85}$ (LSGM). Ishihara et al. published the same result nearly at the same time when he studied the effect of various dopants at the La and Ga sites on the conductivity, and Sr and Mg were found to be the best results among the alkaline-earth cations.

The same authors also extended their study to the family $(\text{La}_{0.9}\text{Ln}_{0.1})_{0.8}\text{Sr}_{0.2}\text{Ga}_{0.8}\text{Mg}_{0.2}\text{O}_{3-\delta}$ with $\text{Ln}=\text{Y}, \text{Nd}, \text{Sm}, \text{Gd}$ and Yb [34]. The conductivity decreases in the order $\text{Nd} > \text{Sm} > \text{Gd} > \text{Yb} > \text{Y}$. This is an illustration of the effect of the crystal lattice symmetry on the oxygen mobility: the conductivity decreases linearly with the departure from the ideal ion radii ratio for a cubic perovskite structure.

The contribution from p and n type electronic conduction was calculated based on the defect model and measured experimentally [35]. When the defect concentrations are controlled by doping, the electroneutrality condition is given by the following:

$$[\text{Sr}'_{\text{La}}] + [\text{Mg}'_{\text{Ga}}] + n = 2[\text{V}^{\bullet\bullet}_{\text{O}}] + p \quad (3.4)$$

Compared to ionic defects, the concentrations of electronic defects are very small. So Eq. (3.4) can be simplified to:

$$[\text{Sr}'_{\text{La}}] + [\text{Mg}'_{\text{Ga}}] = 2[\text{V}^{\bullet\bullet}_{\text{O}}] \quad (3.5)$$

From Eqs. (2.39~40) and (3.5),

$$p = \left(\frac{[\text{Sr}'_{\text{La}}] + [\text{Mg}'_{\text{Ga}}]}{2K_R} \right)^{1/2} \cdot K_e \cdot p_{\text{O}_2}^{1/4} \quad (3.6)$$

Under reducing conditions, the defect equilibrium is same as Eq. (2.37). Assuming the concentrations of the electronic defects are small, the Eq. (3.5) still holds. Then from Eqs. (2.40) and (3.5),

$$n = \left(\frac{2k_R}{[\text{Sr}'_{\text{La}}] + [\text{Mg}'_{\text{Ga}}]} \right)^{1/2} \cdot p_{\text{O}_2}^{-1/4} \quad (3.7)$$

The concentrations of electron holes and electrons in LSGM have 1/4 and -1/4 dependence on the oxygen partial pressure, respectively. Under the working conditions of fuel cells, the number of electron holes and electrons are small, so LSGM is a pure ionic conductor over a wide range of oxygen partial pressure.

Many perovskite oxides such as Sr-doped LaMO_3 ($\text{M}=\text{Mn}, \text{Fe}, \text{Co}, \text{or Ni}$) exhibit very high p type electronic or mixed conductivity at elevated temperatures [36-40]. For example, $\text{La}_{0.9}\text{Sr}_{0.1}\text{MnO}_{3-\delta}$ (LSM) and $\text{La}_{0.6}\text{Sr}_{0.4}\text{CoO}_{3-\delta}$ are well known cathode materials. However, few examples have been given concerning the n type conductivity in LSGM type materials. Only Cr and Mn doped samples show visible increase on the conductivity at low oxygen partial pressure region [41-43]. Since Mn is also well known for providing the p type conductivity, it's interesting to study the possibility of employing Mn doped perovskite oxides for SEA concept.

3.4. Perovskite-type oxide electrolytes II

Generally speaking, protonic transport includes transport of protons (H^+) and any assembly that carries protons (OH^- , H_2O , H_3O^+ , NH_4^+ , HS^- , etc.). The transport of protons (H^+) between relatively stationary host anions is termed the Grotthuss or free-proton mechanism. Transport by any of the other species is termed a vehicle mechanism [21].

Protons are not part of the nominal structure or stoichiometry in perovskite materials. But they are present as defects remaining in equilibrium with ambient hydrogen or water vapour:



which is exothermic so that protons rule at low temperatures and oxygen vacancies at high temperatures.

The systematic investigation of proton conducting perovskite type oxides started with the work of Takahashi and Iwahara in 1980 [44]. Several oxides have been shown to be good conductors. The most well known of these are acceptor doped Sr, Ba cerates and zirconates. These materials have higher proton conductivity especially at lower temperatures than pure oxide ion conductors, making them good candidates for intermediate temperature fuel cells. Another advantage of using a proton conductor for fuel cell is that water will be formed at cathode; hence the fuel at the anode remains pure, eliminating the need for re-circulation.

At high oxygen partial pressures, Eqs. (2.36-37) hold for the equilibrium with the gas, so this type of materials also have high p-type conductivity at high temperature.

The conductivity of perovskite proton conductors decrease in the following order: $BaCeO_3 > SrCeO_3 > SrZrO_3 > CaZrO_3$ [45]. To get higher conductivity, two approaches are under active consideration: (i) to substitute A site cations with lower electronegative elements ($Ba > Sr > Ca$), and (ii) use of easy reduction element in B site ($Ce > Zr$). Some solid electrolyte with perovskite and fluorite structures are good catalysts for the oxidation of hydrogen and hydrocarbons [46], which make it possible to omit the separate electrode as long as the electronic conductivity in the surface region under the working condition is high enough. Electronic conductivities in the perovskite oxides have been investigated for different purpose by several authors. Various dopants were introduced into the lattice. Among them, Hirabayashi et al. reported the result of a fuel cell model operating without an anode, utilizing $BaCe_{0.76}Y_{0.2}Pr_{0.04}O_{3-\delta}$ as the electrolyte [47]. Worrell and his coworkers reported the effect of Pr substitution on the electronic and ionic conductivity of 10% Gd doped barium cerate. The introduction of Pr in the $Ba(Ce_{0.9-y}Pr_yGd_{0.1})O_{2.95}$ solid solutions increase the p-type conductivity [48]. Fukui et al. also observed the increase on electron hole conductivity in $Ba(Pr_{0.6}Gd_{0.4})O_{3-\delta}$ [45,49]. In this work, we will also look at the possible application of this kind of material for SEA concept.

3.5. References

- [1]. M. Rühle, N. Claussen, A.H.Heuer, in "*Advances in Ceramics*", Vol. 12, The American Ceramic Society, Columbus, OH, 1984, 352.
- [2]. N. Bonanos, R.K. Slotwinski, B.C.H. Steele, E.P. Butler, *J. Mater. Sci. Lett.* 3, 1984, 245.
- [3]. T.H. Etsell, S.N. Flengas, *Chem. Res.* 70, 1970, 339.
- [4]. D. Yuan, F.A. Kröger, *J. Electrochem. Soc.* 116, 1969, 594.
- [5]. H.J.M. Bouwmeester, H. Kruidhof, A.J. Burggraaf, P.J.Gellings, *Solid State Ionics* 53-56, 1992, 460.
- [6]. T. Takahashi, in: *Physics of Electrolytes*, ed. J. Hladik, Vol. 2, Academic Press, London, 1972, 989.
- [7]. H.L. Tuller, A.S. Nowick, *J. Electrochem. Soc.* 122, 1975, 255.
- [8]. T. Kudo, H. Obayashi, *J. Electrochem. Soc.* 123, 1976, 415.
- [9]. Mogens, Mogensen, Nigel M. Sammes, Geoff A. Tompsett, *Solid State Ionics* 129, 2000, 63.
- [10]. B.C.H. Steele, *Solid State Ionics* 129, 2000, 95.
- [11]. K. Huang, R. Tichy, J.B. Goodenough, *J. Am. Ceram. Soc.* 81, 1998, 2565.
- [12]. M. Feng, J.B. Goodenough, K. Huang, C. Milliken, *J. Power Sources.* 63, 1996, 47.
- [13]. Cinar Oncel, Mehmet A. Gulgun, *Mat. Res. Soc. Symp. Proc.* Vol. 756, 2003.
- [14]. N.Q. Minh, *J. Am. Ceram. Soc.* 76[3], 1993, 563.
- [15]. K. Yamaji, H. Nehishi, T. Horita, N. Sakai, H. Yokokawa, *Solid State Ionics* 135, 2000, 389.
- [16]. K.D. Kreuer, in: *Annu. Rev. Mater. Res.* 2003, 33:333.
- [17]. S. Stotz, C. Wagner, *Ber. Bunsenges. Phys. Chem.* 70, 1966, 781.
- [18]. H. Iwahara, H. Uchida, S. Tanaka, *Solid State Ionics* 9-10, 1983, 1021.
- [19]. T. Takahashi, H. Iwahara, *Rev. Chim. Miner.* 17, 1980, 243
- [20]. H. Iwahara, H. Uchida, K. Ono, K. Ogaki, *J. Electrochem. Soc.* 135, 1988, 529.
- [21]. Truls Norby, *Solid State Ionics* 125, 1999, 1

- [22]. H. Iwahara, Y. Asakura, K. Katahira, M. Tanaka, *Solid State Ionics* 168, 2004, 299.
- [23]. J.C. Boivin, G. Mairesse, *Chem. Mater.* 10, 1998, 2870.
- [24]. H. Yahiro, Y. Egushi, H. Arai, *J. Appl. Electrochem.* 18, 1988, 527.
- [25]. Y. Egushi, T. Setoguchi, T. Inoue, H. Arai, *Solid State Ionics* 52, 1992, 165.
- [26]. G.B. Balazes, R.S. Glass, *Solid State Ionics* 76, 1995, 155.
- [27]. H. Yahiro, K. Eguchi and H. Arai, *Solid State Ionics* 36, 1989, 71.
- [28]. V. Butler, C.R.A. Catlow, B.E.F. Fender, J.H. Harding, *Solid State Ionics* 8, 1983, 109.
- [29]. T. Inoue, T. Setoguchi, K. Eguchi, H. Arai, *Solid State Ionics* 35, 1989, 285.
- [30]. H. Yahiro, Y. Baba, K. Eguchi and H. Arai, *J. Electrochem. Soc.* 135, 1988, 2077.
- [31]. D.L. Maricle, T.E. Swarr, S. Karavolis, *Solid State Ionics* 52, 1992, 173.
- [32]. Y. Yamamura, C. Ihara, et al. *Solid State Ionics* 160, 2003, 93.
- [33]. V.M. Goldschmidt, T. Barth, G. Lunde, W. Zachariassen, in: *Pt. VII Skrifter Norske Videnskabs-Akademi, Oslo*, 1926, 117.
- [34]. T. Ishihara, H. Matsuda, Y. Takita, *Solid State Ionics* 79, 1995, 147.
- [35]. Jin-Ho Kim, Han-Il Yoo, *Solid State Ionics* 140, 2001, 105.
- [36]. T. Ishihara, S. Ishikawa, C. Yu, et al. *Phys. Chem. Chem. Phys.* 5, 2003, 2257.
- [37]. H.Y. Tu, Y. Takeda, N. Imanishi, O. Yamamoto, *Solid State Ionics* 117, 1999, 277.
- [38]. J.A.M. van Roosmalen, J.P.P. Huijsmans, L. Plomp, *Solid State Ionics* 66, 1993, 279.
- [39]. L.W. Tai, M.M. Nasrallah, H.U. Anderson, D.M. Sparlin, S.R. Sehlin, *Solid State Ionics* 76, 1995, 259.
- [40]. K. Huang, H.Y. Lee, J.B. Goodenough, *J. Electrochem. Soc.* 145, 1998, 3220.
- [41]. S.W. Tao, J.T.S. Irvine, *J. Electrochem. Soc.* 151, 2004, A252.
- [42]. N. Trofimenko, H. Ullmann, *Solid State Ionics* 118, 1999, 215.
- [43]. R.T. Baker, B. Gharbage, F.M.B. Marques, *J. Electrochem. Soc.* 144, 1997, 3130.
- [44]. T. Takahashi, H. Iwahara, *Revue de Chim. Miner.* 17, 1980, 243.
- [45]. T. Fukui, S. Ohara, S. Kawatsu, *Solid State Ionics* 116, 1999, 331.
- [46]. P.J. Gellings, H.J.M. Bouwmeester, *Catal. Today* 58, 2000, 1.

- [47]. D. Hirabayashi, A. Tomita, M.E. Brito, et al. *Solid State Ionics* 168, 2004, 23.
- [48]. R. Mukundan, P.K. Davies, W.L. Worrell, *J. Electrochem. Soc.* 148, 2001, A82.
- [49]. T. Fukui, S. Ohara, S. Kawatsu, *J. Power Sources* 71, 1998, 164.

Chapter 4

Experimental aspects

4.1. Sample preparation

4.1.1 Solid-State Reaction

Most samples were prepared in the way of the conventional solid-state reaction. Metal oxides or carbonates from Chempur, Aldrich, Alfa or Merck products were used as starting materials. The detailed information about the starting oxides is listed in Table 4.1. Before weighting the stoichiometric amounts of the powders, La_2O_3 was annealed in air at 950°C for 24hs to remove the water and carbonate contents; SrCO_3 was always kept in the drying chamber at 120°C . The mixed powders were ground in an agate mortar with a pestle, and then ball milled with isopropanol in the ZrO_2 or Al_2O_3 container for 16~24hs. After drying, the ball-milled mixtures were calcined in Al_2O_3 crucibles first at 1100°C for 10hs. The obtained powders were then ground and ball milled again, and pressed isostatically into cylinders (15mm diameter and 25mm thickness). The last synthesis step was the sintering at 1500°C for 6~10hs. The heating and cooling rates at this step were different for fluorite and perovskite materials. Experimentally, to avoid cracks in the fluorite cylinders the heating and cooling rate were set to be $1^\circ\text{C}/\text{min}$. Generally speaking, there were no cracks found in perovskite materials after sintering, so they could be heated up and cooled down rapidly. The heating and cooling rate in this case were set to be $5^\circ\text{C}/\text{min}$. The obtained samples were cut into small pieces (0.5mm~1mm in thickness) by the diamond saw. Both surfaces of the pellets were polished by the diamond embedded disc with diamond suspension of $10\mu\text{m}$, or $6\mu\text{m}$ ~ $1\mu\text{m}$ when very smooth surfaces were required. For electrical measurement, both surfaces were covered with platinum past, and the electrical contact was made by heating the platinum past at 950°C for 1h. A flow chart of the solid-state preparation process is shown in figure 4.1 in next page.

Table 4.1. Chemical list.

CeO_2 (99.9%, Chempur)	Cr_2O_3 (99%, Alfa)	La_2O_3 (99.99%, Alfa)
Sm_2O_3 (99.9%, Chempur)	CoO (Alfa)	SrCO_3 (99.9%, Aldrich)
Pr_6O_{11} (99.9%, Chempur)	TiO_2 (99.99%, Aldrich)	Ga_2O_3 (99.99%, Alfa)
Fe_2O_3 (99.9%, Alfa)	SnO_2 (99.9%, Merck)	MgCO_3 (Alfa)
CuO (99.9%, Alfa)	Bi_2O_3 (99.999%, Strem)	Mn_2O_3 (99%, Aldrich)
Sb_2O_5 (99.999%, Ventron)	Y_2O_3 (99.99%, Aldrich)	BaCO_3 (99.8%, Alfa)

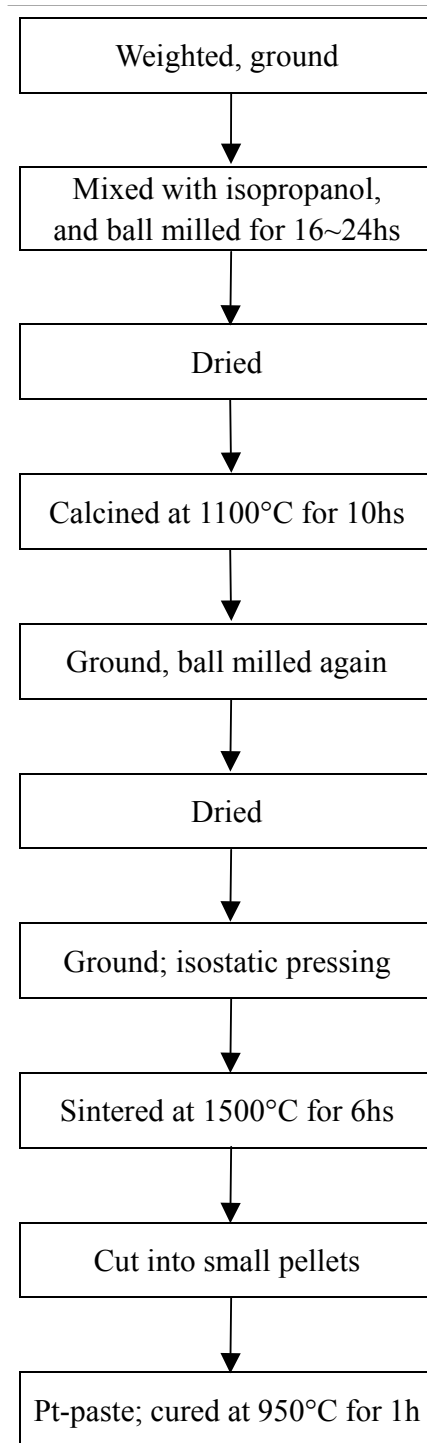
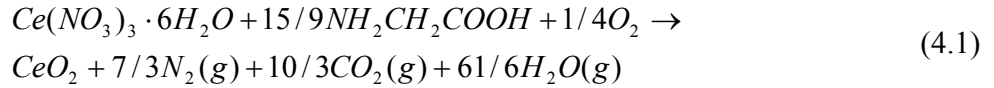


Figure 4.1. Flow chart of solid-state reaction.

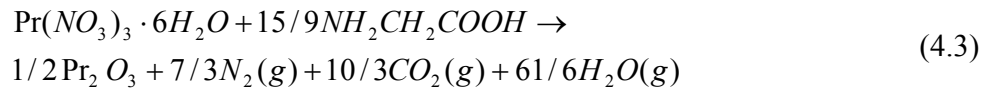
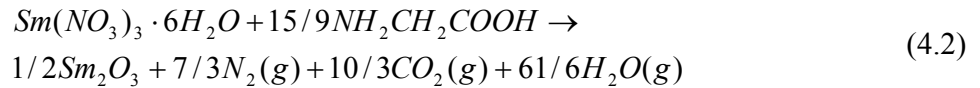
4.1.2 Glycine-nitrate combustion

Glycine-nitrate combustion is a wet chemical process that can produce ultrafine powders of oxide ceramics in a short time at a lower calcination temperature with improved powder characteristics.

Glycine (NH_2CH_2COOH) is known to act as a complexing agent for a number of metal ions as it has a carboxylic acid group at one end and an amino group at the other end [1]. Such types of character of a glycine molecule can effectively complex metal ions of varying ionic sizes, which helps to maintain compositional homogeneity among the constituents. On the other hand, glycine can also serve as a fuel in the combustion reaction, being oxidized by nitrate ions. For a stoichiometric redox reaction between a fuel and an oxidizer, the ratio of the net oxidizing valency of the metal nitrate to the net reducing valency of the fuel should be unity [2]. In the case of glycine-nitrate combustion, primarily N_2 , CO_2 , and H_2O are evolved as the gaseous products. Therefore, carbon and hydrogen are considered as reducing elements with the corresponding valencies of 4+ and 1+, while oxygen is considered as an oxidizing element with the valency of 2-, and nitrogen is assumed to have a valency of zero. Cerium is considered as a reducing element with the valency of 3+ and 4+ in its nitrate and oxide, respectively. Using these valencies of individual elements, the total oxidizing valency of $Ce(NO_3)_3$ works out to be 15+, whereas the total reducing valency of NH_2CH_2COOH is 9+ and the redox reaction can be expressed as follows [3]:



In the same way, the reactions for $Sm(NO_3)_3 \cdot 6H_2O$ and $Pr(NO_3)_3 \cdot 6H_2O$ can be written as the following:



In Eq. (4.3), we have assumed that Pr is fully in 3+ state. Practically, both Pr^{3+} and Pr^{4+} exist in the oxide.

The glycine-to-nitrate molar ratio for these reactions is 0.56 (or metal nitrate-to-glycine molar ratio of 1:1.67). It was also found that fuel-deficient ratios produce favourable powder characteristics due to the relatively lower flame temperature during autoignition [3]. The extreme fuel-deficient ratio was experimentally determined to be metal nitrate-to-glycine molar ratio of

1:0.9. In this work, this ratio was set to be 1:1.2 unless otherwise noted. The flow chart of glycine-nitrate combustion process is shown in figure 4.2.

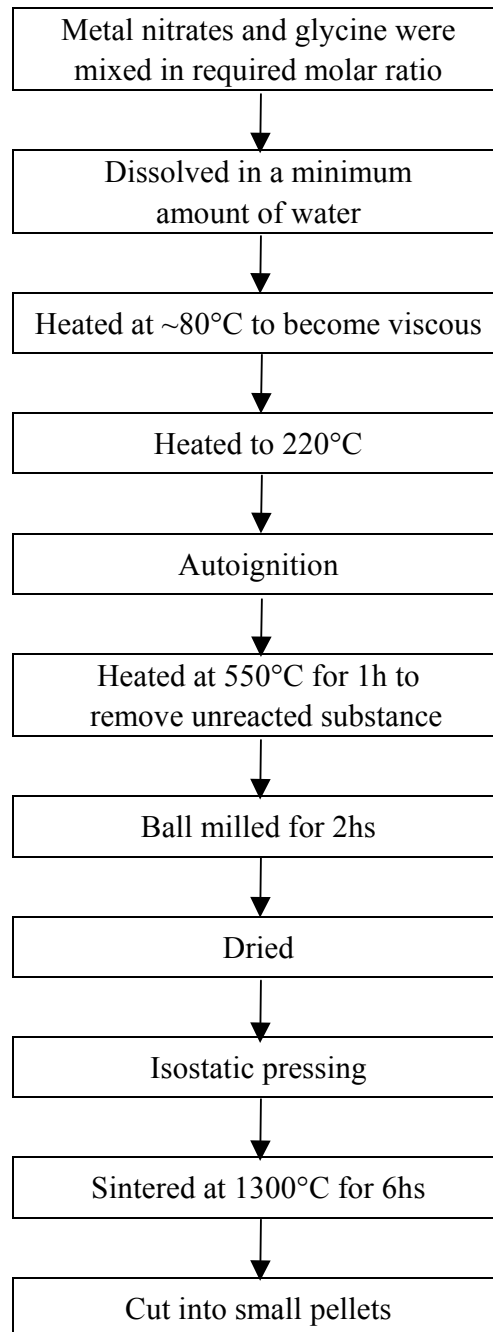


Figure 4.2. Flow chart of glycine-nitrate combustion.

4.2. XRD

Phase characterization was performed by XRD using the Seifert diffractometer (XRD 3000TT or XRD 3000PTS) with Cu K_{α} radiation at room temperature with the operation conditions $U=40\text{kV}$ and $I=30\text{mA}$. Samples either in powder or pellet forms were used.

4.3. Electrical conductivity

The AC electrical conductivity was mostly measured using two-point impedance spectroscopy, employing an HP 4192A impedance analyzer (5Hz~13MHz). Even though, the two-point setup is made with two wires for the current and two for potential measurement. When low frequency ($10^{-4}\text{Hz} \sim 50\text{kHz}$) measurement is required, it can be carried out by using an EIS-6416b impedance spectrometer, combined with a perturbation generator (PG-6416b) and a filter-amplifier (SR-640, Stanford Research Systems Inc.).

Samples were pressed in the sample holder of a Kiel cell with helps of the spring and Al_2O_3 spacers. Pt wires, working as the electrical leads were fixed between the sample pellet and Al_2O_3 spacers by spring load. These leads will be connected with the electrical instrument via the BNC connections. A Ni-NiCr thermocouple was placed very close to the sample to monitor the temperature. The cell is covered by a double wall quartz tube, so the measurement can be taken in various gas atmospheres. A schematic view of Kiel cell is shown in figure 4.3.

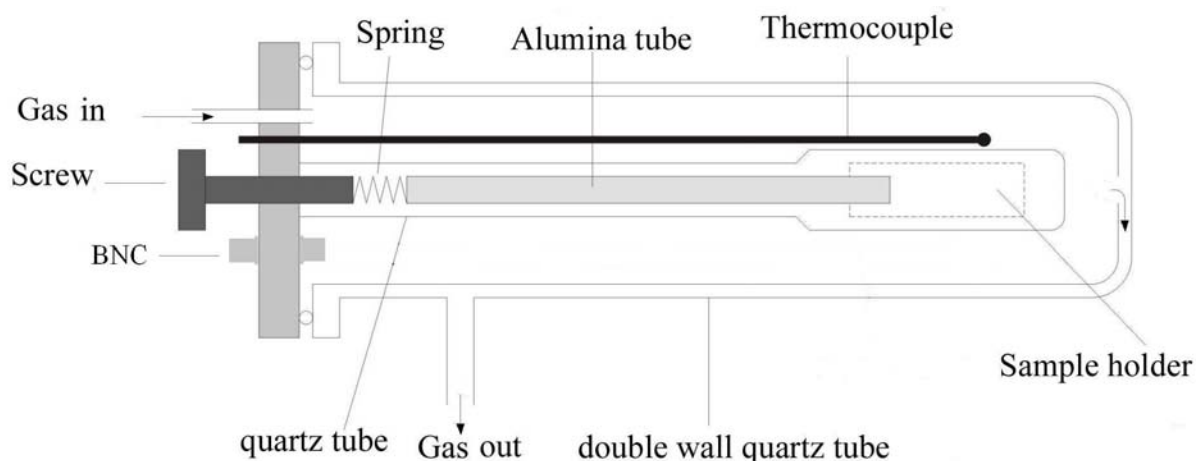


Figure 4.3. Kiel cell

4.4. “Brouwer spectrometer”

The dependence of electrical conductivity on the oxygen partial pressure was measured by using a compact experimental arrangement, the homemade “Brouwer spectrometer”, as shown in figure 4.4.

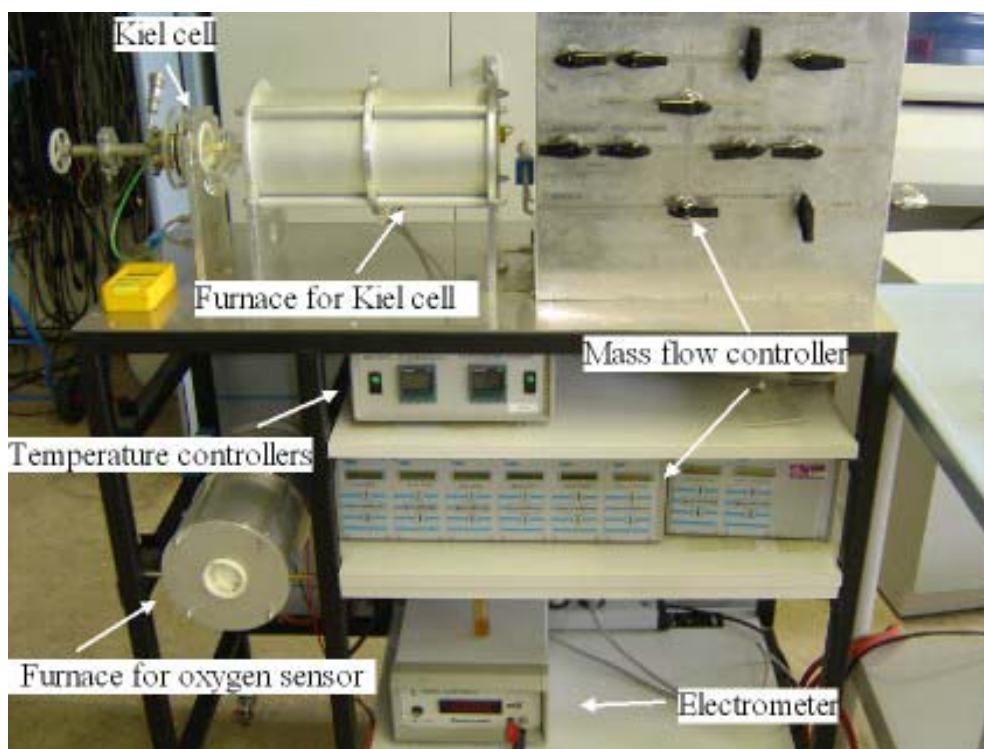


Figure 4.4. “Brouwer spectrometer”

Samples were put into Kiel cell and heated in the cylinder furnace to desired temperature, which was controlled by the temperature controller. Gas mixtures with proper ratio were feed into Kiel cell. Precise amounts of the gases were adjusted by the mass flow controller (Bronkhorst Hi-Tech). The oxygen partial pressure was monitored by a ZrO_2 oxygen sensor located at the outlet of Kiel cell. High and low oxygen partial pressures can be simply obtained by switching the gas mixture between Ar, O_2 or 1000ppm O_2 and H_2 , CO_2 . Impedances as a function of oxygen partial pressure and/or temperature were measured. Before each measurement, samples were held in the new atmosphere for some time until the new gas equilibrium reached, which would take half an hour or several hours depending on the differences of the oxygen partial pressures.

4.5. EMF measurement

4.5.1 Kiukkola-Wagner cell

Kiukkola-Wagner measurement was also conducted in Kiel cell by using the electrodes made from the mixtures of metal and metal oxide such as Ni/NiO and Fe/FeO. Inert gas, like Ar, was kept flowing through the cell to avoid oxidation of the metals in the electrodes at elevated temperatures. EMF as a function of temperature was measured by a multimeter (Keithley 2000), or electrometer (Ionics system EM 1.0), and recorded by the Labview program through a GPIB interface. EMF measured in concentration cells were recorded in the same way.

4.5.2 Gas concentration cell

Two types of setups were used to make the concentration cell measurement. In the first approach, an Al_2O_3 tube was employed to separate the gases. Samples were sealed on top of the tube by ceramic glue and/or AR glass rings. The other approach eliminated the requirement for glues. Two glass/ Al_2O_3 tubes were pressed on each side of the sample pellet by spring load. A gold ring sit in between the sample and the tube, both for electrical contact and sealing purpose, because that gold becomes soft at high temperature. The two experimental setups are shown in figure 4.5 and 4.6, respectively.

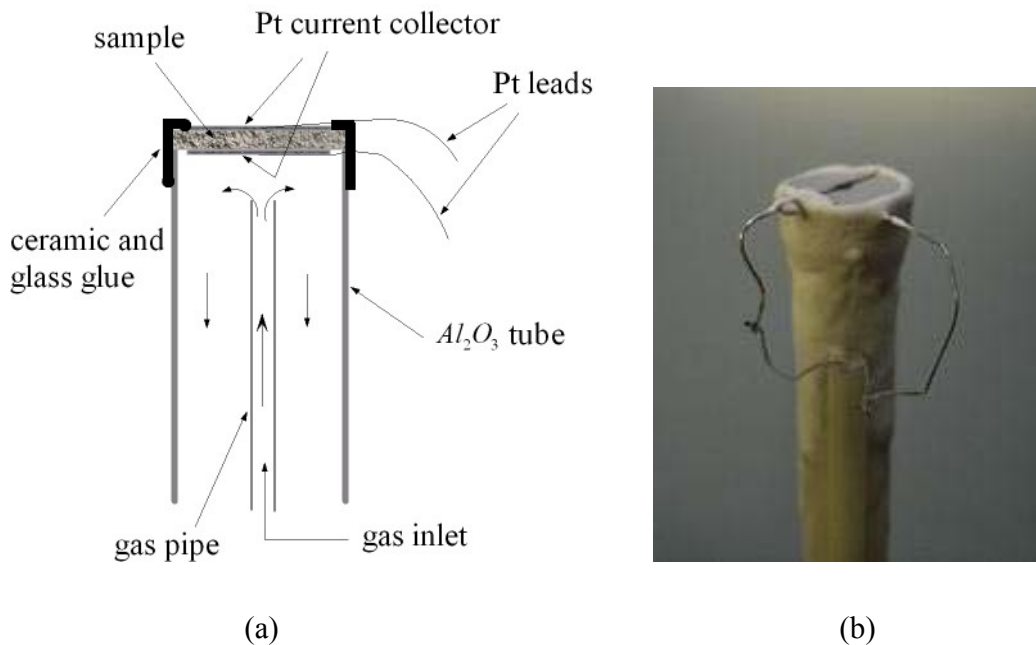


Figure 4.5. (a) Schematic and (b) picture of the experimental setup for EMF measurement.

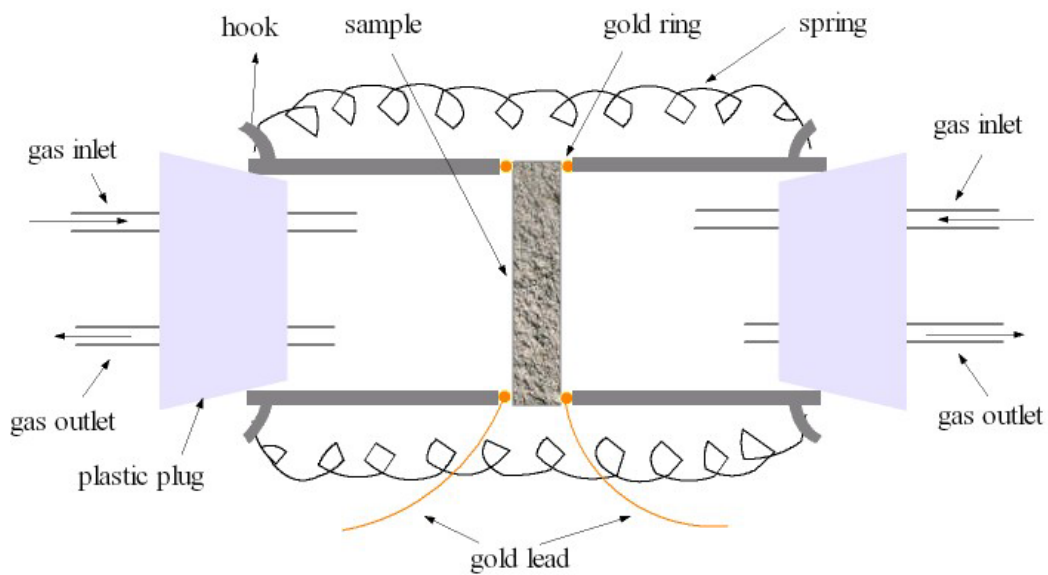


Figure 4.6. Schematic diagram of the new experimental setup for EMF measurement.

4.6. Reference

- [1]. L.A. Chick, L.R. Pederson, G.D. Maupin, J.L. Bates, L.E. Thomas, G.J. Exarhos, *Mater. Lett.* 10, 1990, 6.
- [2]. S.R. Jain, K.C. Adiga, V.R. Pai Verneker, *Combust. Flame* 40, 1981, 71.
- [3]. R.D. Purohit, B.P. Sharma, *Materials Research Bulletin* 36, 2001, 2713.

Chapter 5

Results and discussion I

5.1. Phase characterization

5.1.1 Ceria doped with Sm and Pr

Ceria doped with Sm and Pr with the compositions of $\text{Ce}_{0.8-x}\text{Sm}_{0.2}\text{Pr}_x\text{O}_{2-\delta}$ ($x=0.03\sim 0.1$) and $\text{Ce}_{0.8}\text{Sm}_{0.2-x}\text{Pr}_x\text{O}_{2-\delta}$ ($x=0\sim 0.15$) were prepared in the way described in chapter 4. The XRD patterns of the samples $\text{Ce}_{0.8-x}\text{Sm}_{0.2}\text{Pr}_x\text{O}_{2-\delta}$ ($x=0.03\sim 0.1$) are shown in figure 5.1.

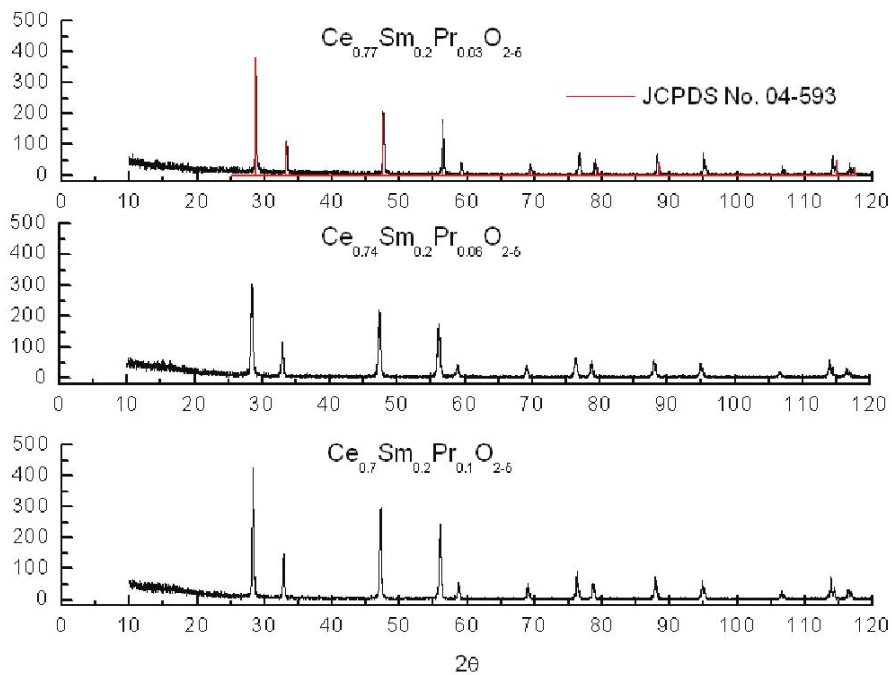


Figure5.1. XRD patterns of $\text{Ce}_{0.8-x}\text{Sm}_{0.2}\text{Pr}_x\text{O}_{2-\delta}$ ($x=0.03\sim 0.1$). All samples show the single fluorite type structure. The red line in the top graph is taken from the XRD database (JCPDS No. 04-593) for pure CeO_2 .

Table 5.1. Ionic radii (CN=8). (R.D. Shannon, Acta Cryst. A32, 751-767 (1976))

Ions (CN=8)	Ce ⁴⁺	Ce ³⁺	Sm ³⁺	Gd ³⁺	La ³⁺	Pr ³⁺	Pr ⁴⁺
Radius (Å)	0.97	1.143	1.079	1.053	1.160	1.126	0.96

All samples show the single fluorite type structure. The red line in the top graph, which is the pattern of pure cerium oxide, was taken from the XRD database (JCPDS No. 04-593). Using the Bragg's law, the strongest (1 1 1) peak at around $2\theta = 28.5$ was chosen to calculate the lattice constant. The results are plotted versus concentration of Pr in figure 5.2. The ionic radii of several ions are listed in Table 5.1

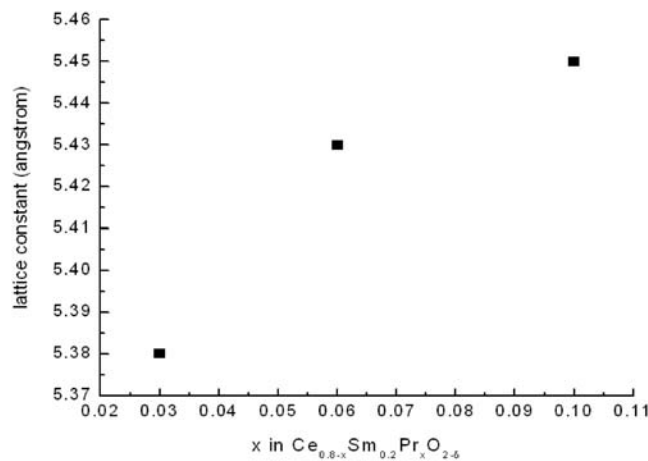


Figure 5.2. Lattice constant of $Ce_{0.8-x}Sm_{0.2}Pr_xO_{2-\delta}$ ($x=0.03\sim 0.1$) vs. the Pr content x . With increasing amount of Pr, the lattice constant slightly increases due to the larger size of Pr^{3+}/Pr^{4+} than Ce^{4+} .

Figure 5.2 shows that the unit cell parameter slightly increases with increasing Pr content due to the larger size of Pr^{3+} compared to Ce^{4+} . This is in agreement with the result of Shuk and Greenblatt [1] who reported that up to 30% of Pr could be doped into ceria ($Ce_{1-x}Pr_xO_{2-\delta}$) without second phase. In order to still maintain the highest ionic conductivity of $Ce_{0.8}Sm_{0.2}O_{1.9}$ among the rare earth doped ceria [2-5], the Pr content was kept below 20% in this work.

The XRD patterns of the other group $Ce_{0.8}Sm_{0.2-x}Pr_xO_{2-\delta}$ ($x=0.02\sim 0.15$) prepared by solid-state reaction are shown in figure 5.3. The lattice constants were also calculated in the same way, and are plotted in figure 5.4. The cell parameter slightly decreases with increasing Pr

content. Although Pr^{3+} is larger than Sm^{3+} according to Table 5.1, it should be noted that both Pr^{3+} and Pr^{4+} exist in the sample after preparation at atmospheric pressure [6]. As a result, the effective radius of $\text{Pr}^{3+}/\text{Pr}^{4+}$ [7] is smaller than that of Sm^{3+} .

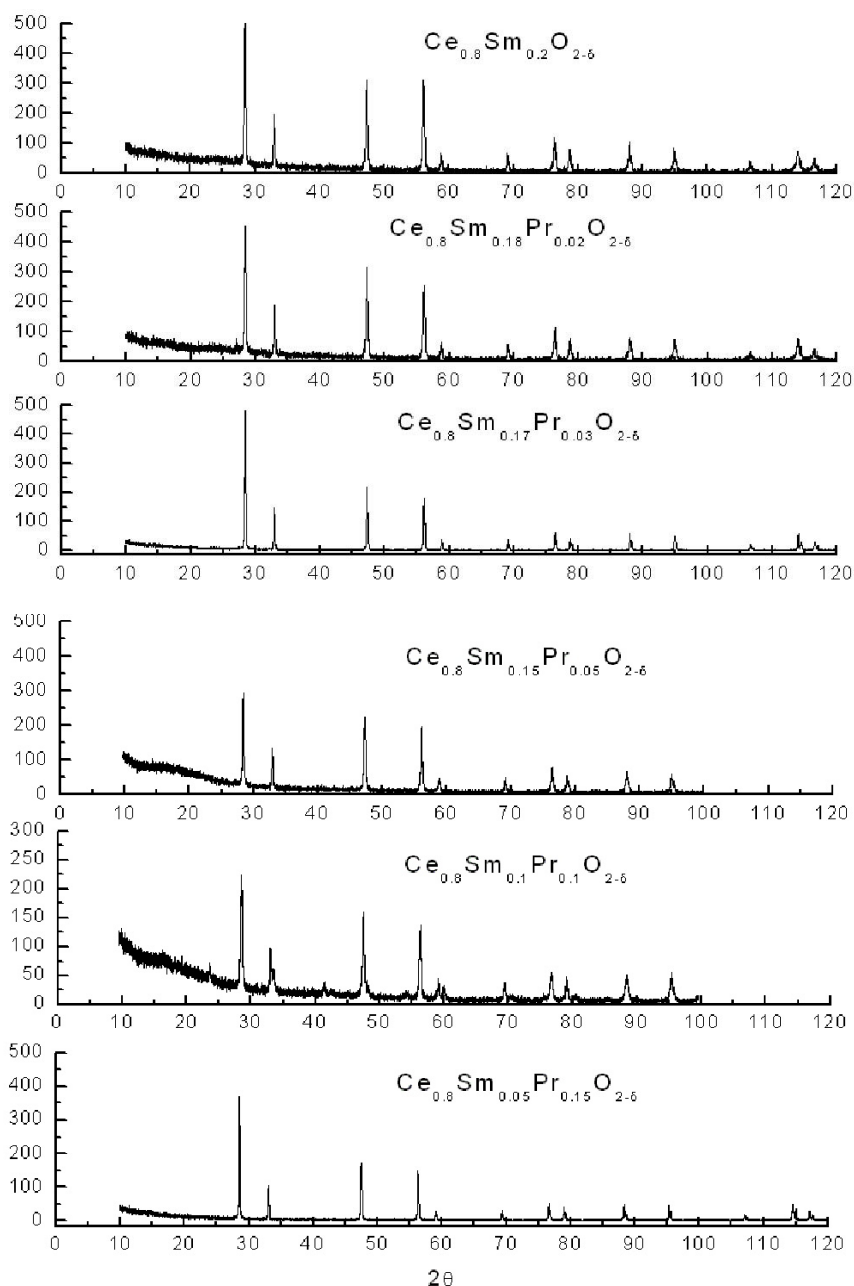


Figure 5.4. XRD patterns of $\text{Ce}_{0.8}\text{Sm}_{0.2-x}\text{Pr}_x\text{O}_{2-\delta}$ ($x=0\sim 0.15$). All samples show the single fluorite type structure.

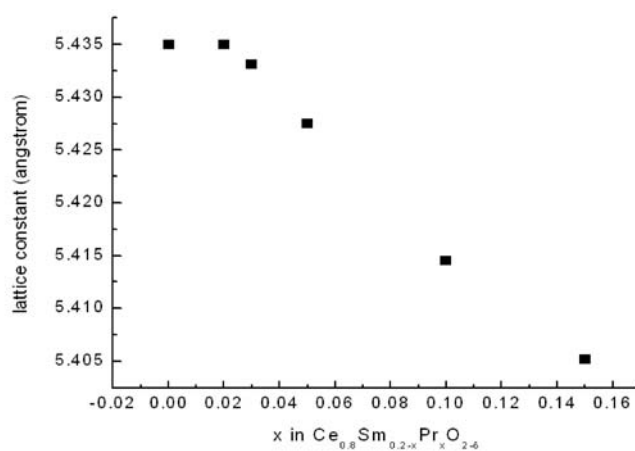


Figure.5.3. Lattice constant of $\text{Ce}_{0.8}\text{Sm}_{0.2-x}\text{Pr}_x\text{O}_{2-\delta}$ ($x=0.03\sim 0.1$) vs. the Pr content x . With increasing amount of Pr, the lattice constant slightly decreases due to the smaller size of $\text{Pr}^{3+}/\text{Pr}^{4+}$ than Sm^{3+} .

5.1.2 Ceria doped with Sm and other metal ions

Transition metal ions, such as Mn, Fe, Co, Cu have been reported as sintering aids for ceria [8-12]. In this work, transition metal ions and some other metal ions were doped into samarium-doped ceria (SDC), and we mainly looked at the influence on the electrical property. For the first approach, the oxygen deficiency of all compositions was kept as $\delta=0.1$ in order to maintain the ionic conductivity. Selected XRD patterns and calculated lattice constants are shown in figure 5.5 and Table 5.2, respectively.

Table 5.2 Lattice constant a of Bi(CN=8), Co(CN=8), Fe(CN=8), Cr(CN=6), Cu(CN=6), Sb(CN=6), and V(CN=6) doped SDC. (R.D. Shannon, Acta Cryst. A32, 751-767 (1976))

	$\text{Fe}^{3+}_{(0.05)}$	$\text{Fe}^{3+}_{(0.1)}$	Co^{2+}	Bi^{3+}	$\text{V}^{5+}_{(\text{CN}=6)}$	$\text{Cr}^{3+}_{(\text{CN}=6)}$	$\text{Cu}^{2+}_{(\text{CN}=6)}$	$\text{Sb}^{3+}_{(\text{CN}=6)}$
r_{ion} (Å)	0.78	0.78	0.90	1.17	0.54	0.615	0.73	0.76
a (Å)	5.418	5.407	5.408	5.459	5.447	5.409	5.414	5.422

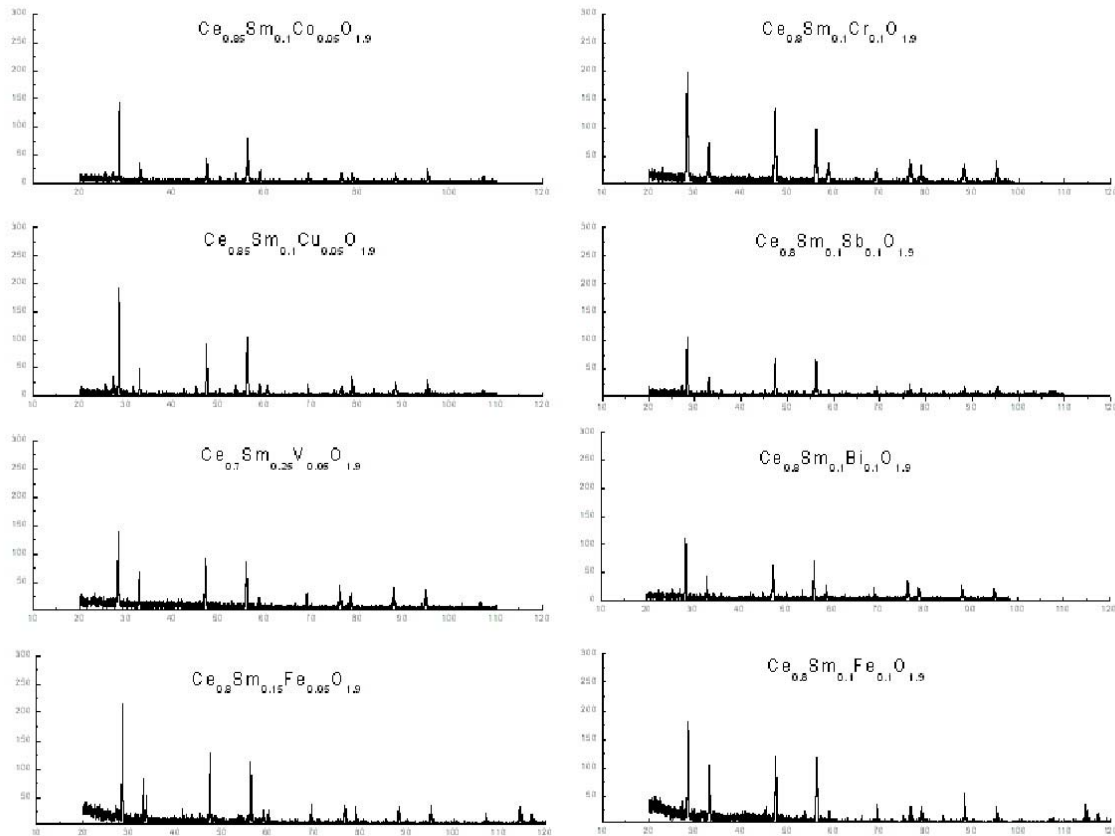


Figure 5.5 XRD patterns of Co, Cr, Cu, Sb, V, Bi and Fe doped SDC. Most of the XRD patterns include small impurity peaks.

In Figure 5.5, all samples have shown the fluorite type structure. But most of the XRD patterns also include small impurity peaks. One explanation to the existence of these impurities could be due to the contamination from the Al_2O_3 ball-milling containers.

From Table 5.2, we can see that:

- i) a decreases with increasing Fe content because Fe is smaller than both Ce and Sm;
- ii) a increases with increasing radius of the dopant, i.e. $\text{Fe}^{3+} < \text{Co}^{2+} < \text{Bi}^{3+}$, $\text{Cr}^{3+} < \text{Cu}^{2+} < \text{Sb}^{3+}$;
- iii) V doped sample has a large lattice constant despite of the smallest size of V^{5+} , because it has the highest Sm content.

5.2. Electrical Conductivity

An initial characterization of all compositions consisted of impedance measurements conducted in air between 473K and 1073K. These data were used to compare the relative performance of all compositions. The ionic conductivity, which is determined by doping is oxygen partial pressure independent over a wide range of oxygen activity. When the oxygen partial pressure is sufficiently high and/or low enough, electronic conductivity may become predominant, which is oxygen activity dependent. To evaluate the electronic contribution to the total conductivity, impedance measurements were performed in different oxygen partial pressures using a ‘Brouwer spectrometer’. The total conductivity obtained from impedance measurement is the sum of the ionic, n-type and p-type conductivities:

$$\sigma_{total} = \sigma_i + \sigma_n + \sigma_p \quad (5.1)$$

where σ_i , σ_n and σ_p are ionic, n-type and p-type conductivities, respectively. If the total conductivity value obtained from the intermediate oxygen partial pressure ($\sim 10^{-5}$ bar) is assumed to be fully ionic, then the deviation from the measured ionic conductivity at high or low oxygen partial pressure could be attributed to the electronic conductivity [13,14].

5.2.1 Ceria doped with Sm and Pr

5.2.1.1 $\text{Ce}_{0.8-x}\text{Sm}_{0.2}\text{Pr}_x\text{O}_{2-\delta}$ ($x=0.03\sim 0.1$)

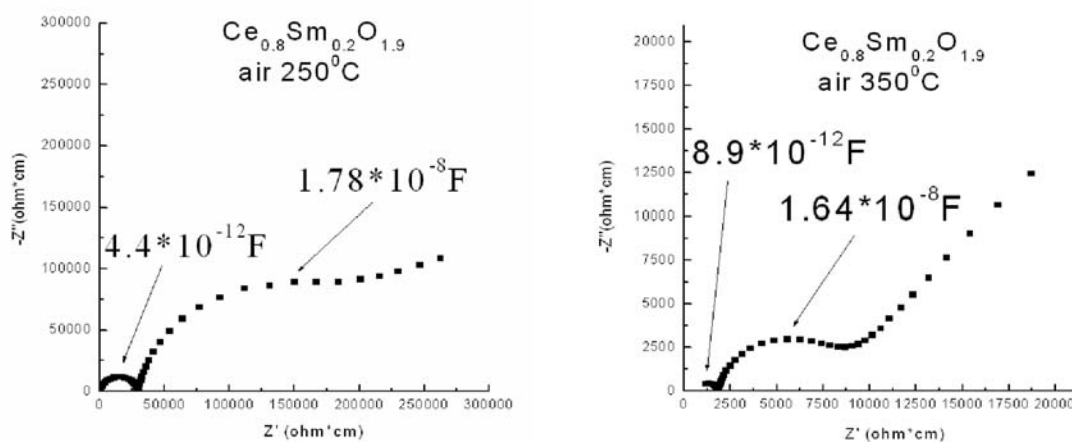


Figure 5.6. Nyquist plots of $\text{Ce}_{0.8}\text{Sm}_{0.2}\text{O}_{1.9}$ measured at 250°C and 350°C in air. The calculated capacitances correspond well to the bulk and grain boundary process.

Figure 5.6 shows the Nyquist plots of $\text{Ce}_{0.8}\text{Sm}_{0.2}\text{O}_{1.9}$ measured at 250°C and 350°C in air. The frequency range is $5\text{Hz}\sim 13\text{MHz}$. At low temperatures, two semicircles can be easily distinguished. The tail at the low frequency is due to the Warburg impedance. Since the resistance decreases with increasing temperature, higher frequencies are required to resolve the semicircles. That's the reason why the first, sometimes even the second semicircles disappear at higher temperatures. The capacitances calculated using Eq. (2.68) indicate well that the two semicircles are corresponding to the bulk and grain boundary processes, respectively, according to Table 2.5. Thus the bulk and grain boundary conductivities were calculated from the diameters of the semicircles. The Nyquist plots of Pr doped samples at 280°C in air are shown in figure 5.7.

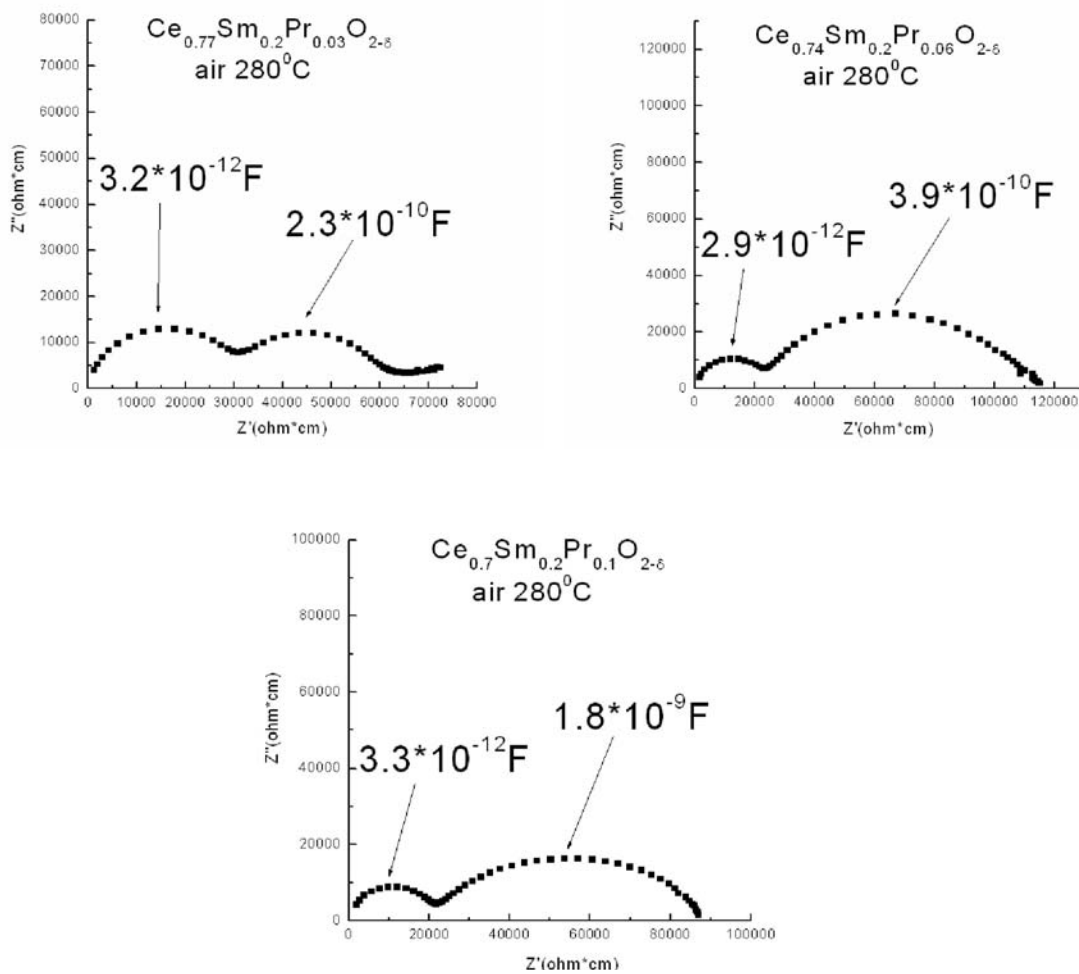


Figure 5.7. Nyquist plots of $\text{Ce}_{0.8-x}\text{Sm}_{0.2}\text{Pr}_x\text{O}_{2-\delta}$ ($x=0.03, 0.06, 0.1$) measured at 280°C in air.

There are two semicircles for all three samples in figure 5.7. However, impedance measurement at higher temperatures and DC measurements reveal that there is another small

semicircle following the first two. The diminishing semicircle at low frequency with increasing Pr content could be explained in the following way:

- i) Better contact between electrolyte and Pt paste;
- ii) Increased catalytic effect due to the presence of Pr [15];
- iii) Increased p-type conductivity through the sample.

The Arrhenius plot of bulk (from the first semicircle) and total (from the sum of the first two semicircles) conductivities of $\text{Ce}_{0.8-x}\text{Sm}_{0.2}\text{Pr}_x\text{O}_{2-\delta}$ are shown in figure 5.8.

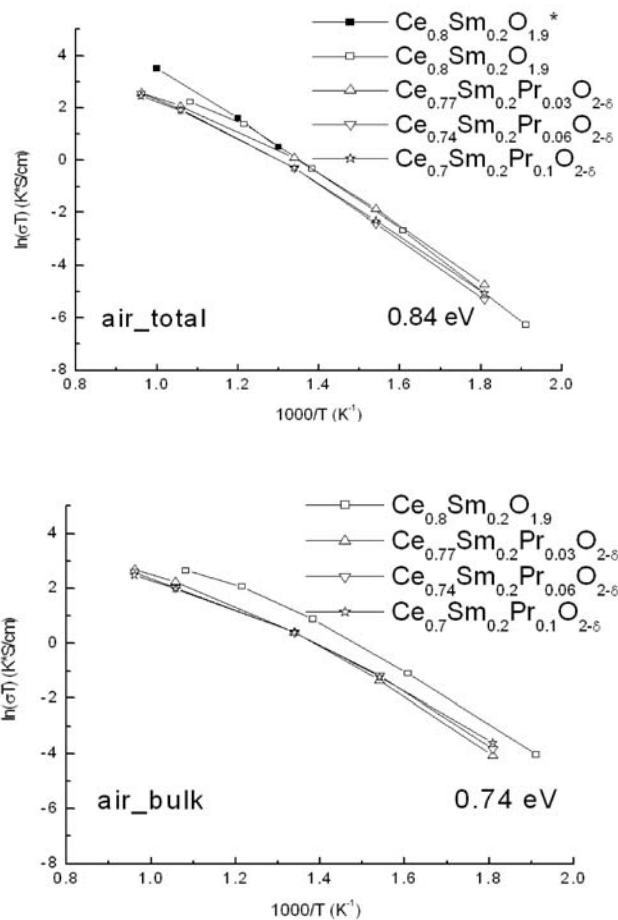


Figure 5.8. Arrhenius plot of the total (top) and bulk (bottom) conductivities of $\text{Ce}_{0.8-x}\text{Sm}_{0.2}\text{Pr}_x\text{O}_{2-\delta}$ ($x=0\sim 0.1$). The asterisk (*) in the top graph refers to literature [5].

The bulk conductivities of Pr doped samples are nearly one order of magnitude lower than that of SDC, while the total conductivities are still close to each other. The activation energies of all samples calculated from the slope show similar values, which are 0.84eV and 0.74eV for total

and bulk conductivity, respectively. The black line in the upper plot is taken from the reference [5] for SDC, which was measured by the DC four point method (Van der Pauw method). It has been reported by several authors that the Arrhenius plot has a curvature at about 580⁰C for several oxide ion conductors [16-18], due to different mechanisms of ionic motion. It should be mentioned here that the deviation from the straight line at high temperature may be due to experimental limitations of low sample resistance compared to all leads at high temperatures.

The dependence of the total conductivity on the oxygen activity is determined by the impedance measurement under different oxygen partial pressures. O₂, air, and the mixture of Ar and 1000ppm O₂ in Ar were used to provide intermediate and high oxygen partial pressures, while the reducing atmosphere for Pr containing samples was simply provided by H₂. The plot of $\log \sigma$ vs. $\log p_{O_2}$ is shown in figure 5.9.

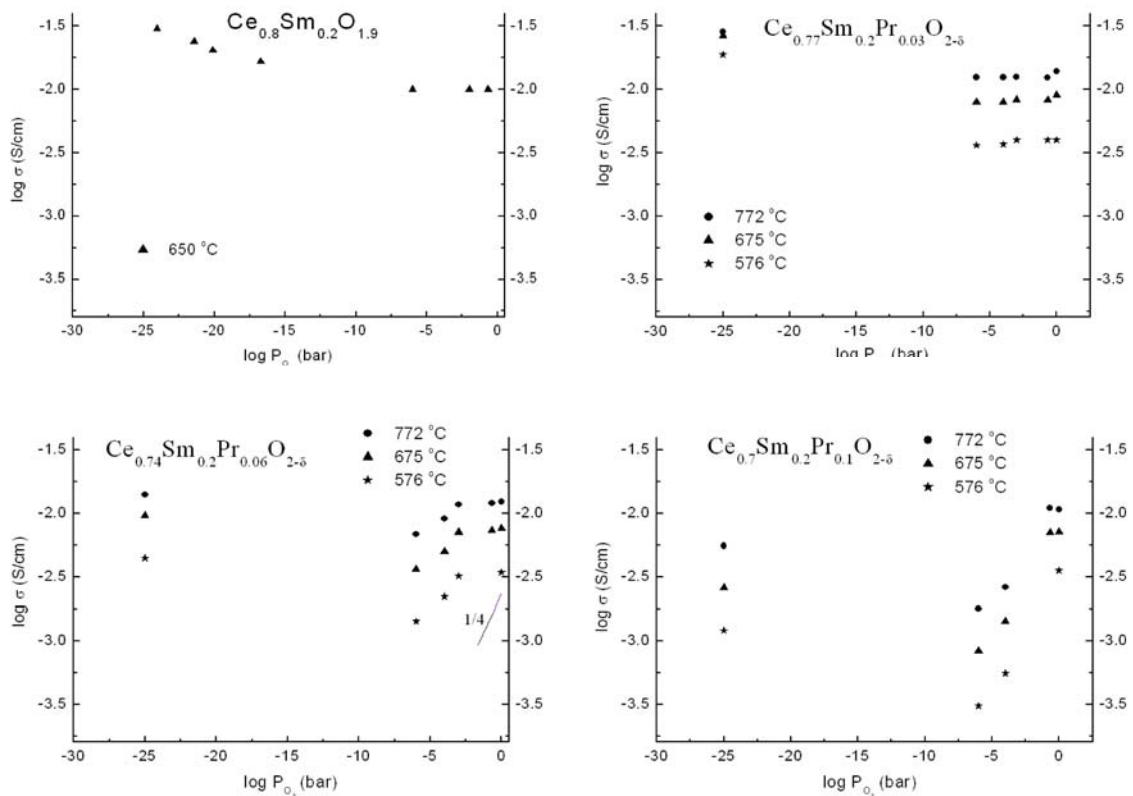


Figure 5.9. Plot of $\log \sigma$ vs. $\log P_{O_2}$ for $Ce_{0.8-x}Sm_{0.2}Pr_xO_{2-\delta}$ ($x=0\sim 0.1$) at 576⁰C, 675⁰C and 772⁰C.

The total conductivity of SDC shows a flat line at high oxygen partial pressures. With increasing Pr content, the conductivities decrease both in reducing condition and intermediate region. Another effect of Pr doping on $Ce_{0.8-x}Sm_{0.2}Pr_xO_{2-\delta}$ is that the electrolyte domain boundary (EDB) can be shifted to lower oxygen activities. It has been reported that Pr might have trapping

effect on electrons [19,20], but this mechanism is still under debating [13,21-23]. If the conductivity at $\log p_{O_2} = -5$ is assumed to be ionic, then the increase of the conductivity in oxygen for $Ce_{0.7}Sm_{0.2}Pr_{0.1}O_{2-\delta}$ has a slope of 1/6. Calculated p-type conductivities of the samples are plotted in figure 5.10. The line for $Ce_{0.8}Gd_{0.17}Pr_{0.03}O_{2-\delta}$ is taken from reference [22], which was obtained by employing the Heb-Wagner method using a Pt microcontact. The decrease of the ionic conductivity of $Ce_{0.8-x}Sm_{0.2}Pr_xO_{2-\delta}$ is due to:

- i) Although $[V_o^{**}]$ increase with increasing Pr content, oxygen deficiency δ exceeds an optimum value ($\delta = 0.1$ for SDC) for ionic conduction [24]. Further increase of the amount of oxygen vacancies will lead large structure distortion, which has a negative influence on the transport of oxide ion;

The increase of p-type conductivity with increasing amount of Pr is due to:

- i) High oxygen partial pressure and large number of oxygen vacancies facilitate the generation of electron holes;
- ii) Increased number of electron holes contribute to the conduction via the polaron mechanism.

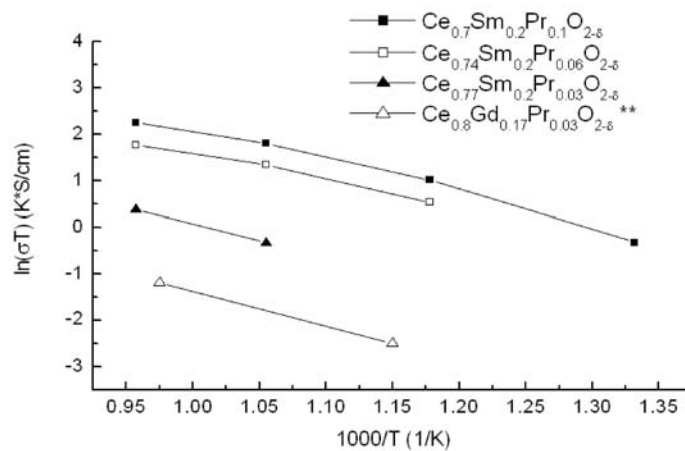


Figure 5.10. Calculated p-type conductivities of $Ce_{0.8-x}Sm_{0.2}Pr_xO_{2-\delta}$ ($x=0.03, 0.06, 0.1$). The asterisks (**) refer to literature [22] for $Ce_{0.8}Gd_{0.17}Pr_{0.03}O_{2-\delta}$.

Although the p-type conductivity under oxidizing condition can be increased by replacing Ce with Pr in $Ce_{0.8-x}Sm_{0.2}Pr_xO_{2-\delta}$, such kind of doping deteriorate the ionic and n-type conductivities. Thus it's not a promising candidate for SEA applications. Different compositions will be discussed.

5.2.1.2 $Ce_{0.8}Sm_{0.2-x}Pr_xO_{2-\delta}$ ($x=0\sim 0.15$)

Figure 5.11 shows the Nyquist plots of $Ce_{0.8}Sm_{0.2-x}Pr_xO_{2-\delta}$ measured at 250⁰C in air. To better understand the conducting behavior of the samples $Ce_{0.8}Sm_{0.1}Pr_{0.1}O_{2-\delta}$ and $Ce_{0.8}Sm_{0.05}Pr_{0.15}O_{2-\delta}$, low frequency impedance measurement was carried out. As shown in figure 5.11, the low frequency semicircle corresponds to the electrolyte/electrode process, but not the grain boundary conduction. One remarkable effect that can be seen from figure 5.11 is the influence of Pr content on the grain boundary conduction. With increasing Pr content, the second semicircle becomes smaller and smaller, and finally disappears at all for $Ce_{0.8}Sm_{0.05}Pr_{0.15}O_{2-\delta}$. The bulk resistance and DC value also have the tendency to decrease when the Pr content is increased.

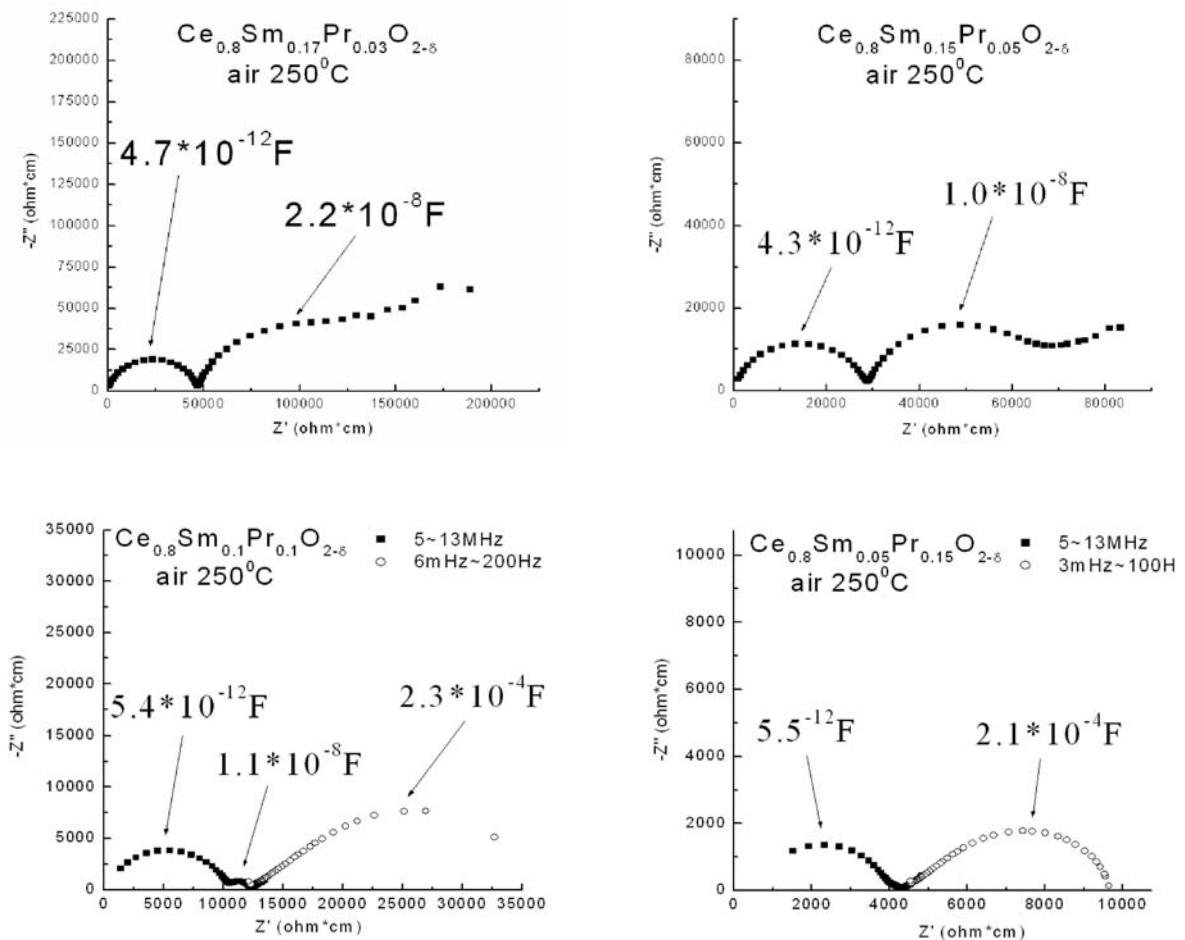


Figure 5.11. Nyquist plots of $Ce_{0.8}Sm_{0.2-x}Pr_xO_{2-\delta}$ ($x=0.03\sim 0.15$) measured at 250⁰C in air. Low frequency impedance measurement was performed for samples $Ce_{0.8}Sm_{0.1}Pr_{0.1}O_{2-\delta}$ and $Ce_{0.8}Sm_{0.05}Pr_{0.15}O_{2-\delta}$. With increasing Pr content, the second semicircle becomes smaller.

Arrhenius plots of the total and bulk conductivities of $\text{Ce}_{0.8}\text{Sm}_{0.2-x}\text{Pr}_x\text{O}_{2-\delta}$ are shown in figure 5.12. These results are compared with the data points taken from reference [5] and [22] for total and bulk conductivities, respectively.

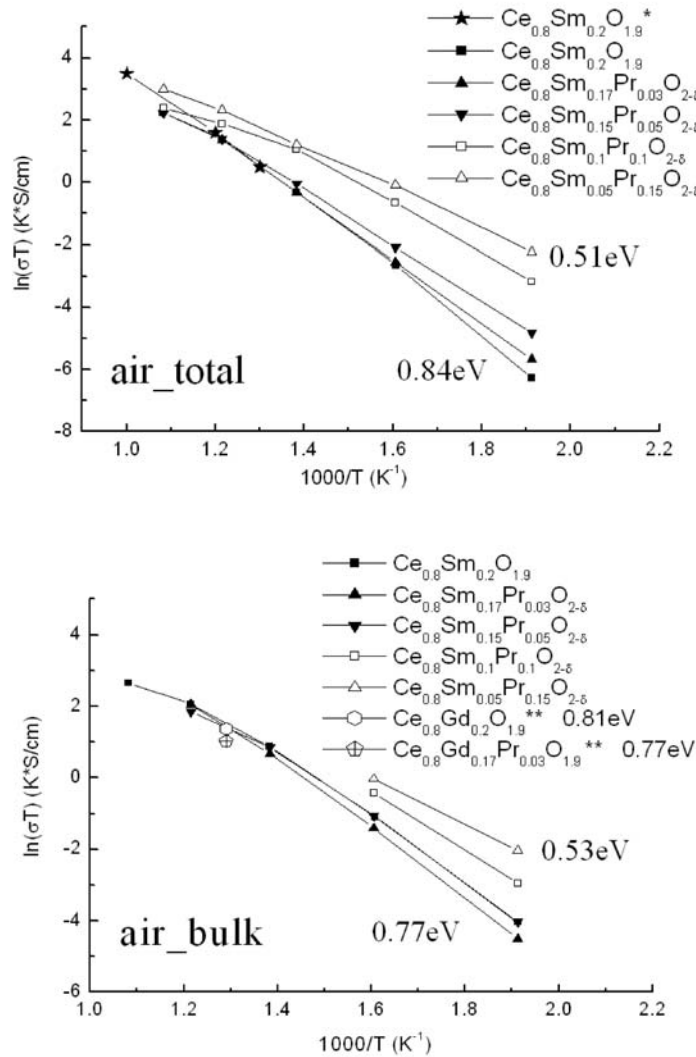


Figure 5.12. Arrhenius plot of total (top) and bulk (bottom) conductivities of $\text{Ce}_{0.8}\text{Sm}_{0.2-x}\text{Pr}_x\text{O}_{2-\delta}$ ($x=0.03, 0.05, 0.1, 0.15$) in air. (*) and (**) stand for reference [5] and [22], respectively.

Compared to figure 5.8, in which the total and bulk conductivities of $\text{Ce}_{0.8-x}\text{Sm}_{0.2}\text{Pr}_x\text{O}_{2-\delta}$ are lower than for SDC, figure 5.12 shows a different behavior for $\text{Ce}_{0.8}\text{Sm}_{0.2-x}\text{Pr}_x\text{O}_{2-\delta}$. With increasing content of Pr, both total and bulk conductivities increase, especially at low temperatures. At temperatures higher than about 630°C, all samples show similar conductivity values. This is once more a proof of the positive effect of Pr doping on the p-type conductivity in

the samples. The activation energy of $\text{Ce}_{0.8}\text{Sm}_{0.2}\text{O}_{1.9}$ and $\text{Ce}_{0.8}\text{Sm}_{0.05}\text{Pr}_{0.15}\text{O}_{2-\delta}$ are labelled in the plot. Because of the highest concentration of Pr, $\text{Ce}_{0.8}\text{Sm}_{0.05}\text{Pr}_{0.15}\text{O}_{2-\delta}$ has the smallest activation energy due to the influence of the increased electronic conduction. At low temperatures, the contribution from electron holes cannot be neglected as in the case of pure SDC. Conduction is thus controlled by a combination of the two processes, bulk and electronic. As long as the temperature is below the point at which ionic conductivity is far larger than the electronic conductivity, both processes play the role for the total conductivity. Once the limiting temperature is reached, ionic conduction becomes predominant because it increases faster with the temperature than the electronic one does. It should be noted here that the increase of bulk conductivity by Pr doping in figure 5.12 doesn't mean that Pr can really improve the bulk property. When there is considerable electronic transfer through the sample, interpretation of the impedance plot is different from the case when pure ionic conductor is employed. The intersection of the first semicircle and real axis is no longer simply the bulk resistance, but a combination with the electronic resistance [25,26]. Figure 5.12 is also an indication that even 15% Pr doping is still not sufficient for providing enough p-type conductivity. This can be easily seen by comparing the impedance of $\text{Ce}_{0.8}\text{Sm}_{0.05}\text{Pr}_{0.15}\text{O}_{2-\delta}$ measured in air and mixtures of CO_2 and H_2 at 700°C (figure 5.13).

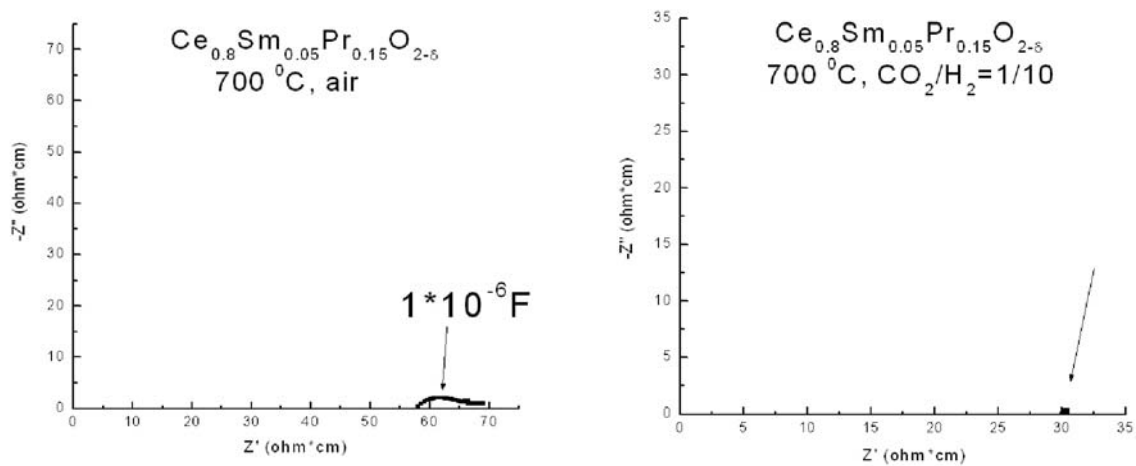


Figure 5.13. Nyquist plots of $\text{Ce}_{0.8}\text{Sm}_{0.05}\text{Pr}_{0.15}\text{O}_{2-\delta}$ measured in air and reducing atmosphere ($\text{CO}_2:\text{H}_2=1:10$) at 700°C .

As shown in Table 2.6, the impedance of a resistor is just a single point on the real axis in the complex plane. When measured at a low oxygen partial pressure ($p_{\text{O}_2} = 10^{-21.5}$ bar for $\text{CO}_2:\text{H}_2=1:10$), only one dot can be seen, indicating a large electronic contribution. When measured in air, there is still a semicircle, which means the sample is predominantly ionic conductor.

A plot of $\log \sigma$ vs. $\log p_{O_2}$ at 700 °C is shown in figure 5.14. Only the sample with highest p-type conductivity, i.e. $Ce_{0.8}Sm_{0.05}Pr_{0.15}O_{2-\delta}$, is shown here.

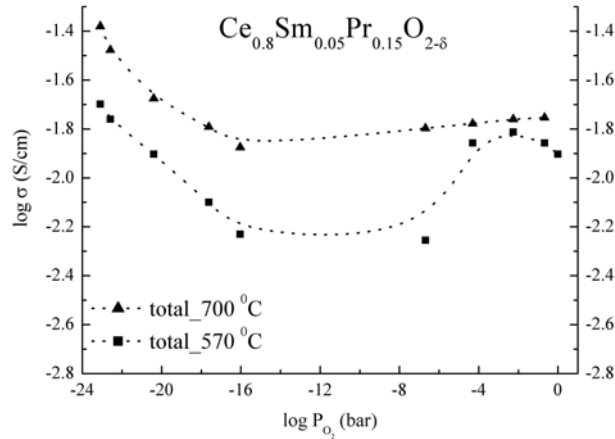


Figure 5.14. Brouwer diagram of the total conductivity for $Ce_{0.8}Sm_{0.05}Pr_{0.15}O_{2-\delta}$ at 570 °C and 700 °C.

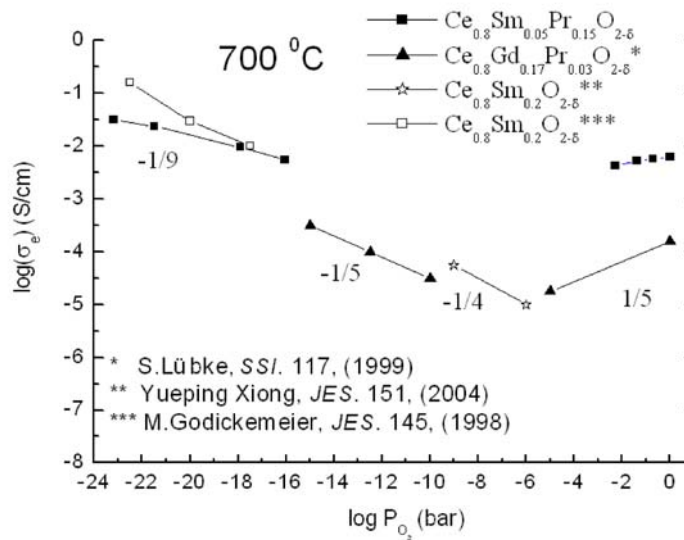


Figure 5.15. Calculated electronic conductivity for $Ce_{0.8}Sm_{0.05}Pr_{0.15}O_{2-\delta}$ at 700 °C. Some

Electronic conductivity calculated from figure 5.14 is plotted in figure 5.15, and compared with some literature values [22,27,28]. $Ce_{0.8}Sm_{0.05}Pr_{0.15}O_{2-\delta}$ has higher p-type conductivity than other compositions, which slightly changes with oxygen partial pressure. The n-type conductivity is in the same order of magnitude as reported by other people with a slope of $-1/9$.

5.2.2 Ceria doped with Sm and other metal ions

5.2.2.1 $Ce_{0.8-y}Sm_{0.2-x}Me_xO_{1.9}$ (Me=Bi, Co, Cr, Cu, Fe, Sb, V)

The effects of small amount of transition metal ions on the densification and grain boundary conduction of gadolinium doped samarium (GDC) have been investigated by several groups [8-12]. Our aim here is to have a first impression of the influences of different metal ions on the electronic conduction, especially the p-type conductivity under oxidizing condition. Impedance measurements were performed in H_2 , air and Ar/O_2 . Because of the high porosity of Fe doped samples (Figure 5.16), no further measurement was conducted on them.

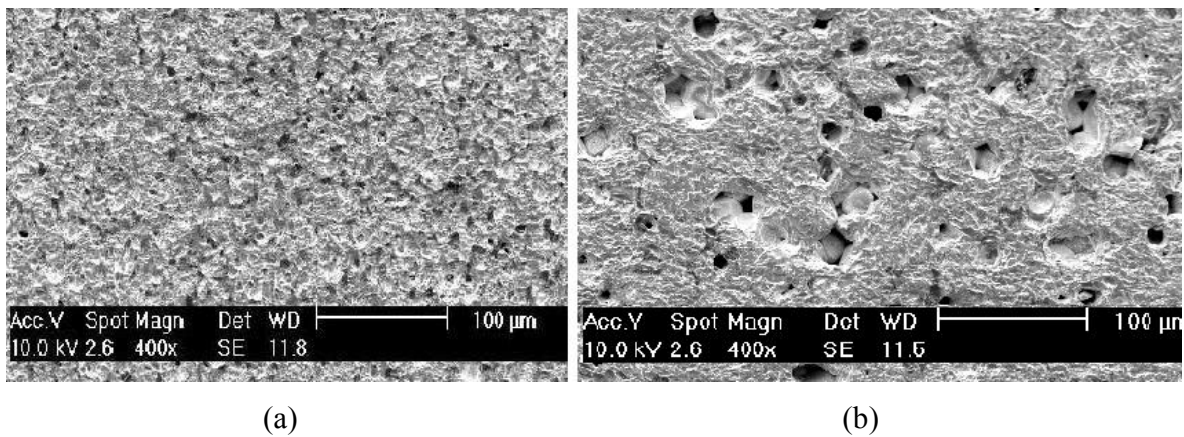


Figure 5.16. SEM of (a) $Ce_{0.8}Sm_{0.15}Fe_{0.05}O_{1.9}$ and (b) and $Ce_{0.8}Sm_{0.1}Fe_{0.1}O_{1.9}$ show high porosity in the samples.

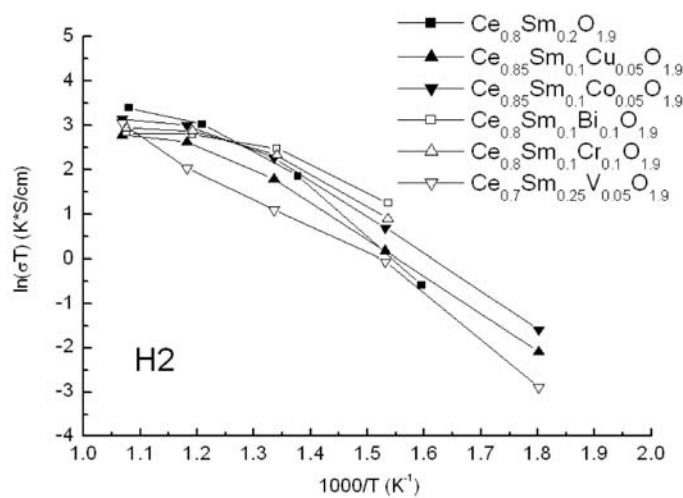


Figure 5.17. Arrhenius plot of the total conductivity for $Ce_{0.8-y}Sm_{0.2-x}Me_xO_{1.9}$ in H_2 .

The reduction of Ce occurred for all the compositions in H_2 , and only a dot can be seen in the complex plane, which looks similar to the one shown in figure 5.13. The Arrhenius plot in H_2 is shown in figure 5.17, which indicates that little effect was made on the n-type conduction. The lowest conductivity of $Ce_{0.7}Sm_{0.25}V_{0.05}O_{1.9}$ at most temperatures is due to the relatively small amount of Ce.

Figure 5.18 shows the Arrhenius plots of $Ce_{0.8-y}Sm_{0.2-x}Me_xO_{1.9}$ in air.

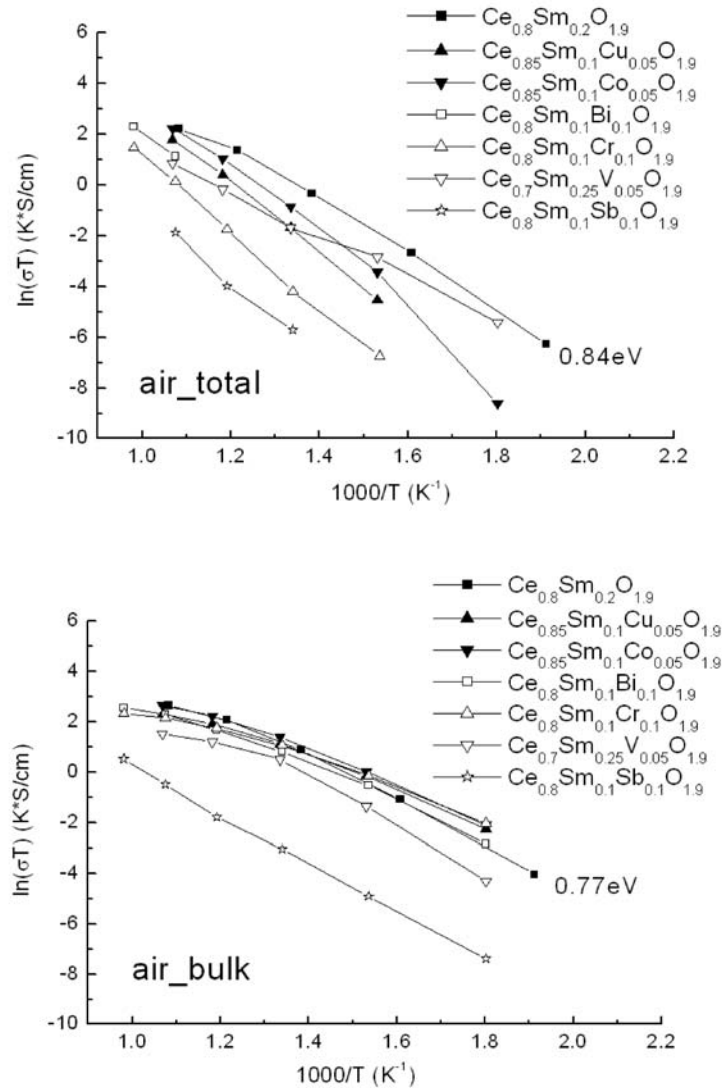


Figure 5.18. Arrhenius plot of the total (top) and bulk (bottom) conductivities of $Ce_{0.8-y}Sm_{0.2-x}Me_xO_{1.9}$ in air.

The Sb doped sample has the lowest value either for total or bulk conductivity. All other samples show bulk values close to SDC, while all the total conductivities are lower, which

indicate a large impedance from the grain boundary. The impedance and Arrhenius plots measured in Ar/O₂ ($p_{O_2} = 10^{-5} \text{ bar}$) are the same as those measured in air, except for a larger low frequency tail, which is due to the slower charge transfer process across the electrode/gas interface because of the lower oxygen activity in Ar/O₂. Thus, the electrical conduction is still dominated by oxide ion at high p_{O_2} . Doping by these metal ions cannot improve the p-type conductivity remarkably.

5.3. EMF and dilatometric measurements

Based on the results of the impedance spectroscopy, Ce_{0.8}Sm_{0.05}Pr₁₅O_{2-δ} was selected for further measurement. EMF measurement was performed using the experimental setup shown in figure 4.5. Sample pellet was sealed on top of the Al₂O₃ tube by glues. H₂ was supplied to the inner side of the sample though a gas pipe inside the Al₂O₃ tube. Because of the large thermal expansion and reduction of Ce⁴⁺ and Pr⁴⁺, the pellet was not mechanically stable, i.e. many cracks can be seen after flushing of H₂ even by naked eyes. To quantify the thermal expansion coefficient and lattice constant after reduction, dilatometry and XRD were performed. Figure 5.19 shows the result from dilatometer working in Ar atmosphere, and the thermal expansion coefficient calculated from Figure 5.19 is $\alpha = 18 \times 10^{-6} / K$. From the XRD pattern, the lattice constant of the sample after reduction is 5.437Å, which is larger than the value before reduction, 5.405Å. As the result of such expansion and reduction, gases could penetrate through the sample by the generated voids and cracks, and then EMF always decreased drastically.

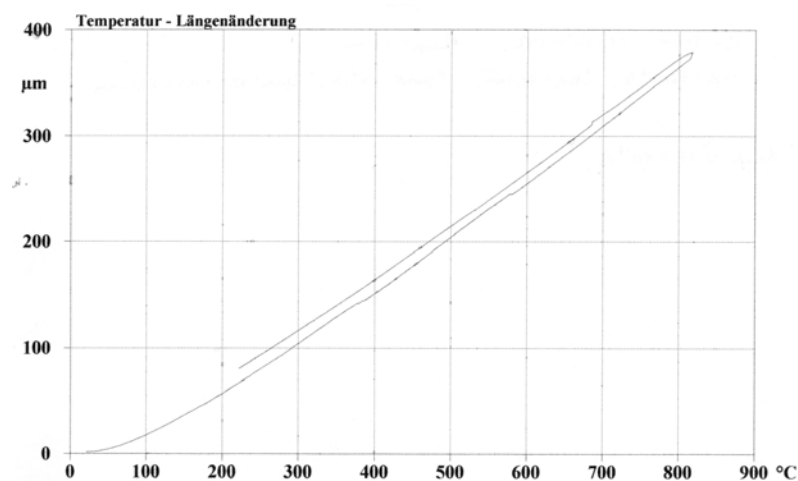


Figure 5.19. Elongation vs. temperature for Ce_{0.8}Sm_{0.05}Pr₁₅O_{2-δ} in Ar. The calculated thermal expansion coefficient is $\alpha = 18 \times 10^{-6} / K$.

5.4. References

- [1]. P. Shuk, M. Greenblatt, *Solid State Ionics* 116, 1999, 217.
- [2]. H. Yahiro, Y. Egushi, H. Arai, *J. Appl. Electrochem.* 18, 1988, 527.
- [3]. Y. Egushi, T. Setoguchi, T. Inoue, H. Arai, *Solid State Ionics* 52, 1992, 165.
- [4]. G.B. Balazes, R.S. Glass, *Solid State Ionics* 76, 1995, 155.
- [5]. Guor-Bin Jung, Ta-Jen Huang, Chung-Liang Chang, *J. Solid State Electrochem.* 6, 2002, 225.
- [6]. H. Inaba, K. Naito, *J. Solid State Chem.* 50, 1983, 100.
- [7]. R.D. Shannon, C.T. Prewitt, *Acta Crystallogr.* 32A, 1976, 751.
- [8]. C. Kleinlogel, L.J. Gauckler, *Solid State Ionics* 135, 2000, 567.
- [9]. G.S. Lewis, A. Atkinson, B.C.H. Steele, J. Drennan, *Solid State Ionics* 152-153, 2002, 567.
- [10]. T.S. Zhang, J. Ma, L.B. Kong, S.H. Chan, P. Hing, J.A. Kilner, *Solid State Ionics* 167, 2004, 203.
- [11]. T.S. Zhang, J. Ma, Y.J. Leng, S.H. Chan, P. Hing, J.A. Kilner, *Solid State Ionics* 168, 2004, 187.
- [12]. G.J. Pereira, R.H.R. Castro, D.Z. de Florio, E.N.S. Muccillo, D. Gouvea, *Materials Letters* 59, 2005, 1195.
- [13]. L. Navarro, F. Marques, J. Frade, *J. Electrochem. Soc.* 144, No.1, 1997, 267.
- [14]. Keqin Huang, Man Feng, J.B. Goodenough, *J. Am. Ceram. Soc.* 81, 1998, 357.
- [15]. V.N. Tikhonovich, V.V. Kharton, E.N. Naumovich, A.A. Savitsky, *Solid State Ionics* 106, 1998, 197.
- [16]. R.T. Dirstine, R.N. Blumenthal, T.F. Kuech, *J. Electrochem. Soc.* 126, 1979, 264.
- [17]. H. Arai, T. Kunisaki, Y. Shimizu, T. Seiyama, *Solid State Ionics* 20, 1986, 241.
- [18]. I. Reiss, *J. Am. Ceram. Soc.* 64, 1981, 479.
- [19]. D.L. Maricle, T.E. Swarr, S. Karavolis, *Solid State Ionics* 52, 1992, 173.
- [20]. D.L. Maricle, T.E. Swarr, H.L. Tuller, *US Patent* 5.001.021, 1991.

- [21]. B.C.H. Steele, K. Zheng, R.A. Rudkin, N. Kiratzis, M. Christie, *Proc. SOFC IV*, vol. 95-1, Electrochemical Society, Pennington, NJ, 1995, 1028.
- [22]. S. Luebke, H.-D. Wiemhoefer, *Solid State Ionics* 117, 1999, 229.
- [23]. V.V. Kharton, F.M. Figueiredo, L. Navarro, E.N. Naumovich, A.V. Kovalevsky, A.A. Yaremchenko, A.P. Viskup, A. Carneiro, F.M.B. Marques, J.R. Frade, *J. Mater. Sci.* 36, 2001, 1105.
- [24]. H. Inaba, H. Tagawa, *Solid State Ionics* 83, 1996, 1.
- [25]. R.A. Huggins, *Ionics* 8, 2002, 300.
- [26]. V. Thangadurai, R.A. Huggins, W. Weppner, *J. Power Sources* 108, 2002, 64.
- [27]. Yueping Xiong, Katsuhiko Yamaji, Teruhisa Horita, Natsuko Sakai, Harumi Yokokawa, *J. Electrochem. Soc.* 151, 2004, A407.
- [28]. M. Gödickemeier, L.J. Gauckler, *J. Electrochem. Soc.* 145, 1998, 414.

Chapter 6

Results and discussion II

6.1. Phase characterization

6.1.1 $\text{BaCe}_{0.76}\text{Y}_{0.2}\text{Pr}_{0.04}\text{O}_{3-\delta}$

It's known that doped BaCeO_3 shows mixed proton and electron conduction in the presence of moisture, whereas in dry oxidizing atmospheres, it exhibits mixed oxide ion and electron hole conducting properties [1-4]. Various doped BaCeO_3 has been investigated for working as electrolyte or electrode materials. Among these materials, $\text{BaCe}_{0.76}\text{Y}_{0.2}\text{Pr}_{0.04}\text{O}_{3-\delta}$ was reported to work as the electrolyte in SOFC without the anode material. In order to further improve the property to fulfil the requirement for SEA concept, materials based on $\text{BaCe}_{0.76}\text{Y}_{0.2}\text{Pr}_{0.04}\text{O}_{3-\delta}$ were prepared by solid state reaction. The last sintering process was performed in air at 1600°C for 6 hours. XRD patterns of $\text{BaCe}_{0.8}\text{Y}_{0.2}\text{O}_{3-\delta}$ and $\text{BaCe}_{0.76}\text{Y}_{0.2}\text{Pr}_{0.04}\text{O}_{3-\delta}$ are shown in figure 6.1.

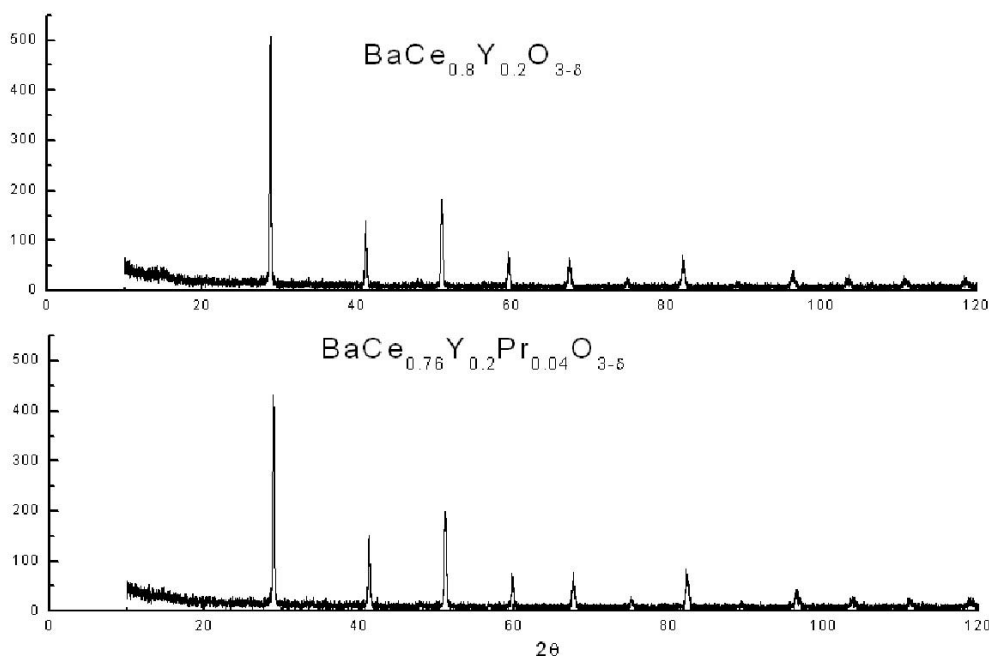


Figure 6.1. XRD patterns of $\text{BaCe}_{0.8}\text{Y}_{0.2}\text{O}_{2.9}$ and $\text{BaCe}_{0.76}\text{Y}_{0.2}\text{Pr}_{0.04}\text{O}_{3-\delta}$. Both samples show single perovskite type structure.

Table 6.1. Ionic radii (CN=6). (R.D. Shannon, Acta Cryst. A32, 751-767 (1976))

Ions (CN=6)	Ce ³⁺	Ce ⁴⁺	Y ³⁺	Pr ³⁺	Pr ⁴⁺	Ti ⁴⁺	Ti ³⁺
Radius (Å)	1.01	0.87	0.900	0.99	0.85	0.605	0.67

No impurity peaks can be found in figure 6.1. The lattice constants calculated from the strongest peak are 4.380Å and 4.383Å for BaCe_{0.8}Y_{0.2}O_{2.9} and BaCe_{0.76}Y_{0.2}Pr_{0.04}O_{3-δ}, respectively. The slight increase is due to the replacement of Ce⁴⁺ by a larger Pr³⁺/Pr⁴⁺ (see Table 6.1).

6.1.2 BaCe_{0.76}Y_{0.2}Pr_{0.04}O_{3-δ} (TiO₂)

Conductivity measurement of BaCe_{0.76}Y_{0.2}Pr_{0.04}O_{3-δ} shows that there is an increase at low P_{O_2} .

Similar effect was also found in SrCe_{1-x}Y_xO_{3-δ}, where the increase of the conductivity was attributed to the H/D isotope effect [5]. Figure 6.2 shows the color change of BaCe_{0.76}Y_{0.2}Pr_{0.04}O_{3-δ} before and after heating in H₂ at 700°C, which is an indication of the type of conduction, as the color of the electronic conductor is normally dark.

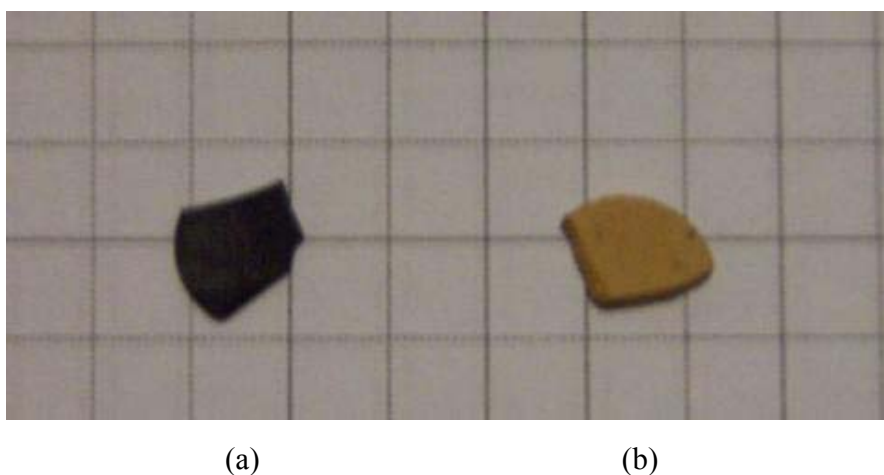


Figure 6.2. Color of BaCe_{0.76}Y_{0.2}Pr_{0.04}O_{3-δ} (a) before and (b) after heating in H₂ at 700°C

TiO₂ was used in ZrO₂ to introduce the n-type conduction under reducing conditions. In order to improve the electronic conductivity, powders of BaCe_{0.76}Y_{0.2}Pr_{0.04}O_{3-δ} and TiO₂ were mixed in a molar ratio of 10:1, and then sintered at 1600°C for 6 hours. The obtained XRD pattern is shown in figure 6.3.

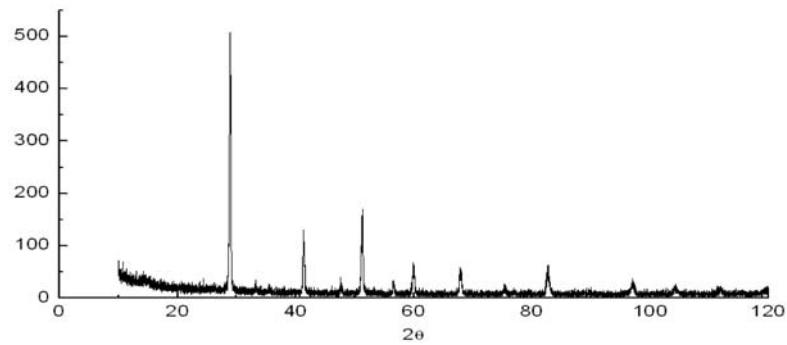


Figure 6.3. XRD pattern of mixture of $\text{BaCe}_{0.76}\text{Y}_{0.2}\text{Pr}_{0.04}\text{O}_{3-\delta}$ and TiO_2 . TiO_2 dissolved into $\text{BaCe}_{0.76}\text{Y}_{0.2}\text{Pr}_{0.04}\text{O}_{3-\delta}$ after sintered at 1600°C for 6 hours.

6.1.3 $\text{BaCe}_{0.8}\text{Y}_{0.2}\text{O}_{2.9} + \text{Ce}_{0.8}\text{Sm}_{0.2}\text{O}_{1.9}$

$\text{BaCe}_{0.8}\text{Y}_{0.2}\text{O}_{2.9}$ was mixed with $\text{Ce}_{0.8}\text{Sm}_{0.2}\text{O}_{1.9}$ with a molar ratio of 1:1 for the same reason as mentioned in the last section, for $\text{Ce}_{0.8}\text{Sm}_{0.2}\text{O}_{1.9}$ is known for the reduction at low P_{O_2} . XRD patterns of the mixture before and after sintering at 1600°C are shown in figure 6.4. Two phases coexist in the mixture. There is no reaction product between $\text{BaCe}_{0.8}\text{Y}_{0.2}\text{O}_{2.9}$ and $\text{Ce}_{0.8}\text{Sm}_{0.2}\text{O}_{1.9}$.

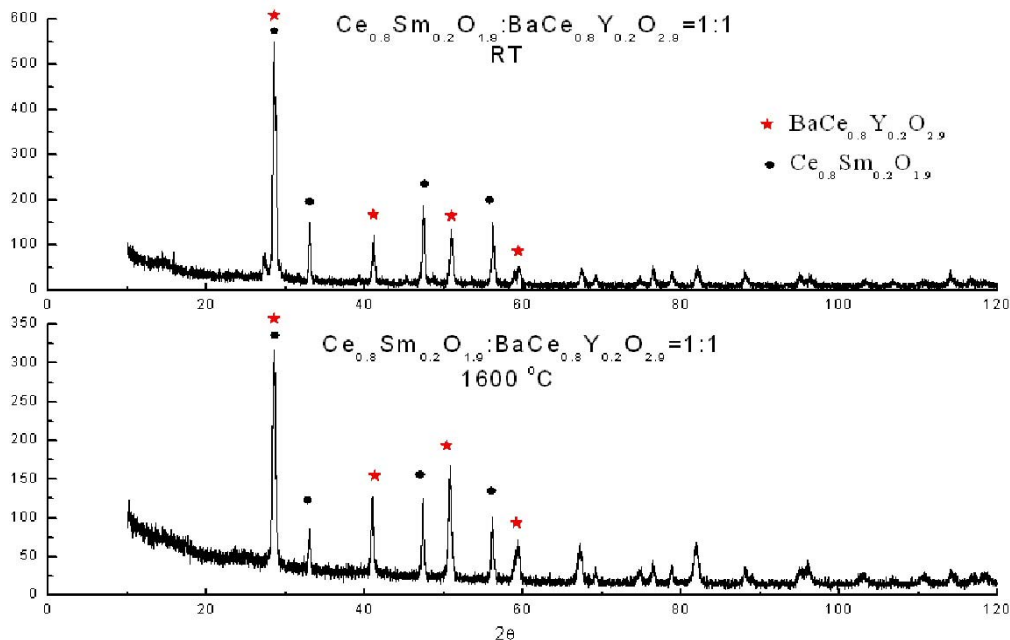


Figure 6.4. XRD patterns of $\text{BaCe}_{0.8}\text{Y}_{0.2}\text{O}_{2.9} + \text{Ce}_{0.8}\text{Sm}_{0.2}\text{O}_{1.9}$ before (top) and after (bottom) sintering at 1600°C . There are still two phases after sintering.

6.2. Electrical Conductivity

6.2.1 $\text{BaCe}_{0.76}\text{Y}_{0.2}\text{Pr}_{0.04}\text{O}_{3-\delta}$

Bulk conductivity Arrhenius plots of $\text{BaCe}_{0.76}\text{Y}_{0.2}\text{Pr}_{0.04}\text{O}_{3-\delta}$ measured in different gases are plotted in figure 6.5. In dry air, the conductivity is due to the combination of holes and oxide ions, since the concentration of protonic defects is small at low $P_{\text{H}_2\text{O}}$. Similarly, the conductivity in dry Ar/O_2 ($P_{\text{O}_2} = 10^{-5}$) is due only to oxide ions, since the concentration of holes is also small at low intermediate P_{O_2} . The activation energies are also shown in the plot. The smaller activation energies, compared to some other reported results [6], are generally thought to be typical of protonic transport in these bulk materials [7].

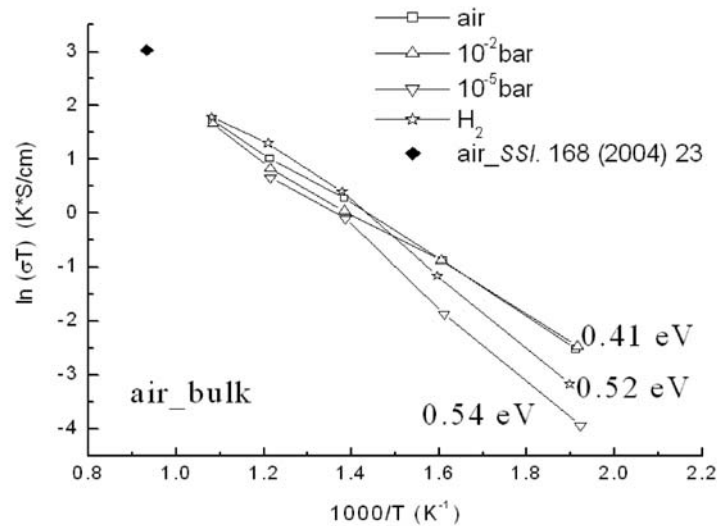


Figure 6.5. Arrhenius plots of the bulk conductivity for $\text{BaCe}_{0.76}\text{Y}_{0.2}\text{Pr}_{0.04}\text{O}_{3-\delta}$ measured in dry atmospheres.

The σ vs. P_{O_2} curve at 650°C is plotted in figure 6.6, which indicates clearly the influence of the oxygen activity on the total conductivity. At high P_{O_2} , the slope is calculated to be 0.08, which agrees well with the result of Hirabayashi [8].

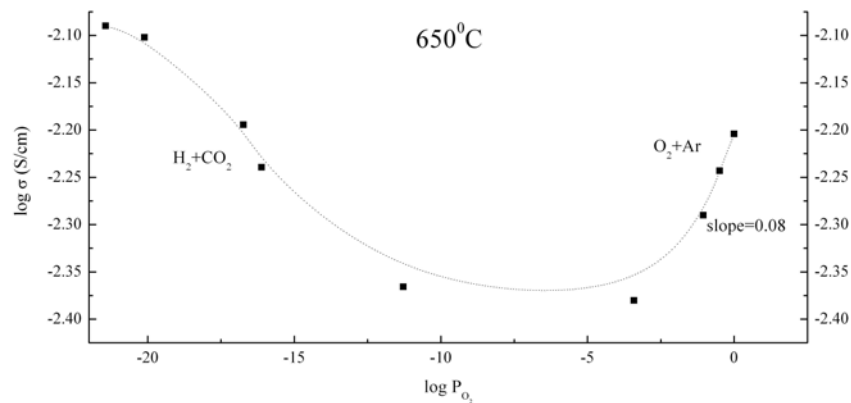
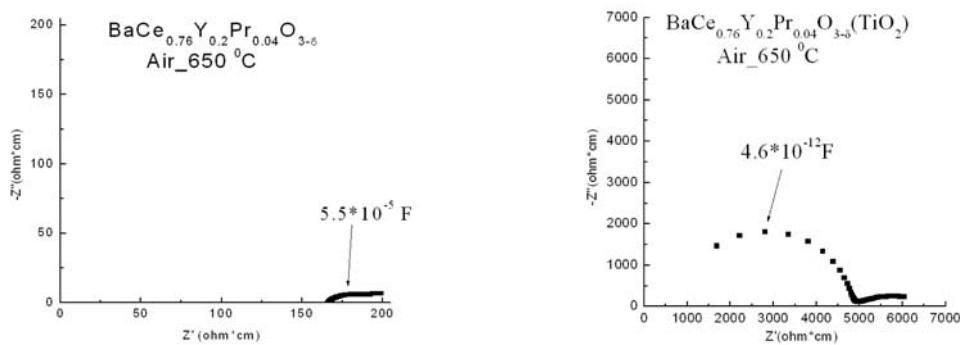


Figure 6.6. Brouwer diagram of the total conductivity for $\text{BaCe}_{0.76}\text{Y}_{0.2}\text{Pr}_{0.04}\text{O}_{3-\delta}$ at 650°C .

The sample pellet became light in colour after the measurements in reducing atmospheres, as already shown in figure 6.2. Accordingly, the increase of the conductivity at low P_{O_2} is not due to the n-type electronic conduction. To increase the electronic conductivity, TiO_2 and $\text{Ce}_{0.8}\text{Sm}_{0.2}\text{O}_{1.9}$ were added to $\text{BaCe}_{0.76}\text{Y}_{0.2}\text{Pr}_{0.04}\text{O}_{3-\delta}$ and $\text{BaCe}_{0.8}\text{Y}_{0.2}\text{O}_{2.9}$, respectively.

6.2.2 $\text{BaCe}_{0.76}\text{Y}_{0.2}\text{Pr}_{0.04}\text{O}_{3-\delta}$ (TiO_2)

Conductivities of $\text{BaCe}_{0.76}\text{Y}_{0.2}\text{Pr}_{0.04}\text{O}_{3-\delta}$ measured in all P_{O_2} ranges are largely degraded by adding TiO_2 . Three examples are given in figure 6.7 to compare the impedance plots of $\text{BaCe}_{0.76}\text{Y}_{0.2}\text{Pr}_{0.04}\text{O}_{3-\delta}$ with and without TiO_2 in air, dry and humidified H_2 at around 650°C . Humidified H_2 was obtained by bubbling the gas through water at room temperature.



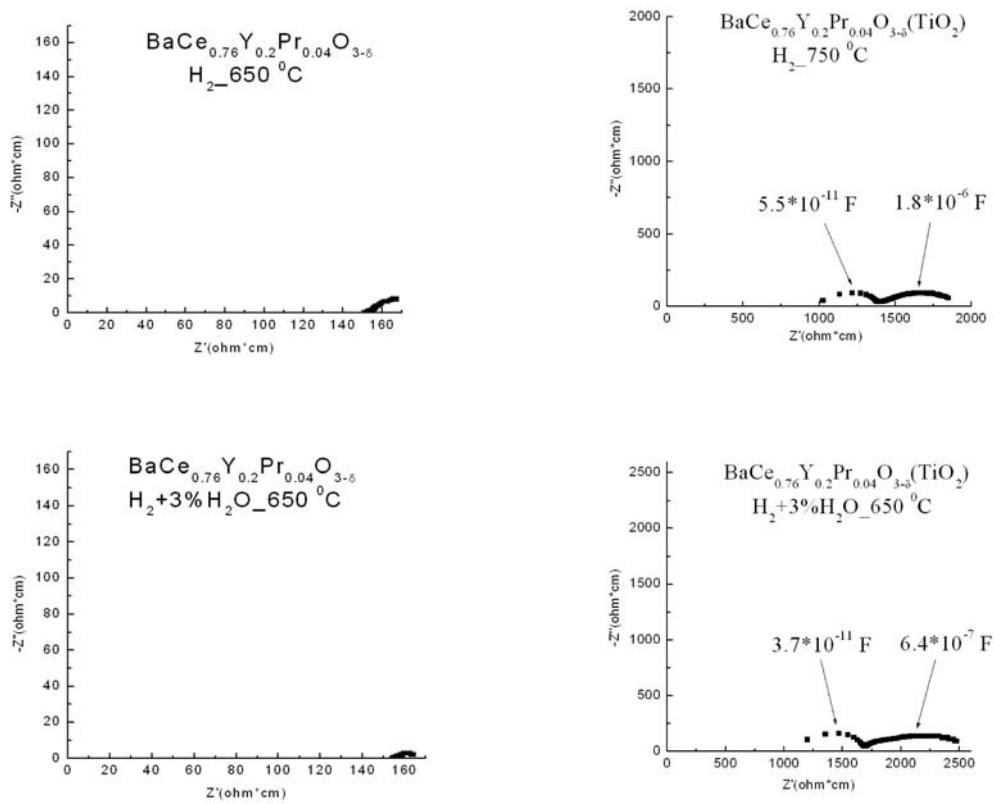


Figure 6.7. Comparisons of impedance plots of $\text{BaCe}_{0.76}\text{Y}_{0.2}\text{Pr}_{0.04}\text{O}_{3-\delta}$ with and without TiO_2 in air, dry and humidified H_2 at around 650°C .

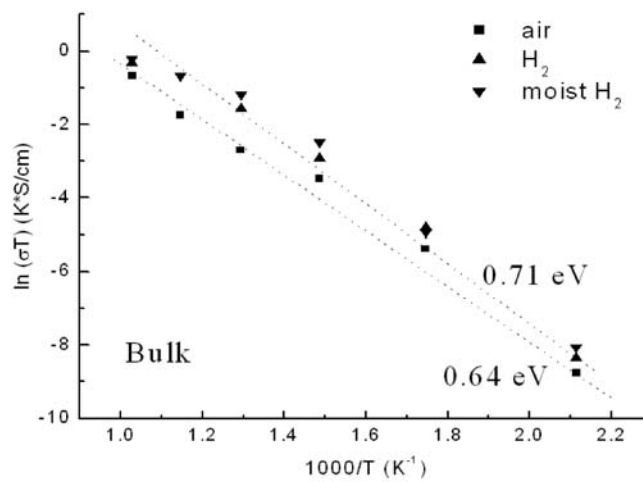


Figure 6.8. Arrhenius plots for the bulk conductivity of $\text{BaCe}_{0.76}\text{Y}_{0.2}\text{Pr}_{0.04}\text{O}_{3-\delta} + \text{TiO}_2$ in air, dry and humidified H_2

Comparing the Nyquist plots in figure 6.7 and Arrhenius plots shown in figure 6.5 and 6.8, the conductivities were lowered more than one order of magnitude by mixing with TiO_2 . Figure 6.3 shows that Ti has been dissolved in $\text{BaCe}_{0.76}\text{Y}_{0.2}\text{Pr}_{0.04}\text{O}_{3-\delta}$. When trivalent cation, such as Pr^{3+} or Y^{3+} , is replaced by tetravalent cation Ti^{4+} , oxygen vacancies will be filled up to maintain the charge neutrality. Thus, the conductivity is lowered by doping TiO_2 .

6.2.3 $\text{BaCe}_{0.8}\text{Y}_{0.2}\text{O}_{2.9} + \text{Ce}_{0.8}\text{Sm}_{0.2}\text{O}_{1.9}$

Figure 6.4 shows that there is no reaction product between $\text{BaCe}_{0.8}\text{Y}_{0.2}\text{O}_{2.9}$ (BCY) and $\text{Ce}_{0.8}\text{Sm}_{0.2}\text{O}_{1.9}$ after sintering. Two phases are homogeneously distributed in the sample. If there are continuous paths through the sample, charge transfer can take place within each phase without interfering with each other. The total conductivity should be dominated by the one with higher conductivity. When there is no continuous path, then the charge carriers have to pass through the interfaces between the two phases, which is normally a rate-determining process. In this case, the total conductivity will be dominated by the interfacial process and the slower conducting phase. The idea of mixing these two compounds is to take advantage of the reduction of cerium under low P_{O_2} and p-type conduction of barium cerate under dry oxidizing atmospheres. However, impedance measurements indicate that the conductivity of the mixture is much worse compared to the single material as shown in the Arrhenius plots in figure 6.9.

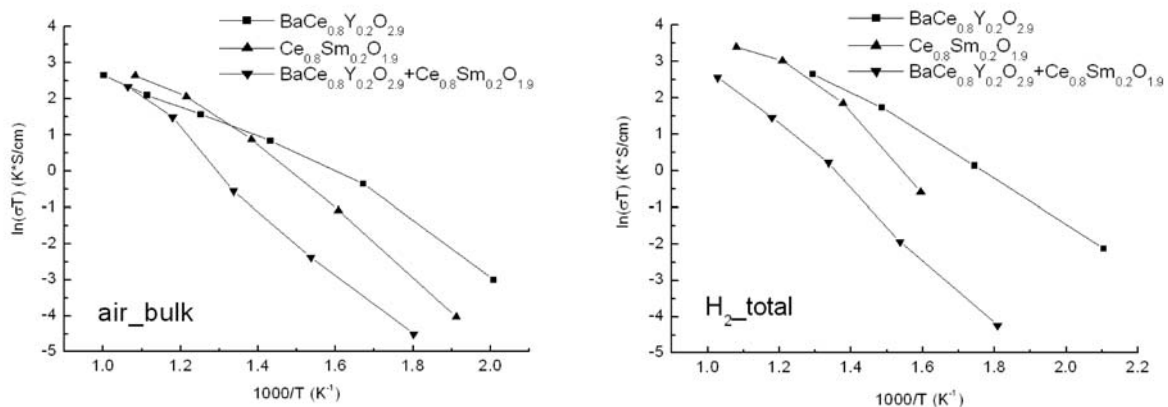


Figure 6.9. Arrhenius plots of the bulk conductivity in air and total conductivity in H_2 for $\text{BaCe}_{0.8}\text{Y}_{0.2}\text{O}_{2.9} + \text{Ce}_{0.8}\text{Sm}_{0.2}\text{O}_{1.9}$.

From figure 6.9, the conductivity of the mixture is much lower than SDC and BCY in air at low temperatures, indicating that the charge carriers are largely impeded by the interface between

SDC and BCY. While at high temperatures, the impeding effect from the interface becomes smaller and not rate determining any more, thus the conductivity of the mixture is determined by BCY, which has a smaller conductivity than SDC. The existence of the interfacial process can also be indicated from the impedance plot, which in principle should have one more semicircle. Figure 6.10 shows the Nyquist plot in air at 380°C. The third semicircle is assigned to the interfacial process.

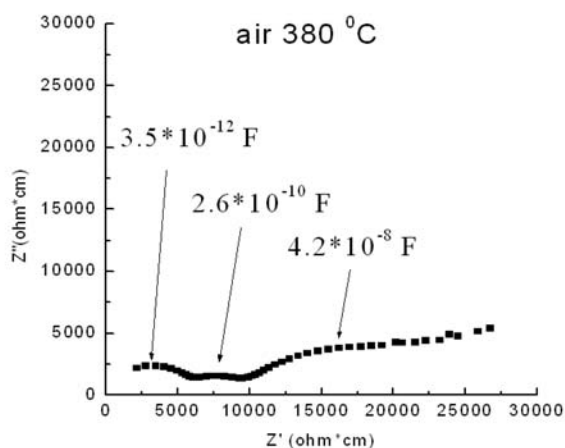


Figure 6.10. Nyquist plot of $\text{BaCe}_{0.8}\text{Y}_{0.2}\text{O}_{2.9} + \text{Ce}_{0.8}\text{Sm}_{0.2}\text{O}_{1.9}$ in air at 380°C.

6.3. EMF measurement

6.3.1 $\text{BaCe}_{0.76}\text{Y}_{0.2}\text{Pr}_{0.04}\text{O}_{3-\delta}$

The EMF was measured using the experimental setup shown in figure 4.6. The working temperature is limited to about 600°C due to the AR glass tube and the metal spring. Because this type of setup eliminates the requirement of any ceramic or glass glues, it can be used to provide fast result. The disadvantage is that the permanent deformation of the springs at high temperatures may lead to loose contact between the sample and the AR glass tube. Also a very flat and smooth surface is required for both the sample and the tube surface. A pellet of $\text{BaCe}_{0.76}\text{Y}_{0.2}\text{Pr}_{0.04}\text{O}_{3-\delta}$ without Pt paste on both sides was pressed in between the two glass tubes. Two gold rings between the tube and the sample were employed here as sealing material and electrical leads. Figure 6.11 shows two parts of the EMF result using air and $\text{H}_2+3\%\text{H}_2\text{O}$. At 450°C and 400°C, the cell has shown a stable EMF of 0.943V and 0.876V, respectively. Further increase of the temperature caused a sharp decrease of the voltage, which could be due to the gas leakage through the cracks inside the sample.

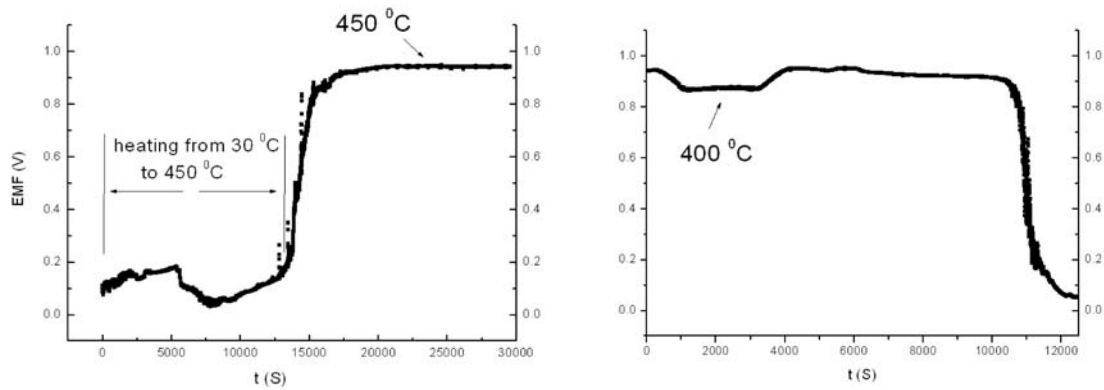


Figure 6.11. EMF of $\text{BaCe}_{0.76}\text{Y}_{0.2}\text{Pr}_{0.04}\text{O}_{3-\delta}$ without Pt paste, using air and $\text{H}_2+3\%\text{H}_2\text{O}$. Two gold rings between the tube and the sample were employed here as sealing material and electrical leads.

6.3.2 $\text{BaCe}_{0.76}\text{Y}_{0.2}\text{Pr}_{0.04}\text{O}_{3-\delta} + \text{TiO}_2$

Samples were measured in the same way as discussed in last section. The only difference was that the anode side of the sample was covered by the Pt paste. The sawtoothed curve was due to the change in H_2 flux. With higher flux, the voltage became smaller. Compared to figure 6.11, the OCV is about 100mV lower than that of $\text{BaCe}_{0.76}\text{Y}_{0.2}\text{Pr}_{0.04}\text{O}_{3-\delta}$, which can be explained by the reduction of Ti.

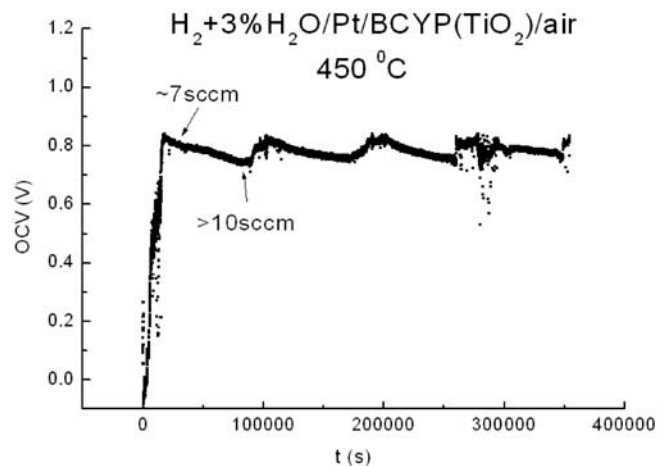


Figure 6.12. EMF of $\text{BaCe}_{0.76}\text{Y}_{0.2}\text{Pr}_{0.04}\text{O}_{3-\delta} (\text{TiO}_2)$ at 450°C . The sawtoothed curve was due to the change in H_2 flux.

6.4. References

- [1]. N. Taniguchi, K. Hato, J. Niikura, T. Gamo, H. Iwahara, *Solid State Ionics* 53-56, 1992, 998.
- [2]. H. Hu, M. Liu, *J. Electrochem. Soc.* 143,1996, 859.
- [3]. N. Bonanos, B. Ellis, K.S. Knight, M.N. Mahmood, *Solid State Ionics*, 35, 1989, 179.
- [4]. H. Iwahara, *Solid State Ionics* 28-30,1988, 573.
- [5]. E.O. Ahlgren, *Solid State Ionics* 97,1997, 489.
- [6]. K.D. Kreuer, Th. Dippel, Yu.M. Baikov, J. Maier, *Solid State Ionics* 86-88, 1996, 613.
- [7]. W. Grover Coors and R. Swartzlander, *Proceedings of the 26th Risø International Symposium on Materials science: Solid State Electrochemistry*. Risø National Laboratory, Roskilde, Denmark, 2005.
- [8]. D. Hirabayashi, A. Tomita, M.E. Brito, T. Hibino, U. Harada, M. Nagao, M. Sano, *Solid State Ionics* 168, 2004, 23.

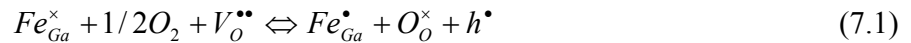
Chapter 7

Results and discussion III

7.1. Phase characterization

7.1.1 $\text{La}_{0.8}\text{Sr}_{0.2}\text{Ga}_{0.6}\text{Fe}_{0.4-x}\text{Ti}_x\text{O}_{3-\delta}$ ($x=0\sim 0.2$)

It was reported that Fe doped La(Sr)GaO₃ exhibited mixed electron hole and oxide ion conductivity over a wide range of oxygen partial pressures, which could be assigned to the formation of Fe⁴⁺[1-4]:



In the following section, we will discuss the influence of Ti doping on the electrical property of Fe doped La(Sr)GaO₃. Firstly, ionic radii of ions and calculated tolerance factors from Eq.(3.3) are shown in Table 7.1 and Table 7.2, respectively.

Table 7.1. Ionic radii. (R.D. Shannon, Acta Cryst. A32, 751-767 (1976))

Ions	Ionic radius (Å)
La ³⁺ (CN=12)	1.36
Sr ²⁺ (CN=12)	1.44
Ga ³⁺ (CN=6)	0.62
Mg ²⁺ (CN=6)	0.72
Fe ³⁺ (CN=6)	0.645
Ti ⁴⁺ (CN=6)	0.605
Sn ⁴⁺ (CN=6)	0.69
Mn ³⁺ (CN=6)	0.645
O ²⁻ (CN=6)	0.140

Table 7.2. Tolerance factors of $\text{La}_{0.8}\text{Sr}_{0.2}\text{Ga}_{0.6}\text{Fe}_{0.4-x}\text{Ti}_x\text{O}_{3-\delta}$. ($x=0\sim 0.2$)

Composition	<i>t</i>
$\text{La}_{0.8}\text{Sr}_{0.2}\text{Ga}_{0.6}\text{Fe}_{0.4}\text{O}_{3-\delta}$	0.9540
$\text{La}_{0.8}\text{Sr}_{0.2}\text{Ga}_{0.6}\text{Fe}_{0.37}\text{Ti}_{0.03}\text{O}_{3-\delta}$	0.9545
$\text{La}_{0.8}\text{Sr}_{0.2}\text{Ga}_{0.6}\text{Fe}_{0.35}\text{Ti}_{0.05}\text{O}_{3-\delta}$	0.9549
$\text{La}_{0.8}\text{Sr}_{0.2}\text{Ga}_{0.6}\text{Fe}_{0.34}\text{Ti}_{0.06}\text{O}_{3-\delta}$	0.9551
$\text{La}_{0.8}\text{Sr}_{0.2}\text{Ga}_{0.6}\text{Fe}_{0.32}\text{Ti}_{0.08}\text{O}_{3-\delta}$	0.9555
$\text{La}_{0.8}\text{Sr}_{0.2}\text{Ga}_{0.6}\text{Fe}_{0.3}\text{Ti}_{0.1}\text{O}_{3-\delta}$	0.9559
$\text{La}_{0.8}\text{Sr}_{0.2}\text{Ga}_{0.6}\text{Fe}_{0.2}\text{Ti}_{0.2}\text{O}_{3-\delta}$	0.9577

Ti^{4+} has similar size to Fe^{3+} , so there is no significant change of the tolerance factor with increasing Ti content. Thus the influence from the distortion of the perovskite structure can be neglected. All the samples were prepared by solid-state reaction, sintered at 1500°C for 6 hours. The XRD patterns in figure 7.1 show pure perovskite phase.

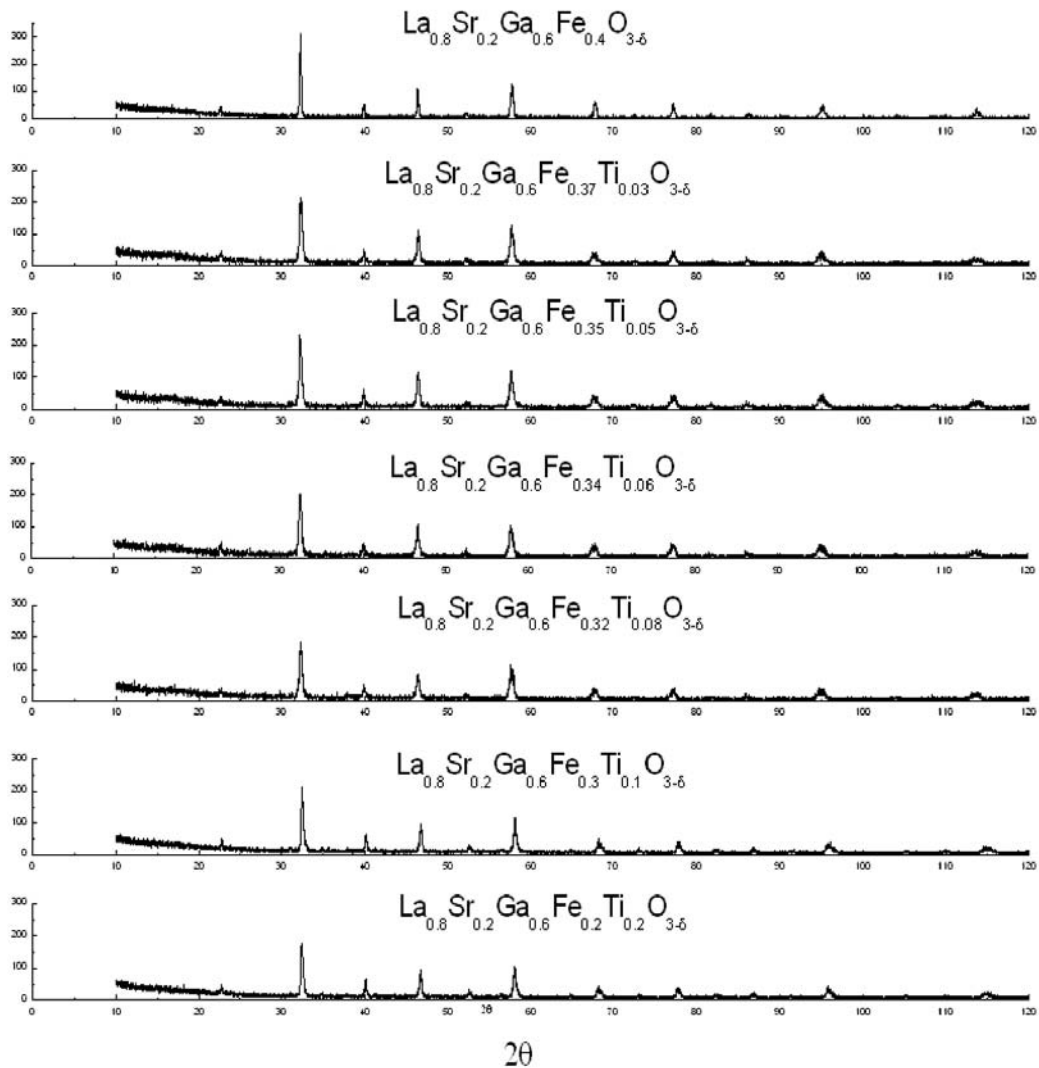


Figure 7.1. XRD patterns of $\text{La}_{0.8}\text{Sr}_{0.2}\text{Ga}_{0.6}\text{Fe}_{0.4-x}\text{Ti}_x\text{O}_{3-\delta}$ ($x=0\sim 0.2$). All samples show single perovskite type structure.

7.1.2 $\text{La}_{0.56}\text{Sr}_{0.44}\text{Ga}_{0.64}\text{Mg}_{0.16}\text{Me}_{0.2}\text{O}_{2.8}$ (Me=Ti and Sn)

Oxide ion conductivity of LaGaO_3 can be greatly improved by aliovalent substitution of Sr and Mg for La and Ga, which introduce oxygen vacancies into the lattice. When Ti tetravalent ions replace the Ga site, no oxygen vacancies can be generated. In order to try to maintain the ionic conductivity while incorporating with certain amount of Ti or Sn for n-type conductivity, the oxygen deficiency of the samples was kept to be 0.2. The corresponding compositions are $\text{La}_{0.56}\text{Sr}_{0.44}\text{Ga}_{0.64}\text{Mg}_{0.16}\text{Ti}_{0.2}\text{O}_{2.8}$ and $\text{La}_{0.56}\text{Sr}_{0.44}\text{Ga}_{0.64}\text{Mg}_{0.16}\text{Sn}_{0.2}\text{O}_{2.8}$. The tolerance factors are 0.958 and 0.950, respectively. XRD patterns are shown in figure 7.2. No impurity peaks can be found.

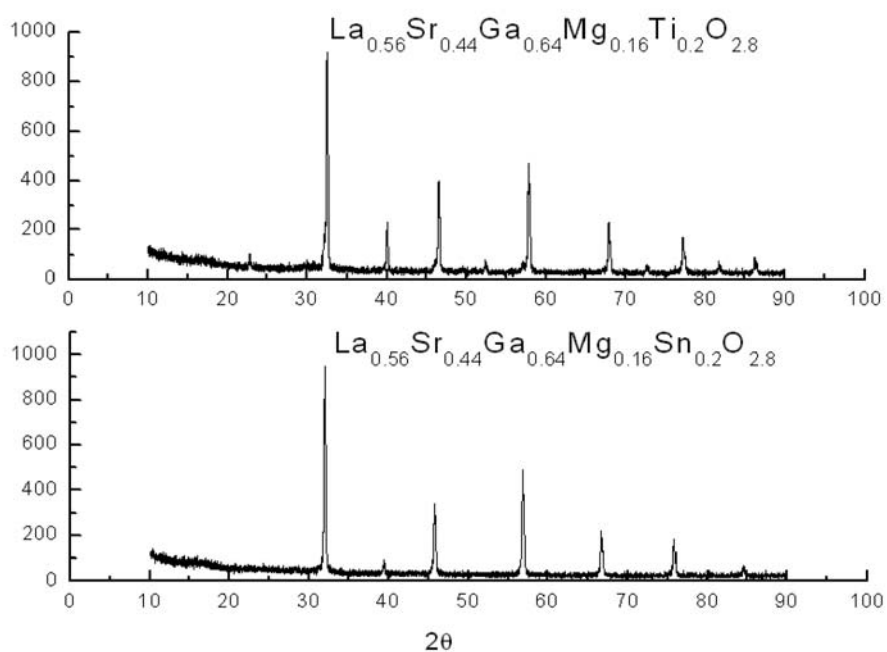


Figure 7.2. XRD patterns of $\text{La}_{0.56}\text{Sr}_{0.44}\text{Ga}_{0.64}\text{Mg}_{0.16}\text{Ti}_{0.2}\text{O}_{2.8}$ (top) and $\text{La}_{0.56}\text{Sr}_{0.44}\text{Ga}_{0.64}\text{Mg}_{0.16}\text{Sn}_{0.2}\text{O}_{2.8}$ (bottom). No impurity peaks were found.

7.1.3 $\text{La}_{0.9}\text{Sr}_{0.1}\text{Ga}_{1-x-y}\text{Mg}_y\text{Mn}_x\text{O}_{3-\delta}$ ($x, y=0\sim 0.2$)

LSGM is a pure ionic conductor over a wide range of oxygen partial pressure, while strontium doped lanthanum manganite (LSM) is a well-known cathode material for fuel cells. In order to investigate the effect of Mn doping on the electrical property of LSGM, especially the electronic conductivity, a series of $\text{La}_{0.9}\text{Sr}_{0.1}\text{Ga}_{1-x-y}\text{Mg}_y\text{Mn}_x\text{O}_{3-\delta}$ compositions were prepared. Different crystal structures of LSGM phase, including cubic, orthorhombic and rhombohedral were reported by different authors [5-8]. XRD patterns show that the best fit to the database is orthorhombic (JCPDS No.24-1102). Splitting of the strongest peak at $2\theta \approx 32.5^\circ$, which is the indication of rhombohedral structure, was not found. Impurities of LaSrGaO_4 and $\text{LaSrGa}_3\text{O}_7$ can be seen in most of the samples, as also previously reported [9,10]. The structure parameters of $\text{La}_{0.9}\text{Sr}_{0.1}\text{Ga}_{1-x-y}\text{Mg}_y\text{Mn}_x\text{O}_{3-\delta}$ compositions are listed in Table 7.3.

Table 7.3. The structural parameters of $\text{La}_{0.9}\text{Sr}_{0.1}\text{Ga}_{0.8-x-y}\text{Mg}_y\text{Mn}_x\text{O}_{3-\delta}$ compositions

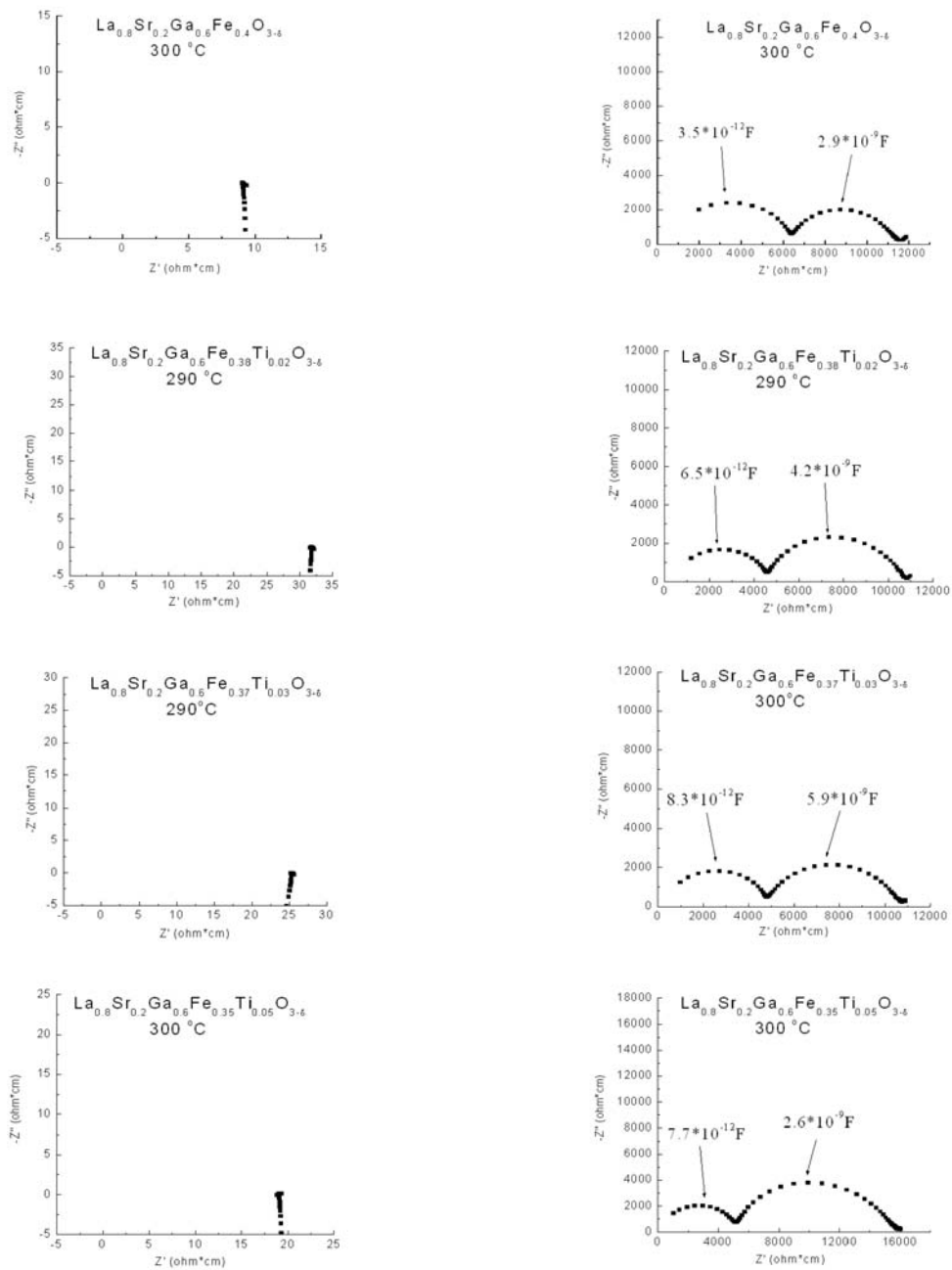
Compositions	t	x	y	a (Å)	b (Å)	c (Å)	Phases*
$\text{La}_{0.9}\text{Sr}_{0.1}\text{Ga}_{0.8}\text{Mg}_{0.2}\text{O}_{2.85}$	0.9456	0	0.2	5.489	5.501	7.745	O+I+II
$\text{La}_{0.9}\text{Sr}_{0.1}\text{Ga}_{0.8}\text{Mg}_{0.15}\text{Mn}_{0.05}\text{O}_{3-\delta}$	0.9472	0.05	0.15	5.490	5.550	7.747	O+I+II
$\text{La}_{0.9}\text{Sr}_{0.1}\text{Ga}_{0.75}\text{Mg}_{0.2}\text{Mn}_{0.05}\text{O}_{3-\delta}$	0.9449		0.2	5.494	5.543	7.754	O+I+II
$\text{La}_{0.9}\text{Sr}_{0.1}\text{Ga}_{0.8}\text{Mg}_{0.1}\text{Mn}_{0.1}\text{O}_{3-\delta}$	0.9488	0.1	0.1	5.499	5.517	7.785	O+II
$\text{La}_{0.9}\text{Sr}_{0.1}\text{Ga}_{0.75}\text{Mg}_{0.15}\text{Mn}_{0.1}\text{O}_{3-\delta}$	0.9465		0.15	5.490	5.532	7.778	O
$\text{La}_{0.9}\text{Sr}_{0.1}\text{Ga}_{0.7}\text{Mg}_{0.2}\text{Mn}_{0.1}\text{O}_{3-\delta}$	0.9442		0.2	5.501	5.527	7.797	O+II
$\text{La}_{0.9}\text{Sr}_{0.1}\text{Ga}_{0.8}\text{Mg}_{0.05}\text{Mn}_{0.15}\text{O}_{3-\delta}$	0.9505	0.15	0.05	5.486	5.504	7.752	O
$\text{La}_{0.9}\text{Sr}_{0.1}\text{Ga}_{0.75}\text{Mg}_{0.1}\text{Mn}_{0.15}\text{O}_{3-\delta}$	0.9481		0.1	5.490	5.529	7.766	O
$\text{La}_{0.9}\text{Sr}_{0.1}\text{Ga}_{0.725}\text{Mg}_{0.125}\text{Mn}_{0.15}\text{O}_{3-\delta}$	0.9470		0.125	5.499	5.581	7.766	O+II
$\text{La}_{0.9}\text{Sr}_{0.1}\text{Ga}_{0.7}\text{Mg}_{0.15}\text{Mn}_{0.15}\text{O}_{3-\delta}$	0.9458		0.15	5.489	5.495	7.772	O
$\text{La}_{0.9}\text{Sr}_{0.1}\text{Ga}_{0.65}\text{Mg}_{0.2}\text{Mn}_{0.15}\text{O}_{3-\delta}$	0.9435		0.2	5.490	5.510	7.775	O
$\text{La}_{0.9}\text{Sr}_{0.1}\text{Ga}_{0.8}\text{Mn}_{0.2}\text{O}_{3-\delta}$	0.9521	0.2	0	5.520	5.660	7.796	O+I+II
$\text{La}_{0.9}\text{Sr}_{0.1}\text{Ga}_{0.7}\text{Mg}_{0.1}\text{Mn}_{0.2}\text{O}_{3-\delta}$	0.9474		0.1	5.512	5.569	7.774	O+II
$\text{La}_{0.9}\text{Sr}_{0.1}\text{Ga}_{0.65}\text{Mg}_{0.15}\text{Mn}_{0.2}\text{O}_{3-\delta}$	0.9451		0.15	5.501	5.552	7.775	O+II
$\text{La}_{0.9}\text{Sr}_{0.1}\text{Ga}_{0.6}\text{Mg}_{0.2}\text{Mn}_{0.2}\text{O}_{3-\delta}$	0.9428		0.2	5.496	5.564	7.761	O+I

* “O”: orthorhombic. “I”: LaSrGaO_4 . “II”: $\text{LaSrGa}_3\text{O}_7$

7.2. Electrical property

7.2.1 $\text{La}_{0.8}\text{Sr}_{0.2}\text{Ga}_{0.6}\text{Fe}_{0.4-x}\text{Ti}_x\text{O}_{3-\delta}$ ($x=0\sim 0.2$)

Figure 7.3 and figure 7.4 shows the impedance plots of $\text{La}_{0.8}\text{Sr}_{0.2}\text{Ga}_{0.6}\text{Fe}_{0.4-x}\text{Ti}_x\text{O}_{3-\delta}$ ($x=0 \sim 0.2$) at around 300°C in air (left) and hydrogen (right), respectively.



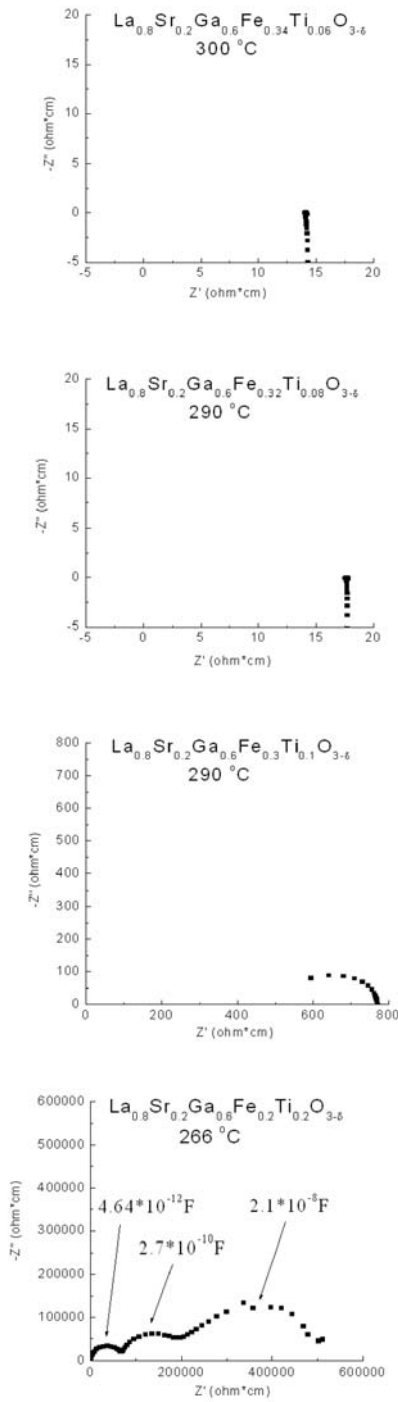


Figure 7.3. Impedance plots at around 300°C in air.

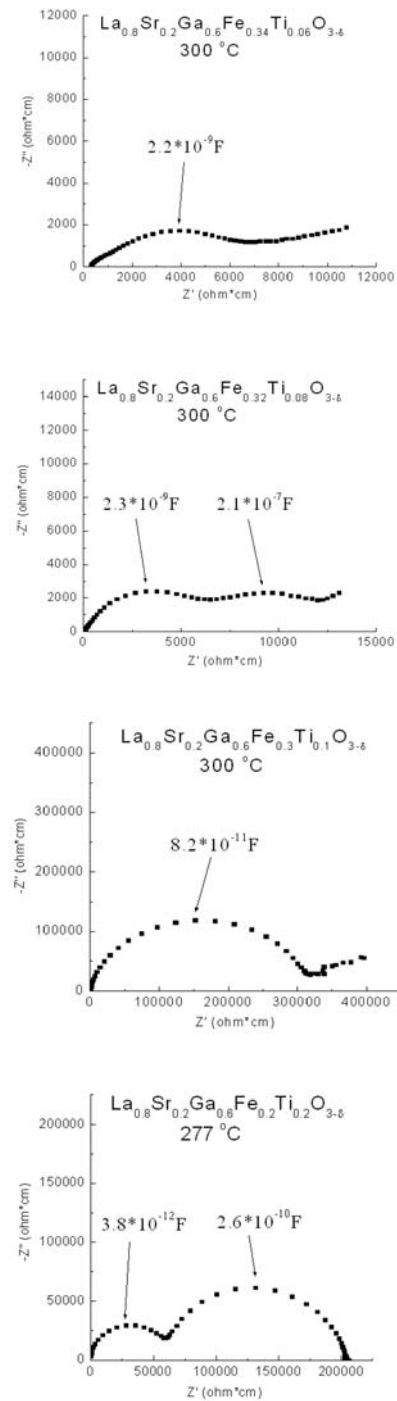
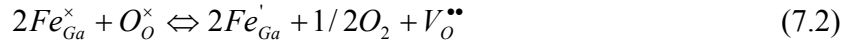


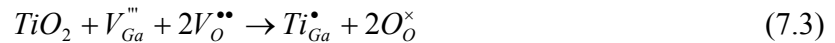
Figure 7.4 Impedance plots at around 300°C in hydrogen.

According to Eq. (7.1), the electron hole conduction of $\text{La}_{0.8}\text{Sr}_{0.2}\text{Ga}_{0.6}\text{Fe}_{0.4}\text{O}_{3-\delta}$ under

oxidizing atmosphere is due to the formation of Fe^{4+} . At low oxygen partial pressure, Fe^{2+} is formed according to the following equation:



Because of the increasing amount of oxygen vacancies and decreasing amount of electron holes, ionic conduction is becoming more dominant at low oxygen partial pressures. When Ti^{4+} is substituted into the lattice, oxygen vacancies will be filled to maintain the electroneutrality condition as shown in Eq. (7.3).



As the result, the electron hole conductivity decreases by doping with Ti. Samples with Ti content less than 10 mol% show similar metallic behavior to $La_{0.8}Sr_{0.2}Ga_{0.6}Fe_{0.4}O_{3-\delta}$ in air. Ionic conduction starts to play a more important role from 10-mol% and becomes predominant when the Ti content reaches 20 mol%. Figure 7.5 and figure 7.6 show the variation of the total conductivity of $La_{0.8}Sr_{0.2}Ga_{0.6}Fe_{0.4-x}Ti_xO_{3-\delta}$ on the Ti content at 300°C. In air, the conductivity drops when Ti is added, and then increases slightly with the Ti content up to 6-mol%. The conductivity decreases quickly when more than 10 mol% Ti is introduced into the lattice. In hydrogen, there is no obvious influence on the conductivity with up to 5-mol% Ti. Samples with 6 and 8-mol% Ti have slightly higher total conductivity than other compositions, because the first semicircles in both cases should be actually the overlap of two semicircles according to the capacitance values. When the Ti content exceeds 8 mol%, the conductivity decreases quickly again. The conductivity of the sample with 20-mol% Ti is higher than the one with 10-mol% Ti. This could be attributed to the increased n-type conductivity due to the larger amount of Ti. But the electronic conductivity is still much small compared to the ionic conductivity, which can also explain the difference between the impedance plots of $La_{0.8}Sr_{0.2}Ga_{0.6}Fe_{0.2}Ti_{0.2}O_{3-\delta}$ measured in air and hydrogen. The first two semicircles measured in two atmospheres are almost the same, and only the third one is missing in the case of hydrogen. This kind of phenomenon also holds at high temperatures.

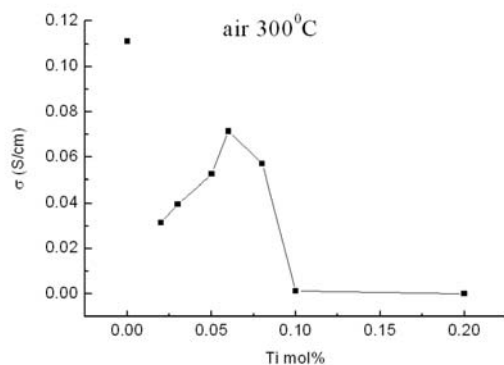


Figure 7.5. Total σ vs. Ti content in air at 300°C for $La_{0.8}Sr_{0.2}Ga_{0.6}Fe_{0.4-x}Ti_xO_{3-\delta}$.

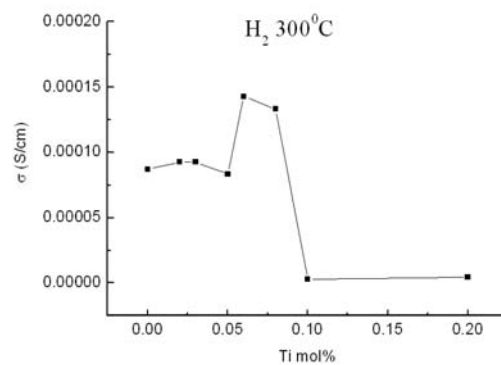


Figure 7.6. Total σ vs. Ti content in H_2 at 300°C for $La_{0.8}Sr_{0.2}Ga_{0.6}Fe_{0.4-x}Ti_xO_{3-\delta}$.

Figure 7.7 and 7.8 show the Arrhenius plots of the total conductivity for $\text{La}_{0.8}\text{Sr}_{0.2}\text{Ga}_{0.6}\text{Fe}_{0.4-x}\text{Ti}_x\text{O}_{3-\delta}$ ($x=0 \sim 0.2$) in air and hydrogen. The Ti free sample always has the highest conductivity in air. Samples with Ti content up to 8-mol% all show metallic behavior. In hydrogen, samples with Ti content less than 10 mol% show higher conductivity than $\text{La}_{0.8}\text{Sr}_{0.2}\text{Ga}_{0.6}\text{Fe}_{0.4}\text{O}_{3-\delta}$ at elevated temperatures due to the formation of Ti^{3+} and liberation of oxygen vacancies.

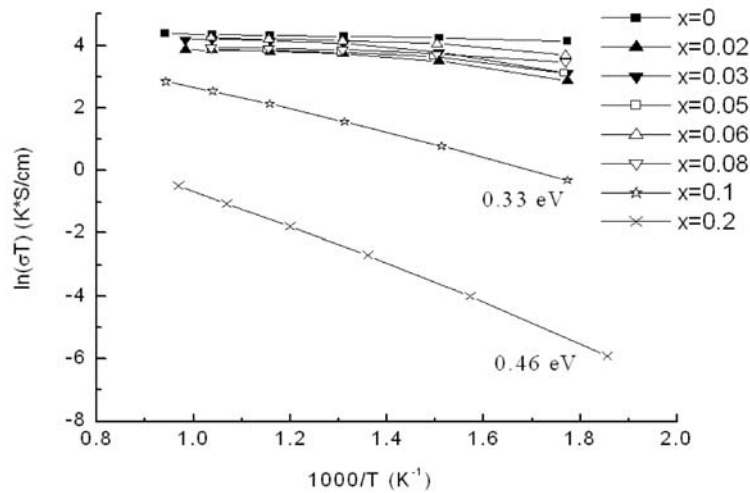
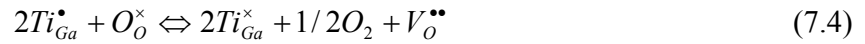


Figure 7.7. Arrhenius plot of the total conductivity of $\text{La}_{0.8}\text{Sr}_{0.2}\text{Ga}_{0.6}\text{Fe}_{0.4-x}\text{Ti}_x\text{O}_{3-\delta}$ ($x=0\sim 0.2$) in air.

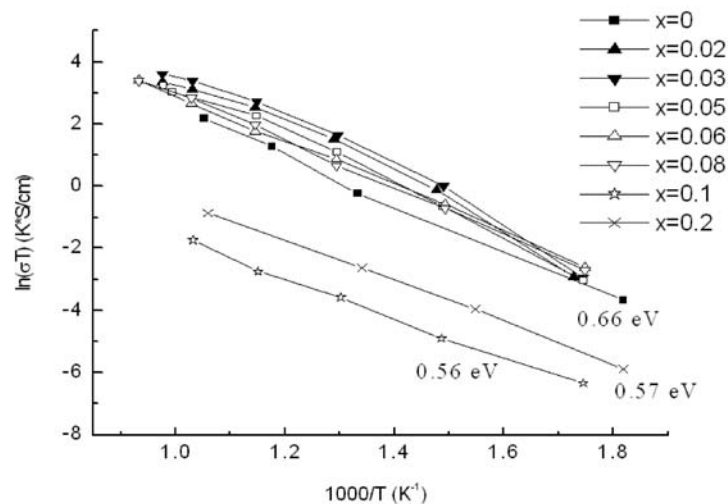


Figure 7.8. Arrhenius plot of the total conductivity of $\text{La}_{0.8}\text{Sr}_{0.2}\text{Ga}_{0.6}\text{Fe}_{0.4-x}\text{Ti}_x\text{O}_{3-\delta}$ ($x=0\sim 0.2$) in H_2 .

In figure 7.8 $\text{La}_{0.8}\text{Sr}_{0.2}\text{Ga}_{0.6}\text{Fe}_{0.37}\text{Ti}_{0.03}\text{O}_{3-\delta}$ and $\text{La}_{0.8}\text{Sr}_{0.2}\text{Ga}_{0.6}\text{Fe}_{0.38}\text{Ti}_{0.02}\text{O}_{3-\delta}$ show the highest conductivities in most of the temperature range. So the dependence of the total conductivity on oxygen partial pressure was also measured and is shown in figure 7.9 and 7.10, respectively. There is no obvious improvement in n-type conductivity under reducing conditions, which is a proof of the previous conclusion, i.e. the increase of conductivities of Ti containing samples in figure 7.8 is due to ionic conduction, but not electronic. n-type electronic conductivity was found in $\text{La}_{0.8}\text{Sr}_{0.2}\text{Ga}_{0.6}\text{Fe}_{0.2}\text{Ti}_{0.2}\text{O}_{3-\delta}$, but both the ionic and electronic conductivities of this composition are too low at working temperatures.

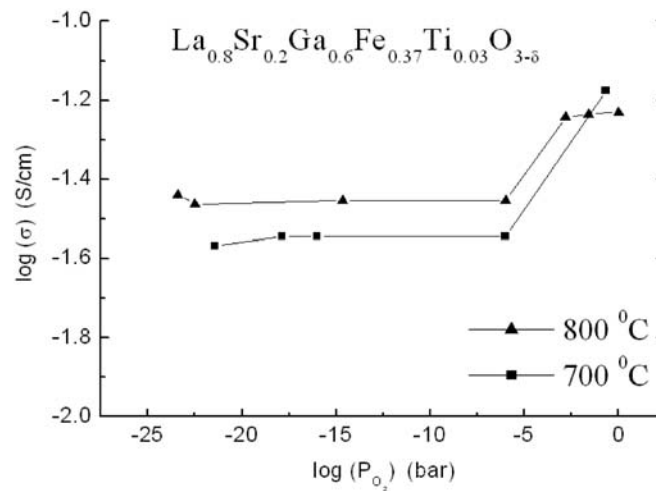


Figure 7.9. The total conductivity of $\text{La}_{0.8}\text{Sr}_{0.2}\text{Ga}_{0.6}\text{Fe}_{0.37}\text{Ti}_{0.03}\text{O}_{3-\delta}$ vs. P_{O_2} .

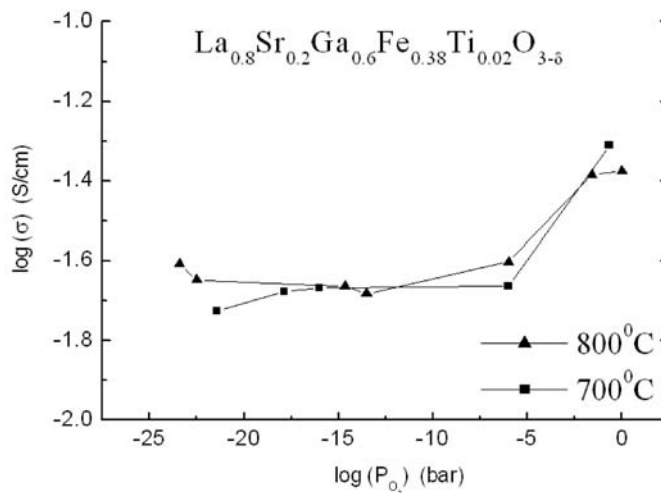


Figure 7.10. The total conductivity of $\text{La}_{0.8}\text{Sr}_{0.2}\text{Ga}_{0.6}\text{Fe}_{0.38}\text{Ti}_{0.02}\text{O}_{3-\delta}$ vs. P_{O_2} .

7.2.2 $\text{La}_{0.56}\text{Sr}_{0.44}\text{Ga}_{0.64}\text{Mg}_{0.16}\text{Me}_{0.2}\text{O}_{2.8}$ (Me=Ti and Sn)

In order to increase the n-type conductivity in LaGaO_3 based materials, Ti was tried to doped into $\text{La}_{0.8}\text{Sr}_{0.2}\text{Ga}_{0.6}\text{Fe}_{0.4}\text{O}_{3-\delta}$, which is a predominant p-type conductor in wide range of oxygen partial pressures. In this section, the possibility of improving the electronic conductivity in an ionic conductor LSGM under reducing conditions by doping of Ti or Sn will be discussed. Since 20-mol% was considered to be the minimum amount of Ti for n-type conduction in case of $\text{La}_{0.8}\text{Sr}_{0.2}\text{Ga}_{0.6}\text{Fe}_{0.4}\text{O}_{3-\delta}$, this amount was maintained in the present study. Concentrations of other components were also adjusted so as to avoid deteriorating the ionic conductivity largely.

7.2.2.1 $\text{La}_{0.56}\text{Sr}_{0.44}\text{Ga}_{0.64}\text{Mg}_{0.16}\text{Ti}_{0.2}\text{O}_{2.8}$

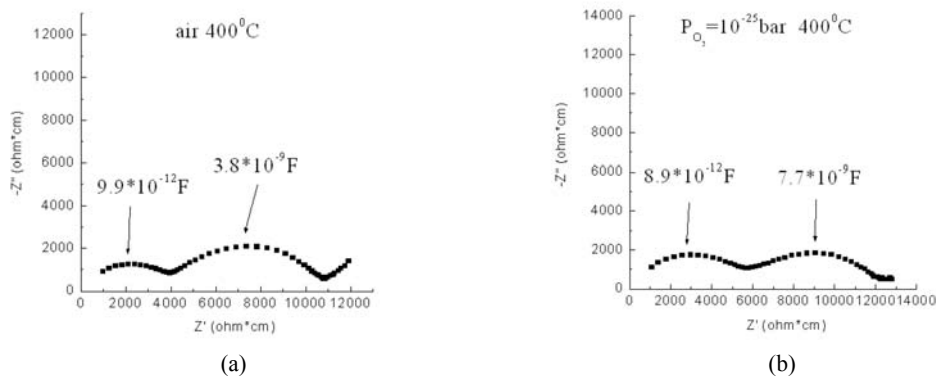


Figure 7.11. Nyquist plots of $\text{La}_{0.56}\text{Sr}_{0.44}\text{Ga}_{0.64}\text{Mg}_{0.16}\text{Ti}_{0.2}\text{O}_{2.8}$ in (a) air and (b) $P_{\text{O}_2}=10^{-25}$ bar at 400°C .

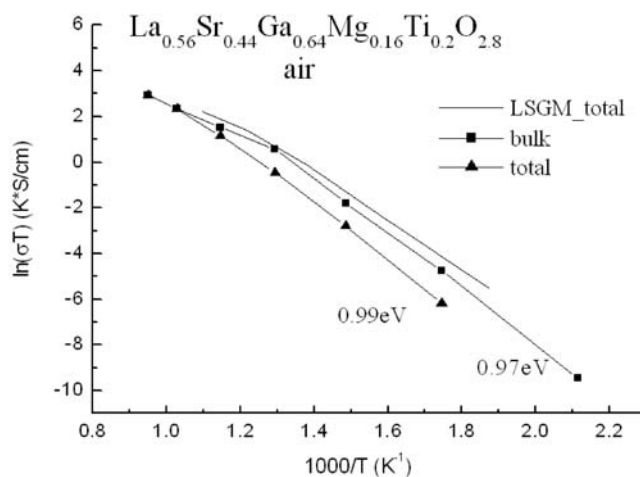


Figure 7.12. Arrhenius plots of bulk and total conductivities for $\text{La}_{0.56}\text{Sr}_{0.44}\text{Ga}_{0.64}\text{Mg}_{0.16}\text{Ti}_{0.2}\text{O}_{2.8}$ in air.

Figure 7.11 shows the impedance plots of $\text{La}_{0.56}\text{Sr}_{0.44}\text{Ga}_{0.64}\text{Mg}_{0.16}\text{Ti}_{0.2}\text{O}_{3-\delta}$ measured in air and reducing atmosphere ($P_{\text{O}_2}=10^{-25}\text{bar}$) at 400°C . From the two semicircles bulk and total conductivities can be determined and the corresponding Arrhenius plots are shown in figure 7.12 and 7.13. The total conductivity of $\text{La}_{0.9}\text{Sr}_{0.1}\text{Ga}_{0.8}\text{Mg}_{0.2}\text{O}_{2.85}$ in air is also plotted in figure 7.12 for comparison. The conductivity of $\text{La}_{0.56}\text{Sr}_{0.44}\text{Ga}_{0.64}\text{Mg}_{0.16}\text{Ti}_{0.2}\text{O}_{3-\delta}$ is much lower than LSGM below 700°C , but close to each other at higher temperatures. So the degradation of ionic conductivity due to the doping of Ti can be compensated by the adjustment of the oxygen deficiency. Comparing the impedance plots in figure 7.11 and Arrhenius plots in figure 7.12 and 7.13, it can be seen that $\text{La}_{0.56}\text{Sr}_{0.44}\text{Ga}_{0.64}\text{Mg}_{0.16}\text{Ti}_{0.2}\text{O}_{3-\delta}$ has nearly the same conductivities in both atmospheres, which is similar to pure LSGM that has a constant conductivity over a wide range of oxygen partial pressures. To further investigate the effect of Ti doping, both AC impedance and DC resistance of $\text{La}_{0.56}\text{Sr}_{0.44}\text{Ga}_{0.64}\text{Mg}_{0.16}\text{Ti}_{0.2}\text{O}_{3-\delta}$ were measured under different atmospheres.

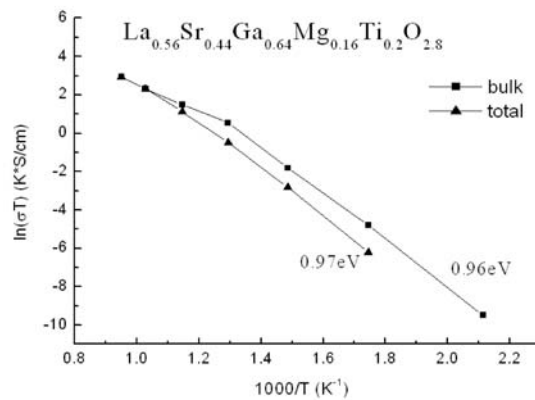


Figure 7.13. Arrhenius plots of the bulk and total conductivities for $\text{La}_{0.56}\text{Sr}_{0.44}\text{Ga}_{0.64}\text{Mg}_{0.16}\text{Ti}_{0.2}\text{O}_{2.8}$ in reducing condition.

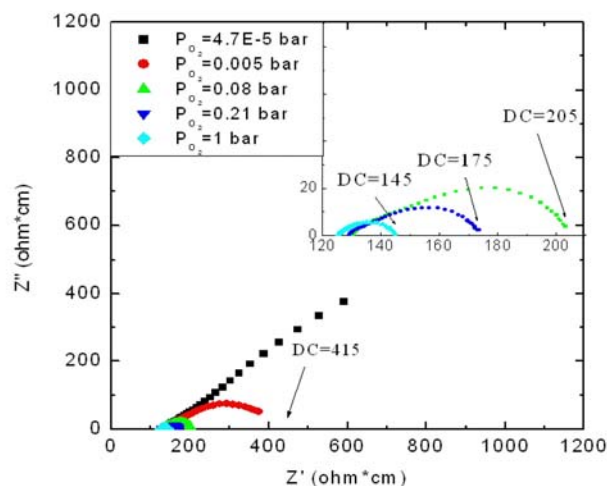


Figure 7.14. Nyquist plots of $\text{La}_{0.56}\text{Sr}_{0.44}\text{Ga}_{0.64}\text{Mg}_{0.16}\text{Ti}_{0.2}\text{O}_{2.8}$ in high oxygen partial pressures at 700°C .

Figure 7.14 shows the Nyquist plots of $\text{La}_{0.56}\text{Sr}_{0.44}\text{Ga}_{0.64}\text{Mg}_{0.16}\text{Ti}_{0.2}\text{O}_{3-\delta}$ in high oxygen partial pressures at 700°C . Successive impedance measurements at lower temperatures indicate that these curves are the overlaps of the second and third semicircles. The intersections of the third semicircle and real axis agree well with the DC results. With increasing P_{O_2} , the DC resistance decreases. This can be explained by fast kinetics at the sample-electrode interfaces due to the increased amount of oxygen species in the surrounding atmosphere. Similar change occurs under reducing conditions, too. But the DC value decreases with decreasing P_{O_2} , as shown in figure 7.15. This phenomenon can be explained either by increased number of H_2 , which will take up oxygen from the sample surface more rapidly, or by increased electronic conductivity with decreasing P_{O_2} due to the reduction of Ti. This can be further confirmed by taking impedance measurements on the samples with different length/area ratios. However, if the electronic conductivity is largely increased, the intersection with the real axis at high frequencies should also be shifted to the left side, which is not the case in figure 7.15. Figure 7.16 shows the dependence of the DC conductivity on P_{O_2} under high and low oxygen partial pressures, respectively. The DC conductivity is mainly controlled by the kinetic processes at the sample/electrode interfaces.

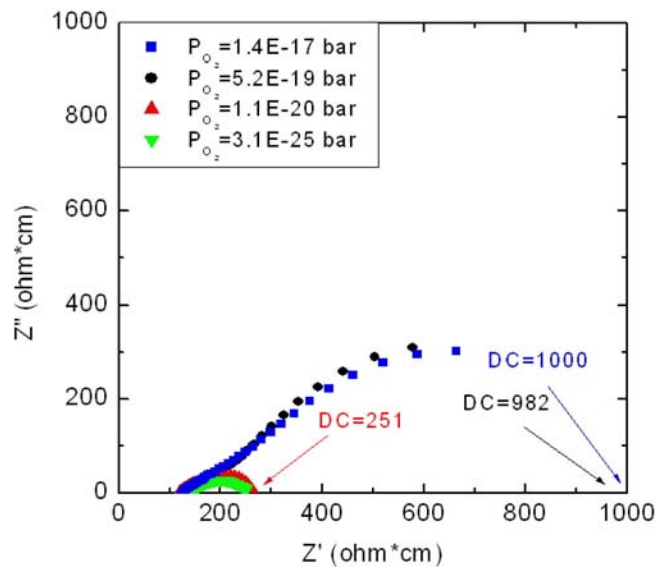


Figure 7.15. Nyquist plots of $\text{La}_{0.56}\text{Sr}_{0.44}\text{Ga}_{0.64}\text{Mg}_{0.16}\text{Ti}_{0.2}\text{O}_{2.8}$ in low oxygen partial pressures at 700°C .

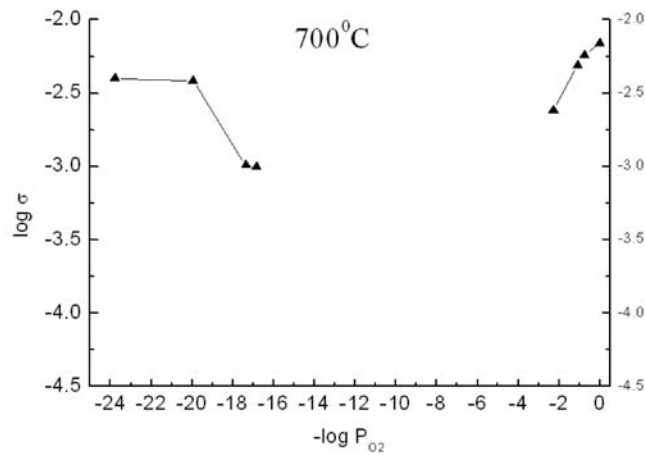


Figure 7.16. DC conductivity of $\text{La}_{0.56}\text{Sr}_{0.44}\text{Ga}_{0.64}\text{Mg}_{0.16}\text{Ti}_{0.2}\text{O}_{2.8}$ vs. P_{O_2} at 700°C .

7.2.2.2 $\text{La}_{0.56}\text{Sr}_{0.44}\text{Ga}_{0.64}\text{Mg}_{0.16}\text{Sn}_{0.2}\text{O}_{2.8}$

$\text{La}_{0.56}\text{Sr}_{0.44}\text{Ga}_{0.64}\text{Mg}_{0.16}\text{Sn}_{0.2}\text{O}_{3-\delta}$ was analyzed in the same way as described in the previous section. Figure 7.17 shows the impedance plots of $\text{La}_{0.56}\text{Sr}_{0.44}\text{Ga}_{0.64}\text{Mg}_{0.16}\text{Sn}_{0.2}\text{O}_{3-\delta}$ measured in air and low oxygen partial pressure at 400°C . The total conductivities measured in these two gases are close to each other. Conductivity of $\text{La}_{0.56}\text{Sr}_{0.44}\text{Ga}_{0.64}\text{Mg}_{0.16}\text{Sn}_{0.2}\text{O}_{3-\delta}$ is also close to that of $\text{La}_{0.56}\text{Sr}_{0.44}\text{Ga}_{0.64}\text{Mg}_{0.16}\text{Ti}_{0.2}\text{O}_{3-\delta}$. One remarkable difference between the two compositions is that the grain boundary resistance of Sn doped sample is much smaller than the bulk resistance. The Arrhenius plots of bulk and total conductivities for the two gases are shown in figure 7.18 and 7.19, respectively.

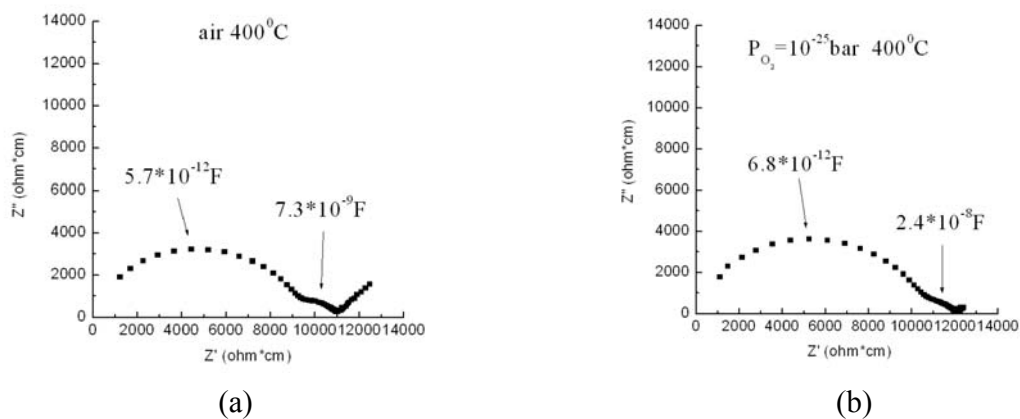


Figure 7.17. Nyquist plots of $\text{La}_{0.56}\text{Sr}_{0.44}\text{Ga}_{0.64}\text{Mg}_{0.16}\text{Sn}_{0.2}\text{O}_{3-\delta}$ in (a) air and (b) $P_{\text{O}_2}=10^{-25}\text{bar}$ at 400°C .

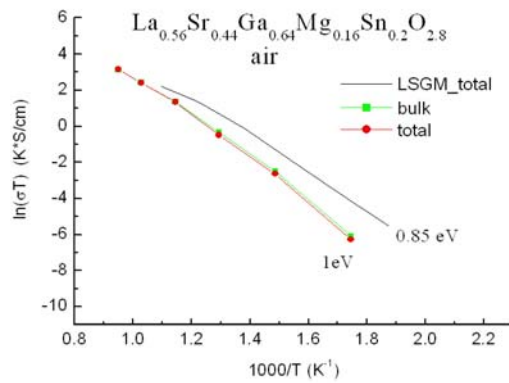


Figure 7.18. Arrhenius plots of the bulk and total conductivities for $\text{La}_{0.56}\text{Sr}_{0.44}\text{Ga}_{0.64}\text{Mg}_{0.16}\text{Sn}_{0.2}\text{O}_{3-\delta}$ in air.

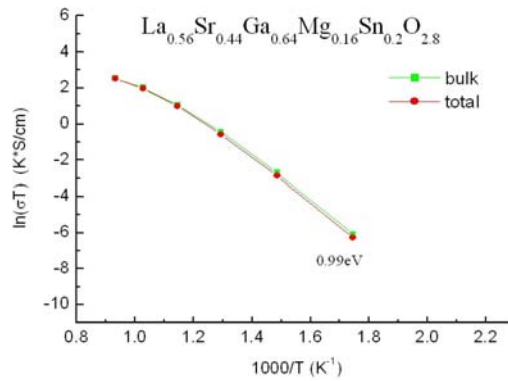


Figure 7.19. Arrhenius plots of the bulk and total conductivities for $\text{La}_{0.56}\text{Sr}_{0.44}\text{Ga}_{0.64}\text{Mg}_{0.16}\text{Sn}_{0.2}\text{O}_{3-\delta}$ in reducing condition ($P_{\text{O}_2} = 10^{-25} \text{ bar}$).

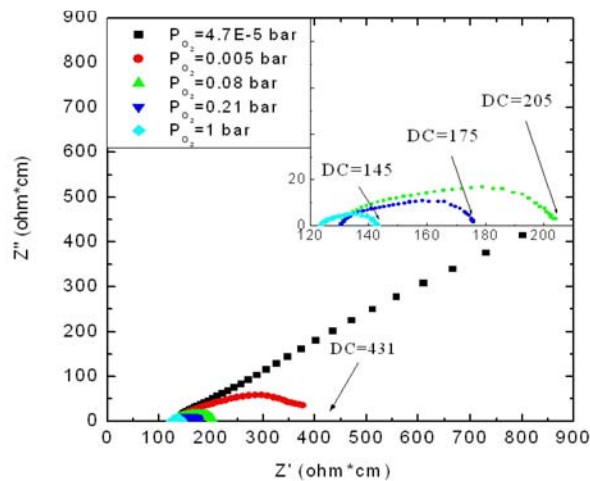


Figure 7.20. Nyquist plots of $\text{La}_{0.56}\text{Sr}_{0.44}\text{Ga}_{0.64}\text{Mg}_{0.16}\text{Sn}_{0.2}\text{O}_{3-\delta}$ in high oxygen partial pressures at 700°C .

Figure 7.20 and 7.21 show the Nyquist plots in high and low oxygen partial pressures at 700°C , respectively. DC conductivity was plotted in figure 7.22 against the oxygen partial pressure. All the conducting properties of $\text{La}_{0.56}\text{Sr}_{0.44}\text{Ga}_{0.64}\text{Mg}_{0.16}\text{Sn}_{0.2}\text{O}_{3-\delta}$ are similar to those of the Ti containing sample.

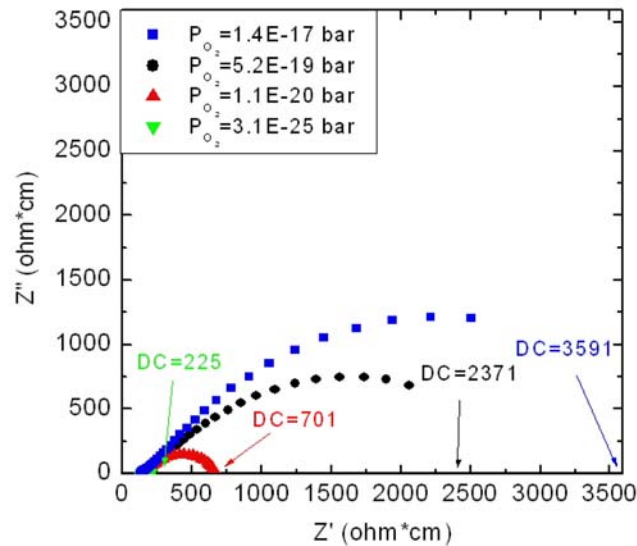


Figure 7.21. Nyquist plots of $\text{La}_{0.56}\text{Sr}_{0.44}\text{Ga}_{0.64}\text{Mg}_{0.16}\text{Sn}_{0.2}\text{O}_{3-\delta}$ in low oxygen partial pressures at 700°C .

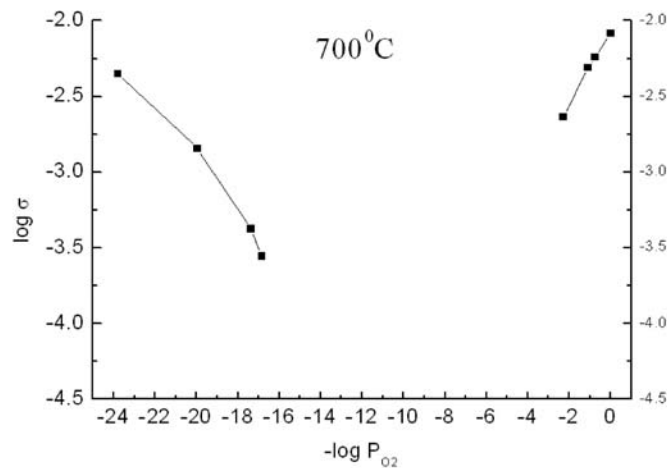
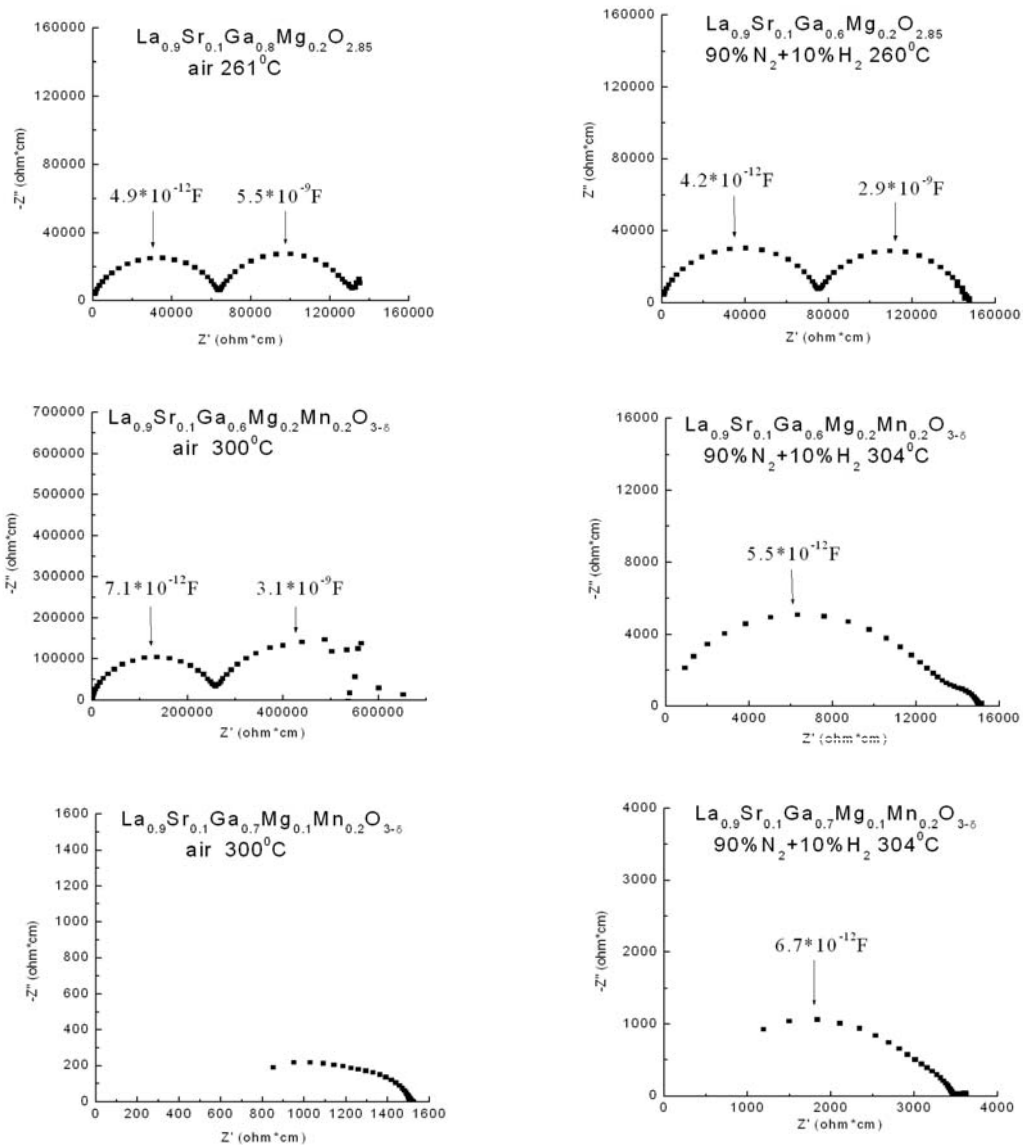


Figure 7.22. DC conductivity of $\text{La}_{0.56}\text{Sr}_{0.44}\text{Ga}_{0.64}\text{Mg}_{0.16}\text{Sn}_{0.2}\text{O}_{3-\delta}$ vs. P_{O_2} at 700°C .

7.2.3 $\text{La}_{0.9}\text{Sr}_{0.1}\text{Ga}_{1-x-y}\text{Mg}_y\text{Mn}_x\text{O}_{3-\delta}$ ($x, y=0\sim 0.2$)7.2.3.1 $\text{La}_{0.9}\text{Sr}_{0.1}\text{Ga}_{0.8-y}\text{Mg}_y\text{Mn}_{0.2}\text{O}_{3-\delta}$ ($y=0\sim 0.2$)

7.2.3.1a. AC impedance

20 mol% Mn was first doped into $\text{La}_{0.9}\text{Sr}_{0.1}\text{Ga}_{0.8}\text{Mg}_{0.2}\text{O}_{2.85}$ in the following three compositions: $\text{La}_{0.9}\text{Sr}_{0.1}\text{Ga}_{0.6}\text{Mg}_{0.2}\text{Mn}_{0.2}\text{O}_{3-\delta}$, $\text{La}_{0.9}\text{Sr}_{0.1}\text{Ga}_{0.7}\text{Mg}_{0.1}\text{Mn}_{0.2}\text{O}_{3-\delta}$, and $\text{La}_{0.9}\text{Sr}_{0.1}\text{Ga}_{0.8}\text{Mn}_{0.2}\text{O}_{3-\delta}$. The impedance spectra of $\text{La}_{0.9}\text{Sr}_{0.1}\text{Ga}_{0.8-y}\text{Mg}_y\text{Mn}_{0.2}\text{O}_{3-\delta}$ at around 300°C in air (left) and forming gas ($90\%\text{N}_2+10\%\text{H}_2$) (right) are shown below in Figure 7.23.



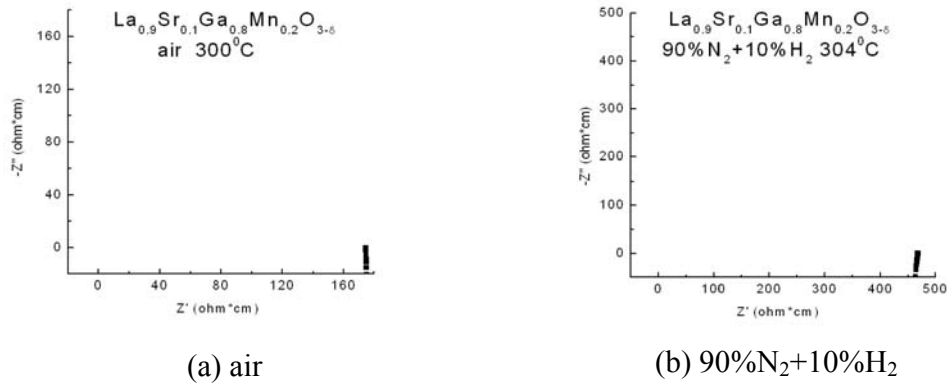


Figure 7.23. Impedance spectra of $\text{La}_{0.9}\text{Sr}_{0.1}\text{Ga}_{0.8-y}\text{Mg}_y\text{Mn}_{0.2}\text{O}_{3-\delta}$ ($y=0\sim 0.2$) at around 300°C in (a) air and (b) forming gas (90% N_2 +10% H_2)

Two semicircles that correspond to bulk and grain boundary conduction, can be easily resolved from the spectra for $\text{La}_{0.9}\text{Sr}_{0.1}\text{Ga}_{0.8}\text{Mg}_{0.2}\text{O}_{2.85}$ at this temperature. The arc after the second semicircle, which is due to the diffusion process through the Pt electrode [11] in air and the blocking behavior in forming gas, can be clearly seen at higher temperatures. No obvious deviation can be found between the spectra measured in air and forming gas, proving a constant ionic conductivity of LSGM through a wide range of oxygen partial pressure. A comparison of the conductivity of LSGM between this work and some other results are given in figure 7.24. The total conductivity from this work agrees well with other authors' result below 500°C . The relative large deviation at high temperature is mostly due to the experimental limitations of low sample resistance compared to all leads at high temperatures. If not specially stated, the self-made LSGM is used for comparison with Mn doped samples in the following chapters.

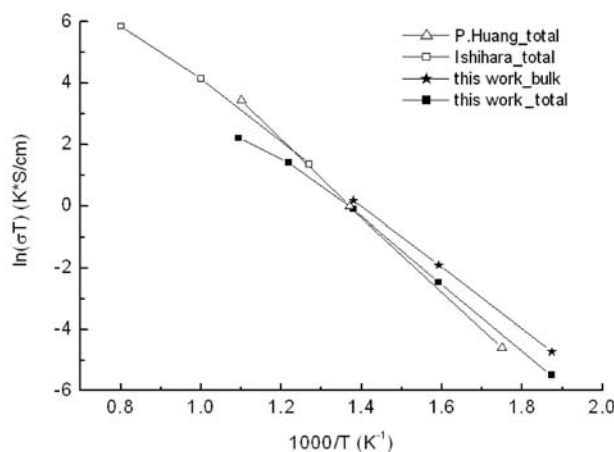


Figure 7.24. Arrhenius plot of the bulk and total conductivity of LSGM in air. The literature data are taken from reference [5,12].

The electrical properties of $\text{La}_{0.9}\text{Sr}_{0.1}\text{Ga}_{0.8-y}\text{Mg}_y\text{Mn}_{0.2}\text{O}_{3-\delta}$ ($y=0\sim 0.2$) differ from each other despite of the same amount of Mn doping. With increasing amount of Ga and decreasing of the same amount of Mg, $\text{La}_{0.9}\text{Sr}_{0.1}\text{Ga}_{0.8-y}\text{Mg}_y\text{Mn}_{0.2}\text{O}_{3-\delta}$ become more and more electronic conductive in both atmospheres.

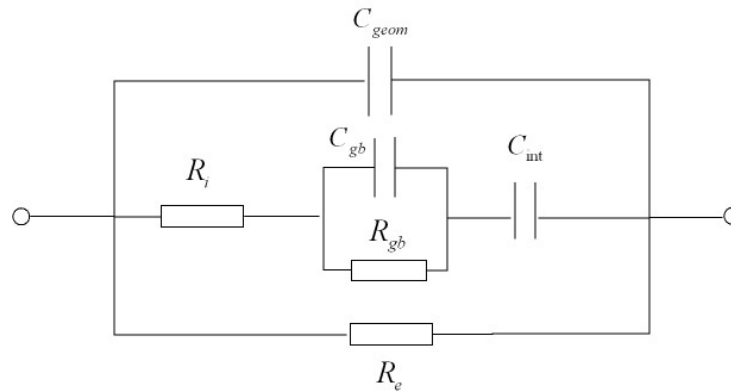


Figure 7.25. Schematic equivalent circuit for an electrochemical cell with a mixed ionic and electronic conductor between two ionically-blocking, but electronically-conducting, electrodes.

$\text{La}_{0.9}\text{Sr}_{0.1}\text{Ga}_{0.6}\text{Mg}_{0.2}\text{Mn}_{0.2}\text{O}_{3-\delta}$ has two distinguishable semicircles. Compared to LSGM, its total conductivity is lower in air, but higher in forming gas. Successive impedance spectra and magnification of the low frequency part reveal that there are indeed three semicircles for $\text{La}_{0.9}\text{Sr}_{0.1}\text{Ga}_{0.6}\text{Mg}_{0.2}\text{Mn}_{0.2}\text{O}_{3-\delta}$ in forming gas. The increased conductivity and the last two depressed semicircles can be explained by increased electronic conductivity under reducing conditions. When there is considerable electronic conduction throughout the sample, which can be schematically represented by a resistor in parallel with the ionic path in the equivalent circuit (figure 7. 25), the interpretation of the impedance plot is changing as well.

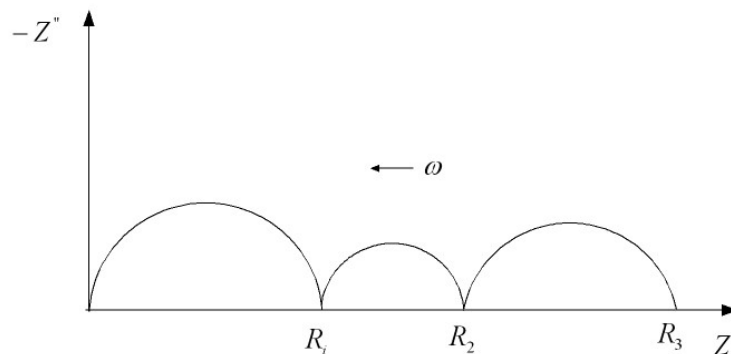


Figure 7.26. Complex plane plot for the case of a mixed conductor between two ionically-blocking, but electronically-conducting, electrodes.

If there are three semicircles representing bulk, grain boundary and electronic conduction (figure 7.26), then the three intersections with the real axis ($R_1 < R_2 < R_3$) will have the following meanings according to Huggins' calculation [13]:

$$R_1 = \frac{R_e R_b}{R_e + R_b} \quad (7.4)$$

$$R_2 = \frac{R_e (R_b + R_{gb})}{R_e + R_b + R_{gb}} \quad (7.5)$$

$$R_3 = R_e \quad (7.6)$$

where R_e , R_b and R_{gb} are the resistances to electronic, bulk and grain boundary conduction, respectively. When R_e is small, which means a relative large electronic conductivity, R_1 , R_2 and R_3 are all approaching to R_e . From Eqs. (7.4~7.6), R_e , R_b and R_{gb} can be calculated as:

$$R_e = R_3 \quad (7.7)$$

$$R_b = \frac{R_3 R_1}{R_3 - R_1} \quad (7.8)$$

$$R_{gb} = \frac{R_3 R_2}{R_3 - R_2} - \frac{R_3 R_1}{R_3 - R_1} \quad (7.9)$$

In the spectrum of $\text{La}_{0.9}\text{Sr}_{0.1}\text{Ga}_{0.6}\text{Mg}_{0.2}\text{Mn}_{0.2}\text{O}_{3-\delta}$ in forming gas at 304°C , $R_1 \approx 14000\Omega \cdot \text{cm}$, $R_2 \approx R_3 \approx 15000\Omega \cdot \text{cm}$, thus using Eq. (7.8):

$$R_b = \frac{R_3 R_1}{R_3 - R_1} \approx 210000\Omega \cdot \text{cm},$$

which agrees well with $R_1 \approx 250000\Omega \cdot \text{cm}$ in air at 300°C . The higher bulk conductivity in forming gas is due to the reduction of Mn. This also suggests that ionic conduction is predominant for $\text{La}_{0.9}\text{Sr}_{0.1}\text{Ga}_{0.6}\text{Mg}_{0.2}\text{Mn}_{0.2}\text{O}_{3-\delta}$ in air.

$\text{La}_{0.9}\text{Sr}_{0.1}\text{Ga}_{0.7}\text{Mg}_{0.1}\text{Mn}_{0.2}\text{O}_{3-\delta}$ shows incomplete arc with lower resistance than LSGM in both air and forming gas at 300°C . At temperatures higher than 400°C , $\text{La}_{0.9}\text{Sr}_{0.1}\text{Ga}_{0.7}\text{Mg}_{0.1}\text{Mn}_{0.2}\text{O}_{3-\delta}$ exhibits metallic behavior in all atmospheres.

$\text{La}_{0.9}\text{Sr}_{0.1}\text{Ga}_{0.8}\text{Mn}_{0.2}\text{O}_{3-\delta}$ shows only dots in all impedance spectra at 300°C . It's a p-type conductor in air. Figure 7.27 and 7.28 show the Arrhenius plot for the total conductivity of $\text{La}_{0.9}\text{Sr}_{0.1}\text{Ga}_{0.8-y}\text{Mg}_y\text{Mn}_{0.2}\text{O}_{3-\delta}$ ($y=0\sim 0.2$) in air and forming gas, respectively.

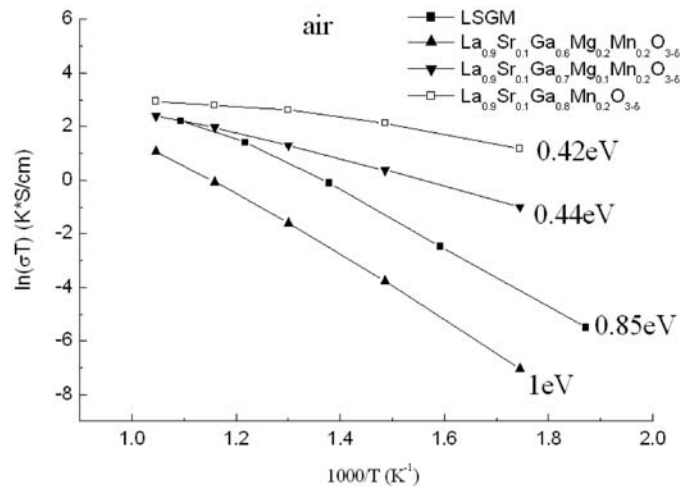


Figure 7.27 Arrhenius plot of the total conductivity of $\text{La}_{0.9}\text{Sr}_{0.1}\text{Ga}_{0.8-y}\text{Mg}_y\text{Mn}_{0.2}\text{O}_{3-\delta}$ ($y=0\sim 0.2$) in air.

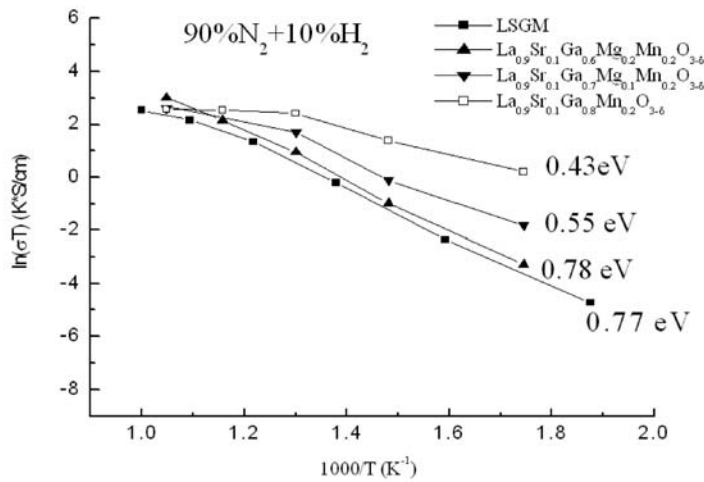


Figure 7.28. Arrhenius plot of the total conductivity of $\text{La}_{0.9}\text{Sr}_{0.1}\text{Ga}_{0.8-y}\text{Mg}_y\text{Mn}_{0.2}\text{O}_{3-\delta}$ ($y=0\sim 0.2$) in $90\%\text{N}_2+10\%\text{H}_2$.

As shown in figure 7.27 and 7.28, $\text{La}_{0.9}\text{Sr}_{0.1}\text{Ga}_{0.7}\text{Mg}_{0.1}\text{Mn}_{0.2}\text{O}_{3-\delta}$ and $\text{La}_{0.9}\text{Sr}_{0.1}\text{Ga}_{0.8}\text{Mn}_{0.2}\text{O}_{3-\delta}$ have higher conductivity and lower activation energy than LSGM. While keeping the same amount of Mn, the activation energy decreases with increasing Ga content. The major difference between the two plots is the sharp change of $\text{La}_{0.9}\text{Sr}_{0.1}\text{Ga}_{0.6}\text{Mg}_{0.2}\text{Mn}_{0.2}\text{O}_{3-\delta}$ due to the n-type

conduction, as what we have discussed before. In order to further prove the existence of n-type electronic conductivity in $\text{La}_{0.9}\text{Sr}_{0.1}\text{Ga}_{0.6}\text{Mg}_{0.2}\text{Mn}_{0.2}\text{O}_{3-\delta}$ and to identify the conduction of $\text{La}_{0.9}\text{Sr}_{0.1}\text{Ga}_{0.7}\text{Mg}_{0.1}\text{Mn}_{0.2}\text{O}_{3-\delta}$ and $\text{La}_{0.9}\text{Sr}_{0.1}\text{Ga}_{0.8}\text{Mn}_{0.2}\text{O}_{3-\delta}$ at low oxygen partial pressures, dependence measurement of total conductivity on the oxygen partial pressure and Kiukkola-Wagner measurements were performed.

7.2.3.1b. Brouwer diagram of total conductivity

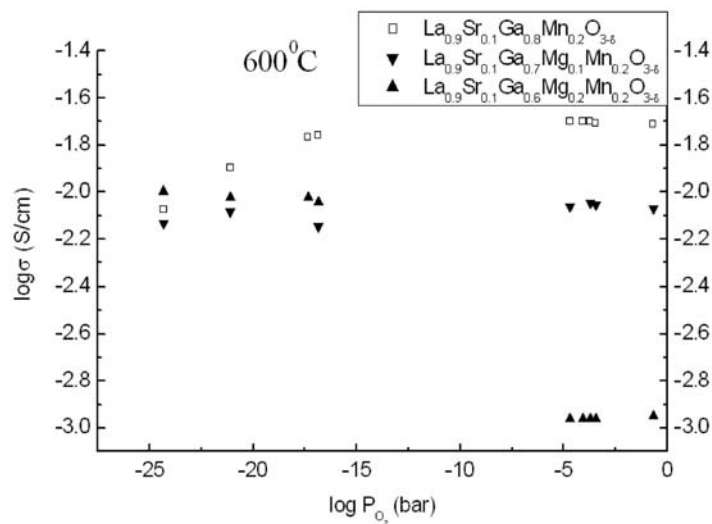


Figure 7.29. The total conductivity of $\text{La}_{0.9}\text{Sr}_{0.1}\text{Ga}_{0.8-y}\text{Mg}_y\text{Mn}_{0.2}\text{O}_{3-\delta}$ ($y=0\sim 0.2$) vs. P_{O_2} at 600°C .

Figure 7.29 shows the Brouwer diagram of total conductivity of $\text{La}_{0.9}\text{Sr}_{0.1}\text{Ga}_{0.8-y}\text{Mg}_y\text{Mn}_{0.2}\text{O}_{3-\delta}$ ($y=0\sim 0.2$) at 600°C . At high oxygen partial pressures, all three compositions keep nearly constant conductivities. Although $\text{La}_{0.9}\text{Sr}_{0.1}\text{Ga}_{0.7}\text{Mg}_{0.1}\text{Mn}_{0.2}\text{O}_{3-\delta}$ has a small scattering at low P_{O_2} , the conductivity is close to the values at high P_{O_2} . $\text{La}_{0.9}\text{Sr}_{0.1}\text{Ga}_{0.8}\text{Mn}_{0.2}\text{O}_{3-\delta}$ starts to decrease the conductivity below $P_{\text{O}_2} \approx 10^{-16} \text{ bar}$. Only $\text{La}_{0.9}\text{Sr}_{0.1}\text{Ga}_{0.6}\text{Mg}_{0.2}\text{Mn}_{0.2}\text{O}_{3-\delta}$ has a higher conductivity at low P_{O_2} .

7.2.3.1c. Kiukkola-Wagner measurements

Figure 2.28 tells us the equilibrium oxygen partial pressures from Ni/NiO and Fe/FeO electrodes are 10^{-19} bar and 10^{-25} bar at 600°C , respectively, which is suitable to check the conduction mechanism for the present samples.

For the pure ionic conductor LSGM, the result agrees well with the theoretical calculation between 600°C and 800°C, as shown in figure 7.30.

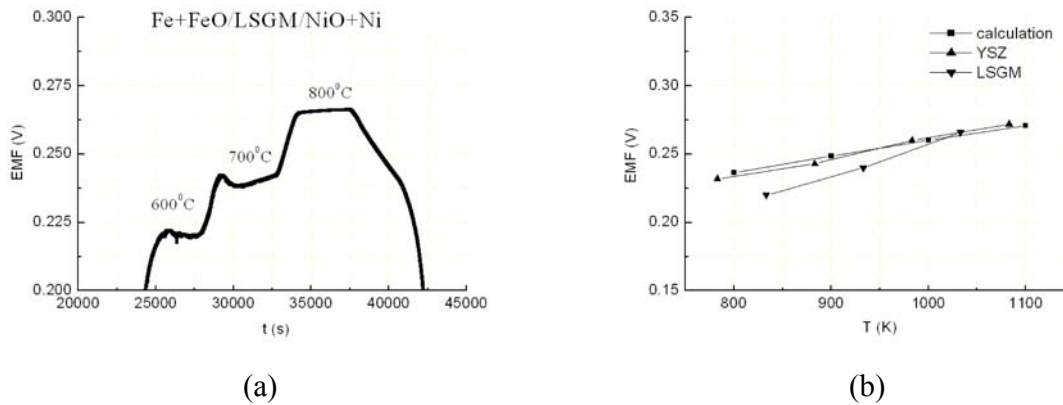


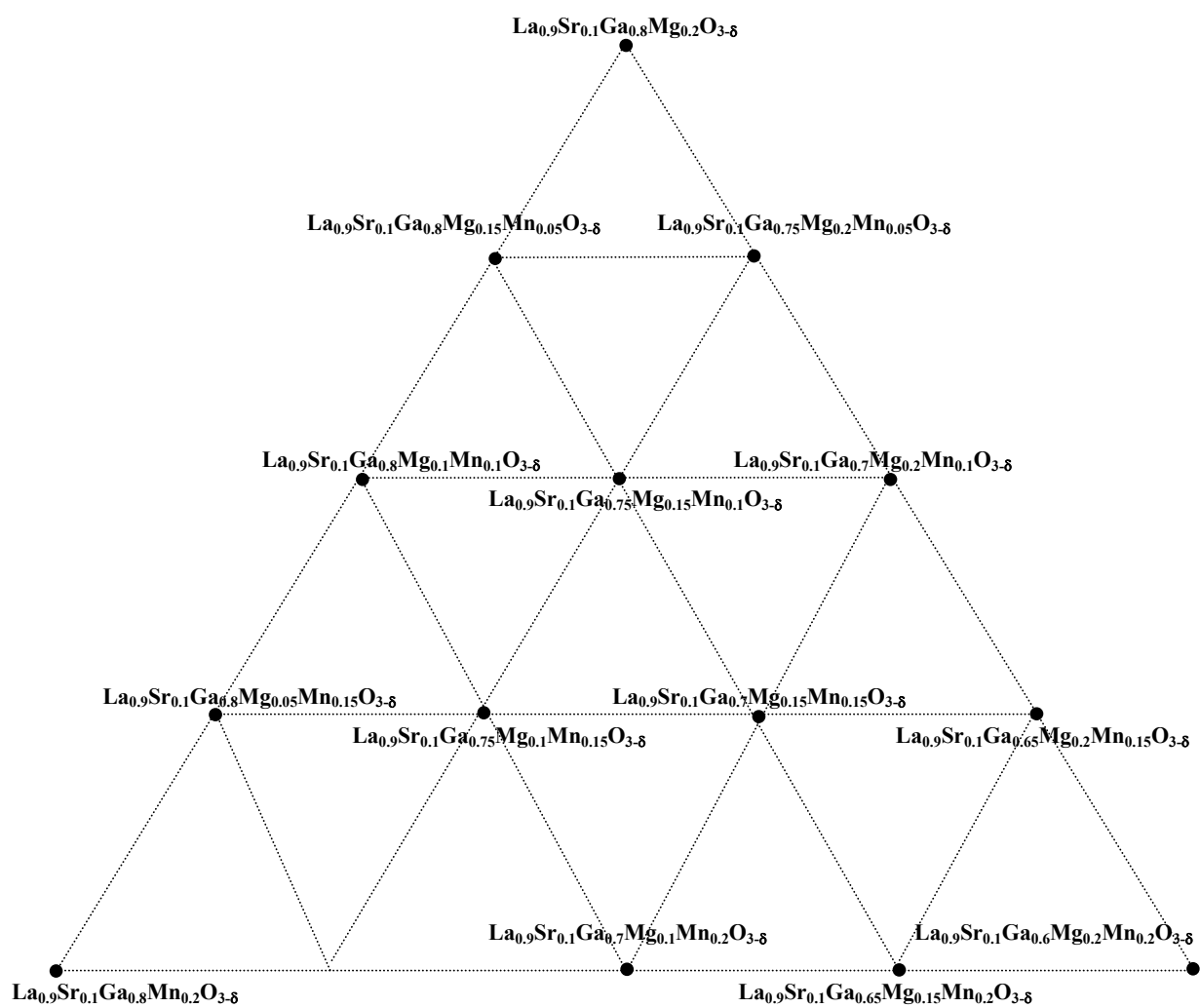
Figure 7.30. Plots of (a) EMF vs. time and (b) EMF vs. temperature for the cell Fe+FeO / LSGM / Ni+NiO.

Kiukkola-Wagner measurements of the other three samples didn't show any voltage at 600°C, indicating that they are all predominantly electronic conducting under the given experimental conditions.

So far we can draw the following conclusions for the three compositions at the working temperature, based on the combined results of impedance spectroscopy, Brouwer diagram and Kiukkola-Wagner measurements:

- i. $\text{La}_{0.9}\text{Sr}_{0.1}\text{Ga}_{0.6}\text{Mg}_{0.2}\text{Mn}_{0.2}\text{O}_{3-\delta}$ is an predominantly ionic conductor at high oxygen partial pressure, and a n-type electronic conductor at low oxygen partial pressure;
- ii. $\text{La}_{0.9}\text{Sr}_{0.1}\text{Ga}_{0.7}\text{Mg}_{0.1}\text{Mn}_{0.2}\text{O}_{3-\delta}$ and $\text{La}_{0.9}\text{Sr}_{0.1}\text{Ga}_{0.8}\text{Mn}_{0.2}\text{O}_{3-\delta}$ are p-type electronic conductors in all the range of oxygen partial pressures under discussion;
- iii. The usual $\pm 1/4$ dependences of the electronic conductivity on oxygen partial pressure were not seen in Brouwer diagram. In stead, the electronic conductivities are fairly stable in the certain pressure range. This is because the amount of electronic charge carriers are determined in this case by the doping level, which is not dependent on the oxygen activities, as what was discussed in chapter 2.2.4.

LSGM is the well-known ionic conductor. 20-mol% Mn doped LSGM show different electrical properties, depending on the relative amount of Ga and Mg. Both n and p-type electronic conductivities can be dominate in various compositions. Mn plays a very important role in modifying or controlling the conducting behaviour of LaGaO_3 based materials. If we now draw a triangle with the composition of $\text{La}_{0.9}\text{Sr}_{0.1}\text{Ga}_{0.8}\text{Mg}_{0.2}\text{O}_{2.85}$, $\text{La}_{0.9}\text{Sr}_{0.1}\text{Ga}_{0.8}\text{Mn}_{0.2}\text{O}_{3-\delta}$ and

Figure 7.32. Compositional triangle of $\text{La}_{0.9}\text{Sr}_{0.1}\text{Ga}_{1-x-y}\text{Mg}_y\text{Mn}_x\text{O}_{3-\delta}$ ($x, y=0\sim 0.2$)

7.2.3.2 $\text{La}_{0.9}\text{Sr}_{0.1}\text{Ga}_{1-x-y}\text{Mg}_y\text{Mn}_x\text{O}_{3-\delta}$ ($x, y=0\sim 0.2$)

In this chapter we will group the compositions according to the Mn content.

7.2.3.2a. $\text{La}_{0.9}\text{Sr}_{0.1}\text{Ga}_{0.95-y}\text{Mg}_y\text{Mn}_{0.05}\text{O}_{3-\delta}$ ($y=0.15, 0.2$)

Impedance measurements and Brouwer diagram reveal that there is only negligible effect on the electrical property of LSGM by incorporating 5-mol% Mn. Figure 7.33 show the impedance of $\text{La}_{0.9}\text{Sr}_{0.1}\text{Ga}_{0.8}\text{Mg}_{0.15}\text{Mn}_{0.05}\text{O}_{3-\delta}$ and $\text{La}_{0.9}\text{Sr}_{0.1}\text{Ga}_{0.75}\text{Mg}_{0.2}\text{Mn}_{0.05}\text{O}_{3-\delta}$ in air at 305°C . The Arrhenius plots for the total conductivities are shown in figure 7.34.

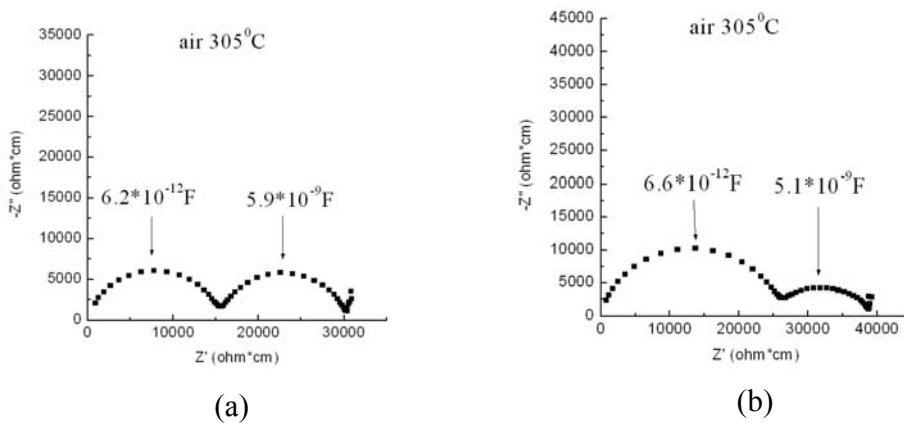


Figure 7.33. Nyquist plots of (a) $\text{La}_{0.9}\text{Sr}_{0.1}\text{Ga}_{0.8}\text{Mg}_{0.15}\text{Mn}_{0.05}\text{O}_{3-\delta}$ and (b) $\text{La}_{0.9}\text{Sr}_{0.1}\text{Ga}_{0.75}\text{Mg}_{0.2}\text{Mn}_{0.05}\text{O}_{3-\delta}$ in air at 305°C .

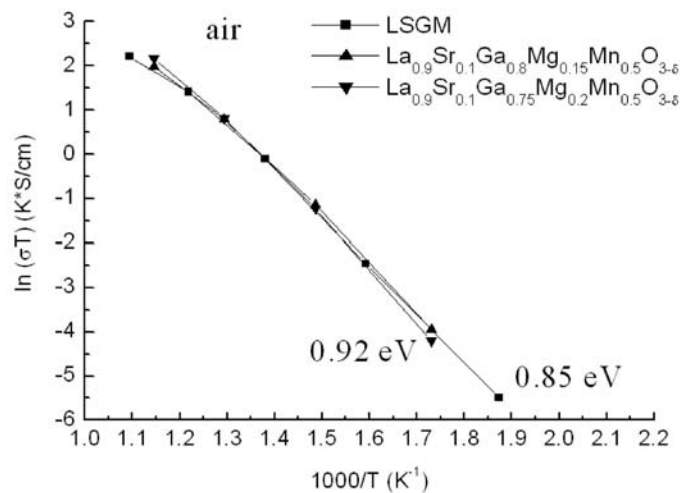


Figure 7.34. Arrhenius plots of the total conductivity of $\text{La}_{0.9}\text{Sr}_{0.1}\text{Ga}_{0.8}\text{Mg}_{0.15}\text{Mn}_{0.05}\text{O}_{3-\delta}$ and $\text{La}_{0.9}\text{Sr}_{0.1}\text{Ga}_{0.75}\text{Mg}_{0.2}\text{Mn}_{0.05}\text{O}_{3-\delta}$ in air.

Table 7.4 Activation energies of bulk and total conductivities in air.

Compositions	$E_{A,\text{bulk}}$ (eV)	$E_{A,\text{total}}$ (eV)
LSGM	0.86	0.85
$\text{La}_{0.9}\text{Sr}_{0.1}\text{Ga}_{0.8}\text{Mg}_{0.15}\text{Mn}_{0.05}\text{O}_{3-\delta}$	0.91	0.88
$\text{La}_{0.9}\text{Sr}_{0.1}\text{Ga}_{0.75}\text{Mg}_{0.2}\text{Mn}_{0.05}\text{O}_{3-\delta}$	0.97	0.94

The total conductivities of all three samples are close to each other, except a small increase at high temperature for Mn containing samples. This result is similar to that reported by Ishihara [1,3], who found that the conductivity of LSGM could be slightly increased by small amounts of doping of Fe or Co. Table 7.4 lists the activation energies of bulk and total conductivities for LSGM, $\text{La}_{0.9}\text{Sr}_{0.1}\text{Ga}_{0.8}\text{Mg}_{0.15}\text{Mn}_{0.05}\text{O}_{3-\delta}$ and $\text{La}_{0.9}\text{Sr}_{0.1}\text{Ga}_{0.75}\text{Mg}_{0.2}\text{Mn}_{0.05}\text{O}_{3-\delta}$ in air. Although $\text{La}_{0.9}\text{Sr}_{0.1}\text{Ga}_{0.75}\text{Mg}_{0.2}\text{Mn}_{0.05}\text{O}_{3-\delta}$ has the highest activation energy, its conductivity is higher than $\text{La}_{0.9}\text{Sr}_{0.1}\text{Ga}_{0.8}\text{Mg}_{0.15}\text{Mn}_{0.05}\text{O}_{3-\delta}$ at high temperatures. Mn is known as a mixed valence cation and the trivalent one is predominant in perovskite in air. Assuming the valence states (or contribution to the oxygen vacancies) of Mn are the same in both $\text{La}_{0.9}\text{Sr}_{0.1}\text{Ga}_{0.8}\text{Mg}_{0.15}\text{Mn}_{0.05}\text{O}_{3-\delta}$ and $\text{La}_{0.9}\text{Sr}_{0.1}\text{Ga}_{0.75}\text{Mg}_{0.2}\text{Mn}_{0.05}\text{O}_{3-\delta}$, then the number of oxygen vacancies only varies with the content of the lower valent cation Mg^{2+} .

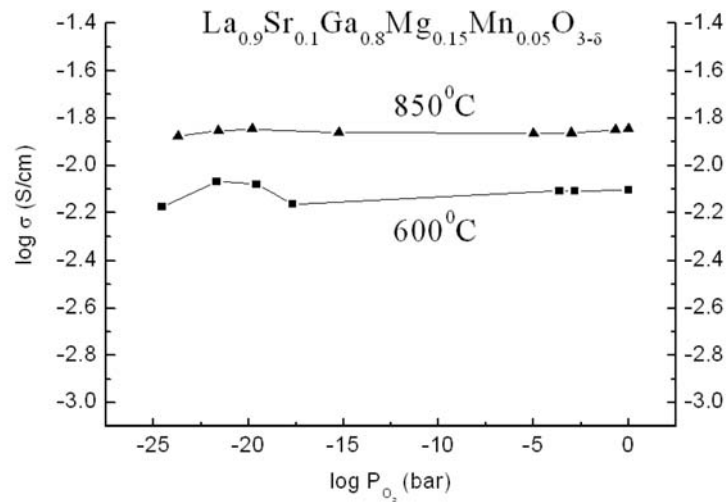


Figure 7.35. Brouwer diagram of the total conductivity for $\text{La}_{0.9}\text{Sr}_{0.1}\text{Ga}_{0.8}\text{Mg}_{0.15}\text{Mn}_{0.05}\text{O}_{3-\delta}$ at 600°C and 850°C .

Figure 7.35 and 7.36 show the Brouwer diagrams of the total conductivity at 600°C and 850°C for $\text{La}_{0.9}\text{Sr}_{0.1}\text{Ga}_{0.8}\text{Mg}_{0.15}\text{Mn}_{0.05}\text{O}_{3-\delta}$ and $\text{La}_{0.9}\text{Sr}_{0.1}\text{Ga}_{0.75}\text{Mg}_{0.2}\text{Mn}_{0.05}\text{O}_{3-\delta}$, respectively. In both cases, the total conductivities are about the same in the experimental range of the oxygen partial pressures.

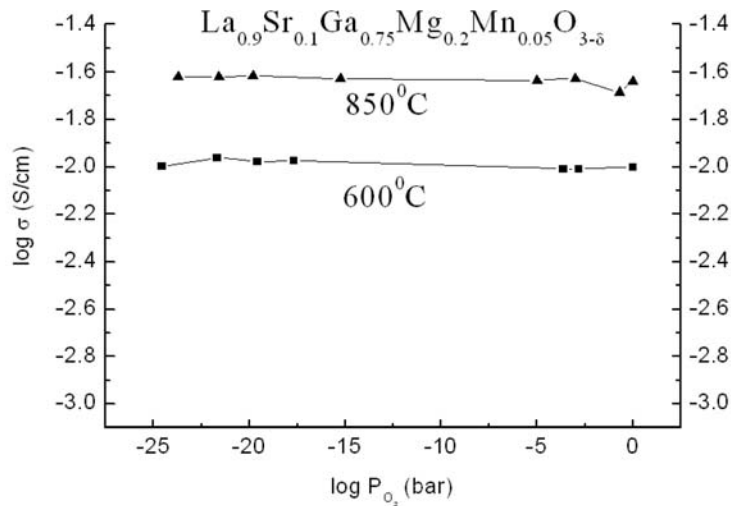
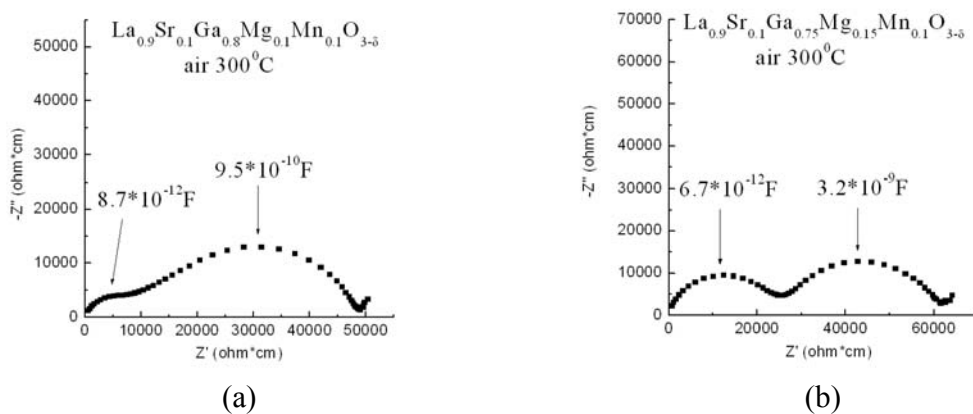


Figure 7.36. Brouwer diagram of the total conductivity for $\text{La}_{0.9}\text{Sr}_{0.1}\text{Ga}_{0.75}\text{Mg}_{0.2}\text{Mn}_{0.05}\text{O}_{3-\delta}$ at 600°C and 850°C .

7.2.3.2b. $\text{La}_{0.9}\text{Sr}_{0.1}\text{Ga}_{0.9-y}\text{Mg}_y\text{Mn}_{0.1}\text{O}_{3-\delta}$ ($y=0.1, 0.15, 0.2$)

Figure 7.37 shows the impedance plots of 10-mol% Mn doped samples in air at 300°C . Two semicircles can be seen at this temperature. All samples showed similar impedance plots as in the case of LSGM at higher temperatures.



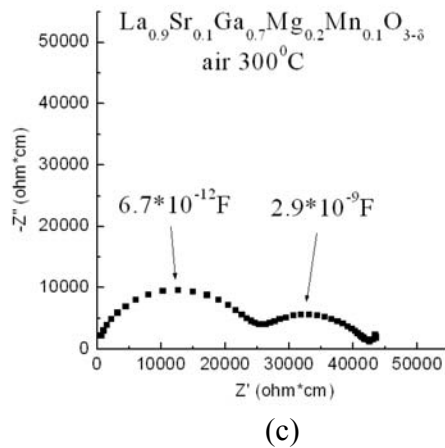


Figure 7.37. Nyquist plots of (a) $\text{La}_{0.9}\text{Sr}_{0.1}\text{Ga}_{0.8}\text{Mg}_{0.1}\text{Mn}_{0.1}\text{O}_{3-\delta}$ and (b) $\text{La}_{0.9}\text{Sr}_{0.1}\text{Ga}_{0.75}\text{Mg}_{0.15}\text{Mn}_{0.1}\text{O}_{3-\delta}$ and (c) $\text{La}_{0.9}\text{Sr}_{0.1}\text{Ga}_{0.7}\text{Mg}_{0.2}\text{Mn}_{0.1}\text{O}_{3-\delta}$ in air at 300°C .

Samples with 10-mol% Mn are still predominantly ionic conductors in air. Arrhenius plots (Figure 7.38) shows that their conductivities are of the same order of magnitude as LSGM. $\text{La}_{0.9}\text{Sr}_{0.1}\text{Ga}_{0.7}\text{Mg}_{0.2}\text{Mn}_{0.1}\text{O}_{3-\delta}$ has the highest conductivity among the Mn containing samples because of the highest amount of Mg. The activation energy for bulk and total conduction are listed in Table 7.5.

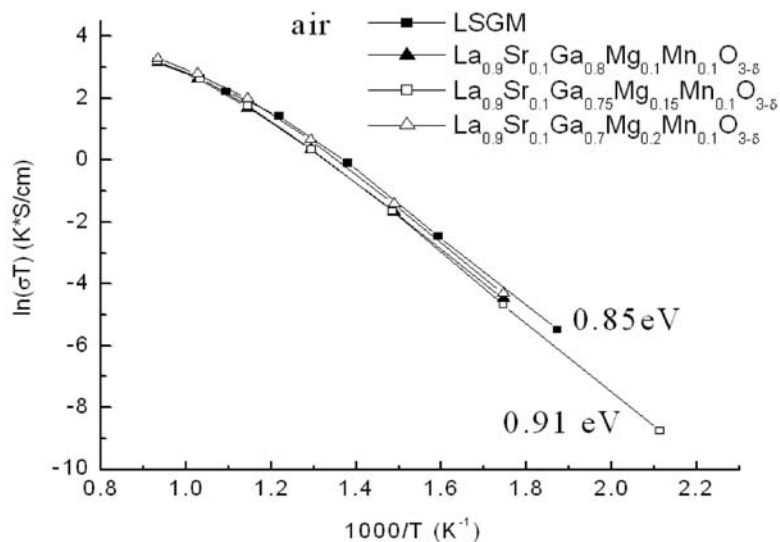
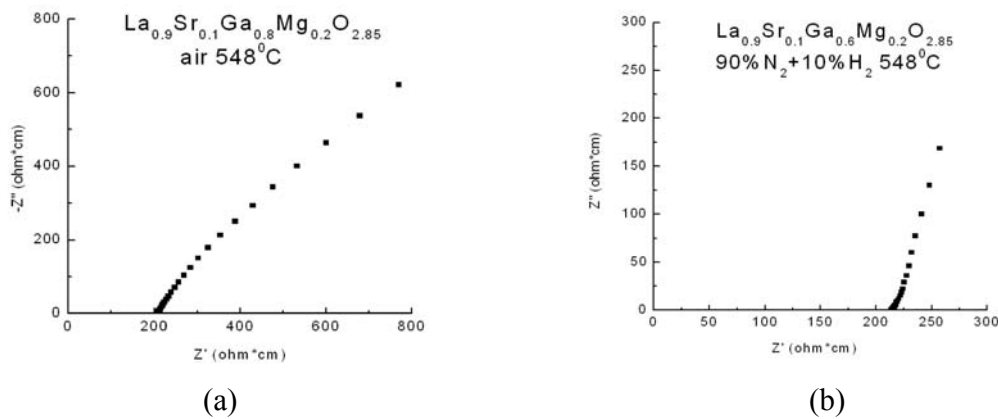


Figure 7.38. Arrhenius plots of the total conductivity of $\text{La}_{0.9}\text{Sr}_{0.1}\text{Ga}_{0.9-y}\text{Mg}_y\text{Mn}_{0.1}\text{O}_{3-\delta}$ ($y=0.1, 0.15, 0.2$) in air.

Table 7.5 Activation energies of bulk and total conductivities in air.

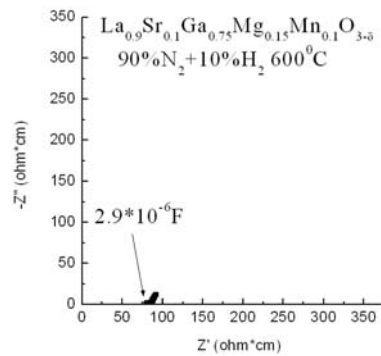
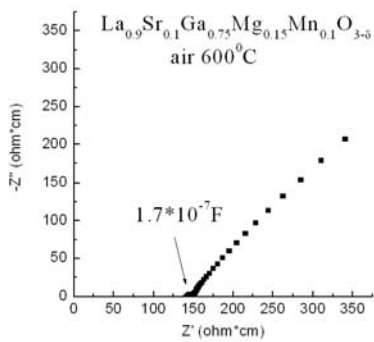
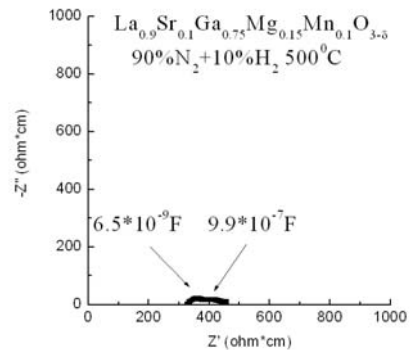
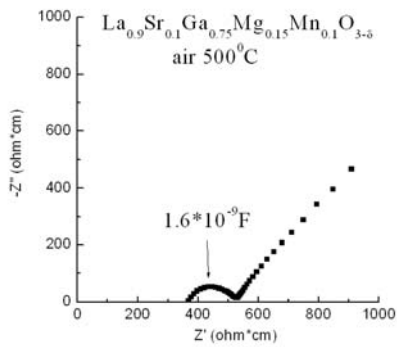
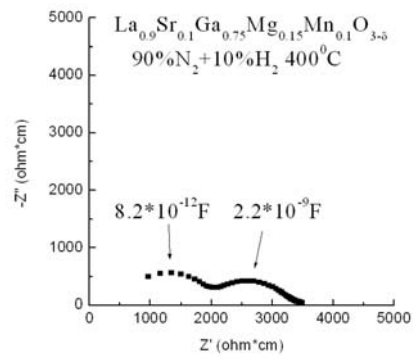
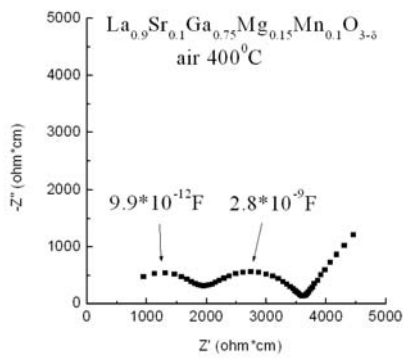
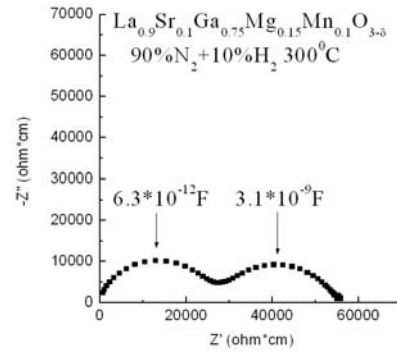
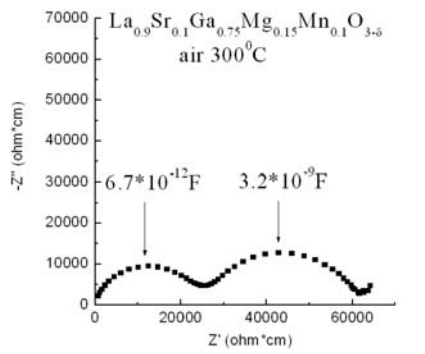
Compositions	$E_{A,\text{bulk}}$ (eV)	$E_{A,\text{total}}$ (eV)
LSGM	0.86	0.85
$\text{La}_{0.9}\text{Sr}_{0.1}\text{Ga}_{0.8}\text{Mg}_{0.1}\text{Mn}_{0.1}\text{O}_{3-\delta}$	0.81	0.85
$\text{La}_{0.9}\text{Sr}_{0.1}\text{Ga}_{0.75}\text{Mg}_{0.15}\text{Mn}_{0.1}\text{O}_{3-\delta}$	0.90	0.91
$\text{La}_{0.9}\text{Sr}_{0.1}\text{Ga}_{0.7}\text{Mg}_{0.2}\text{Mn}_{0.1}\text{O}_{3-\delta}$	0.87	0.90

The investigated samples show similar conducting behavior as LSGM in air, indicating that there is less effect on p-type conduction. To check the influence of Mn on n-type conduction, samples were measured in reducing atmospheres. Firstly, the impedance plots of LSGM in air and forming gas at 548⁰C are shown in figure 7.39 for comparison.

Figure 7.39. Nyquist plot of LSGM in (a) air and (b) forming gas at 548⁰C

In figure 7.39(a), a straight line with the slope of 45⁰ can be seen at low frequency. This line corresponds to the Warburg diffusion of oxygen through the Pt electrodes. Under reducing conditions, Pt works as a fully blocking electrode. Thus figure 7.39(b) shows the typical blocking behavior.

When a sufficient amount of Mn is added to LSGM, the electrical property will be modified due to the reduction of Mn^{3+} . Thangadurai et al [14] reported reduction of Mn in $\text{La}_{0.9}\text{Sr}_{0.1}\text{Ga}_{0.8}\text{Mn}_{0.2}\text{O}_{3-\delta}$ occurring at around 250⁰C and 500⁰C. The impedance measurement confirmed that the reduction of Mn started below 300⁰C, for the tails at low frequency shown in figure 7.37 vanished completely in forming gas. Figure 7.40 shows the impedance plots of $\text{La}_{0.9}\text{Sr}_{0.1}\text{Ga}_{0.75}\text{Mg}_{0.15}\text{Mn}_{0.1}\text{O}_{3-\delta}$ in air and forming gas from 300⁰C to 700⁰C. The other two samples are not shown here because they have exactly same tendency as $\text{La}_{0.9}\text{Sr}_{0.1}\text{Ga}_{0.75}\text{Mg}_{0.15}\text{Mn}_{0.1}\text{O}_{3-\delta}$.



(a)

(b)

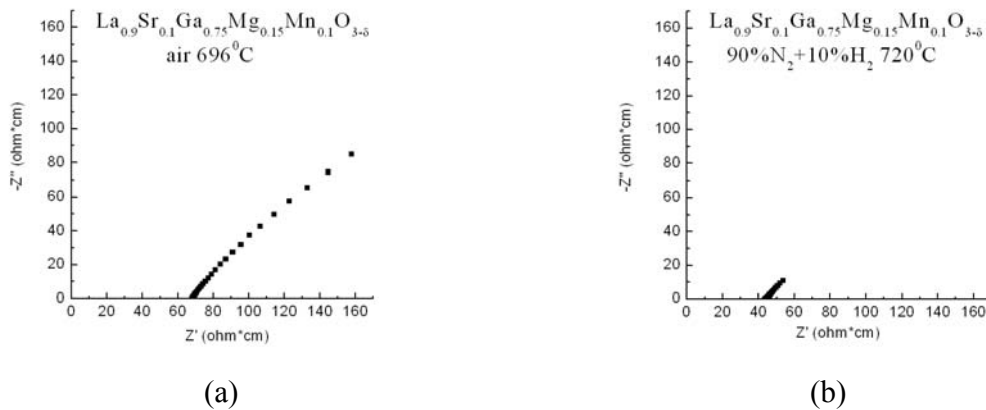


Figure 7.40. Nyquist plots of $\text{La}_{0.9}\text{Sr}_{0.1}\text{Ga}_{0.75}\text{Mg}_{0.15}\text{Mn}_{0.1}\text{O}_{3-\delta}$ in (a) air and (b) forming gas.

In figure 7.40(a), the Warburg contribution can be seen in air at all temperatures. Such kind of tails disappeared in forming gas (figure 7.40(b)). Below 500°C there is no tails at low frequency. As Mn started to be reduced at 250°C , diminishing of the tail could be attributed to the increasing of the electronic conductivity. Starting from 500°C , after the first three semicircles there is a small tail coming up, which became more and more obvious with increasing temperatures. Such changes of the low frequency behavior could be explained in the following way:

- i) n-type electronic conductivity increases due to the reduction of Mn. The increased electronic conductivity facilitates the charge transfer between the sample and the electrodes, so the semicircle that corresponds to the sample-electrode process is not visible below 500°C . Comparing the impedance plots between air and forming gas, it can be seen that there is no obvious difference for the first two semicircles, which should not be the case if there would have been electronic short-circuit throughout the sample. So it's likely that the concentration of electronic charge carriers is increased due to the presence of Mn, but the electronic conduction does not occur throughout the sample because of the low mobility of the electronic charge carriers;
- ii) When Mn^{3+} is reduced to Mn^{2+} , $\text{La}_{0.9}\text{Sr}_{0.1}\text{Ga}_{0.75}\text{Mg}_{0.15}\text{Mn}_{0.1}\text{O}_{3-\delta}$ should have a higher conductivity than that measured in air because of higher concentration of divalent cation after reduction;
- iii) The electronic conduction occurs via the hopping mechanism between Mn^{3+} and Mn^{2+} . With the reduction process of Mn^{3+} , the electronic conductivity will increase first and then decrease.

Table 7.6 Activation energies of bulk and total conductivities in forming gas.

Compositions	$E_{A,\text{bulk}}$ (eV)	$E_{A,\text{total}}$ (eV)
LSGM	0.88	0.91
$\text{La}_{0.9}\text{Sr}_{0.1}\text{Ga}_{0.8}\text{Mg}_{0.1}\text{Mn}_{0.1}\text{O}_{3-\delta}$	0.70	0.85
$\text{La}_{0.9}\text{Sr}_{0.1}\text{Ga}_{0.75}\text{Mg}_{0.15}\text{Mn}_{0.1}\text{O}_{3-\delta}$	0.90	0.99
$\text{La}_{0.9}\text{Sr}_{0.1}\text{Ga}_{0.7}\text{Mg}_{0.2}\text{Mn}_{0.1}\text{O}_{3-\delta}$	0.88	0.92

Figure 7.41 shows the Arrhenius plots for the total conductivity of the investigated materials in forming gas. The activation energies for bulk and total conduction are shown in Table 7.6. Arrhenius plots show that the total conductivities are close to each other. Only ionic conduction was observed in all the samples. At high temperatures higher than 500°C , Mn containing samples have slightly higher conductivity than LSGM due to the fully reduction of Mn^{3+} .

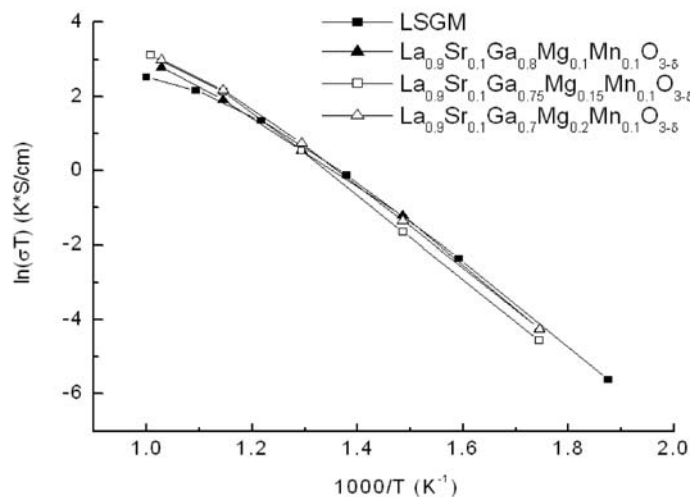


Figure 7.41. Arrhenius plots of the total conductivity of $\text{La}_{0.9}\text{Sr}_{0.1}\text{Ga}_{0.9-y}\text{Mg}_y\text{Mn}_{0.1}\text{O}_{3-\delta}$ ($y=0.1, 0.15, 0.2$) in forming gas.

The total conductivities of $\text{La}_{0.9}\text{Sr}_{0.1}\text{Ga}_{0.9-y}\text{Mg}_y\text{Mn}_{0.1}\text{O}_{3-\delta}$ ($y=0.1, 0.15, 0.2$) at 600°C are plotted in the Brouwer diagram (Figure 7.42). Similar to what has been discussed before, the conductivities measured at low oxygen partial pressures are higher than those measured at high oxygen partial pressures. In most of the pressure ranges, the conductivities of the samples are of the order of $\text{La}_{0.9}\text{Sr}_{0.1}\text{Ga}_{0.8}\text{Mg}_{0.1}\text{Mn}_{0.1}\text{O}_{3-\delta} < \text{La}_{0.9}\text{Sr}_{0.1}\text{Ga}_{0.75}\text{Mg}_{0.15}\text{Mn}_{0.1}\text{O}_{3-\delta} < \text{La}_{0.9}\text{Sr}_{0.1}\text{Ga}_{0.7}\text{Mg}_{0.2}\text{Mn}_{0.1}\text{O}_{3-\delta}$.

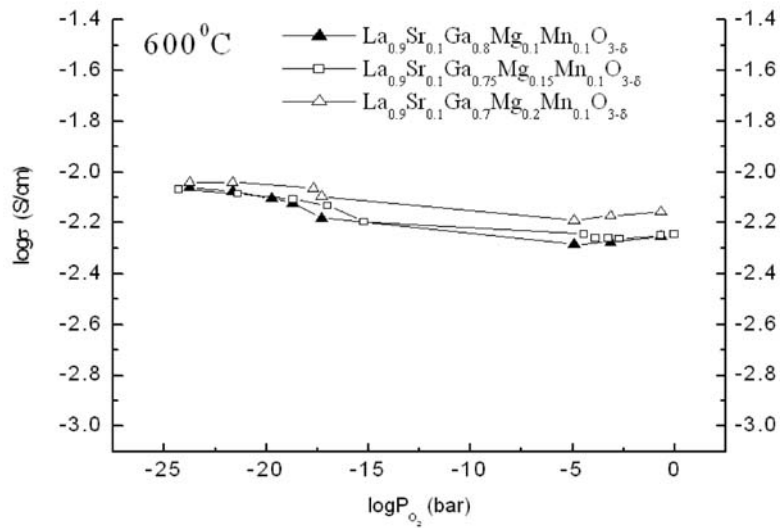
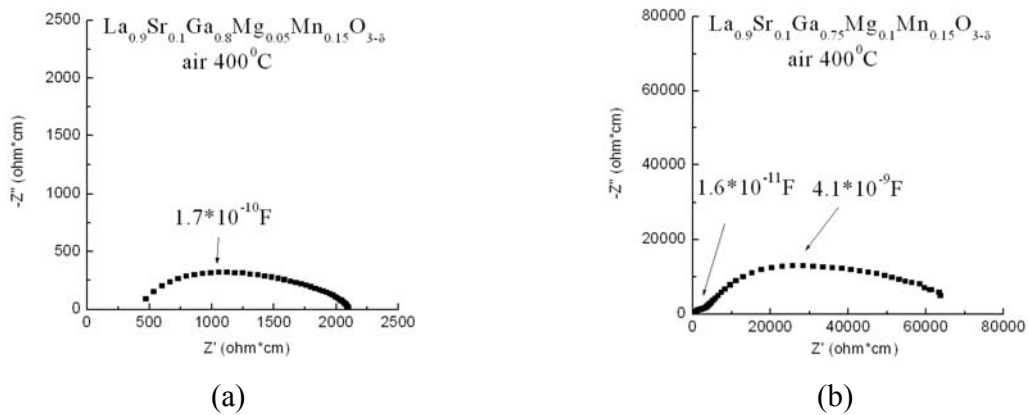


Figure 7.42. Brouwer diagram of the total conductivity of $\text{La}_{0.9}\text{Sr}_{0.1}\text{Ga}_{0.9-y}\text{Mg}_y\text{Mn}_{0.1}\text{O}_{3-\delta}$ ($y=0.1, 0.15, 0.2$) at 600°C .

7.2.3.2c. $\text{La}_{0.9}\text{Sr}_{0.1}\text{Ga}_{0.85-y}\text{Mg}_y\text{Mn}_{0.15}\text{O}_{3-\delta}$ ($y=0.05, 0.1, 0.15, 0.2$)

The impedance plots of $\text{La}_{0.85}\text{Sr}_{0.1}\text{Ga}_{0.9-y}\text{Mg}_y\text{Mn}_{0.15}\text{O}_{3-\delta}$ ($y=0.05, 0.1, 0.15, 0.2$) at 400°C in air are shown in figure 7.43. $\text{La}_{0.9}\text{Sr}_{0.1}\text{Ga}_{0.8}\text{Mg}_{0.05}\text{Mn}_{0.15}\text{O}_{3-\delta}$ and $\text{La}_{0.9}\text{Sr}_{0.1}\text{Ga}_{0.75}\text{Mg}_{0.1}\text{Mn}_{0.15}\text{O}_{3-\delta}$ in figure 7.43(a) and 7.43(b) exhibit typical behavior when there is an electronic conduction in parallel with the ionic conduction. Figure 7.43(c) and 7.43(d) show that $\text{La}_{0.9}\text{Sr}_{0.1}\text{Ga}_{0.7}\text{Mg}_{0.15}\text{Mn}_{0.15}\text{O}_{3-\delta}$ and $\text{La}_{0.9}\text{Sr}_{0.1}\text{Ga}_{0.65}\text{Mg}_{0.2}\text{Mn}_{0.15}\text{O}_{3-\delta}$ are still predominantly ionic conductors in air.



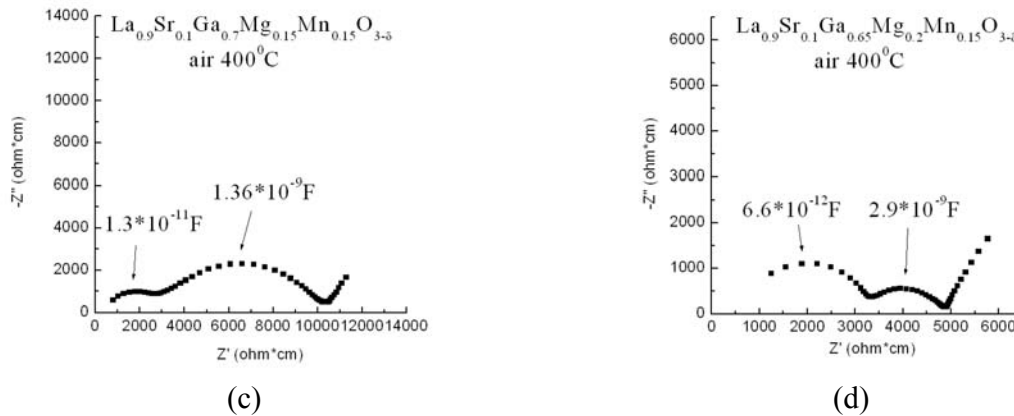


Figure 7.43. Nyquist plots of $\text{La}_{0.9}\text{Sr}_{0.1}\text{Ga}_{0.85-y}\text{Mg}_y\text{Mn}_{0.15}\text{O}_{3-\delta}$ at 400°C in air.

$\text{La}_{0.9}\text{Sr}_{0.1}\text{Ga}_{0.8}\text{Mg}_{0.05}\text{Mn}_{0.15}\text{O}_{3-\delta}$ exhibits electronic conduction at all measured temperatures ($200^\circ\text{C}\sim 800^\circ\text{C}$). Each of the impedance spectra consists of a distorted arc, indicating a comparable ionic conductivity to electronic conductivity. If the electronic conductivity is much larger than the ionic conductivity, then there should only be a dot in the Nyquist plot, but not an arc. The arc consists of overlapped semicircles. Using Eqs.(7.7~7.8), the bulk and electronic conductivity can be calculated. The results are listed in Table 7.7, and the corresponding Arrhenius plots are shown in figure 7.44.

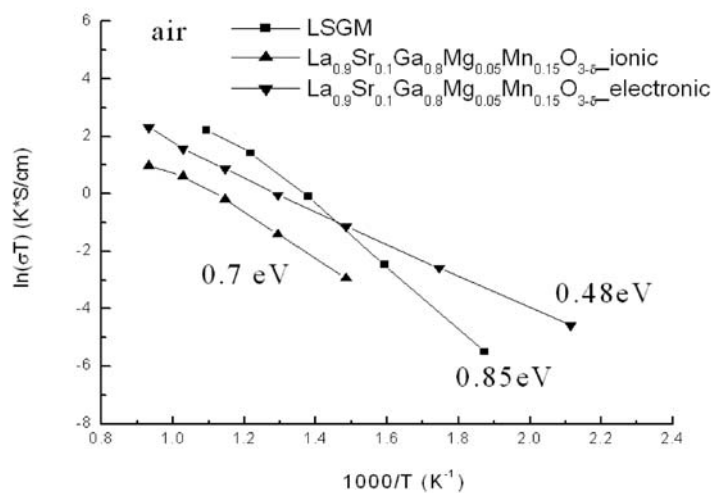


Figure 7.44. Arrhenius plots of the ionic and electronic conductivities of $\text{La}_{0.9}\text{Sr}_{0.1}\text{Ga}_{0.8}\text{Mg}_{0.05}\text{Mn}_{0.15}\text{O}_{3-\delta}$ in air. The ionic and electronic conductivities were calculated here using the model given by Huggins.

Table 7.7 Ionic and electronic resistivities of $\text{La}_{0.9}\text{Sr}_{0.1}\text{Ga}_{0.8}\text{Mg}_{0.05}\text{Mn}_{0.15}\text{O}_{3-\delta}$ in air.

	R_1 (Ωcm)	R_2 (Ωcm)	R_3 (Ωcm)	R_b (Ωcm)	R_b+Rg_b (Ωcm)	R_e (Ωcm)
200 ^o C			42400			42400
300 ^o C			7500			7500
400 ^o C	450	1800	2100	573	12600	2100
500 ^o C	320	700	900	496	3150	815
600 ^o C		280	382		1049	382
700 ^o C		147	204		526	204
800 ^o C		82	103		402	103

$\text{La}_{0.9}\text{Sr}_{0.1}\text{Ga}_{0.75}\text{Mg}_{0.1}\text{Mn}_{0.15}\text{O}_{3-\delta}$ shows electronic behavior in the impedance plots below 500^oC. The bulk resistivities calculated using Eq.(7.8) are listed in Table 7.8. The bulk values of $\text{La}_{0.9}\text{Sr}_{0.1}\text{Ga}_{0.7}\text{Mg}_{0.15}\text{Mn}_{0.15}\text{O}_{3-\delta}$ and $\text{La}_{0.9}\text{Sr}_{0.1}\text{Ga}_{0.65}\text{Mg}_{0.2}\text{Mn}_{0.15}\text{O}_{3-\delta}$ taken from the impedance plots are also listed in Table 7.8 for comparison. The bulk resistivities of the three samples are of the same order of magnitude. Although the electronic resistance is more than one order of magnitude higher than the bulk resistance, the very low ionic conductivity is due to the large impeding effect from the grain boundary. Since the activation energy for ionic conduction is larger than that for electronic conduction, the ionic conductivity increases faster with temperature. Figure 7.45 shows the bulk and electronic conductivities of $\text{La}_{0.9}\text{Sr}_{0.1}\text{Ga}_{0.75}\text{Mg}_{0.1}\text{Mn}_{0.15}\text{O}_{3-\delta}$ in air.

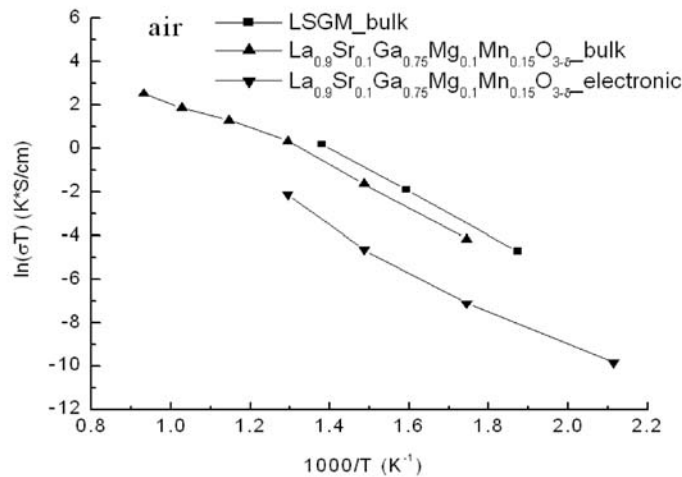


Figure 7.45. Bulk and electronic conductivities of $\text{La}_{0.9}\text{Sr}_{0.1}\text{Ga}_{0.75}\text{Mg}_{0.1}\text{Mn}_{0.15}\text{O}_{3-\delta}$ in air. The bulk conductivity was calculated using Eq. (7.8).

Table 7.8 Bulk resistivities R_b (ohm-cm) of $\text{La}_{0.9}\text{Sr}_{0.1}\text{Ga}_{0.75}\text{Mg}_{0.1}\text{Mn}_{0.15}\text{O}_{3-\delta}$ in air below 500°C .

	$\text{La}_{0.9}\text{Sr}_{0.1}\text{Ga}_{0.75}\text{Mg}_{0.1}\text{Mn}_{0.15}\text{O}_{3-\delta}$			$\text{La}_{0.9}\text{Sr}_{0.1}\text{Ga}_{0.7}\text{Mg}_{0.15}\text{Mn}_{0.15}\text{O}_{3-\delta}$	$\text{La}_{0.9}\text{Sr}_{0.1}\text{Ga}_{0.65}\text{Mg}_{0.2}\text{Mn}_{0.15}\text{O}_{3-\delta}$
	R_1	R_3	R_b		
300°C	35000	700000	36842	30000	35500
400°C	3300	70000	3463	3000	3350
500°C	500	6500	542	530	700

$\text{La}_{0.9}\text{Sr}_{0.1}\text{Ga}_{0.7}\text{Mg}_{0.15}\text{Mn}_{0.15}\text{O}_{3-\delta}$ and $\text{La}_{0.9}\text{Sr}_{0.1}\text{Ga}_{0.65}\text{Mg}_{0.2}\text{Mn}_{0.15}\text{O}_{3-\delta}$ show two distinguishable semicircles, which correspond to bulk and grain boundary conduction. As listed in Table 7.8, their bulk values are in the same order of magnitude. But the grain boundary resistances of $\text{La}_{0.9}\text{Sr}_{0.1}\text{Ga}_{0.7}\text{Mg}_{0.15}\text{Mn}_{0.15}\text{O}_{3-\delta}$ are much larger than those of $\text{La}_{0.9}\text{Sr}_{0.1}\text{Ga}_{0.65}\text{Mg}_{0.2}\text{Mn}_{0.15}\text{O}_{3-\delta}$.

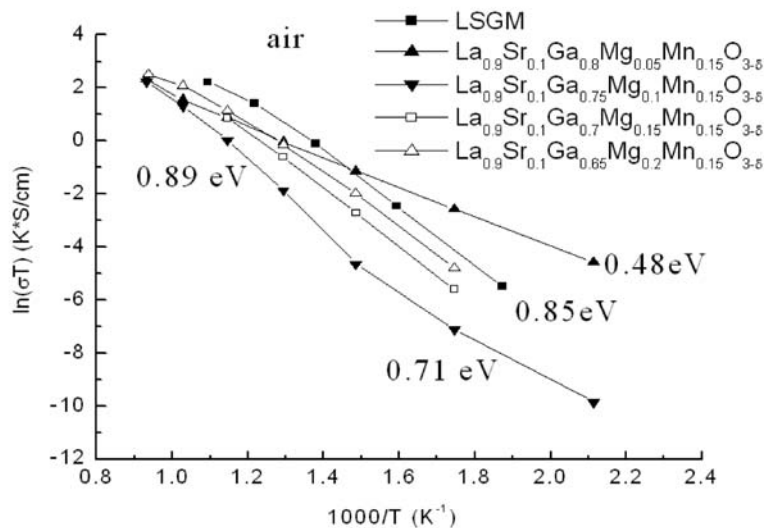


Figure 7.46. Arrhenius plots of the total conductivity of $\text{La}_{0.9}\text{Sr}_{0.1}\text{Ga}_{0.85-y}\text{Mg}_y\text{Mn}_{0.15}\text{O}_{3-\delta}$ ($y=0.05, 0.1, 0.15, 0.2$) in air.

The Arrhenius plots for the total conductivity of $\text{La}_{0.9}\text{Sr}_{0.1}\text{Ga}_{0.85-y}\text{Mg}_y\text{Mn}_{0.15}\text{O}_{3-\delta}$ ($y=0.05, 0.1, 0.15, 0.2$) in air are shown in figure 7.46. $\text{La}_{0.9}\text{Sr}_{0.1}\text{Ga}_{0.8}\text{Mg}_{0.05}\text{Mn}_{0.15}\text{O}_{3-\delta}$ has the highest conductivity below 400°C because of the high electronic conduction. It should be mentioned here that the ‘total’ conductivities of $\text{La}_{0.9}\text{Sr}_{0.1}\text{Ga}_{0.75}\text{Mg}_{0.1}\text{Mn}_{0.15}\text{O}_{3-\delta}$ plotted in figure 7.46, especially at the temperatures below 500°C , are not the real total conductivities, but the electronic conductivities at these temperatures. That’s why the conductivity is much lower than other

compositions. The activation energy changes from 0.71eV to 0.89eV at around 400°C, which means a more ionic contribution to the total conduction at elevated temperatures. The total conductivity of $\text{La}_{0.9}\text{Sr}_{0.1}\text{Ga}_{0.7}\text{Mg}_{0.15}\text{Mn}_{0.15}\text{O}_{3-\delta}$ and $\text{La}_{0.9}\text{Sr}_{0.1}\text{Ga}_{0.65}\text{Mg}_{0.2}\text{Mn}_{0.15}\text{O}_{3-\delta}$ are lower than LSGM. The one with higher amount of Mg has higher ionic conductivity.

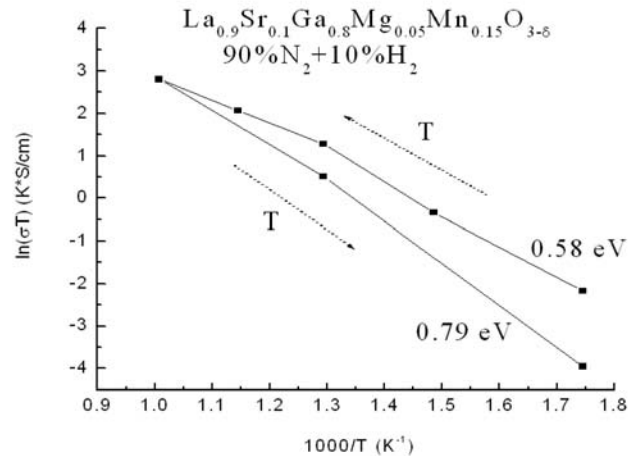


Figure 7.47. Arrhenius plot of the conductivity of $\text{La}_{0.9}\text{Sr}_{0.1}\text{Ga}_{0.8}\text{Mg}_{0.05}\text{Mn}_{0.15}\text{O}_{3-\delta}$ during heating and cooling in forming gas.

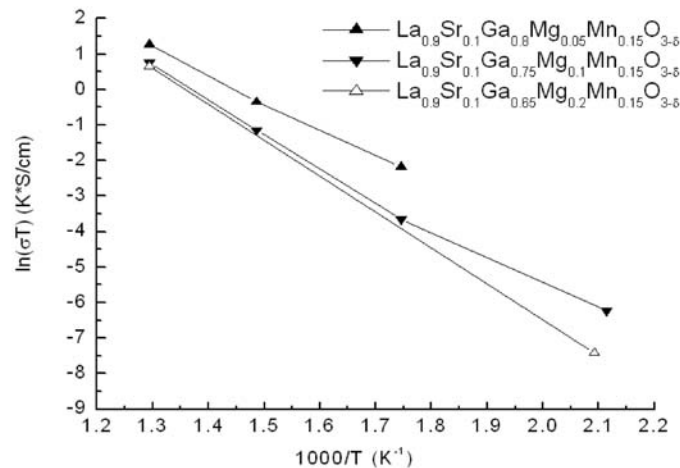


Figure 7.48. Arrhenius plot of the n-type electronic conductivity of $\text{La}_{0.9}\text{Sr}_{0.1}\text{Ga}_{0.85-y}\text{Mg}_y\text{Mn}_{0.15}\text{O}_{3-\delta}$ during heating process of $\text{La}_{0.9}\text{Sr}_{0.1}\text{Ga}_{0.85-y}\text{Mg}_y\text{Mn}_{0.15}\text{O}_{3-\delta}$ in forming gas.

Figure 7.47 shows the Arrhenius plot of $\text{La}_{0.9}\text{Sr}_{0.1}\text{Ga}_{0.8}\text{Mg}_{0.05}\text{Mn}_{0.15}\text{O}_{3-\delta}$ in forming gas. As reduction of Mn starts when heated in reducing atmospheres, the n-type electronic conductivity of $\text{La}_{0.9}\text{Sr}_{0.1}\text{Ga}_{0.8}\text{Mg}_{0.05}\text{Mn}_{0.15}\text{O}_{3-\delta}$ will increase until a certain amount of Mn is reduced, while the ionic conductivity will also increase at the same time. During heating, n-type conductivity is predominant, and the activation energy is 0.58eV. During cooling, Mn cannot be oxidized in forming gas. The total conductivity is predominantly ionically conducting, with an activation energy of 0.79eV. Such kind of behavior was also found for other samples below 500°C. Figure 7.48 shows the n-type electronic conductivity of $\text{La}_{0.9}\text{Sr}_{0.1}\text{Ga}_{0.85-y}\text{Mg}_y\text{Mn}_{0.15}\text{O}_{3-\delta}$ in forming gas. With increasing amount of Mg, the electronic conductivity decreases slightly.

Figure 7.49 shows the Arrhenius plots for the total conductivity of $\text{La}_{0.9}\text{Sr}_{0.1}\text{Ga}_{0.85-y}\text{Mg}_y\text{Mn}_{0.15}\text{O}_{3-\delta}$ ($y=0.05, 0.1, 0.2$) in forming gas. Only the data taken from cooling process are plotted. All the samples show similar total conductivities as in the case of LSGM after heating in reducing conditions.

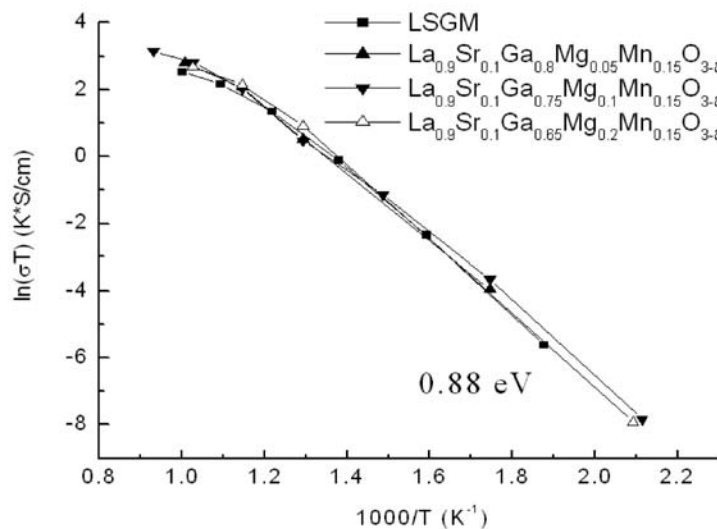


Figure 7.49. Arrhenius plots of the total conductivity of $\text{La}_{0.9}\text{Sr}_{0.1}\text{Ga}_{0.85-y}\text{Mg}_y\text{Mn}_{0.15}\text{O}_{3-\delta}$ ($y=0.05, 0.1, 0.2$) in forming gas.

The total conductivities of $\text{La}_{0.9}\text{Sr}_{0.1}\text{Ga}_{0.85-y}\text{Mg}_y\text{Mn}_{0.15}\text{O}_{3-\delta}$ ($y=0.05, 0.1, 0.15, 0.2$) as a function of the oxygen partial pressure at 600°C are shown in figure 7.50. All the samples increase their conductivities under reducing conditions due to the increased n-type electronic and ionic conduction.

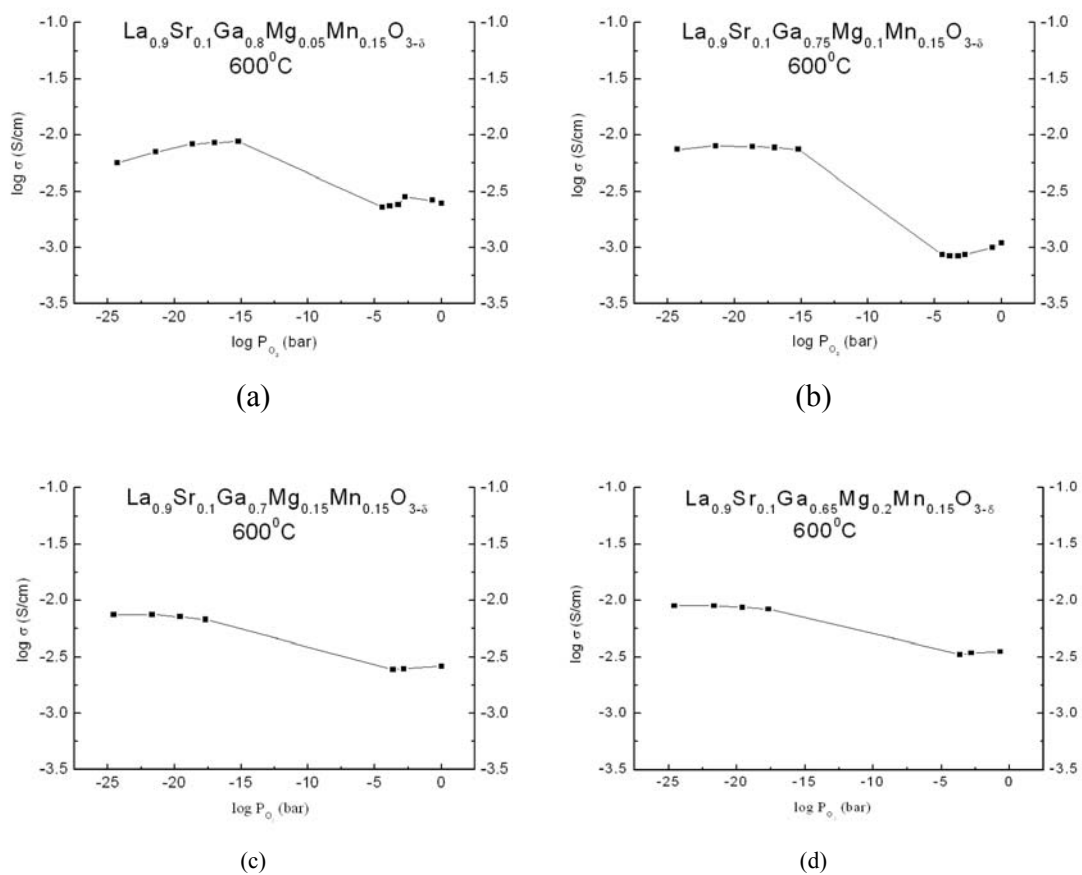


Figure 7.50. Brouwer diagrams of the total conductivity of $\text{La}_{0.9}\text{Sr}_{0.1}\text{Ga}_{0.85-y}\text{Mg}_y\text{Mn}_{0.15}\text{O}_{3-\delta}$ ($y=0.05, 0.1, 0.15, 0.2$) at 600°C .

7.2.3.3 Summary

(a). Effect on the ionic conductivity in air

Although the main purpose of doping Mn into LSGM in this study is to investigate the electronic conduction, it's also important not to deteriorate the ionic conductivity significantly. Mn exists in the samples mainly in a high valence state (+3, +4) after preparation. Replacement of Ga by trivalent or tetravalent Mn will decrease the ionic conductivity because of decreased concentration of oxygen vacancy. Generally speaking, the ionic conductivity of $\text{La}_{0.9}\text{Sr}_{0.1}\text{Ga}_{1-y-x}\text{Mg}_y\text{Mn}_x\text{O}_{3-\delta}$ ($x, y=0\sim 0.2$) decreases with increasing amount of Mn. For example, at 500°C in air ($2.92\times 10^{-3}\text{S/cm}$ for LSGM),

$$\sigma_{\text{Mg}_{0.15}\text{Mn}_{0.05}} (2.86\times 10^{-3}\text{S/cm}) > \sigma_{\text{Mg}_{0.1}\text{Mn}_{0.1}} (1.78\times 10^{-3}\text{S/cm}) > \sigma_{\text{Mg}_{0.05}\text{Mn}_{0.15}} (3.17\times 10^{-4}\text{S/cm})$$

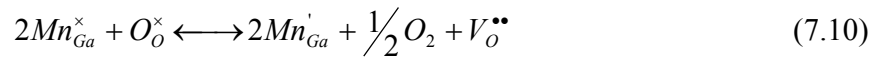
$$\sigma_{\text{Mg}_{0.2}\text{Mn}_{0.05}} (2.94\times 10^{-3}\text{S/cm}) > \sigma_{\text{Mg}_{0.15}\text{Mn}_{0.1}} (1.89\times 10^{-3}\text{S/cm}) > \sigma_{\text{Mg}_{0.1}\text{Mn}_{0.15}} (1.54\times 10^{-4}\text{S/cm})$$

$$\sigma_{\text{Mg}_{0.2}\text{Mn}_{0.1}} (2.42\times 10^{-3}\text{S/cm}) > \sigma_{\text{Mg}_{0.2}\text{Mn}_{0.1}} (1.14\times 10^{-3}\text{S/cm}) > \sigma_{\text{Mg}_{0.2}\text{Mn}_{0.2}} (2.67\times 10^{-4}\text{S/cm})$$

Keeping the same amount of Ga, the ionic conductivity decreases with increasing amount of Mn, for less Mg means less oxygen vacancies. While at a same doping level of Mn, the ionic conductivity increases with increasing of Mg content, except for $\text{La}_{0.9}\text{Sr}_{0.1}\text{Ga}_{0.75}\text{Mg}_{0.1}\text{Mn}_{0.15}\text{O}_{3-\delta}$, which has a very large grain boundary resistance.

(b). Effect on the ionic conductivity under reducing conditions

Under reducing conditions, trivalent Mn can be reduced to divalent cation, generating oxygen vacancies.



Both ionic and n-type electronic conductivities should be increased. It should be mentioned again here that all the Mn containing samples have a conductivity difference between the first heating and cooling below 500°C . The total conductivity became lower during cooling, as shown in figure 7.45. This difference can be explained by the reduction of Mn. The n-type conduction occurs via a hopping mechanism, which requires sufficient amount of Mn^{2+} and Mn^{3+} so that mobile electrons can jump from one Mn to a neighboring one, but with different valence. If more Mn^{3+} is reduced at high temperature, then the electronic conductivity will be decreased. The data taken from the cooling process were used to plot the Arrhenius diagrams, if not specially mentioned.

For all the compositions, except for $\text{La}_{0.9}\text{Sr}_{0.1}\text{Ga}_{0.8}\text{Mn}_{0.2}\text{O}_{3-\delta}$ and $\text{La}_{0.9}\text{Sr}_{0.1}\text{Ga}_{0.7}\text{Mg}_{0.1}\text{Mn}_{0.2}\text{O}_{3-\delta}$, higher conductivities were found at low oxygen partial pressures. The difference of the conductivity between high and low oxygen partial pressures is dependent on the concentration of Mn. The larger the amount of Mn there is, the larger is the difference of the conductivity. However, Brouwer diagrams show that the conductivities of all the samples, except for $\text{La}_{0.9}\text{Sr}_{0.1}\text{Ga}_{0.8}\text{Mn}_{0.2}\text{O}_{3-\delta}$, are at the same level ($7.9 \times 10^{-3} \text{S/cm} \sim 9.5 \times 10^{-3} \text{S/cm}$ at 600°C) and fairly constant under reducing atmospheres. So the magnitude of the total conductivity is less influenced by Mn at low oxygen partial pressures than at high oxygen partial pressures. And the larger difference on the conductivity is mainly due to the decreasing ionic conductivity with increasing Mn content at high oxygen partial pressures.

(c). Effect on the electronic conductivity

Compared to LSGM, the typical low frequency tail in the Nyquist plot due to the blocking behavior from the sample/electrode interfaces is greatly minimized or completely removed in all Mn containing compositions under reducing conditions, suggesting the existence of n-type conductivity. Kiukkola-Wagner measurements also suggest the predominant effect of electronic conduction at low oxygen partial pressures. There is no doubt that the n-type conduction is the result of Mn doping, and it seems easy to understand the increase of total conductivity under reducing conditions, especially for the samples which have high Mn Content. The only exceptions are $\text{La}_{0.9}\text{Sr}_{0.1}\text{Ga}_{0.8}\text{Mn}_{0.2}\text{O}_{3-\delta}$ and $\text{La}_{0.9}\text{Sr}_{0.1}\text{Ga}_{0.7}\text{Mg}_{0.1}\text{Mn}_{0.2}\text{O}_{3-\delta}$, which are predominantly p-type electronic conductors at both high and low oxygen partial pressures. The n-type conductivities of several compositions have been shown by analyzing the impedance plots using a simple approach. However, this method is indirect to samples, which have insignificant portion of the electronic conduction. Therefore it's difficult to separate the electronic conductivity from ionic conductivity by this simple method for all the compositions. To do so, different techniques such as DC measurement and Hebb-Wagner polarization measurement should be applied.

For the same reason, p-type conductivity was not quantitatively determined for the samples, whose electronic conductivity could be ignored compared to the ionic conductivity. The p-type conductivity of Mn doped LSGM increases with the amount of Mn. In the present study, ionic conduction is predominant in 5mol% and 10mol% Mn doped samples, and no obvious electronic conduction was found. In 15-mol% Mn doped samples, $\text{La}_{0.9}\text{Sr}_{0.1}\text{Ga}_{0.8}\text{Mg}_{0.05}\text{Mn}_{0.15}\text{O}_{3-\delta}$ and $\text{La}_{0.9}\text{Sr}_{0.1}\text{Ga}_{0.75}\text{Mg}_{0.1}\text{Mn}_{0.15}\text{O}_{3-\delta}$ exhibit electronic behavior in air. The electronic conductivity obtained from impedance measurement decreases with increasing Mg content. For example, at 500°C ,

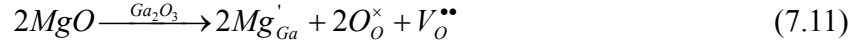
$$\sigma_{\text{La}_{0.9}\text{Sr}_{0.1}\text{Ga}_{0.8}\text{Mg}_{0.05}\text{Mn}_{0.15}\text{O}_{3-\delta}} (1.11 \times 10^{-3} \text{S/cm}) > \sigma_{\text{La}_{0.9}\text{Sr}_{0.1}\text{Ga}_{0.75}\text{Mg}_{0.1}\text{Mn}_{0.15}\text{O}_{3-\delta}} (1.54 \times 10^{-4} \text{S/cm}).$$

In 20mol% Mn doped samples, all compositions show electronic conductivities. At 500°C , the p-type conductivities are in the following order:

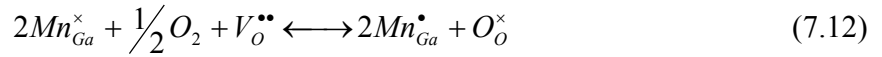
$$\sigma_{\text{Ga}_{0.8}\text{Mn}_{0.2}} (1.82 \times 10^{-2} \text{S/cm}) > \sigma_{\text{Mg}_{0.1}\text{Mn}_{0.2}} (4.87 \times 10^{-3} \text{S/cm}) > \sigma_{\text{Mg}_{0.15}\text{Mn}_{0.2}} (5.26 \times 10^{-4} \text{S/cm})$$

With increasing amount of Mg, the p-type electronic conductivity decreases. Such kind of relation can be explained in the following way:

When Ga is replaced by Mg, oxygen vacancies can be generated:



Under oxidizing conditions, Mn can be oxidized:



with the equilibrium constant:

$$K = \frac{[\text{Mn}^\bullet_{\text{Ga}}]^2}{[\text{Mn}^\times_{\text{Ga}}]^2 \cdot [\text{V}^{\bullet\bullet}_{\text{O}}] \cdot P_{\text{O}_2}^{1/2}} \quad (7.13)$$

The electroneutrality condition is:

$$[\text{Sr}'_{\text{La}}] + [\text{Mg}'_{\text{Ga}}] = p + 2[\text{V}^{\bullet\bullet}_{\text{O}}] + [\text{Mn}^\bullet_{\text{Ga}}] \quad (7.14)$$

in which the very small concentration of electrons is not considered here. Eq. (7.14) can be rewritten to:

$$\text{const.} \approx p + [\text{Mn}^\bullet_{\text{Ga}}] \quad (7.15)$$

When $[\text{V}^{\bullet\bullet}_{\text{O}}]$ is increased in Eq. (7.13) due to the increased concentration of Mg, $[\text{Mn}^\times_{\text{Ga}}]$ and $[\text{Mn}^\bullet_{\text{Ga}}]$ will be decreased and increased, respectively. Then from Eq. (7.15), the p-type conductivity should be decreased.

7.3. References

- [1]. T. Ishihara, Y. Tsuruta, Yu Chungying, T. Todaka, H. Nishiguchi, Y. Takita, *J. Electrochem. Soc.* 150 (1), 2003, E17.
- [2]. H. Arikawa, T. Yamada, T. Ishihara, H. Nishiguchi, Y. Takita, *Chem. Lett.* 1999, 1257.
- [3]. T. Ishihara, T. Yamada, H. Arikawa, H. Nishiguchi, Y. Takita, *Solid State Ionics* 135, 2000, 631.
- [4]. R.T. Baker, B. Gharbage, F.M. Marques, *J. Electrochem. Soc.* 144 (9), 1997, 3130.
- [5]. Peng-nian, Huang, Anthony Petric, *J. Electrochem. Soc.* 143 (5), 1996, 1644.
- [6]. Keqin Huang, Robin S. Tichy, J.B. Goodenough, *J. Am. Ceram. Soc.* 81 (10), 1998, 2565.
- [7]. M.S. Islam, P.R. Slater, J.R. Tolchard, T. Dings, *Dalton Trans.* 2004, 3061.
- [8]. V.V. Kharton, A.P. Viskup, A.A. Yaremchenko, R.T. Baker, B. Gharbage, G.C. Mather, F.M. Figueiredo, E.N. Naumovich, F.M.B. Marques, *Solid State Ionics* 132, 2000, 119.
- [9]. K. Huang, M. Feng, C. Milliken, J.B. Goodenough, *J. Electrochem. Soc.* 144, 1997, 3620.
- [10]. A. Cüneyt Tas, P.J. Majewski, F. Aldinger, *J. Am. Ceram. Soc.* 83 (12), 2000, 2954.
- [11]. Keqin Huang, Robin S. Tichy, J.B. Goodenough, *J. Am. Ceram. Soc.* 81 (10), 1998, 2576.
- [12]. T. Ishihara, H. Matsuda, Y. Takity, *Solid State Ionics* 79, 1995, 147.
- [13]. Robert A. Huggins, *Ionics* 8, 2002, 300.
- [14]. V. Thangadurai, A.K. Shukla, J. Gopalakrishnan, *Chem. Commun.* 1998, 2647.

Chapter 8

Summary

Different from the traditional PEN structured fuel cells, the novel SEA (Single Element Arrangement) concept consists of a single material to complete the whole galvanic cell. The essential of the SEA concept is the in-situ electrode formation. Such kind of material becomes mixed ionic and electronic conducting in the surface region, while still being predominantly ionically conducting inside under the working conditions. The surface region could be either n type or p type electronic conducting depending on the oxygen activity. Separate electrodes can therefore be omitted if the electronic conductivity in the surface region is high enough. The electronic short circuit will be blocked by the region where ionic conduction is dominant, allowing the generation of electromotive force. Since the oxygen activity drops continuously through the material from cathode to anode, there must be such a region in between. The advantages of SEA are obvious. Any impeding effects and matching problems at the interfaces between electrolyte and electrodes can be eliminated or highly reduced.

In this work, several materials that were considered to be possible candidates for SEA applications were investigated, with the focus on modification of the electronic conductivity by appropriate doping in the well-known electrolyte materials, including samarium doped ceria (SDC), yttria doped barium cerate and LSGM.

There are a number of methods being normally used to separate the electronic and ionic components of the total charge transport. These methods include Faraday's method, Hebb-Wagner method and open circuit potential method. A relatively new and simple technique was mostly used in this work to evaluate the electronic and ionic contributions to the total conduction. This technique is based on AC impedance spectroscopy using ion-blocking electrodes. It's easy to determine whether there is an electronic leakage through the sample by looking at the capacitive tail at low frequencies in the Nyquist plot. If such tail is invisible, then there is considerable electronic conduction through the sample. In this case, interpretation of the intersections with the real axis in Nyquist diagram will be different from the case when there is only ionic conduction. Information of electronic and ionic resistivities can be derived from these intersections.

(a) Materials based on SDC

SDC was chosen as the starting material because it has high oxide ion conductivity, and Ce can be reduced at low oxygen partial pressure, leading n-type conduction. Pr and several other metal ions (Bi, Co, Cr, Cu, Fe, Sb, V) were doped into SDC to try to improve the p-type conductivity in air.

Up to 15-mol% Pr was doped into SDC in two groups. In one group the amount of Sm was

kept constant ($\text{Ce}_{0.8-x}\text{Sm}_{0.2}\text{Pr}_x\text{O}_{2-\delta}$), while in the other group the amount of Ce was kept constant ($\text{Ce}_{0.8}\text{Sm}_{0.2-x}\text{Pr}_x\text{O}_{2-\delta}$).

Among the $\text{Ce}_{0.8-x}\text{Sm}_{0.2}\text{Pr}_x\text{O}_{2-\delta}$ samples, the ionic conductivity decreases with increasing amount of Pr. 20-mol% Sm doped ceria is known to have the highest conductivity among ceria based materials. Replacing Ce by Pr will generate more oxygen vacancies, which will cause large distortion of the structure but not contribute to the conduction. The increased number of oxygen vacancies will facilitate the incorporation of oxygen from surrounding atmospheres at high oxygen partial pressures, which will increase the number of electron holes. The mobile electron holes can be transferred by hopping between Pr^{3+} and Pr^{4+} . Thus, the p-type conductivity increases with increasing number of Pr. For example, the p-type electronic conductivity at 600°C in air increases from $\text{Ce}_{0.77}\text{Sm}_{0.2}\text{Pr}_{0.03}\text{O}_{2-\delta}$ ($5.15 \times 10^{-4} \text{S/cm}$) to $\text{Ce}_{0.7}\text{Sm}_{0.2}\text{Pr}_{0.1}\text{O}_{2-\delta}$ ($3.80 \times 10^{-3} \text{S/cm}$). In this group of samples, Pr has an effect of shifting the electrolyte domain boundary to lower oxygen partial pressures. With increasing Pr content, the n-type conductivity decreases under reducing conditions, partially also due to the reduced amount of Ce. For instance, the electronic conductivity at 600°C in H_2 is $1.99 \times 10^{-2} \text{S/cm}$ for $\text{Ce}_{0.77}\text{Sm}_{0.2}\text{Pr}_{0.03}\text{O}_{2-\delta}$ and $1.58 \times 10^{-3} \text{S/cm}$ for $\text{Ce}_{0.7}\text{Sm}_{0.2}\text{Pr}_{0.1}\text{O}_{2-\delta}$.

Among the $\text{Ce}_{0.8}\text{Sm}_{0.2-x}\text{Pr}_x\text{O}_{2-\delta}$ samples, the total conductivity increases with the Pr content due to the increased p-type conductivity. The highest electron hole conductivity at 700°C in air was found to be $5.62 \times 10^{-3} \text{S/cm}$ for $\text{Ce}_{0.8}\text{Sm}_{0.05}\text{Pr}_{0.15}\text{O}_{2-\delta}$. Although the n-type electronic conductivity of $\text{Ce}_{0.8}\text{Sm}_{0.05}\text{Pr}_{0.15}\text{O}_{2-\delta}$ is lower than SDC, they are of the same order of magnitude. Based on the Brouwer diagrams of the total conductivity, $\text{Ce}_{0.8}\text{Sm}_{0.05}\text{Pr}_{0.15}\text{O}_{2-\delta}$ was supposed to be a possible composition for SEA concept among all of the Pr doped samples. The thermal expansion coefficient of $\text{Ce}_{0.8}\text{Sm}_{0.05}\text{Pr}_{0.15}\text{O}_{2-\delta}$ was measured to be $18 \times 10^{-6} / \text{K}$. The problems related to the thermal expansion and reduction expansion should be solved prior to the fuel cell test.

Several other metal ions (Bi, Co, Cr, Cu, Sb, V) were also doped into SDC. The amount of dopant was adjusted to keep the same calculated oxygen deficiency. No obvious improvement on the electronic conduction was observed in these materials.

(b) Materials based on BCY

It's known that doped BaCeO_3 shows mixed proton and electron conduction in the presence of moisture, whereas in dry oxidizing atmospheres, it exhibits mixed oxide ion and electron hole conducting properties. In order to improve the electronic conductivity under reducing conditions, TiO_2 was tried to mix with $\text{BaCe}_{0.76}\text{Y}_{0.2}\text{Pr}_{0.04}\text{O}_{3-\delta}$ in a molar ratio of 1:10. After sintering at 1600°C , TiO_2 is completely dissolved in $\text{BaCe}_{0.76}\text{Y}_{0.2}\text{Pr}_{0.04}\text{O}_{3-\delta}$. Thus both the ionic and electron hole conductivity of $\text{BaCe}_{0.76}\text{Y}_{0.2}\text{Pr}_{0.04}\text{O}_{3-\delta}$ are lowered by an order of magnitude by mixing with TiO_2 , because the number of oxygen vacancies is largely reduced by the replacement of a lower valent cation, i.e. Y^{3+} or Pr^{3+} , by a higher valent cation Ti^{4+} . A composite electrolyte, $\text{BaCe}_{0.8}\text{Y}_{0.2}\text{O}_{2.9} + \text{Ce}_{0.8}\text{Sm}_{0.2}\text{O}_{1.9}$, was also prepared in view of the reduction of SDC under

reducing conditions and the electron hole conduction of BCY under oxidizing conduction. There is no side product between SDC and BCY after sintering at 1600°C. The conductivity of the two phase mixture is lower than each of the individual material especially at temperatures lower than 600°C, suggesting a large impeding effect from the interface between the two compositions.

(c) Materials based on LSGM

LSGM is a well-known ionic conductor over a wide range of oxygen activities. Doping of transition metals such as Fe, Co, Mn in LSGM was reported to increase the electron hole conductivity. Few authors also reported the n-type conduction introduced by Mn. So Mn was chosen to improve both n and p-type conductivities.

Replacement of Ga or Mg by trivalent or tetravalent Mn will decrease the ionic conductivity because of the decreased concentration of oxygen vacancies. The ionic conductivity decreases with increasing amount of Mn. For instance, $\text{La}_{0.9}\text{Sr}_{0.1}\text{Ga}_{0.8}\text{Mg}_{0.15}\text{Mn}_{0.05}\text{O}_{3-\delta}$ ($2.86 \times 10^{-3} \text{S/cm}$) has higher ionic conductivity than $\text{La}_{0.9}\text{Sr}_{0.1}\text{Ga}_{0.6}\text{Mg}_{0.2}\text{Mn}_{0.2}\text{O}_{3-\delta}$ ($2.67 \times 10^{-4} \text{S/cm}$) at 500°C in air. At the same doping level of Mn, the ionic conductivity increases with increasing Mg content because of the increasing amount of oxygen vacancies.

All the investigated compositions in this study are inside of a compositional triangle with LSGM, $\text{La}_{0.9}\text{Sr}_{0.1}\text{Ga}_{0.8}\text{Mn}_{0.2}\text{O}_{3-\delta}$ and $\text{La}_{0.9}\text{Sr}_{0.1}\text{Ga}_{0.6}\text{Mg}_{0.2}\text{Mn}_{0.2}\text{O}_{3-\delta}$ at the three corners, respectively. $\text{La}_{0.9}\text{Sr}_{0.1}\text{Ga}_{0.8}\text{Mn}_{0.2}\text{O}_{3-\delta}$ is a predominant p-type electronic conductor over the entire range of the interested oxygen partial pressures ($P_{\text{O}_2} = 10^{-25} \sim 1 \text{bar}$); $\text{La}_{0.9}\text{Sr}_{0.1}\text{Ga}_{0.6}\text{Mg}_{0.2}\text{Mn}_{0.2}\text{O}_{3-\delta}$ is a predominant ionic conductor at high oxygen partial pressures, and shows n-type electronic conductivity under reducing conditions ($\sim 7.08 \times 10^{-3} \text{S/cm}$ at 600°C). So there should be a composition inside the triangle, which will be predominantly electronic conducting at high and low oxygen partial pressures, and ionic conducting at intermediate oxygen partial pressures.

All the Mn containing samples show electronic conducting behaviour under reducing atmospheres. The electrolyte/electrode process can be largely improved by Mn, due to the increased electronic conduction in the surface region and the catalytic effect of Mn, which is more effective to the oxidation of H_2 than to the reduction of O_2 . Thus, Mn containing perovskite materials should also be possibly used as anode materials for SOFC.

p-type conductivity of Mn doped LSGM increases with the amount of Mn, and decrease with increasing Mg content. At 500°C,

$$\sigma_{\text{Ga}_{0.8}\text{Mn}_{0.2}} (1.82 \times 10^{-2} \text{S/cm}) > \sigma_{\text{Mg}_{0.1}\text{Mn}_{0.2}} (4.87 \times 10^{-3} \text{S/cm}) > \sigma_{\text{Mg}_{0.15}\text{Mn}_{0.2}} (5.26 \times 10^{-4} \text{S/cm})$$

It has been observed that both 15-mol% Pr doped SDC and 15~20mol% Mn doped LSGM showed interesting properties, which are close to the requirement of SEA. The suitable material may have a very narrow range of stoichiometry. This region has already been largely narrowed in this work.

Chapter 9

Outlook

In view of the simple construction, absence of the problems arising from thermal mismatch and impeding effect at the electrolyte/electrodes interfaces, SEA concept is considered to be a promising candidate for ITSOFC. Our initial study has shown that n and p-type electronic conductions were observed in a single material under reducing and oxidizing atmospheres, respectively. Materials based on Pr doped SDC and Mn doped LSGM have been investigated to a certain extent. One big hurdle to overcome for the further investigation of Pr doped samples is the poor mechanical strength at high temperature. Both thermal and reductional expansions, in view of the Ce^{4+}/Ce^{3+} and Pr^{3+}/Pr^{4+} transformation, always cause cracking and failure of the samples. One possible way to solve this type of problem is to enhance the mechanical strength, while still keeping the electrical property by proper doping. LSGM itself has the problem in preparation because of the narrow stoichiometry range. When Mn is involved, this region is further narrowed. Small amount of variation in the Mn content may lead large change in the electrical property. The stoichiometry region, where the suitable compositions for SEA concept are located, has been narrowed to a great extent in the compositional triangle. Tailoring of the components inside the small region is necessary to achieve the right compositions. Composite electrolyte might also be a choice for the purpose. Although it's not a really 'single' material, the composition is still homogeneously distributed throughout the sample. Problems due to the large expansion might also be easily solved by choosing the components with different expansion coefficient.

Acknowledgements

My grateful acknowledgements are due to:

Prof. Werner. Weppner: for his invaluable guidance, patient and scientific discussions, continuous support and encouragement;

Prof. Franz. Faupel
Prof. Helmut. Föll examination committee
Dr. habil. George Popkirov

Prof. Eckhard. Quandt for his kind support;

Dr. Wing-Fong Chu: for his useful discussions and kind support in my study and research;

Gregor Holstermann: for his warmhearted guidance and important assistance in experimental aspect. Many thanks are due to him for his help and friendship;

All members in the chair: for the nice working and living atmosphere;

Y.M. Zhu and W. Chen: for our friendships;

My family.

Curriculum Vitae

Name	Fang, Qingping
Date of birth	Dec. 06th, 1976
Place of birth	Hunan, P.R. China
09.1983~06.1989	Primary school of Zhengzhou University of Light Industry Zhengzhou, Henan province, P.R. China
09.1989~06.1995	Henan Province Experimental High School Zhengzhou, Henan province, P.R. China
09.1995~07.1999	B.Sc. in Engineering Mechanics Northwestern Polytechnical University Xi'an, Shanxi province, P.R.China
09.1999~10.2000	Master study in Engineering Mechanics Northwestern Polytechnical University Xi'an, Shanxi province, P.R.China
11.2000~09.2002	M.Sc. in Materials Science Christian-Albrechts-University of Kiel Kiel, Germany
10.2002~04.2007	Ph.D study Chair for Sensors and Solid State Ionics Christian-Albrechts-University of Kiel Kiel, Germany